TESIS DE LA UNIVERSIDAD DE ZARAGOZA

2021

274

Jesús Francisco Beltrán López

Magnetic Refrigeration: Design, construction and evaluation of a valve switched rotary prototype. Numerical modeling of a solid state magnetocaloric heat elevator.

Director/es
Palacios Latasa, Elías

ISSN 2254-7606

Prensas de la Universidad
Universidad Zaragoza

ISSN 2254-7606

Universidad Zaragoza
1542

Tesis Doctoral

MAGNETIC REFRIGERATION: DESIGN, CONSTRUCTION AND EVALUATION OF A VALVE SWITCHED ROTARY PROTOTYPE. NUMERICAL MODELING OF A SOLID STATE MAGNETOCALORIC HEAT ELEVATOR.

Autor

Jesús Francisco Beltrán López

Director/es

Palacios Latasa, Elías

UNIVERSIDAD DE ZARAGOZA
Escuela de Doctorado

Programa de Doctorado en Física

2021

Universidad Zaragoza

Universidad de Zaragoza

Tesis Doctoral

Magnetic Refrigeration:

Design, construction and evaluation of a valve switched rotary prototype.

Numerical modeling of a solid state magnetocaloric heat elevator.

Jesús Francisco Beltrán López

supervised by

Dr. Elías A. Palacios Latasa

May 7, 2021

Señor, dame una brizna de locura
para entender este mundo.

Pedro Beltrán Montesano,
caricaturista, dibujante, pintor, empresario y querido padre.

A mis padres, Pedro e Isabel, allá donde estén,
mi esposa Maricarmen, y mis hijos Valero y María,
verdaderas luces que alumbran mi camino.

Contents

SUMMARY

This work is aimed to bring some new light to the possibilities of magnetic refrigeration technologies to be brought closer to the market, displacing vapor compression systems out of their throne.

In the introduction to this thesis, a brief overview of the basics of this technology and its "boundary conditions" is presented and some discussions and personal reflections are included. A rotary magnetic refrigeration prototype has been designed and built, to test an at the time and to our knowledge, new design. This prototype's singularity resides in the use of solenoid valves in conjunction with a continuous fluid pumping system. Another important remark about this prototype is that the design of the magnet was done using an original optimization process. Some tests with Gd and GdEr compounds were done and their results are presented and discussed, also finding the main sources of losses in the device. A computer simulation model was developed to evaluate the temperature relaxation times of porous packed beds of spheres of a magnetocaloric material, as a function of their diameter. This simulation helped to know the limiting values and select the diameter of the magnetocaloric materials' particles to be used. Finally, a comparative study of the use of thermoelectric-magnetocaloric hybrid systems was done. For this purpose, an original master equation was introduced for the use of this technology with first order transition materials, and a computer model was programmed to carry out simulations under different working conditions. With this, it was determined how the working parameters of the system had to be selected to obtain performance improvements with respect to pure thermoelectric cooling conditions.

The thesis is structured in a general introduction and two separate parts, namely, the building of a rotary magnetic refrigeration prototype and the comparative study of hybrid thermoelectric-magnetocaloric systems. The introduction constitutes a single chapter and the two separate parts comprise eight and two chapters, respectively.

The introduction starts with an analysis of the significance of refrigeration technologies and the importance of reducing their impact in world's energy consumption and their relation with different strategic and ecologic concerns. It follows addressing the need of finding new refrigeration technologies that avoid or minimize the hindrances of vapor compression systems. Magnetocaloric cooling technologies are introduced making a brief historical overview and a short review about relevant magnetocaloric materials and the thermodynamics of the magnetocaloric effect. The introduction ends with an analysis of the cooling power and temperature span conditions to be met by magnetocaloric refrigerators, to comply with European energy labelling regulations. Also, a personal discussion about how to interpret cooling power *versus* temperature span graphs from a practical point of view is presented.

Part I presents the design and construction of a rotary magnetic refrigerator. A complete description of the design process is structured in different sections and subsections that comprehend different parts of the design process. Starting from the basic specifications in chapter 2, the selection of the magnetocaloric materials and their shape is described in chapter 3. This chapter includes a 1D model of thermal relaxation for a packed bed of spheres, that was used to see the limitations of the heat exchange between different diameters of spheres and the fluid flowing through the bed. Chapter 4 explains the process of design of the regenerators block enclosure, describing the main problematic issues to solve and the decisions made about them. This chapter includes also a description of the thermocouple fabrication and installation process, as well as a description of tooling that had to be designed and constructed to obtain shaped screen meshes, to separate and retain the spherical particles in the regenerators. In chapter 5, the optimization of a magnet design using an original process is thoroughly explained. A comparison of the optimized design with measurements of the manufactured magnet is included. In chapter 6, the fluid distribution system design is described and considerations about the piping, thermocouple insertion, cold spot design and pumping system characterization are presented. Chapter 7 describes the data acquisition system. Finally, chapter 8 presents the testing process and the results obtained, to end with a discussion about the losses and sources of inefficiency observed. This discus-

sion includes a thermal relaxation test performed, that points out the location of the principal loss areas in the device.

Part II, although shorter, contains the development of important simulations that light up the path for further consideration of thermoelectric-magnetocaloric-thermoelectric sandwiches as building bricks for not-in-kind magnetic cooling, taking advantage of the best parts of both thermoelectrics and magnetocalorics. Chapter 9 is an introduction where the basic concept is explained and chapter 10 relates the simulation of the hybrid system. In this last chapter describes the model of the sandwich, including the fixed parameters of some commercial Peltier cells used in it, and the particularities to be taken into account when working with first and second order phase transition materials. Of special relevance is the introduction of a master equation that allows proper modeling of the heat transfer in first order transition materials. Pure thermoelectric cooling, pure magnetocaloric cooling with passive thermal diodes, and hybrid magnetocaloric-thermoelectric cooling are compared. Finally, these results are compared with those of other authors and an explanation about their bad results is given.

In addition to this, Appendix C provides a set of drawings with the design of different parts of the prototype and additional tools, developed for the construction of the prototype.

RESUMEN

Este trabajo tiene como objetivo aportar una nueva luz a las posibilidades de que las tecnologías de refrigeración magnética se acerquen al mercado, desplazando de su trono a los sistemas de compresión de vapor.

En la introducción a esta tesis, se presenta una breve descripción de los conceptos básicos de esta tecnología y sus "condiciones de frontera", y se incluyen algunas discusiones y reflexiones personales. Se ha diseñado y construido un prototipo rotatorio de refrigeración magnética para probar lo que, en ese momento y según nuestro conocimiento, constituye un nuevo diseño. La singularidad de este prototipo reside en el uso de electroválvulas en conjunto con un sistema de bombeo de fluido continuo. Otro comentario importante sobre este prototipo es que el diseño del imán se realizó mediante un proceso de optimización original. Se llevaron a cabo algunas pruebas con compuestos Gd y GdEr, y se presentan y discuten sus resultados, encontrando también las principales fuentes de pérdidas en el dispositivo. Se desarrolló un modelo de simulación por ordenador para evaluar los tiempos de relajación de temperatura de lechos porosos de esferas de un material magnetocalórico, en función de su diámetro. Esta simulación ayudó a conocer los valores límite y seleccionar el diámetro de las partículas de los materiales magnetocalóricos a utilizar. Finalmente, se realizó un estudio comparativo del uso de sistemas híbridos termoeléctricos-magnetocalóricos. Para ello, se introdujo una ecuación maestra original para el uso de esta tecnología con materiales de transición de primer orden y se programó un modelo informático para realizar simulaciones en diferentes condiciones de trabajo. Con esto, se determinó cómo debían seleccionarse los parámetros de trabajo del sistema para obtener mejoras de rendimiento con respecto a las condiciones de enfriamiento termoeléctrico puro.

La tesis se estructura en una introducción general y dos partes separadas, a saber, la construcción de un prototipo rotatorio de refrigeración magnética y el estudio comparativo de sistemas híbridos termoeléctrico-magnetocalóricos. La introducción constituye un solo capítulo y las dos partes separadas comprenden ocho y dos capítulos, respectivamente.

La introducción comienza con un análisis de la relevancia de las tecnologías de refrigeración y la importancia de reducir su impacto en el consumo energético mundial, así como su relación con diferentes aspectos estratégicos y ecológicos. A continuación, se aborda la necesidad de encontrar nuevas tecnologías de refrigeración que eviten o minimicen los perjuicios de los sistemas de compresión de vapor. Las tecnologías de enfriamiento magnetocalórico se introducen haciendo un breve resumen histórico y una pequeña revisión sobre los materiales magnetocalóricos relevantes, así como de la termodinámica del efecto magnetocalórico. La introducción finaliza con un análisis de la potencia de refrigeración y las condiciones de salto térmico que deben cubrir los refrigeradores magnetocalóricos, para cumplir con la regulación europea de etiquetado energético. Además, se presenta una discusión personal sobre cómo interpretar los gráficos de salto térmico frente a potencia de enfriamiento desde un punto de vista práctico.

La Parte I presenta el diseño y construcción de un refrigerador magnético rotatorio. Una descripción completa del proceso de diseño está estructurada en diferentes secciones y subsecciones que comprenden diferentes partes del proceso de diseño. A partir de las especificaciones básicas del capítulo 2, la selección de los materiales magnetocalóricos y su forma se describe en el capítulo 3. Este capítulo incluye un modelo 1D de relajación térmica para un lecho de bolas, que se utilizó para ver las limitaciones del intercambio de calor con diferentes diámetros de esferas y el fluido que fluye a través del lecho. El capítulo 4 explica el proceso de diseño de la carcasa del bloque de regeneradores, describiendo las principales problemáticas a resolver y las decisiones tomadas al respecto. Este capítulo incluye también una descripción del proceso de fabricación e instalación de termopares, así como una descripción de las herramientas que tuvieron que diseñarse y construirse para obtener mallas conformadas, para separar y retener las partículas esféricas en los regeneradores. En el capítulo 5, se explica detalladamente la optimización del diseño de un imán mediante un proceso original. Se incluye también una comparación del diseño optimizado con las medidas del imán fabricado. En el capítulo 6, se describe el diseño del sistema de distribución de fluidos y se presentan las consideraciones sobre la tubería, la inserción del termopar, el diseño del punto frío

y la caracterización del sistema de bombeo. El capítulo 7 describe el sistema de adquisición de datos. Finalmente, el capítulo 8 presenta el proceso de prueba y los resultados obtenidos, para finalizar con una discusión sobre las pérdidas y fuentes de ineficiencia observadas. Esta discusión incluye una prueba de relajación térmica realizada, que señala la ubicación de las principales áreas de pérdidas en el dispositivo.

La Parte II, aunque más corta, contiene el desarrollo de importantes simulaciones que iluminan la posibilidad de que los sándwiches termoeléctricos-magnetocalóricos-termoeléctricos sigan siendo considerados como ladrillos de construcción para equipos de enfriamiento magnético alternativo, aprovechando las mejores características de termoeléctricos y magnetocalóricos. El capítulo 9 es una introducción donde se explica el concepto básico y el capítulo 10 relata la simulación del sistema híbrido. En este último capítulo se describe el modelo del sándwich, incluyendo los parámetros fijos de algunas celdas Peltier comerciales que se utilizan en él, y las particularidades a tener en cuenta a la hora de trabajar con materiales de transición de fase de primer y segundo orden. De especial relevancia es la introducción de una ecuación maestra que permite modelar adecuadamente la transferencia de calor en materiales con transición de primer orden. Se comparan el enfriamiento termoeléctrico puro, el enfriamiento magnetocalórico puro con diodos térmicos pasivos y el enfriamiento magnetocalórico-termoeléctrico híbrido. Finalmente, se comparan también estos resultados con los de otros autores y se da una explicación sobre sus malos resultados.

Además de esto, En el Anexo C se proporcionan un conjunto de dibujos con el diseño de diferentes partes del prototipo y utillajes adicionales, desarrollados para la construcción del prototipo.

Nomenclature

Roman characters

$\bar{B}$	Mean magnetic field intensity	[T]
$\bar{d}_{sv}$	Surface to volume mean	[m]
$\dot{Q}_c$	Cooling power	[W]
$\dot{W}$	Work power	[W]
$\mathbf{B}$	Magnetic flux density vector	[T]
$\mathbf{H}$	Internal magnetic field vector	$[\mathrm{A\,m^{-1}}]$
$\mathbf{M}$	Magnetization vector	$[\mathrm{A\,m^{-1}}]$
$\mathcal{E}$	Energy barrier	[J]
$\mathcal{Q}$	Volumetric flow rate	$[\mathrm{m^3\ s^{-1}}]$
$\mathcal{U}$	Overall heat transfer coefficient	$[\mathrm{W\,K^{-1}\,m^{-2}}]$
A	Cross sectional area of bed	$[\mathrm{m^2}]$
a	Specific surface area, ratio of heat transfer surface area of particles to volume of bed	$[\mathrm{m^{-1}}]$
B_J	Brillouin function for spin J	[-]
C	Heat capacity	[J/K]
C	Thermal conductance	$[\mathrm{W\,m^{-2}\,K^{-1}}]$
c	Specific heat capacity	$[\mathrm{J\ Kg^{-1}\ K^{-1}}]$
C_J	Curie's constant for angular momentum J	[K]
COP	Coefficient of performance	[-]
d_p	Particle diameter	[m]
d_{sv}	Surface to volume diameter	[m]
E	Elastic or Young's modulus	[GPa]
Ex_Q	Exergetic cooling power	[W]
F	Functional	
F_N	Number of particles per unit volume	[particles $\times$ volume$^-$1]
G	Gibbs energy	[J]
g	Gyro-magnetic ratio	$[\mathrm{rad\,s^{-1}\,T^{-1}}]$
H	Magnetic field strength	$[\mathrm{A\,m^{-1}}]$

h	Convection heat transfer coefficient	[W m^{-2} K^{-1}]
J	Spin number, angular momentum	[-]
J_Q	Heat current density	[W m^{-2}]
k	Thermal conductivity	[W m^{-1} K^{-1}]
K_v	Flow coefficient	[m^3 h^{-1}]
L	Length	[m]
M	Magnetization	[A m^{-1}]
M_m	Molar mass	[g mol^{-1}]
M_s	Saturation magnetization	[T]
N	Number of moles	[mol]
P	Electric power	[W]
p	Pressure	[Pa or bar]
P_{field}	Time fraction in which the AMR is in the high flux region	[–]
Pr	Prandtl number	[-]
Q	Heat	[J]
R	Electrical resistance	[Ω]
R	Radius	[mm]
R_0	Electrical resistance of thermoelectric cell	[Ω]
RC	Refrigerant capacity	[J]
RCP_S	Refrigerant entropic cooling power	[J]
RCP_T	Refrigerant thermal cooling power	[K^2]
Re_d	Reynolds number	[-]
S	Total entropy	[J K^{-1}]
s	Specific entropy	[J kg^{-1} K^{-1}]
T	Temperature	[K or °C]
t	Time	[s]
T_C	Curie temperature	[K or °C]
U	Internal energy	[J]
V	Volume	[m^3]
v_d	Flow speed in regenerator	[m s^{-1}]
V_{field}	Volume of the magnet's high field region	[m^3]
V_{frac}	Void regenerator fraction blow	[-]
V_{mag}	Volume of the permanent magnets	[m^3]
x	Longitudinal position	[m]
x	Optimizable parameter	
ZT	Figure of merit	[-]

Greek characters

α	Parameter	[-]
β	Transition line slope	[-]
δ	Displacement, deformation	[mm]

ϵ	Seebek coefficient	$[\mathrm{V\,K^{-1}}]$
η	Efficiency	[- or %]
μ	Total magnetic moment	$[\mathrm{J\,T^{-1}}]$
Φ	Thermodynamic potential	[J]
ϕ	Phase shift between magnetic field and fluid flow	[°]
ϕ	Scaling, sphericity or shape factor	[-]
σ	Electrical conductivity	$[\mathrm{S\,m^{-1}}]$
σ	Mechanical tension	[MPa]
τ	Semi period	[s]
ε	Porosity	[-]
ϑ	Arbitrary constant parameter	

Mixed characters

Λ_{cool}	Magnet's cooling performance parameter	$[\mathrm{T^{2/3}}]$
$\mu_r =$	Relative magnetic permeability	[-]
μ_s	Specific energy	[W]
μ_f	Dynamic viscosity of the fluid	[Pa·s]
σ_s	Tensile strength	[MPa]
n_δ	Deformation security coefficient [-]	
n_σ	Stress security coefficient [-]	

Subscripts

AMR	Active magnetic regenerator
ap	Aperture
B	Constant magnetic field
$blow$	HTF impulsion blow
$Carnot$	Carnot cycle
e	Effective
el	Electronic
$exch$	Exchange
ext	External
f	Final
f	Fluid
Fe	Iron
gap	Gap, opening
$high$	High value
i	Index value
i	Initial
int	Internal
L	Lattice

l	Length
lim	Limiting value
low	Low value
M	Magnetic
m	molecular
mag	Magnet
max	Maximum
MCM	Magnetocaloric material
mec	Mechanical
p	Constant pressure
S	Constant entropy
s	Solid
T	Constant temperature
th	Thermal, thermodynamic
$cold$	Cold side, low temperature
hot	Hot side, high temperature

Upperscripts

$AMR\ block$	Of the AMR block
$magnet$	Of the magnet

Physical constants

μ_B	Bohr's magneton	$[9.2741 \times 10^{-24}\,\mathrm{J\,T^{-1}}]$
k_B	Boltzmann constant	$[8.617\,333\,262 \times 10^{-5}\,\mathrm{eV\,K^{-1}}]$
N_A	Avogadro constant	$[6.022\,045 \times 10^{23}\,\mathrm{mol^{-1}}]$
R	Gas constant	$[8.314\,41\,\mathrm{J\,mol^{-1}\,K^{-1}}]$

Acronyms

AE	Annual energy consumption
EEI	Energy efficiency index
$FWHM$	Full width at half maximum
SAE	Standard annual energy consumption
1D	One dimensional
3D	Three dimensions
AC	Alternating current
AMR	Active magnetic regenerator
BASF	Badische Anilin und Soda Fabrik, Badisch Aniline and Soda Factory
CALORICOOL	Caloric Materials Consortium
CFC	Chlorofluorocarbon

CSIC	Consejo Superior de Investigaciones Científicas
DAQ	Data acquisition
DDMC	Delft Days on Magnetocalorics
DTU	Danmarks Tekniske Universitet, Technical University of Denmark
EDM	Electric discharge machining
EU	European Union
FGRP	Fiber glass reinforced polymer
FOPT	First order phase transition
GHG	Greenhouse gas
GPIB	General Purpose Interface Bus
GWP	Global warming potential
HCFC	Hydrochlorofluorocarbon
HFC	Hydrofluorocarbon
HTF	Heat transfer fluid
ICMA	Instituto de Ciencia de Materiales de Aragón
IEC	International Electrotechnical Commission
IEEE	Institute of Electrical and Electronics Engineers
IIR	International Institute of Refrigeration
INMA	Instituto de Nanociencia y Materiales de Aragón
ITA	Instituto Tecnológico de Aragón
LLDPE	Linear Low Density Polyethylene
MC	Magnetocaloric
MCE	Magnetocaloric effect
MCM	Magnetocaloric material
NIK	Not-in-kind
ODG	Ozone depleting gas
ODP	Ozone depleting potential
P.R.C.	People's Republic of China
PAI	Polyamide-imides
PEEK	Polyether ether ketone
PEI	Polyethylenimine
PFA	Perfluoroalkoxy alkane
PLC	Programmable logic controller
POM	Polyoxymethylene, acetal, polyacetal or polyformaldehyde
PSU	Polysulfone
PTFE	Polytetrafluoroethylene
PU	Polyurethane
PVC	Polyvinyl chloride
R600a	Isobutane refrigerant
RTD	Resistance Temperature Detector
SOPT	Second order phase transition
TE	Thermoelectric

THERMAG Thermomagnetic refrigeration, used to name the International Conference on Magnetic Refrigeration at Room Temperature until 2018; now, International Conference on Caloric Cooling
TRL Technology Readiness Level
U.K. United Kingdom
U.S.A. United States of America
VAC Vacuumschmelze GmbH & Co. KG.

Chapter 1

Introduction

"A person who never made a mistake, never tried anything new."

Albert Einstein

The development of modern refrigeration systems is perhaps one of the most important technical contributions to food security, health and global welfare, making possible to maintain and transport perishable goods throughout the world, as well as the evolution of a great deal of actual industrial activities regarding food industry, air conditioning, chemical industry and a constellation of different applications for which cooling or freezing are either key elements, or just a source of comfort. This development was initially based on the use of simple physical principles, when earthenware pitchers or pots, caves, holes, and snow wells were used to keep food or drink cool, hindering the spoiling of the goods and assuring their availability for a longer period of time. Starting from the 4^{th} century AD, chemistry came to the aid of physics when the first chemical processes were used to lower the temperature by adding sodium and potassium nitrates to water. Chemistry, physics and engineering have been working together ever since to develop the refrigeration systems that modern society gives now for granted without giving much attention to their vital contribution to our daily lives.

As with any human activity in this overpopulated world, refrigeration has proved its good side, but it also has shown some dark facts. Early refrigerants like sulfur dioxide, methylchloride and ammonia were toxic if leaked and caused health problems and deaths. In the 1930's, new sinthetic refrigerants came to light, starting the era of chlorofluorocarbons (CFCs). These refrigerants were odorless and had very low toxicity, but, in the long term, their action as ozone depleting gases (ODGs) and greenhouse gases (GHGs) was discovered, which forced their phasing out after the Vienna Convention for the Protection of the Ozone Layer, signed in 1985, the Montreal Protocol on Substances that Deplete the Ozone Layer of 1987 and the Kyoto Protocol to the United Nations Framework Convention on Climate Change of 1997. CFCs phased out in the 1990s. This ban forced the agreement to use alternative refrigerants like hydrochlorofluorocarbons (HCFCs) which were less active in their ozone depleting and greenhouse effects; however, HCFCs phase out deadline was set to year 2020. In the last decades, there has been a continuous quest for new refrigerants that do not represent an environmental hazard, but many alternative substances are associated to a low energy efficiency, high pressures, flammability or even explosion hazards [1]. According to the International Institute of Refrigeration (IIR), around 37% of the global-warming impact of refrigeration technologies is due to direct emissions of fluorinated refrigerants like CFCs, HCFCs and hydrofluorocarbons (HFCs) (representing 7.8% of global GHG emissions), while the remaining 63% are due to indirect emissions from the electricity production required to power the systems [2]. The global energy demand and the use of fossil fuels to produce electricity and other forms of energy is therefore another important concern.

The use of fossil fuels produces CO_2, among other pollutants, which is known to be an important green effect gas. Although the greenhouse activity of CO_2 is not as high as other known gaseous pollutants like CFCs, HCFCs or HFCs, the amount of this gas dumped to the atmosphere is very large and a drastic cut in its production is therefore needed to reduce its effect. Even though the growth rate of the primary energy demand has slowed down in the last 50 years, global energy demands grows regardless the efforts to achieve energy-saving systems, due to the non-stop world population increase and the development progress of the underdeveloped countries, and a great deal of this increase is related to refrigeration demand [3–5]. A century ago, the energy needed to extract 100 barrels of petroleum was equivalent to one barrel of the same. Today, in some locations, the same barrel produces only 35 and when it comes to unconventional sources like shale oil and tar sands, that barrel produces only 5 at most; moreover, the first is claimed to be a dirty source of oil and in the last one, carbon dioxide emissions are 15% higher than in

conventional sources [6, 7].

Vapor compression technology has dominated the market for more than 100 years, has matured and has only a small potential for significant improvements in efficiency [8]. It is hence of utmost importance to seek an alternative, energy-saving technology, aimed to substitute a very mature and widely used one, which accounts for a good deal of the world's energy demand, GHGs and ODGs present in the atmosphere.

1.1 Global impact of refrigeration technologies

The economic impact of refrigeration technologies is quite more relevant than generally regarded. Refrigeration technologies are present not only in household refrigerators and supermarket refrigerated cabinets, but also in many other sectors as relevant as food industry, healthcare, energy and air conditioning among others.

Refrigeration has a direct impact on human health, not only through preservation of foods and pharmaceuticals, but also through new low-temperature therapies. It inhibits the development of bacteria and toxic pathogens therefore preventing foodborne diseases and it also reduces drastically the need for chemical preservatives in food. The impact of refrigeration in the food sector is paramount, ensuring the preservation of perishable foodstuffs and providing safe and wholesome products to consumers. According to the IIR, the lack of a cold chain causes significant global food losses, estimated in almost 20% of the global food supply [2]. Refrigeration also plays a key role in chemical, plastic, steel, building and other advanced industries, such as electronic-data processing or biotechnology.

The refrigeration sector, not only plays a major role in global economy, but it also accounts for an important piece of the worldwide electricity demand pie: about 20% of it, with an increase of around 3% of the share from 2015 to 2019 and some estimations state that global electricity demand for refrigeration could more than double by 2050. Air-conditioning, for example,

is expanding dramatically and is expected to increase its importance in the context of climate change: about 2.8 billion people live in the hottest parts of the world, but only 8% currently possess air conditioners and most of the projected growth in energy use comes from emerging economies like India, China or Indonesia, which together add up to half of it. In addition to this, it has to be considered that cooling is a big contributor to the heat island effect produced in many cities under certain conditions, which generates the need for more cooling, creating a feedback loop [2, 9, 10].

Aware of its impact in global warming, stakeholders have focused their fight on the reduction of direct emissions of fluorinated refrigerants to the atmosphere, the development of alternative refrigerants with negligible or no climate impact and the reduction in primary energy use by increasing the efficiency of refrigerating systems [2]. Incresing energy costs, unequal world distribution of primary energy reserves, and sustainability awareness have been some of the main increasing industrial and governmental concerns driving the search for alternative technologies in the last decades.

Brown and Domanski explained the situation very clearly in [11]:*"While implementing refrigerants with zero ozone depletion potential (ODP) was the main industry objective in the 1990s, the current primary goal is the identification and introduction of high efficiency, low global warming potential (GWP) fluids to minimize both the direct and indirect effects of air conditioning and refrigeration equipment on the earth's climate. The need for high efficiency systems cannot be overemphasized because the majority of electrical energy is produced from the burning of fossil fuels, and the amount of energy consumed for space cooling and refrigeration is enormous."*

1.2 Not-in-kind refrigeration technologies

Following the need to find efficient and harmless alternatives, many different alternative refrigeration technologies have been devised and tested to different degrees of depth. Outlines of some of these not-in-kind refrigeration technologies have appeared in many research papers; however, relatively recent relevant publications that include more extensive reviews of not-in-kind (NIK)

technologies worth to mention are [1, 11, 12] and [13]. NIK cooling technologies can be classified in many ways, depending on what the classification is based on, and hence, authors have proposed different taxonomies for the cooling technologies. Some of these technologies have already made their way out to the market, but their market penetration has not gone further from specific niche applications. These NIK technologies cover a broad spectrum of energy sources and effects; however, I will concentrate here on those classified with the tag of "solid-state cooling", and only on those that are considered most relevant.

The most relevant solid-state cooling technologies include thermoelectric and the so-called "caloric" cooling technologies, which comprise magnetocaloric, electrocaloric, barocaloric, elastocaloric and multicaloric technologies. These technologies are based on the alike-named physical effects.

The thermoelectric cooling technology is based on the Peltier effect, which refers to the cooling of a junction and the heating of another while an electric current passes through a circuit made of two different conductors. Thermoelectric cooling is a NIK technology that has been in the market for a long time already and it has the advantage of lacking of moving parts; however, the main drawbacks of this technology are the low power density and that the efficiency is only moderate.

Caloric cooling technologies are held as very promising and magnetocaloric refrigeration, which is the subject of this thesis, has been the closest to get to market due to the research effort made in the last decades, but the quest is proving longer than it was initially foreseen. Other caloric technologies are thus being investigated. Magnetocaloric cooling will not be addressed in this section, but treated in other sections throughout this entire work.

The underlying physics of the electrocaloric energy conversion is the electrocaloric effect, which is expressed as the temperature change in a dielectric material subjected to a variable electric field. To put it in simple words, the electrocaloric material heats up as it is subjected to a positive electric field change, yet as the electric field is turned off the material cools down. Thermodynamically, this effect is analogous to the magnetocaloric effect, though instead of a magnetic field gradient, an electric field change is required. Electrocaloric cooling technology has some potential advantages over magnetocaloric

refrigeration: higher power density and compactness of devices, no dependence on rare-earth materials, no moving parts involved, less vibrations, silent operation, etc. According to Qian et al., a relevant challenge for this technology is the limitation in the shape of materials, since only thin films can be used [13]. Nevertheless, electrocaloric cooling has only recently attracted an increasing attention from the scientific community and, therefore, it is still at an early stage.

Barocaloric cooling is based on the barocaloric effect, which is the property of some magnetic materials expressed as a temperature change of the material, upon varying pressure. Also as an analogue of the magnetocaloric effect, the barocaloric material heats up when subjected to an increase of the external pressure and vice versa. This technology has not received much attention from the scientific community and, to the best of my knowledge, there is a lack of any real device based on barocaloric energy conversion and many technical problems have to be addressed before a real prototype can be constructed [1, 14].

The elastocaloric or thermoelastic effect, is associated with the shape-memory and superelastic effect, and is the base of the elastocaloric cooling. This effect is a physical phenomenon associated with the entropy and/or temperature changes of certain materials when subjected to external mechanical stress. A stress-induced transformation of martensite into austenite is exothermic, while the reverse transformation is endothermic. Some alloys may present a relevant transformation latent heat, as high as $20\,\mathrm{J\,g^{-1}}$, according to Shaw et al. [15], cited by Kitanovski [1]. If the transformation is forced by a load quickly enough to be considered adiabatic, the material heats up, and it cools down when unloaded. The major limitation of elastocaloric cooling is the limited fatigue life of the elastocaloric materials. Also, the mechanical hysteresis should be reduced to allow a simpler application of this technology [1]. Even though the elastocaloric is the oldest-known caloric effect, cooling device prototyping using it is in the early stages of development.

A further step in NIK systems resides in materials that exhibit more than one of the above mentioned effects, which are described as a multicaloric materials, with multicaloric effects. Also worth to mention is the possibility of combining subsystems using any of the NIK methods into hybrid systems with the intention of improving the overall result. Such is the case of combining magnetocaloric cooling with thermoelectric devices working as controllable

heat switches[1, 12, 16][1]. This kind of hybrid system is a promising alternative and is further discussed in section 1.2.1 and in part II of this thesis.

1.2.1 Thermoelectric-Magnetocaloric hybrid systems

Traditional magnetic cooling devices have a high dependency on the use of heat transfer fluids and their use constitutes a problem for the system's performance. To the amount of energy required to push the fluid through the system, we have to add the power of the control systems, the technical complexity of the installation, the requirements to build the MCM container (regenerator) and the difficulties to obtain a good heat transfer between solid and fluid.

The thermoelectric-magnetocaloric (TE-MC) hybrid system concept appeared as a possibility to break away from these problems, with the possibility of obtaining a really compact completely solid device that gives no or a very small chance for any fluids to leak out. The use of a HTF may still be necessary to carry heat from the cold heat exchanger to the cold end of the cascade system and from the hot side of the cascade to the hot heat exchanger. This depends on the disposition of the cascading sandwiches in the magnet and the ease to put their ends in thermal contact with the exterior of the magnet´s gap. Nevertheless, if needed, the installation and management of such a system would be a lot easier and would require a much lower energy input. The idea of using thermal diodes, was first introduced by Kitanovski and Egolf in 2010 [17], and opens the possibility of constructing an AMR device that does not need a periodic flow like in a classic AMR. The flow may in this case be continuous, eliminating the need of any flow switching system and avoiding high viscous losses. The fluid would flow directly through the cold side of the AMR—a heat exchanger directly in contact with the cold side of a thermoelectric-magnetocaloric-thermoelectric sandwich (TE-MC-TE)—to the cold spot and back to the hot side of the AMR—a heat exchanger directly in contact with the hot side of the same TE-MC-TE sandwich. A further advantage of thermal diode AMRs is that they enhance the heat transfer rate,

[1] A heat switch here is not, as is often found in literature, a heat driven switching device, but a device that can be controlled to switch between high and low thermal conductivity conditions, allowing the obtention of a function similar to that often referred to as "thermal diode" when combined with magnetocaloric cycling.

opening the possibility of using less MCM at a much higher frequency of operation.

These systems are meant to combine the best of both worlds, with devices that can obtain a high cooling power with a very high performance—i.e. coefficient of performance (COP), see section 1.7.2. Their operation principle takes advantage of the ability of a thermoelectric module (TEM) to operate as a thermal diode, changing its heat conduction from nearly zero to a somewhat high value. This ON and OFF change of conductive state can be achieved with a small energy consumption and high COP, as long as no or very little heat pumping is demanded from the TEMs, forcing the heat to be naturally conducted from a cold to a hot spot. The building bricks of such systems would be TE-MC-TE sandwiches which can be combined to obtain a cascade device that constitutes a thermal ladder between its ends, where the cold and the hot spots are located (see chapter 9 and subsequent chapters for further information). The MCM acts like in a traditional magnetic cooler, heating up while magnetized and cooling down while demagnetized. The Peltier cell (TE cell) diode on the hot side of a magnetized MCM plate is energized to evacuate heat to the next MCM plate, which is slightly cooler, cooling the active plate down (cold blow), while the TE cell on the cold side of the sandwich blocks the heat transfer to the cold end. When the plate is at about the temperature of the neighbor plate on its hot side, the diode is shut off and the plate of the sandwhich cools even further as it is demagnetized, opening then the diode on the cold side of the plate, to absorb heat from the neighbor plate on its cold side (hot blow), to start the cycle again.

The implementation of this concept in a real device is not exempt of certain difficulties, remaining its benefits still controversial and, to my knowledge, no TE-MC cascading device has been presented in specialized literature. A good review about these special mechanisms can be found in the book of Kitanovski et al. [1], and some works show the great potential of this kind of systems [16, 18–20].

Part II of this thesis is devoted to the simulation of a single TE-MC-TE sandwich under different working conditions and more detailed explanations are presented in it. The discussions and conclusions of these simulations bring a relevant new light to some adverse conclusions published about the matter [21, 22].

1.3 Magnetic refrigeration comes to the rescue?

Magnetic refrigeration is a technology based on the exploitation of the magnetocaloric effect (MCE) to refrigerate a heat source. The MCE is a physical phenomenon occurring in magnetic materials which either heat or cool when they are subjected to the influence of a varying magnetic field. The magnetic materials that show this effect are known as magnetocaloric materials (MCMs). This technology has been used successfully for a long time in cryogenic lab equipments with low loads, but the real interest comes from the possibility of using it at room temperature and with higher cooling power in order to replace the actual vapor-compression systems. Magnetic refrigeration is held as a promising candidate to substitute vapor compression technology because it is attributed certain advantages. Apart from a large number of specific papers, the fundamental sources of information about magnetic refrigeration, are the book of Tishin and Spichkin [23], and the book of Kitanovski et al. [1][2]. Both books are used as basic sources of information for this work.

A magnetic refrigerator is meant to be environmentally friendlier than a conventional one, since the refrigerant is solid and cannot leak, causing therefore, no direct impact in the atmosphere. Also, it is claimed that these magnetic refrigerators will have a high efficiency, potentially lowering the energy consumption up to 30% with respect to conventional vapor compression systems, based on the high reversibility of the MCE, especially when using a MCM with no or negligible hysteresis [24]. Other claims include: small volume, low noise and longevity. However, all these expectations are in reality hardly being met. Although the friction of the compressor is eliminated, a heat transfer fluid (HTF) pumping system is still needed, noise is in many cases way over the desired levels and, also, problems have been reported in the magneto-thermal cycling of certain MCMs, which added to chemical compatibility and structural stability issues, could pose a serious longevity problem. In addition to this, the almost maintenance free configuration of modern household refrigerators is not completely assured on a long term in magnetic cooling devices . Ultimately, the truth about some of the claimed benefits of magnetic refrigeration will depend on the solutions adopted for the different components of the appliance.

[2]The book of Tishin and Spichkin was published in 2003 and a lot of developments have been published since then. The book of Kitanovski et al. is a more recent publication from year 2015, but it is more focused on refrigeration systems prototyping

Since a common magnetic refrigerator's refrigerant is a solid, there is no risk of ODGs of GHGs leaks; however, to my knowledge, all the prototypes constructed so far need to use an intermediate HTF to operate. For room temperature applications, this HTF could be liquid water, which would be a great solution from the cost and environmental points of view, but water brings about corrosion problems that need to be solved using additives, bringing up new contamination and toxicity issues.

The need of a heat transfer fluid is also a handicap, since this leads to inefficiencies rarely taken into account when considering the Carnot efficiency. In most cases, only the magnetic work required for the thermodynamic cycle is taken into account. A pumping work is necessary to circulate the HTF and pressure losses and viscous dissipation appear. Adding this to the solid to fluid heat transfer, which is inherently inefficient, there is an important risk of obtaining a low efficiency. Also, HTF management introduces complexity to the design of a magnetic refrigerator: watertight flow circuit, avoid dead volumes in the regenerator, space management within the magnet's gap, pipe connections, lower the flow's losses in the circuit, heat gains in the circuit from ambient or other heat conductive elements of the machine ... To all this, one has to add the need of a specifically designed magnet and a good list of contradictory requirements to manage. Technically speaking, building a magnetic refrigerator is a very complex and multidisciplinary problem.

The MCE of a MCM obtained as a result of its excitation with the magnetic field produced by a permanent magnet is rather low compared to the spans managed in a household refrigerator. This problem is solved by means of a regenerator, which allows generating a larger temperature span, but, once again, this brings back the solid to fluid heat transfer inefficiency and also other heat conduction problems, lowering the efficiency of the system even more. All these technical issues are addressed in more detail in section 1.6.

The MCM itself poses another controversial problem. Most MCM families showing good MCE behavior, have problematic elements in their composition. Some families contain highly toxic elements like As, Sb or Pb, some contain precious metals like Pt or Pd and most of them rely on the use of rare earth elements, either as main component or as Curie temperature (T_C) tuning agents. The use of rare earth and other scarce elements is not only restricted to the MCMs, but some are also used in the fabrication of the magnetic field source. In order to achieve a strong field and a high efficiency of the prototype, most

proposed magnetic field sources rely on the use of strong permanent magnets, which nowadays means NdFeB magnets; by far, the most expensive component of the magnetic refrigerator. These materials are problematic as they are subjected, not only to the usual ups and downs of the market, but also to geostrategic issues since their mining activities constitute an oligopoly controlled by China, which accounts for more than 90% of world's production between 2001 and 2005 according to a report of the U.S. Geological Survey [25]. China has been known to produce artificial increases of price since the beginning of the 21st century, by cutting down the exports of these strategic materials. The commercial war in which the United States and China have been involved in the last years is deeply connected to this fact and to the increasing demand of strategic materials that the so called 'green technologies' need. Although no mention to strategic metals is made in the document, this was perhaps one of the key factors for China to sign the Paris Agreement of 2015 and for the U.S. to withdraw from it. Also, the mining processes to obtain the above mentioned elements in countries with a lax environmental regulation, pose a very serious environmental threat [24, 26–28]. Efforts are being made to improve the recycling of rare earth materials; especially those coming from NdFeB magnets but, in general, establishing a circular economy with rare earths and other strategic metals has still many issues pending to be solved to become relevant, environmentally safe and economically worth [26, 29–35].

A comparative life cycle assessment published by Monfared, Furberg and Palm in 2014 showed that magnetic refrigerators have larger environmental impacts than conventional ones, *"mainly due to the use of rare-earth metals in their magnet assembly"* [36]. An interesting remark in this work is that, the cleaner the energy mix used for the operation of the refrigerator, the more pronounced will this shortcoming become, since this would increase the relative share of the magnetic materials in the total environmental impacts. According to this source, there are doubts as to whether improving the efficiency of the magnetic refrigerator may compensate its production stage extra impacts or not. The situation could be different for large refrigerators with higher power consumption. However, besides improving the efficiency of the refrigerator, the more effective solution to this dilemma is the reduction of the use of rare-earth elements and the reuse of the magnetic materials containing them, (i.e., magnets and MCMs).

In a study published in 2016, Bjørk, Bahl and Nielsen estimated the lifetime cost of a magnetic refrigerator in comparison with a conventional A^{+++} refrigerator. The lowest combined total cost for a lifetime of 15 years shows

very similar costs for both refrigerators, with a slight advantage of the magnetic one if it is assumed that the cost of the magnet can be recovered at the end of life. In this work, the cost of the magnet ends up being the highest, followed closely by the operation cost. The cost of the MCM ends up being negligible [37]. Although not clarified in the paper, assuming that the total cost of the magnet will be returned is not realistic, and this interesting work clearly shows that magnetocaloric cooling is not ready to jump out of the labs, yet.

Industry *versus* Academy

Academic researchers have been pointing out the good prospects of magnetocaloric cooling for many years now, but from the point of view of home appliance industry[3], these benefits are not as impressive as claimed, and those that could be held as a clear advantage, are slowly being dwarfed by steady improvements in the vapor compression technology.

The traditional environmental claim of being a technology with no refrigerants with ODP or GWP still holds, although there are now in the market gaseous refrigerants which have no ODP and a low GWP like R600a (isobutane refrigerant), with a market penetration in Europe of about 50%, for example.

The high efficiency claim of magnetocaloric cooling is very controversial. Just as an example, high efficiency compressors can exceed 60% of Carnot efficiency, pushing up the overall efficiency of vapor compression household appliances in the market, which are close to 45% of Carnot's, making everyday harder overcoming it in a competitive measure.

Also, it has been claimed that magnetic cooling devices are silent and vibration free. This depends on the final design of the magnetic cooling device, but today's refrigerators in the market only produce between 33 and 42 $dB(A)$, which matches a reading room whispering.

Finally, an important reason to await remarkable improvements compared

[3]The information commented in these paragraphs has been obtained from meetings with representatives of the home appliance industry and follow the trend shown by Beers (General Electric Appliances) in a speech given in Delft Days in 2015, [38]

to vapor compression devices is the expected cost of the appliance. A high efficiency compressor, including the associated electronics, can have a price as low as 50€[4], which is hardly comparable to the much higher cost of a regenerator plus its magnet, with associated drive and electronics.

1.3.1 Is the balloon deflating?

Magnetic cooling (i.e., magnetocaloric refrigeration) has been held for many years, as the most promising alternative to traditional vapor compression cooling. However, in their review of 2014 about alternative cooling technologies, Brown and Domanski concluded that the progress in the development of emerging technologies (which included magnetic cooling) since 1994 had been much slower than predicted by experts working in their respective fields. Among those technologies, magnetocaloric refrigeration was having the highest research activity at the time, but they pointed out that *"better magnetocaloric materials and other technical breakthroughs are needed"* to implement it, and that they did not foresee any of the emerging technologies *"achieving widespread displacement of vapor compression technology in the immediate future because of their lower energy efficiencies or higher costs, or both"*, needing significant technical breakthroughs to advance the market prospect of novel cooling concepts [11]. Even though progress was made in the following years, the situation in 2018 was described by Zimm et al. as requiring *"more work to enable widespread application and cost effectiveness"*, pointing out again the need of improvements in MCMs regarding their MCE and long-term structural stability. The need to develop *"economical fabrication techniques for effective AMR regenerators"* was also mentioned [39].

The International Conferences on Magnetic Refrigeration at Room Temperature (THERMAG) started in 2005 as a biennial international conference on magnetic refrigeration at room temperature which was a big step forward; but in the 2016 edition (THERMAG VII), a critical review authored by Kitanovski, Tomc and Poderos, presented a rather disappointing picture of the magnetocaloric refrigeration research and development activities held in the last years, pointing out redundancies, surprisingly small and slow improvements, useless efforts in already discarded matters, rather small international cooperation and very little work on the engineering side of the problem done

[4] From a meeting with a BSH Hausgeräte GmbH representative.

Table 1.1: European Union (EU) Technology Readiness Levels specifications used for the H2020 framework program[6].

TRL1	Basic principles observed
TRL2	Technology concept formulated
TRL3	Experimental proof of concept
TRL4	Technology validated in lab
TRL5	Technology validated in relevant environment (industrially relevant environment in the case of key enabling technologies)
TRL6	Technology demonstrated in relevant environment (industrially relevant environment in the case of key enabling technologies)
TRL7	System prototype demonstration in operational environment
TRL8	System complete and qualified
TRL9	Actual system proven in operational environment (competitive manufacturing in the case of key enabling technologies; or in space)

by engineers. In this review, the technology readiness of magnetic cooling technology was rated as having a Technology Readiness Level of only 3 or 4[5] [40]. The specification of the European Union TRLs for H2020 are shown in table 1.1.

Also, in 2008 took place the first "Delft Days on Magnetocalorics" (DDMC), another biennial meeting which was organized at the Delft University of Technology in Delft (Netherlands), alternating its meetings with those of THERMAG. This meeting was held until 2017, when the meeting was hosted at the Risø Campus of the Technical University of Denmark (DTU), in Roskilde (Danemark), with its name (and hence its scope) changed to "Danish Days on Caloric Materials and Devices". To my surprise, Delft Days made a return in 2019 and, once again, focused on magnetocalorics.

In 2018, the THERMAG Conference changed its scope and was transformed into the International Conference on Caloric Cooling, in order to include *"the growing fields of elastocalorics, electrocalorics, barocalorics, multicalorics and thermomagnetic energy conversion in order to fulfill the needs of the scientific community"*, as was stated in its proceedings [41]. THERMAG IX which is

[5] Technology Readiness Levels (TRLs) were developed at NASA in the 1970s, as a method for estimating the maturity of technologies during the acquisition phase of a program. The European Space Agency adopted the TRL scale in the mid-2000s and the European Union started using its own version for the H2020 framework program.

[6] Available at:
https://ec.europa.eu/research/participants/data/ref/h2020/wp/2014_2015/annexes/h2020-wp1415-annex-g-trl_en.pdf.

meant to be held in June 2021, has the same scope.

Companies such as Camfridge Ltd. (U.K.[7]), Astronautics Corporation of America (U.S.A.[8]), General Electric Appliances (U.S.A.), Haier (P.R.C.[9]) or Cooltech Applications, Ubiblue since 2019 (France), have been active in the research effort. However, their advances are today surrounded by a mist halo. It could be related to the industrial secrecy involved in their works, but the absence of any remarkable news, publications or commercial launches is uncomfortable. Fortunately, Camfridge and Ubiblue (former Cooltech) showed in DDMC 2019, that they are still there. However, I must point out that to my knowledge:

- Cooltech Applications suffered economic drawbacks in 2018 as some investors stopped supporting their project.
- Astronautics does not show any remarkable sign of works related to magnetic cooling since 2015. As of November 19, 2020 no later notice of the subject is found in their website and no remarkable paper has appeared as far as I know. The only signs of activity I found were given in a short review in 2018 [39].
- General Electric Appliances' magnetic cooling project public information seems to have ceased since 2014, and GE Appliances was purchased by Haier in 2016, which announced in 2015 a magnetocaloric wine cooler prototype in collaboration with Astronautics Corporation of America and BASF (Badische Anilin und Soda Fabrik), but no further notice can be found about the subject.
- Camfridge was promoting in THERMAG VIII (2018) a small magnetic cooler which was supposed to come soon to market. No news whatsoever can be found in their website about any specific product in the market.
- Other companies that presented research results or made publicity about their magnetic cooling projects in the past, are nowhere to be seen today.

The THERMAG IX Conference was meant to take place in June 2020 in Maryland, U.S.A., but the coronavirus pandemic restrictions forced to resched-

[7] United Kingdom
[8] United States of America
[9] People's Republic of China

ule it for June 2021. A great opportunity of getting a real feeling of the state of the art has been postponed.

1.3.2 Is there still some hope?

So far, the image projected presents a bit disappointing panorama with the main technical problems, disadvantages and research and development problems of room temperature magnetocaloric refrigeration; however, there is still hope.

Different machine concepts have been proposed and are being checked by different research groups, and materials research is a very active field. The optimization of the magnets has improved, resulting in more economical designs, with less weight of rare earth materials. There are also works checking the possibility of using electromagnets instead of permanent magnets [42], and the search for alternative MCMs that have a strong MCE with lower magnetic field increments is an active field of research. These last two milestones would make a great difference in the design, cost and efficiency of magnetic refrigerators; especially, if they can ever be combined. The use of electromagnets would end with the need of the expensive NdFeB magnets, lowering the expected lifetime cost of a magnetic refrigerator way below a conventional A^{+++} one. Further, finding an MCM with a strong MCE at low field increments would result, either in weaker and less massive magnets that could lead to using cheaper and cleaner magnetic materials, or in a lower size and energy need in a design with electromagnets. Although compressor efficiencies are approaching 70% and motor and power conditioning 95%, there is less room for improvements everyday and the cost of each compressor increases with each percent of performance improvement. Here is a chance for magnetic cooling to bring down the cost difference [38].

Several research lines have addressed the rare-earth issue in magnetocalorics under the 7^{th} European Union Framework Programme 2007-2013 and under the European Union Horizon 2020 Framework Programme 2014-2020. The pursue of alternatives to rare earths has also been the subject of research programs in the United States, such as those from the Caloric Materials Con-

sortium (CALORICOOL) [10]. Some of these research programs are focused on the reduction and recovery of rare-earth materials, as well as on obtaining alternative materials for permanent magnets.

1.4 A brief history of magnetic refrigeration

Although no exhaustive review is seeked here, it is interesting making just a brief summary of the most relevant milestones in the history of magnetic refrigeration. A very interesting publication covering the beginnings of the MCE was published by Smith in 2013 [43]. Further and interesting details about early and later prototypes can be obtained also in the review of Yu, Liu, Egolf and Kitanovski, [44] and the book from Kitanovski et al., [1]. Most of the information presented here can be found in these sources.

The MCE was first predicted by Thomson in 1860 and was initially known as Thomson heating. He considered that if the magnetization depended on temperature, a temperature change should arise a magnetization change due to an external magnetic field, assuming the effect as reversible [45].

The experimental discovery of the MCE was made by Weiss and Piccard in 1917 [46], although it is mistakenly attributed to Warburg in 1881 by many authors [47], due to a misunderstanding in a paper from Tishin of 1999, which was later widely cited [48]. This misunderstanding was clarified in a paper published by Smith in 2013 [43]. Weiss and Piccard observed a reversible heating in Ni of 0.7 ^{o}C close to its Curie temperature, in an applied field of 1.5 T. The reversibility of the effect was enough not to be mistaken with hysteresis heat, whose associated rise in temperature is several orders of magnitude smaller. The authors named this discovery *"novel magnetocaloric phenomenon"*, coining incidentally the word *"magnetocaloric"* at the same time. They established that the MCE is a consequence of the molecular field that Weiss introduced in 1907 as an extension to ferromagnets of Langevin's theory on paramagnetic gases, and derived a thermodynamic relation for the temperature change [43].

[10] However, as of November 19, 2020, the last news update in the CALORICOOL website (https://www.caloricool.org/news), dates from May 16, 2018.

It was not until 1926 when Debye and Giauque in 1927, independently proposed the first application: the use of magnetic refrigeration cycles with paramagnetic salt, to cool He below its boiling temperature. In 1933 Giauque and MacDougall reached a temperature of 250 mK by means of adiabatic demagnetization of gadolinium sulphate, $Gd_2(SO_4)_3{\cdot}8H_2O$, taking advantage of the very low heat capacity of paramagnetic salts at low temperatures, enhancing thus their MCE. The low thermal conductivity of paramagnetic salts is a disadvantage for adiabatic demagnetization cooling and this fact raised the interest in intermetallic compounds, which have a high thermal conductivity. As a result, $PrNi_5$ was used in a refrigerator setting a low temperature record at the time at 27 μK [8].

1.4.1 Continuous magnetic refrigeration

Continuous magnetic refrigeration started with the independent works in low temperature refrigeration of Collins and Zimmerman [49], and Heer, Barnes and Daunt [50], who built the two first continuous magnetic refrigerators, cooling a material which was not the MCM itself. The 1960s saw some works of Resler and Rosensweig on the use of ferrofluids as fluid MCMs in heat-to-energy machines [51, 52]. Ferrofluids could be a good choice to avoid the inneficient solid-to-fluid heat transfer; however, it appears that no prototype was ever built because of the poor performance and the hydrodynamic problems these materials presented [44].

The first known magnetic refrigerator at room temperature was reported by Brown in 1976, using gadolinium as MCM [53]. An important advance was the introduction of the concept of active magnetic regenerator (AMR) by Steyert in a prototype [54, 55]. The AMR converted the MCM into a double purpose component: on the one hand, it was the active cooling material and, on the other hand, it served as regenerator, forming a more efficient device for the obtention of larger temperature spans beyond that of the MCE of the active material. AMRs are further discussed in section 1.6.

In 1988, Kirol came with an improvement of Steyert's design, using permanent magnets for the first time [56]. Another important step forward was the introduction of the multi-layered AMR in a prototype reported by Green,

Chafe, Stevens and Humphrey in 1990. This kind of AMR enlarges the temperature span of the MCM even more by setting in an ordered serie, layers of MCM with different Curie temperatures [57]. It was finally in 1998 when Zimm et al. demonstrated with their prototype that magnetic refrigeration could be an alternative to conventional room temperature systems. This reciprocating prototype used Gd spheres as MCM and a superconducting magnet as field source, but it was seen that at a field of 1.5 T a span of 7 K could be achieved, with a specific cooling power of 70 W kg^{-1} and a coefficient of performance (COP) over 4 [1, 58]. 1.5 T is a field that can be achieved with NdFeB permanent magnets and it could be used in a home appliance.

1.4.2 The 'Giant Magnetocaloric Effect'

An important breakthrough for the development of room temperature magnetic refrigeration systems was the discovery in 1997 of the so-called 'Giant Magnetocaloric Effect'. Pecharsky and Gschneidner reported that $Gd_5Si_2Ge_2$ exhibits at the same time an order-disorder magnetic transition, as well as an order-order structural one, which leads to a sharp enhancement of the MCE around its ordering temperature (276 K) [59]. Nevertheless, due to the first order nature of Gd-Si-Ge alloys, they show a high magnetic hysteresis, creating parasitic losses [1].

It must be noted that the computed MCE was overestimated due to the presence of a spurious spike, which led the authors to state mistakenly that the measure exceeded at least by a factor of 2, that of any known MCM at the time [60]. However, this work acted as a catalyst in the research community, increasing the activity of room temperature cooling research in prototypes, as well as in MCMs.

1.4.3 Gaining a brief insight of magnetocaloric materials

The magnetocaloric material is the principal component of the magnetic cooling device, since they are responsible for the physical effect upon which the refrigeration is obtained. MCMs suffer a phase transition from ferromagnetic to

paramagnetic states at their Curie temperature (T_C). Above this temperature, the spontaneous magnetization dissapears, and the material turns paramagnetic. The MCE expresses its maximum values at this phase transition. It is necessary to clarify, that the MCE can be observed only when there is a change in the magnetic field between two set values (commonly from zero to a determined maximum value), and it does not make sense to make reference to a precise value without having in mind that, in reality, it refers to a jump of the magnetic field value from, let's say 0 T to the mentioned value. Thus, in this section, when making henceforth any reference at an increasing or decreasing value of the magnetic field, it has to be understood that this increase or decrease belongs to the magnetic field jump, and not of a "static" value of the field.

In general, MCMs are divided into two groups (summarized in figure 1.1) depending on the order of their phase transition (ferromagnetic to paramagnetic) and they are called thus first-order phase transition (FOPT) and second-order phase transition (SOPT) materials. Both groups show certain specific characteristics of the MCE shown. The main characteristic of SOPT materials is the continuous change of the magnetization around the T_C, while in FOPT materials the magnetization has a discontinuity associated to a structural deformation. The magnetic entropy change increases with the field in both, SOPT and FOPT materials; however, in FOPTs, a further magnetic field increase after a certain value widens the temperature range in which the value shows high values. In both kinds of transition, the ΔT_S shows an increasing peak as the magnetic field increases, but the peak is broader in SOPT materials. Also, the specific heat presents a sharp peak at a lower field jump, which decreases and broadens as this field increment is increased, but with no significant temperature shift in its peak. On the other hand, in FOPT materials the specific heat does not present a significant change its maximum value, but it has a significant shift in the temperature at which the peak value appears.

Lyubina et al., [61] established a further classification of the FOPT materials following Landau theory to obtain the magnetic component of the thermodynamic potential as a function of its magnetization, close to the transition point between paramagnetic and ferromagnetic states:

$$\Phi = \Phi_0 + \frac{1}{2}aM^2 + \frac{1}{4}bM^4 + \frac{1}{6}cM^6 \dots \tag{1.1}$$

They concluded that in FOPT materials the function $\Phi(M)$, equation (1.1),

showed two minima separated by an energy barrier, $\mathcal{E}$, and that overcoming this barrier, which is around 25 meV near room temperature, is a thermally activated process with a characteristic energy k_BT, where k_B is the Boltzmann constant. As a result, first order materials can also be subdivided into weak FOPT and strong FOPT materials, *"according to the relation of the height of the energy barrier E between magnetic states below and above the transition point to the thermal energy k_BT"*. Strong FOPTs are characterized by a high energy barrier $\mathcal{E} \gg k_BT$, and is often observed when a strong magnetostructural coupling or an order-order magnetic transition are present (e.g. $Gd_5Si_2Ge_2$). In FOPT materials, the first derivatives of the Gibbs energy (e.g. entropy, magnetization and volume) present a theoretical discontinuity, which is translated to sharp changes of entropy, magnetization, volume and derived magnitudes, in a very narrow temperature range. FOPT materials present also an important magneto-thermal hysteresis due to the latent heat.

Weak FOTPs, which are typically observed in materials that have an itinerant electron metamagnetic transition (paramagnetic to ferromagnetic), have an energy barrier comparable to the thermal energy $\mathcal{E} \geq k_BT$. It is typical of material families with a gradually migrating behavior from FOPT to SOPT (e.g. $LaFe_{13-x}Si_x$), exhibiting characteristics in between strong FOPT and SOPT materials, showing a lower hysteresis than strong FOPT materials, with a tendency to fade as the FOPT material migrates to a SOPT one. The already mentioned theoretical discontinuities of FOPT materials are also present, but they are not as sharp as in strong FOPT materials. Apart from the classification presented, there are many aspects to be considered when selecting the MCM to be used in a device. General criteria for MCM selection can be found in the book of Kitanovski et al. [1], as well as in other works like [62] and [61]; however, some additional criteria can be also included, as is shown in figure 1.2, and not all of them are related to the material's physics. The selection criteria include:

Suitable T_C of the Material: The MCE has to occur within the expected working temperature range.

Intensity of the MCE: The most important condition. If the MCM is to be used in an AMR, ΔT_S is more important than ΔS_T and is, therefore, the MCE parameter to be maximized due to its effect in the heat transfer process. The effect on the performance of the AMR is detailed in [63].

Wide Temperature Range of MCE: A wide MCE response ensures an in-

Figure 1.1: Summary diagram of the classification of magnetocaloric materials, according to their transition order.

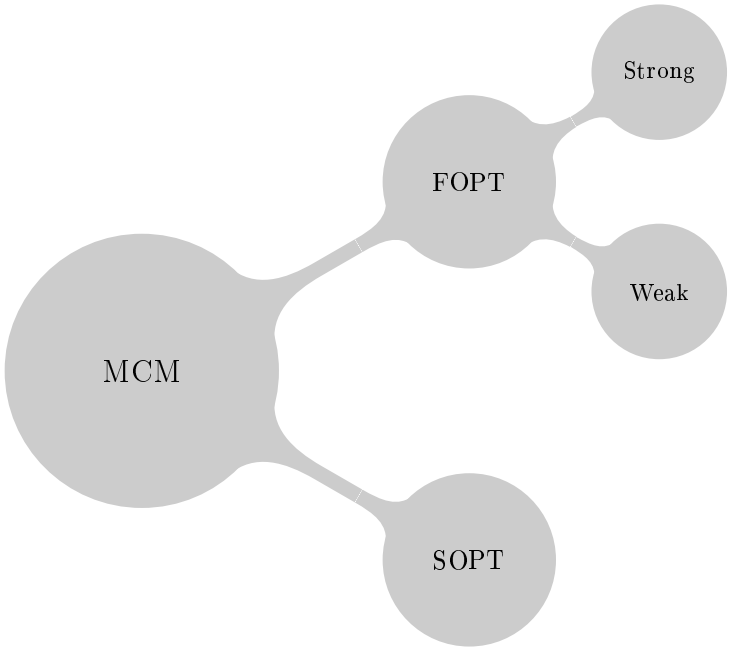

tense effect over a wider temperature range and, hence, over the entire regenerator length, allowing for designs with less layers.

Near-Zero Hysteresis of MCE: Hysteresis results in energy losses and hence, an increase of input work of the thermodynamic cycle due to the generation of entropy, which can reduce drastically the MCE and the efficiency of a cyclic device [64]. Hysteresis is generally related to the FOPT and its structural changes, and in general, does not occur in SOPT materials.

High Thermal Conductivity and Diffusivity: High thermal conductivity and diffusivity are traduced into faster and more intense MCM-HTF heat transfer; in general then, the higher the better. However, a high longitudinal thermal conductivity in the MCM can also reduce the performance of the AMR, caused by the fast decay of the longitudinal temperature ramp between its cold and hot sides. The optimal thermal conductivity value depends on the AMR length and, in the case of short AMRs, also on the operation frequency [65]. It would also be desirable the presence of an anisotropic thermal conductivity, with a high azimuthal and radial component in order to achieve fast thermal homogenization of the MCM in those directions, but preserving a much slower longitudinal transfer. However, modern MCMs do not show any significant thermal conduction anisotropy.

Figure 1.2: MCM selection criteria.

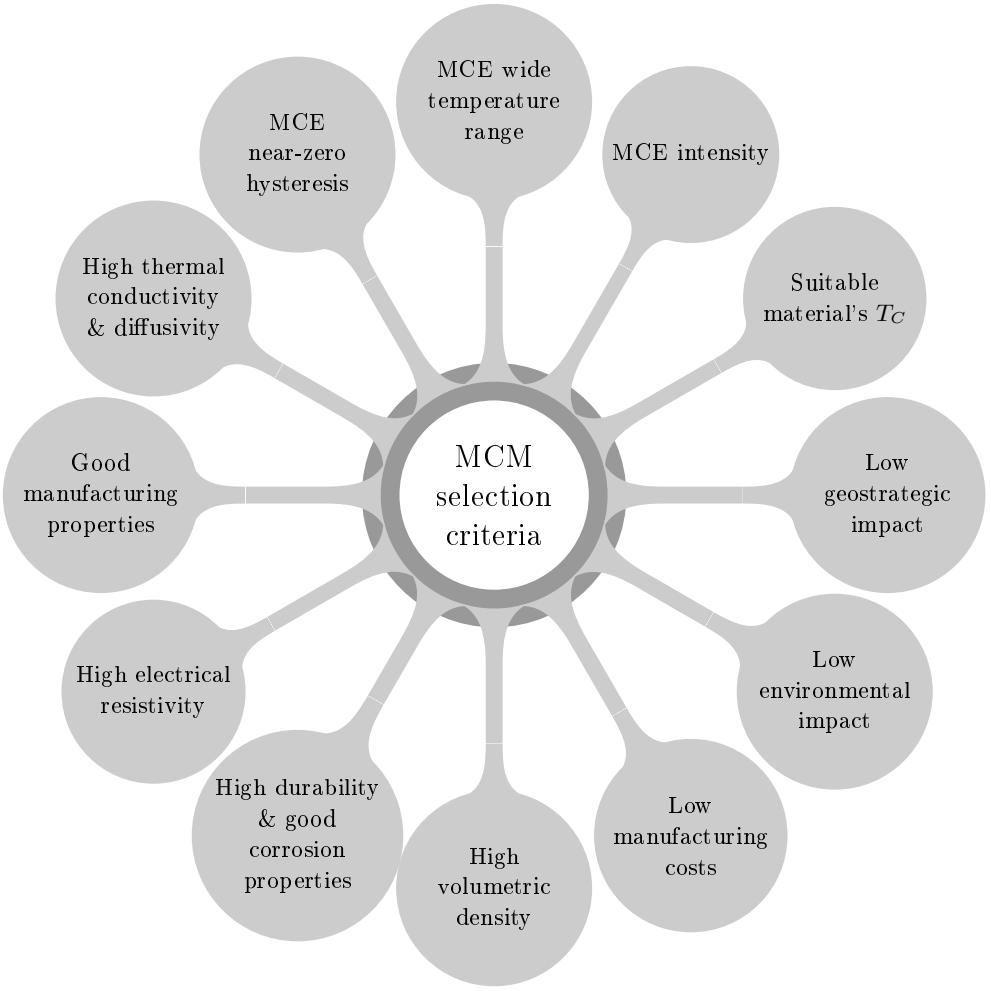

Good Manufacturing Properties: The material has to allow the use of manufacturing processes meant to conform it into the required shape. Brittle materials are not good candidates for machining or cutting processes and this is especially relevant in FOPT materials that have a T_C around the temperature of machining.

High Electrical Resistivity: To prevent Eddy currents. However, for applications operating at frequencies lower than 10 Hz, as it is nowadays, the Eddy currents' impact is in general negligible.

High durability & Good Corrosion Properties: MCM durability is a must in order to develop long lasting maintenance free devices that can be marketed. FOPTs have an inherent change of volume that causes stresses during cycling, producing microfractures that limit considerably the ma-

terials' shape life span. The introduction of internal porosity in the FOPT MCMs or MCM bonding with elastic matrices—e.g. epoxi bonding or metallic coating—have been proposed as stress releasing solutions. With the exception of ceramic manganite MCMs, magnetocaloric solid refrigerants need to be protected against corrosion, especially when they are in direct contact with aqueous HTF. This protection can be provided by surface passivation, coatings and/or using a HTF with corrosion inhibitors. This last method is widely used, but it compromises the claimed environmental safety of this technology and it usually has an impact in the fluid's viscosity and, hence, can bring pressure drop issues affecting the overall performance of the device.

High volumetric density: Which results in a greater MCM mass concentration in the high and low field regions of the device's magnet. This has the effect of concentrating the cooling power in a smaller area, allowing for more compact designs, smaller magnet gaps, or thicker insulation of the regenerator walls.

Low manufacturing costs: Materials cost is important, but low processing costs are essential for large scale production. Good manufacturing properties have a big impact in lowering manufacturing costs. Also, the possibility of using cost effective manufacturing methods that do not imply machining can also be a plus.

Low environmental impact: Since MCMs are solid, the chance of having an environmental impact during their lifetime can be considered negligible. However, care must be taken cradle-to-grave (life-cycle assessment) and the environmental issues arise mainly during mining, processing, and recycling, waste management or disposal, and this impact can be directly related to the nature of the chemical elements involved or indirectly derived from the industrial processes involved. In any case, the use of highly toxic elements should be avoided, even though sometimes they can produce very promising MCMs.

Low geostrategic impact: As it has been explained in section 1.3, the use of rare earth materials is a source of geoestrategic conflicts, and these conflicts will increase with the increasing dependence on strategic materials, as a result of the so-called green economy, and the geographic concentration of their principal sources. Avoiding the use of rare earths in MCMs would contribute to the reduction of the dependence on strategic materials, increasing greatly the supply security of the raw materials and reducing the risk of political and armed conflicts.

Some relevant room temperature MCM families

Obtaining materials with a better MCE profile is one of the most wanted developments of the magnetic cooling research community. MCM research is a very active area and improvements are eagerly expected. A mere outline of some relevant room temperature MCM families is here presented, to give a glimpse of some relevant material families that are subjected to intensive research nowadays. A recent and much deeper review about MCMs can be found in [66].

- Gd and Gd alloys:

  Gadolinium was the first material considered for near room temperature refrigeration, since it is the only pure element with a Curie temperature at room temperature, undergoing a ferromagnetic to paramagnetic transition. The T_C of Gd depends much on its homogeneity and purity, and has been reported as being at around 294 K in a single crystal or as 99.7 % pure polycrystalline [67–72]. Gd is considered a comparison benchmark of magnetic refrigerants' performance. Due to the second order nature of its Curie transition, no hysteresis is observed and it has a moderate ΔS_T. Despite of this, its relatively high thermal conductivity ($\sim$10 $\mathrm{W\,K^{-1}\,m^{-1}}$), fairly low specific heat ($\sim$300 $\mathrm{J\,kg^{-1}\,K^{-1}}$), and sizable ΔT_S, it shows a good overall performance.

  Gadolinium is very ductile and allows being shaped into thin plates and foils, although a severe plastic deformation can change its microstructure and reduce its MCE [73]. Also, Gd can be alloyed with other lanthanides, in order to lower the resulting T_C [8, 74].

  Although gadolinium has been widely used, tested, and used as reference, it has the drawback of being scarce (significantly less abundant than other rare earths) and, thus, also expensive.

- $Gd_5(Si_xGe_{1-x})_4$ family:

  The first known giant MCE material was $Gd_5Si_2Ge_2$ (see section 1.4.2), which belongs to this family of materials. This MCMs exhibit a FOPT for $0.24 \leq x \leq 0.5$, having a T_C =270 K for $x = 0.5$ that decreases with x down to about 20 K. For $x > 0.5$, there is a sudden change to SOPT and the T_C increases to about 336 K for $x = 1$ [75]. The hysteresis present in these materials lowers considerably the performance and, even though the hysteresis can be reduced significantly adding small amounts

of Fe or other metals, the transition of the compounds is transformed to SOPTs with a usually downscaled MCE, compared to that of pure Gd, due to the lower relative content of this element [76]. Adding this to the high cost of Gd and Ge, this family of materials does not seem to be very promising.

- $La(Fe_{13-x}Si_x)$ family:

  La-Fe-Si based MCMs are held as very promising compounds, possible cheaper alternatives to Gd-based MCMs. A large MCE was discovered in 2001 by Hu et al., as a result of a FOPT in $LaFe_{11.4}Si_{1.6}$ at 208 K [77]. It was later discovered that the T_C could be tuned either by adding H to the structure [78], or by partial substitution of Fe with Al, Co or Mn [79–81]. Partial hydrogenation leads to a two-phase segregation after some time of being stored at a temperature close to its T_C. This problem can be solved using Mn substitution as tuning strategy, plus a full hydrogenation of the compound, which now has a general formulation: $LaFe_{13-x-y}Mn_ySi_xH_{1.5}$ [82]. Partial substitution of Fe for Al, Co or Mn, or La for Pr, introduces a gradual change from FOPT to SOPT. This family of materials shows large magnetocaloric properties and low hysteresis, they are derived from inexpensive raw materials and large scale production through powder metallurgy is possible. All this turns La-Fe-Si intermetallic compounds into very promising materials for magnetic cooling and are already being commercialized[11]. However, La-Fe-Si material family is known for being brittle and not being good at withstanding magnetothermal cycling: the cycling induces stress in the material, causing crack growth that can turn the material to dust. Intrinsic porosity generation, polymeric bonding or metallic coating techniques are indeed needed. Corrosion preventing measures are also required. Regarding the manufacturing process, improvements in the precision of the T_C tuning are needed, since the first order transition nature implies narrow MCE curves and AMR layering allows for only around two degrees of T_C separation, which is nowadays the on demand manufacturer's process error margin[12].

- $MnFeP_{1-x}Si_x$ family:

  $MnFeP_{1-x}Si_x$ materials, with $0 \leqslant x \leqslant 0.7$, show a weak FOPT [61] and they are derived from the $MnFeP_{1-x}As_x$ family as a result of the presence of As, which is very toxic. It was found that substituting As for Si and Ge keeps the FOPT, but introduces a large hysteresis. This hysteresis was found to be tunable by varying the Mn to Fe ratio, but

[11] Calorivac®, Vacuumschmelze GmbH & Co. KG.
[12] Vacuumschmelze GmbH & Co. KG.

at the price of inducing a gradual change from FOPT to SOPT [83, 84]. Also, substituting Fe for Co and Ni [85], or B for P can also have the same effect [86].

Mn-Fe-P-Si materials and the like are inexpensive, promising MCMs that can be tuned for different T_C and low hysteresis. Large scale production can be achieved through melt spinning. Like in the case of La-Fe-Si materials, avoiding corrosion and thermomagnetic cycling mechanical failure due to the anysotropic volume changes produced by the FOPT are the main problems to solve when using this family of materials.

- Manganites:

  Manganites are ceramic materials, oxides with perovskite structure that show potential for use in magnetic cooling. There is a large number of different manganite MCMs, about which Phan and Yu published a comprehensive review in 2007 [87]. The general formula of manganites is $R_{1-x}M_xMnO_3$, where R is at least one rare earth element and M is a divalent alkaline earth, Na^+, Ag^+, or K^+.

  Most manganites are SOPT materials, with a relatively low (lower than Gd) but wide MCE, but there are exceptions like the LCSM family: $La_{0.67}Ca_{0.33-x}Sr_xMnO_3$, where $0 < x < 0.33$ tunes the T_C from 267 to 369K, which exhibits a FOPT. LCSM family has limited MCE: ΔS_T is moderate, comparable to that of Gd, but ΔT_S is much lower due to their large heat capacity, and the MCE decreases with increasing x[13].

  In spite of the limitations of LCSMs they are still a promising group of MCMs, mostly due to their low price, good corrosion resistance, easy tunability of the TC and processing ease [62, 88].

1.5 Introduction to the thermodynamics of the magnetocaloric effect

The magnetocaloric effect is an intrinsic characteristic of magnetic solids due to a coupling of the magnetic sublattice with the magnetic field, and it consists on a thermal response of the material whenever a magnetic field is either applied to or removed from it. The thermal response can be 'normal' or 'inverse'. In the first case, the material heats up when the magnetic field

[13] For $x = 0$ at ΔB =1.2 T, $|\Delta S_T|$ is 5.9 J kg^{-1} K^{-1} and ΔS_T is only 2 K.

is applied and it cools down when the field is removed. In the second case, the material heats up when the magnetic field is removed and it cools down when the field is applied. The normal MCE is found in paramagnets and materials experiencing disorder-order phase transitions upon the application of a magnetic field, which is the case of most ferromagnets and ferrimagnets. An inverse MCE is presented in materials undergoing a disorder-order phase transition when removing the magnetic field. An example of the last materials are the Heusler alloys. Since in practice, the most frequent MCE observed and used is the normal MCE, I will focus on it henceforth.

At constant pressure, the total entropy of a magnetic solid is a function of the magnetic field and temperature, which can be expressed as the combination of magnetic, S_M, lattice, S_L, and electronic, S_{el} contributions:

$$S(T, B) = S_M(T, B) + S_L(T) + S_{el}(T). \tag{1.2}$$

The isothermal magnetization of a paramagnetic or ferromagnetic material near its spontaneous magnetic ordering temperature—the Curie temperature, T_C—implies the ordering of the its spin system, reducing thus its magnetic entropy in a reversible process, while the total entropy remains constant. If the field is applied under adiabatic conditions, the entropy of the lattice system must increase to compensate the reduction of the magnetic entropy, maintaining the total entropy of the system constant. This increase of the lattice entropy represents a rise of the material's temperature, which is the visible part of the MCE. The MCE of a material can be hence quantified by two parameters: ΔS_T and ΔT_S (i.e., the isothermal entropy change and the adiabatic temperature change, respectively). Figure 1.3 represents both properties for a typical ferromagnet presenting normal MCE. The figure shows that as a result of an isothermal increase of the magnetic field, a negative isothermal entropy change takes place and that an adiabatic increase of the magnetic field, produces a positive adiabatic temperature change.

Different approaches to address the calculation of the above mentioned characteristic parameters of the MCE, and other related thermodynamic parameters, can be found in many publications. Perhaps the most complete specific source is the book of Tishin and Spichkin published in 2003, [23]. Also, a later interesting reference is the 2015 book of Kitanovski et al. [1], which addresses briefly the basic thermodynamic relations and cycles. Other

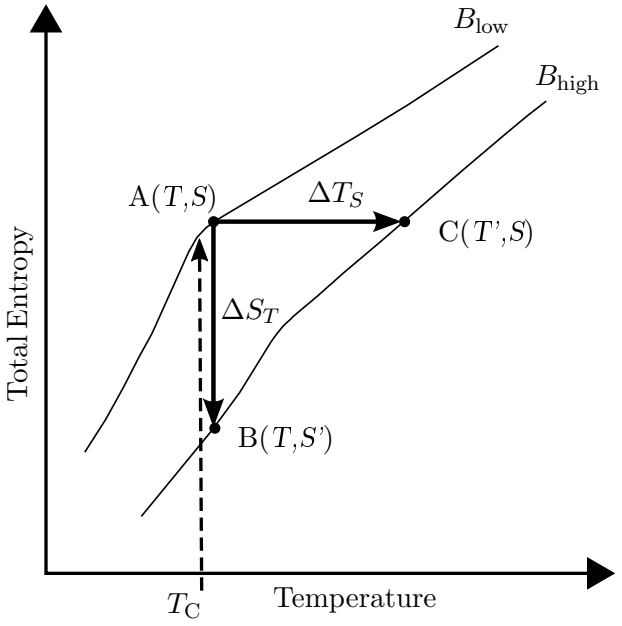

Figure 1.3: Total entropy of a common ferromagnet showing normal MCE, versus temperature. The figure shows the isothermal entropy change, ΔS_T, and adiabatic entropy change, ΔT_S, when changing from a low magnetic field, B_{low}, and a non-zero magnetic field, B_{high}, in the vecinity of T_C. A-B and A-C refer to adiabatic and isothermal processes, respectively.

interesting sources of information are [89, 90] and [48]. Most of what follows is a summary extracted from the sources [1, 23] and [89].

1.5.1 Heat capacity

We can obtain an expression for the heat capacity, starting from the Gibbs energy of a magnetic material, which can be expressed as a function of temperature T, pressure p and magnetic field B as:

$$G = U - TS + pV - MB, \tag{1.3}$$

being U, S, V and M the internal energy, total entropy, volume and magnetization of the material, respectively.

Since Gibbs energy is a state function, it does not depend on the route taken to go from one state to the other. Hence, the differential change between two states, ΔG, can be expressed as a function of differential changes in the variables involved—T, p and B. Translating this to an equation describing the total derivative of the Gibbs function we obtain,

$$\mathrm{d}G = -S\mathrm{d}T - M\mathrm{d}B + V\mathrm{d}p, \tag{1.4}$$

which we can rewrite as:

$$\mathrm{d}G = \left(\frac{\partial G}{\partial T}\right)_{B,p}\mathrm{d}T + \left(\frac{\partial G}{\partial B}\right)_{T,p}\mathrm{d}B + \left(\frac{\partial G}{\partial p}\right)_{T,B}\mathrm{d}p. \tag{1.5}$$

The terms of equation (1.5) are hence:

$$S(T,B,p) = -\left(\frac{\partial G}{\partial T}\right)_{B,p}, \tag{1.6a}$$

$$V(T,B,p) = \left(\frac{\partial G}{\partial p}\right)_{T,B}, \tag{1.6b}$$

$$M(T,B,p) = \left(\frac{\partial G}{\partial B}\right)_{T,p}, \tag{1.6c}$$

and due to the fact that the Gibbs energy is an exact differential, we can obtain one of the Maxwell relations making the derivative of equations 1.6a and 1.6c:

$$\left(\frac{\partial S}{\partial B}\right)_{T,p} = \left(\frac{\partial M}{\partial T}\right)_{B,p}. \tag{1.7}$$

The heat capacity at constant pressure and field, is obtained from the second derivative of the Gibbs energy with respect to temperature:

$$C_{p,B} = -T\left(\frac{\partial^2 G}{\partial T^2}\right)_{p,B}. \tag{1.8}$$

Also, we can consider that the heat capacity C at constant parameter ϑ is defined as:

$$C_\vartheta = \left(\frac{\delta Q}{\mathrm{d}T}\right)_\vartheta, \tag{1.9}$$

where δQ is the heat quantity changing the system temperature on $\mathrm{d}T$. Here, we can apply the second law of thermodynamics, $\mathrm{d}S = \delta Q/T$. The heat capacity expression obtained with both approaches is hence:

$$C_{p,B} = T\left(\frac{\partial S}{\partial T}\right)_{p,B}. \tag{1.10}$$

1.5.2 Isothermal entropy change

To obtain an expression for the isothermal entropy change, the procedure is similar to that with the Gibbs energy and the heat capacity, but posing the expression of the differential of the total entropy for a magnetic system, as a function of the same parameters used so far—i.e., T, p and B. We start hence with

$$\mathrm{d}S = \left(\frac{\partial S}{\partial T}\right)_{B,p}\mathrm{d}T + \left(\frac{\partial S}{\partial B}\right)_{T,p}\mathrm{d}B + \left(\frac{\partial S}{\partial p}\right)_{T,B}\mathrm{d}p. \tag{1.11}$$

Taking into account that the three processes pointed out in equation (1.11) are considered as reversible processes, considering a differential change in the magnetic field at constant pressure and temperature, and substituting the Maxwell relation of equation (1.7), equation (1.11) is reduced to:

$$\mathrm{d}S = \left(\frac{\partial M}{\partial T}\right)_{p,B}\mathrm{d}B. \tag{1.12}$$

From here, we can calculate the isothermal (and isobaric) entropy change due to a change of the magnetic field from an initial low field B_i, to a final high field B_f, $\Delta B = B_\mathrm{f} - B_\mathrm{i}$, obtaining as a result:

$$\Delta S_T = \int_{B_\mathrm{i}}^{B_\mathrm{f}} \left(\frac{\partial M}{\partial T}\right)_{p,B}\mathrm{d}B. \tag{1.13}$$

1.5.3 Adiabatic temperature change

If we consider equation (1.11) under adiabatic and isobaric conditions (i.e., $\mathrm{d}S = 0$ and $\mathrm{d}p = 0$) and make the substitutions shown in equations 1.7 and 1.10, we obtain an expression for the differential of the adiabatic (and isobaric) temperature change as a function of the change of an external magnetic field applied:

$$\mathrm{d}T = -\frac{T}{C_{p,B}} \left(\frac{\partial M}{\partial T} \right)_{p,B} \mathrm{d}B. \tag{1.14}$$

Integrating equation (1.14) we can determine the adiabatic temperature change due to a magnetic field change $\Delta B = B_\mathrm{f} - B_\mathrm{i}$ as:

$$\Delta T_S = -\int_{B_\mathrm{i}}^{B_\mathrm{f}} \frac{T}{C_{p,B}} \left(\frac{\partial M}{\partial T} \right)_{p,B} \mathrm{d}B. \tag{1.15}$$

Finally, we can establish a relationship between the adiabatic temperature change and the isothermal entropy change combining equations 1.12 and 1.14, and then integrating to obtain:

$$\Delta S_T = S(T,B) - S(T,0) = -\int_{T}^{T+\Delta T_S} \frac{C_{p,B}(T)}{T}\, \mathrm{d}T. \tag{1.16}$$

It has to be noted that this value of entropy is negative, but very often it is presented with its absolute value, omitting this nuance to the reader.

1.5.4 Addressing the material performance

When selecting materials, having some way to measure the performance is indispensable to easily compare the different options available. Apart from the physical magnitudes addressed in the last sections (i.e. heat capacity, isothermal entropy change and adiabatic temperature change), other figures-of-merit have been proposed in the literature as a single number, to establish a comparison basis among different magnetocaloric refrigerant candidates. Wood and Potter introduced the concept of refrigerant capacity (RC) in 1985, defined in equation (1.17), which according to the authors, should be maximized in any refrigeration cycle [91]. This RC concept, applied to a refrigeration cycle between a cold temperature side, T_{cold} and a hot temperature side, T_{hot} gives the equation:

$$RC = \Delta S_{cold}(T_{hot} - T_{cold}) \ , \tag{1.17}$$

being ΔS_{cold} the entropy absorbed at the cold side per cycle which is identified with the material's ΔS_T at the T_{cold}. The maximization of RC is therefore equivalent to maximizing the area of the rectangle that fits within the $|\Delta S_T|$ vs. T curve. RC clearly focuses on the shape of the material's ΔS_T, and no considerations about ΔT_S are made, which gives this figure a limited suitability for the evaluation of MCMs. As a result of this fact, extended definitions of the RC figure-of-merit have been proposed.

A proposed extension of the refrigeration capacity concept by Pecharsky and Gschneidner Jr. [92], is:

$$RC' = \int_{T_{cold}}^{T_{hot}} |\Delta S_T| \mathrm{d}T \ . \tag{1.18}$$

This version represents the area below the $|\Delta S_T|$ curve, between T_{cold} and T_{hot}. Although this value collects more information about ΔS_T, it still does not include any information about ΔT_S. Also, the value of RC' increases monotonously with the temperature span, leading to misleading values when evaluating temperature ranges that include temperatures with no effective cooling power, or when the material presents a very wide but rather low $|\Delta S_T|$.

Gschneidner Jr. and Pecharsky also proposed a set of two performance parameters which collect width and height information about both, ΔS_T and ΔT_S [93]. This is known as the relative cooling power (RCP), and produces two values that should be given together to provide the complete picture of the figure[14] an isoentropic and an isothermal RCP value—i.e., RCP_S and RCP_T—obtained as:

$$\begin{cases} RCP_S = |\Delta S_{T,max}| \, \delta T_{FWHM,S} \ , \\ RCP_T = \Delta T_{S,max} \, \delta T_{FWHM,T} \ , \end{cases} \tag{1.19}$$

where $\delta T_{FWHM,S}$ and $\delta T_{FWHM,T}$ are the full width at half maximum temperature changes of the entropy and temperature increment graphs, respectively.

Even though the use of the RCP couple as figures-of-merit seems to be an improvement, while RCP_S is physically meaningful (measured in J), RCP_T has no physical meaning (dimension is K^2). Tishin suggested that the figures

[14] This does not always happen and turns the given single figure a very limited, and often error leading, comparison basis. A clear example can be seen in [87]

should be normalized to the magnetic field change value, since RCP increases with it, being thus more convenient using $RCP_S/\Delta B$ (or $RCP_S/\Delta H$) and $RCP_T/\Delta B$ (or $RCP_T/\Delta H$) [23]. Also, the use of $FWHM$ values to describe the broadness of the graphs has brought up some qualms, and Lei et al. proposed using a shape factor applied to the $|\Delta S_T|$ curve to better describe the width of the curves [94]. It has to be noted that none of these proposals include any information about the hysteresis shown by the MCMs. Further details about performance parameters can be obtained from [23, 61, 62, 91–93] and [94]; however, and as a summary, it is clear that none of the above mentioned figures-of-merit guarantees a correct evaluation of the MCM performance.

1.6 Magnetocaloric thermodynamic cycles

Any refrigerator has to follow a thermodynamic cycle to pump heat from a source to a sink. In order to achieve this goal, work has to be applied to the system. In the case of conventional refrigerators like those developed as home appliances, the refrigeration process is based on a cyclic compression and expansion of a gaseous refrigerant. A well known thermodynamic cycle that could be used in refrigeration is the Carnot cycle which, as any other theoretical process, is ideal and reality transforms it by introducing losses and alternative thermodynamical states, according to the technically possible reproduction of the ideal process. The real cycle that is followed is only an as-good-as-has-been-possible approximation to the theoretical one. The ideal vapor compression version of the Carnot cooling cycle, which could be used in a household refrigerator, consists on the following steps:

- isentropic compression of the gaseous refrigerant,
- isothermal heat rejection with ambient at constant pressure,
- isentropic expansion of the gas,
- isothermal heat absorption from the inner chamber of the fridge.

Theoretical cycles stand on paper all right, but real machines never follow them strictly, and this is the real challenge of designing and building a pro-

totype. The isentropic process is really never isentropic and the isothermal process is never isothermal. The builder can try to get as close as he can to the ideal processes, but differences will arise as soon as obstacles like size, time of cycling and different losses come into play: lack of room availability confronts the need of insulation in the system, fast cycles rise heat transfer timing problems while too slow cycles cannot cope with the unwanted heat transfer losses with the environment—i.e., difficulties in obtaining true isothermal or adiabatic processes (non-isothermal heat transfer and non-adiabatic magnetization/demagnetization), heat leaks and friction losses, typical entropy generating processes and thus, sources of inefficiencies.

Apart from Carnot's, other thermodynamic cycles are also useful in cooling systems mainly Brayton or Ericsson cycles. Their magnetic counterparts are also named after them due to their clear similarities with the vapor compression versions.

A short introductory overview of the three above mentioned cycles' magnetic versions follows. Theoretical magnetic cooling thermodynamic cycles are usually addressed depicting isofield lines as straight parallel lines in T–S or S–T diagrams. Here, generic, but more realistic isofield lines according to the behavior of a MCM have been used. More in-depth information about magnetic cooling thermodynamic cycles can be found, for example, in [1, 23, 90, 95, 96].

1.6.1 Magnetic Carnot cycle

The Carnot cycle runs along two adiabatic and two isothermal processes, and is the most efficient cycle that can be followed by any machine working between a hot sink and a cold source. However, speaking of room temperature refrigeration systems, it is only useful as a reference for comparison with other refrigeration cycles, since it has a very limited cooling capacity to be used for practical purposes. The cycle works between only two temperatures T_{hot} and T_{cold}, which is a non-regenerative process, being the obtainable temperature span limited by the MCE of the refrigerant material. Its practical use is restricted to temperatures below 20 K. According to Tishin and Spichkin in [23], the main problem is that the lattice entropy of the solids increases strongly around that temperature, and hence, the separation between isofield

lines decreases, leaving a very small area for the Carnot cycle.

In a similar way as that described above in this section for the vapor compression version, the Carnot cooling cycle, as shown in figure 1.4, consists on the following steps:

- adiabatic magnetization (A–B): magnetization starts and the MCM heats up from T_{cold} to T_{hot} without heat exchange,
- isothermal magnetization (B–C): heat rejection to the hot sink at constant temperature while magnetization continues to its maximum value,
- adiabatic demagnetization (C–D): demagnetization begins and the MCM cools down from T_{hot} to T_{cold} without heat exchange,
- isothermal demagnetization (D–A): heat absorption from the cold source while the magnetization ends, cooling down the cold source.

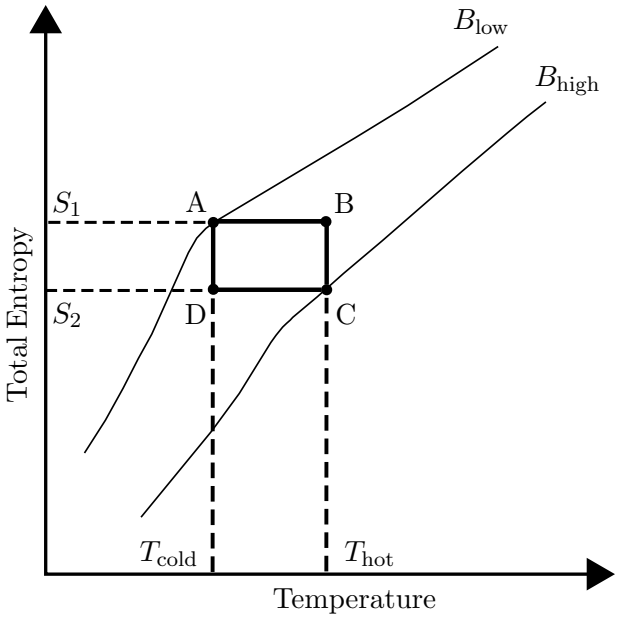

Figure 1.4: S–T diagram of the Carnot thermodynamic cycle for magnetic refrigeration. Two isofield curves are shown: B_{low}, ideally $0\,T$, and $B_{high} \neq 0\,T$.

Room temperature magnetic refrigerators need to use other cycles that include

processes at constant magnetic field to enhance the area of the cycle between the two given extreme isofield lines.

Regeneration

For room temperature applications normally permanent magnets are used, obtaining moderate magnetic fields, mostly between 0.8 and 1.5 T, which lead to a maximum ΔT_S of about 5 K with current MCMs. Most applications require a higher temperature span between hot and cold sources and this is what moves the search for different ways of enhancing it.

In order to solve the practical limitations of the Carnot cycle, a regenerative cycle can be used. A regenerator is a device that transfers heat between different parts of a regenerative thermodynamical cycle, which allows the temperature span of the refrigeration device to increase. Regeneration is very important in magnetic refrigeration, because the ΔT_S in these devices is much lower than in refrigerators using gasous refrigerants. The efficiency of a regenerative cycle in a room temperature magnetic refrigerator is higher than that of Carnot or Ericsson cycles [97].

A magnetic refrigeration cycle can hence become regenerative by using a regenerator. Passive regenerators can be either internal or external. The regenerator has to have a considerably larger heat capacity than the MCM to preserve the temperature gradient of the MCM.

An external regenerator is a solid material and, therefore, it has to be located in a separate location from the MCM. An HTF has to be used to establish the thermal connection between the MCM and the regenerator, which means a double heat exchange between solid and fluid, which is not very efficient.

Internal regenerators are liquids and can be placed permeating the MCM, which is submerged and soaked by the liquid, constituting only one heat exchange between solid and liquid, being thus more efficient than the external regenerators. The handicap of these liquid regenerators is that the internal

temperature gradient of the fluid and, consequently, of the MCM, is very easily ruined by the flow through the MCM, which mixes the fluid particles that are meant to maintain the temperature gradient.

Whenever the thermal mass of the refrigerant material is used as an internal regenerator, we refer to the device as an active magnetic regenerator (AMR). Some details about the AMRs and their thermodynamic cycles are given in section 1.6.4.

Regeneration is an important part of some cooling cycles like Ericsson and Brayton cycles, explained in sections 1.6.2 and 1.6.3, respectively.

1.6.2 Magnetic Ericsson cycle

An Ericsson cycle is characterized by two isothermal and two isofield processes as shown in figure 1.5. The cycle consists on the following steps:

- isothermal magnetization (A–B): magnetization of the MCM releasing heat to the hot sink at constant temperature,
- isofield regeneration (B–C): heat is released to the regenerator at a constant high magnetic field. The MCM transfers heat to the regenerator, lowering the temperature of the MCM to that of the cold source, T_{cold},
- isothermal demagnetization (C–D): demagnetization of the MCM, which cools down and absorbs heat from the cold source at constant temperature, T_{cold},
- isofield regeneration (D–A): heat absorption from the regenerator at low magnetic field, increasing the temperature of the MCM to that of the hot sink, T_{hot}.

The isothermal processes, in which the MCM exchanges heat with the regenerator, can be achieved by using a liquid regenerator—i.e., heat transfer fluid—and making it flow during those steps.

The energy transfer to and from the MCM in both isofield stages of the cycle should be balanced in order to satisfy the conservation of energy and also, ideally, the entropy change in the cycle should be constant—i.e. $S_{\mathrm{A}} - S_{\mathrm{B}} = \mathrm{D} - S_{\mathrm{C}} = -\Delta S = constant$—beign the isofield lines parallel. In this case, the second law constraint ($\Delta S_{hot} + \Delta S_{cold} \geq 0$) is fulfilled and the cycle is executed with maximum Carnot efficiency. It is clear from figure 1.5 that, in general, this is not fulfilled.

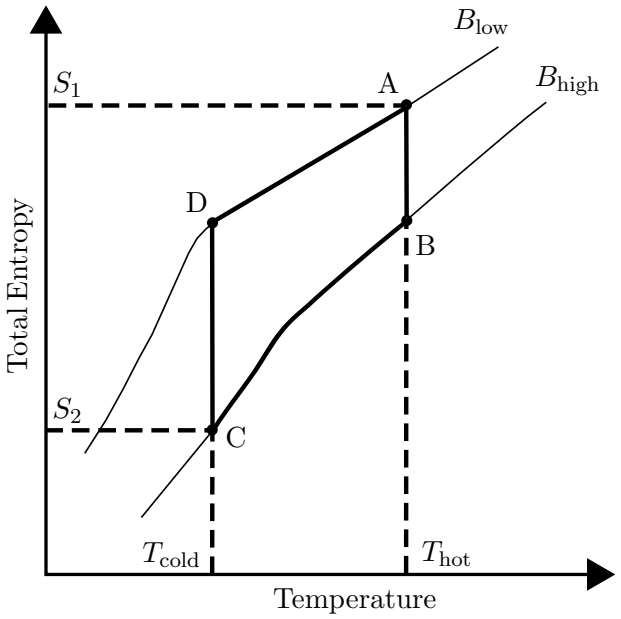

Figure 1.5: S–T diagram of the Ericsson thermodynamic cycle for magnetic refrigeration.

1.6.3 Magnetic Brayton cycle

The Brayton cycle is also one of the basic cycles of magnetic refrigeration. As it appears in figure 1.6, a refrigerator based on this cycle operates between two isentropic curves and two isofields.

- adiabatic magnetization (A–B): total entropy remains constant, but due to the magnetization, the temperature of the MCM increases,

- isofield heat rejection (B–C): heat is released to the regenerator at a constant high magnetic field. The MCM transfers heat to the regenerator, lowering the temperature of the MCM to that of the cold source, T_{cold},
- adiabatic demagnetization (C–D): demagnetization of the MCM, which cools down to $T_{cold} - \Delta T_S$ and absorbs heat from the cold source,
- isofield regeneration (D–A): heat absorption from the regenerator at low magnetic field, increasing the temperature of the MCM to that of the hot sink, T_{hot}.

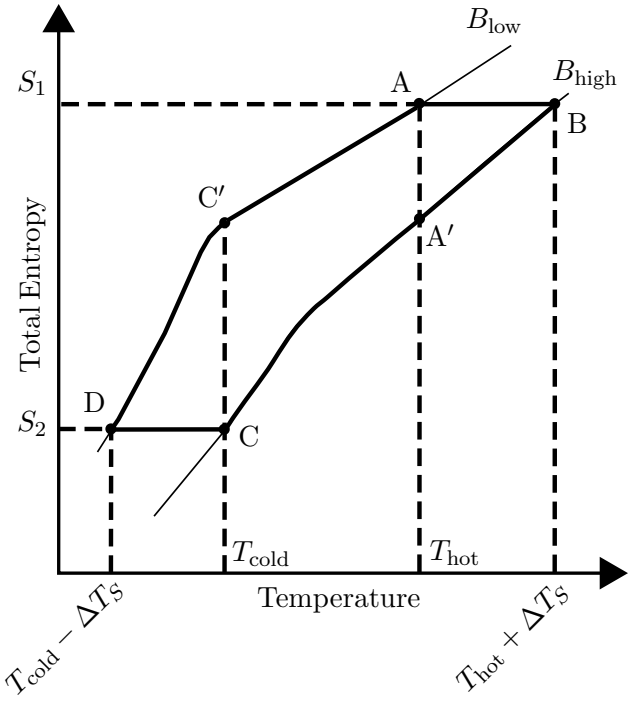

Figure 1.6: S–T diagram of the Brayton thermodynamic cycle for magnetic refrigeration.

As it is shown in figure 1.6 the Brayton cycle encloses an Ericsson one (cycle A–A'–C–C'). Both cycles differ in the way the field change is accomplished. In the Ericsson cycle it is through an isothermal process and in the Brayton cycle through an adiabatic one. The isofield processes in both cases necessarily involve heat regeneration.

The Brayton cycle rejects more heat to the hot sink and absorbs less heat from the cold sink than the Ericsson cycle, having the former, thus, less efficiency. In practice, the adiabatic processes of the Brayton cycle are easier to

achieve than the isothermal counterparts of the Ericsson, by means of a fast magnetic field operation; however, the fact is that there is very little difference between both cycles once reality strikes with deviations from the theoretical processes in the cycles. Brayton and Ericsson cycles are equivalent in their responses to varying material systems [95].

1.6.4 Active magnetic regeneration cycle

A further evolution of the regeneration systems applied to magnetic cooling systems is the AMR, which was introduced by Steyert in 1978 [55] and further developed by Barclay [98, 99]. Since then, different variations of the conventional AMR cycle have been proposed and used in research projects [1]. Although conceived for the Brayton cycle, the AMR cycle can be used in any regenerative cooling cycle and is the preferred option in magnetic cooling research. Nevertheless, I am going to focus here on the basic AMR Brayton cycle.

As was already mentioned at the beginning of this section, in an AMR, the thermal mass of the MCM is used as an internal regenerator. This means that the MCM is not only the material providing the MCE, but it also serves as regenerator, achieving an increased temperature span between hot and cold sinks with a smaller volume. According to Chen [97], an AMR cycle is, apart from Carnot's, the most efficient magnetic cycle possible in magnetic refrigeration.

The heat transfer mechanism is similar to that of an ordinary regenerator, except for the fact that the change of temperature is due to the application and removal of the magnetic field—i.e., the term 'active' refers to the application and removal of the magnetic field, in opposition to a passive regenerator where the magnetic field is zero (or at its lowest value). The regenerative process is established with the oscillatory flow of the HTF, performing each infinitesimal part of the MCM its own thermodynamic cycle. AS a net result, the HTF carries the heat from the cold to the hot source, exchanging heat with the MCM to lower its temperature while flowing through its porous structure, until a steady state is reached.

The AMR cycle is usually described as consisting of two adiabatic and two isofield steps namely, a Brayton cycle (figure 1.6). Furthermore, the MCM is assumed as having a higher heat capacity than that of the HTF. Its steps are hence:

- adiabatic magnetization (A–B): total entropy remains constant, but due to the magnetization, the temperature of the MCM increases according to the MCE, ΔT_S,
- isofield heat rejection (B–C): HTF is pumped through the MCM bed from the cold side to the hot side and heat is absorbed by the HTF, releasing it at the hot sink, pushing down the temperature profile of the MCM,
- adiabatic demagnetization (C–D): the MCM cools down ΔT_S,
- isofield regeneration (D–A): HTF is cooled down as it is pumped through the MCM from the return of the hot sink (ideally at ambient temperature) to the cold sink, and exits the bed to be put in contact with the cold source, which transfers its heat load to the colder fluid, while increasing the temperature of the MCM.

The repetition of the cycle cools down the cold source, releasing its heat to the ambient. The adiabatic temperature span, ΔT_S, during the demagnetization defines the maximum temperature span of the fluid that exits and enters the MCM at its cold side, and is limited by the efficiency of the heat transfer between the HTF and the MCM. This reasoning also applies to the warm side of the AMR.

The adjacent MCM elements in the AMR follow overlapping nonregenerative Brayton cycles connected by the HTF. They work as elemental coolers acting in parallel to exchange heat with the HTF [100]. Figure 1.8 shows a simplified S–T diagram of an AMR cycle. It must be pointed out, that in order to achieve a reversible cycle, a linear $\Delta T(T)$ profile is not strictly required inside the regenerator bed; furthermore, there is an infinite number of profiles satisfying zero entropy production [100].

Practical designs of refrigerators using AMR can be divided into two main

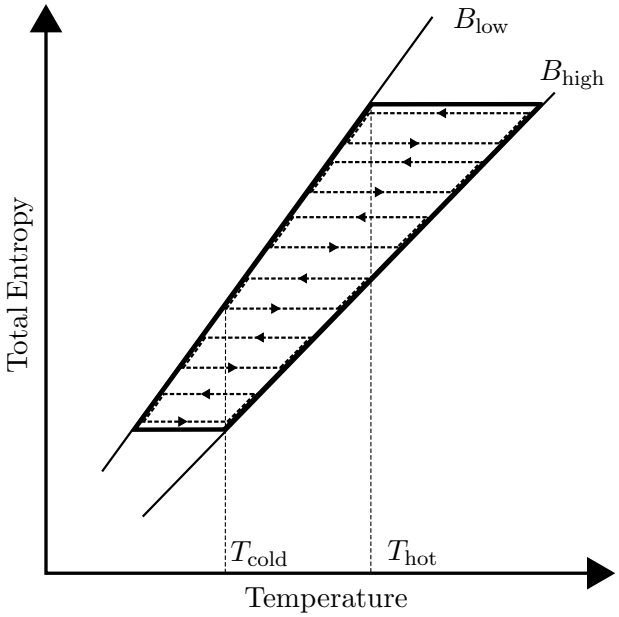

Figure 1.7: Simplistic S–T diagram of the AMR refrigeration cycle.

groups, depending on the manner in which the fluid flow is accomplished: reciprocating and steady regime pumping systems.

1.6.5 Multi-material regeneration

An implied problem of regeneration systems is that the operation temperature limits of the MCM are pushed away from the Curie temperature of the MCM, obtaining a decrease of the cooling power as the temperature span is broadened.

A solution to increase the temperature span obtained with an AMR, while lowering the impact of cooling power decrease with increasing ΔT is to divide its length and fill each section with layers of different MCM. Having each MCM a slightly different Curie temperature and setting them in an ordered sequence based on this parameter, each material ends up working close to its Curie temperature, according to the temperature profile along the regenerator. Each material is therefore set in a working environment where its MCE is highest.

This solution is especially important when magnetocaloric materials with first order phase transition (FOPT) are used, since the shape of their MCE is very sharp and narrow in temperature compared with that of those presenting a second order phase transition (SOPT).

1.7 Today's in-the-market household refrigerators

Since this thesis deals with the application of magnetic refrigeration to home appliances, apart from the aspects already mentioned in 1.3, a brief description of today's market conditions of household refrigeration an their relationship with different aspects of magnetic cooling characteristics is necessary to define the scenario in which this work is enveloped and the market requirements for any disruptive technology that comes into play in the household appliance refrigeration sector. Some criticism is also introduced for some aspects of the research that has been done so far in this field. Much of the information presented in this section refers to the compliance with regulatory aspects[15].

A commercial refrigerator is a complete system, not just the compressor, and that is something to understand when addressing the design of a magnetic cooler too, because the focus must be put on the complete system to achieve the intended results, and not just on the regenerator. Performance metrics are introduced in section 1.7.2, but it has to be here clarified that the system COP is not the compressor COP and with the new EU regulation, the system has to be optimized for two temperatures instead of one (16 °C and 32 °C)[16]. Most of the appliances sold are fridge-freezer combinations, which brings the need to reach freezer temperatures or magnetic cooling will end up serving only as niche market product, like wine coolers. Attention must be paid to the requirements of the different compartments as defined in regulations, in order to have a focus on the temperature goals of a refrigerator design. Temperatures for different compartments as defined in EU-regulation 1060/2010 [17] are summarized in

[15] European Union energy label EU 1060/2010 is scheduled to change on March 1, 2021. The new regulation, EU 2019/2016, is available at: https://eur-lex.europa.eu/legal-content/EN/TXT/?uri=CELEX%3A02019R2016-20191205.

[16] Actual figures of EN 62552 standard, which is the bases of Energy Efficiency Index (EEI), used in EU regulations for the energy classification of refrigeration appliances

[17] The document is available at: https://eur-lex.europa.eu/legal-content/EN/TXT/?uri=

table 1.2.

Table 1.2: Temperature of refrigerator compartments according to European Union regulation EU 1060/2010. The differences with the new regulation EU 2019/2016 are very slight and do not affect the temperature of the freezer or the fresh food storage compartments.

Compartment	T_{max} [°C]	T_{min} [°C]
Wine storage	+20	+5
Cellar	+14	+8
Fresh food storage	+8	0
Chill	+3	-2
One-star	-6	-
Two-star	-12	-
Food freezer / three star	-18	-

European regulations establish several climate classes for household refrigeration appliances, to adapt the working temperature specifications they should meet to operate in different geographic locations, according to the local climate (see table 1.3). The climate class sets the hot sink temperature that should be used in the design of the refrigerator.

Table 1.3: Climate classes according to European Union regulation EU 1060/2010. These values do not change in the new regulation EU 2019/2016.

Class	Symbol	Ambient average temperature [°C]
Extended temperate	SN	+ 10 to + 32
Temperate	N	+ 16 to + 32
Subtropical	ST	+ 16 to + 38
Tropical	T	+ 16 to + 43

According to the information provided so far, the temperature span needed for a commercially viable SN-class magnetic fridge-freezer combination is not less than 50 K. However, the most demanding and commercially interesting span would be that of a T-class, 61 K. It can hardly be emphasized enough that these calculated temperatures correspond to values of ambient and inner compartment of the freezer chamber, they are minimum values of required span, and they have to be maintained in the different compartments simultaneously. These figures are less demanding for a single chamber fridge: 32 K

CELEX%3A02010R1060-20200809.

for an SN-class without chiller and 43 K for an identical T-class, but as already mentioned, it would hardly be a commercially competitive product for household refrigeration. However, the real demand is even higher, since the difference between source and sink is not the reality. An appliance is not an ideal machine and it has real heat exchangers that also need a temperature difference to work. The temperature difference at the heat exchangers extends the ideal cycle span from source and sink to rejection to absorption temperatures and accounting for imperfect heat exchangers adds another 10 to 20 K to the span required [38]. We are now ranging from 60 to 81 K of span.

A further issue is the cooling power requirements. The heat flux through the cabinet is affected by three factors:

1. size of the cabinet,
2. temperature difference between ambient and inside chambers,
3. quality of insulation.

The resulting dependence of the heat flux with temperature is, for a given appliance, linear, using the overall heat transfer coefficient, $\mathcal{U}$:

$$Q = \mathcal{U}A\,\Delta T, \tag{1.20}$$

being Q the heat loss, A the heat transfer area and ΔT the temperature difference between the cabinet and the ambient. Solving equation (1.20) for $\mathcal{U}A$, we obtain the heat conductance of the appliance:

$$\mathcal{U}A = \frac{\Delta T}{Q} = \frac{1}{R_{\mathrm{t,equiv}}}, \tag{1.21}$$

where $R_{\mathrm{t,equiv}}$ is the total equivalent heat transfer resistance.

Taking as an example some typical values:

$\mathcal{U}A = 1.2$ W/K,

$T_{\mathrm{cabinet}} = 5$ °C and

$$T_{\text{ambient}} = 43\ ^{\circ}\text{C (T-appliance)},$$

and using equation (1.21), a minimum cooling power need of about 46 W is obtained. For an SN-appliance, changing T_{ambient} to 32 °C, the power need lowers to about 33 W, provided that the $\mathcal{U}A$ is not higher and that we focus only on a fridge. If we want to include a freezer, we go up to 60 W for an SN-appliance and 74 W for a T class. A summary of the minimum values obtained for a fridge-freezer combination are presented in table 1.4; however, it should be stressed that these values should be augmented with other possible losses like heat transfer in tubing or in AMR's container walls, heat transfer inefficiencies in the AMR or HTF viscous losses, for example.

Table 1.4: Summary of the minimum temperature span and cooling power needed for a fridge-freezer combination to comply with EU 1060/2010 standards, assuming a typical $\mathcal{U}A = 1.2$ W/K.

Climate class	ΔT	Power [W]
SN	60	60
T	81	74

Even though the EU standard tests measure the power consumption at a single temperature (25 °C now, but the average of 16 °C and 32 °C from March 1, 2021), the real ambient temperature is in general an uncontrolled variable and the requirements must be met under all working conditions provided in the regulations. The heat flux through the cabinet in a standard appliance can be 7 times higher at the highest temperature span than at the lowest[18]. This implies that for real running conditions, a variable cooling power is needed. Typical solutions in vapor compression are to switch the compressor on and off, and the use of variable speed compressor. In a magnetic refrigerator, this has consequences in the amount of MMC material per stage, the frequency, the energy consumption and, of course, the COP finally obtained.

Two factors determine the power of a magnetocaloric machine: the amount of MCM and the strength of the MCE. Unique properties of such a machine are its highest cooling power is obtained at zero temperature span and that no cooling power is obtained at the maximum span. It is therefore clear that the

[18] From a meeting with a BSH Hausgeräte GmbH representative.

best operating condition is somewhere in between and, hence, when designing to deliver cooling power, enough temperature span capacity has to be foreseen. This means that when considering the span aimed in the design, the actual true regenerator span needed is higher and more span means more MCM. However, the addition of material also adds more pressure drop and this very often leads to a short design and the attempts to obtain more span, stall the machine and break down the temperature cascade within the AMR, since it is unable to reject enough heat to sustain the cycle.

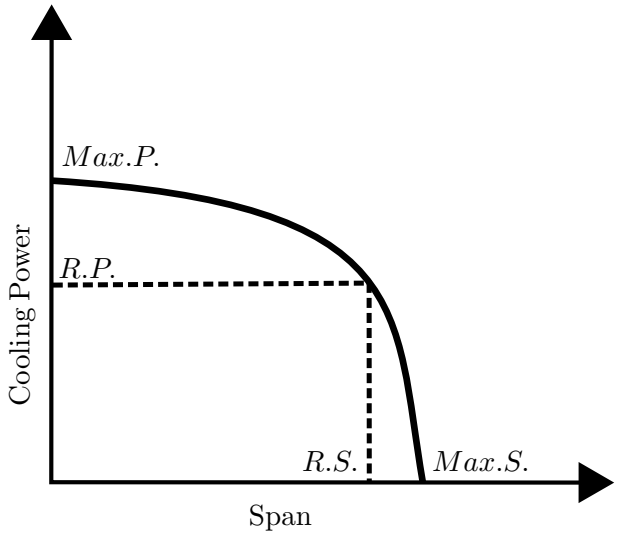

Figure 1.8: Typical cooling power-span curve for multi-material magnetocaloric machine. "R.P." stands for Required Cooling Power and "R.S." stands for Required Temperature Span, while "Max.P." and "Max.S." stand for Maximum Power and Maximum Span, respectively. Note that maximum span must exceed design span and that maximum cooling power must exceed design power. More details about the cooling power vs span curve are given in 1.7.1.

Another factor to take into account when designing a refrigerator is that once the required cooling power has been determined, using that value as design value would mean a 100% runtime. If someone opens the door of the cabinet, the heat load immediately increases, exceeding the machine's capacity. Common solutions to this problem are simply adding more capacity in a normal working mode, or variable capacity design by means of speed control, plumbing features or a combination of both. An excess of cooling power allows for a run time below 100% and there is enough capacity to cope with occasional

perturbations of the load. Using more material or more speed allows more cooling power for load surges as large load of warm goods or pull down after an off period.

Great expectations have been held for magnetocaloric cooling improvement of the COP. Early expectations were of 50% improvement [38]; however, many research papers have neglected collateral space and mechanism effects, and very often, pumping power and pump and motor efficiencies are not accounted for. Also, the cold source is often a single point of negligible mass—i.e., a thermocouple—within the insulated tubing system, providing a negligible initial heat load, which is not a realistic situation. A clear map of losses is necessary to use a Pareto analysis that points to the important subjects of further research.

Any refrigerator must hence simultaneously meet two basic criteria, temperature span and cooling power. Enough span and cooling power are needed for magnetic refrigeration technology to be useful, but to be disruptive and displace vapor compression, it must also be more efficient. The introduction of the energy label pushed down power consumption of home appliances in general, and of household refrigeration systems in particular. According to BSH, the fridge-freezer combination lowered its consumption 75% in the period between year 2000 and 2015[19]. Nevertheless, efficiency measurement can still be tricky.

1.7.1 Cooling power vs. temperature span

The cooling power vs. temperature span diagram presents a phenomenological behavior with certain interesting characteristics. The correlation between ΔT and $\dot{Q}_c$ shows characteristic shapes depending on whether the AMR comprises one or more materials. Further differences come alight when comparing a first order multi-material curve with a second order one.

The ΔT–$\dot{Q}_c$ correlation curve for a single material AMR is linear with a negative slope. At its Y-intercept (Y-axis is the $\dot{Q}_c$ axis), the machine produces

[19] From a meeting with a BSH Hausgeräte GmbH representative.

its maximum cooling power and the temperature span at the hot and cold sides are the same. Also, at its X-intercept the span, ΔT, the machine produces just enough cooling power to compensate its losses and reaches its maximum span. These axis intercept situations apply also for multi-material AMRs, although their shape is not that of a straight line, but rather curved. Figure 1.9 shows correlation samples of cooling power vs. temperature span for these three cases.

As a reference system to help explaining the curves in multi-material AMRs, Benedict et al. introduced a division in three areas which fits very well for first order multi-material AMRs: plateau, knee and drop-off [101]. Multi-material AMRs with second order compounds show a similar shape, but they do not match very well with the mentioned divisions. The knee is a clear sharp turn downwards in AMRs with FOPT materials, but in those composed of SOPT materials, the knee is blunt even to the point of fading away, and the curve changes smoothly downwards. Consequently, the last case, the plateau and the drop-off areas cannot really be named as such. Also, in some experimental results, an additional section has been detected in multi-material curves. Jacobs et al./ present in [102] an ending tail, consequence of a change in the curvature of the graphs, after they have reached the drop-off area, bending down the curve towards the X-axis intercept. These areas are just generalizations that are used to help explain results and are marked in figure 1.9.

The tail represented in figure 1.9 with a green dotted curve was reported by Jacobs et al. in [102]. This tail appeared in both, experimental and simulation results in a FOPT multi-material AMR. To the best of my knowledge, an explanation about the origin of this tail has not been published and I have not found any further examples of it.

The general shapes and differences of the multi-material AMRs are easy to understand when thinking about the shape of the MCE of FOPT and SOPT materials. FOPT materials have a sharp response and the aim of the multi-material AMR is for the MCMs to work under maximum response conditions. The same sharp character of the response is what produces the knee and sharp drop-off. The knee lays at the point where all FOPT materials are working right at their own peak response temperatures. This is actually an unstable situation and a small perturbation makes the system rapidly change either to the plateau or to the drop-off areas, because the MCMs are pushed out of their MCE peak temperatures, starting from the cold end. Whenever a material is

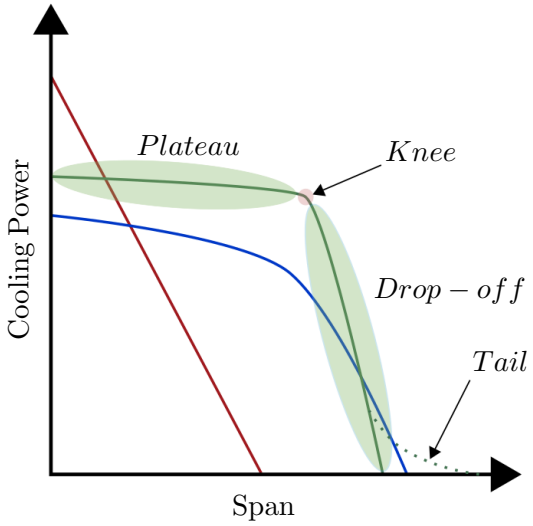

Figure 1.9: Typical cooling power vs. temperature span graphs. The garnet straight line corresponds to a single-material AMR while the curves correspond to multi-material AMRs. The green curve belongs to an AMR composed of FOPT materials while the blue one shows the behavior of a SOPT material AMR. The dotted curve is a tail observed by Jacobs et al. in [102].

out of the peak response, it starts acting as a dead volume[20].

While the desired point of operation of the FOPT material AMR is at the knee point—high cooling power and high temperature span—and some authors like Benedict et al. assure that *"this point is where commercial and other applications are likely to run because they can provide large amounts of cooling capacity at useful spans"*, and mathematically define the knee point as that where the product of span and power is maximized; however, the reasonable working area of the AMR in a real device is probably the drop-off area. The purpose of a refrigerator is to produce a defined stable temperature (or range of temperatures), lower than that of the ambient inside its cabinet. At the drop-off area, the temperature of the machine would be more stable than at the plateau or the knee, and measurable increments of cooling power demand would not mean a drastic decrease of the cabinet´s temperature. An analogy to this situation can be found in the torque vs. speed characteristic curve of an induction electric motor, as shown in figure 1.10. As it will be explained in section 1.7.2, the point of operation marks the efficiency of the

[20]Further explanations about "dead volume" are given in section 4.1.

system and working at its maximum value is one of the main goals seeked with magnetic cooling technology; however, the real functioning condition of a given machine will be set by the cabinet's inner temperature, the ambient temperature and the sudden appearance of a perturbation in the cabinet's heat load when introducing goods at temperatures different from that of the cabinet[21]. Also, Smith et al. points out that for FOPT materials, the specific heat and magnetic entropy peaks shift towards higher temperature in a high applied field [62]. According to Lei et al., it is implied that the best working temperature for the FOPT materials is expected to be higher than the Curie temperature [103].

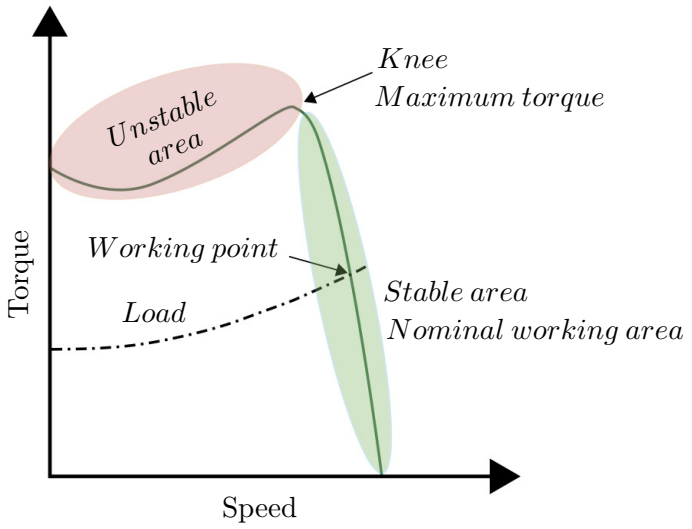

Figure 1.10: Torque vs. speed characteristic curve of an induction electric motor. The nominal speed and torque are usually located just below the midheigth of the stable area marked in green. The motor's physics works as a self-stabilizer when a disturbance in the torque demand lowers or increases the speed of the machine.

In principle, like in the case of induction motors shown in figure 1.10, the AMR working within the drop-off area of the FOPT materials should act as a self-stabilizing system. Starting from a steady state, the introduction of goods at a higher temperature that the cabinet's nominal value lowers the machine's

[21] Each magnetic refrigerator has its own intrinsic (constructive) characteristics, and power and span limitations—i.e., FOPT materials, specific losses of the refrigerator's construction, maximum cooling power and maximum temperature span. The discussion in this paragraph assumes the case of a given machine with some fixed constructive characteristics and limitations, under different real working conditions.

span and, automatically the cooling power increases to compensate the situation, starting a transitory trying to recover the nominal temperature. If the perturbation is in the opposite direction, introducing goods at a lower temperature than the cabinet´s nominal, the span is increased and the cooling power diminishes, pointing to a compensation of the perturbation. However, as in the case of the induction motor, some restrictions apply to this reasoning. The heat load introduced in the cabinet should not be higher than the maximum cooling power of the refrigerator under the risk of driving the system out of the temperature specifications of the cabinet, although this happens almost everyday that the user shops refrigerated goods for a week or more (many modern vapor compression refrigerators have a button for a special setting to increase the cooling power in this kind of situation). The possibility of not recovering from the transitory situation does not seem realistic, since in this case the heat source, unlike those used in testing magnetic refrigeration prototypes, is not continuously powered. The load is introduced suddenly and no other heat flux (apart from the machine's losses) enters the limits of the system. When the refrigerator is left to get back to a steady state, the heat that was introduced is slowly drained out by the AMR. However, the question remains as to whether a big temperature perturbation that really drives the AMR's cold end temperature profile far out of the MCE peak of the last materials, would allow a recovery of the previous steady state situation. A first thought to this situation makes me believe that a transitory working condition would slowly drive the system back to the original steady state working point, although the temperature of the cabinet will often be out of the desired range for a while. For a given refrigerator, the recovery time will mainly depended on the difference between the machine's maximum cooling power and the heat load that was suddenly introduced and the goal should be to have a recovery in a reasonable time, according to industry standards.

Tests and simulations addressing the study of transitory perturbations of the refrigeration system would be of interest. Although some authors have discussed about the shape of this phenomenological correlation of cooling power vs. temperature span, to the best of my knowledge, no specific simulations or tests have been reported checking the expected behavior described above. As to my knowledge only Lei et al. published a work with a study of sensitivity to the working temperature; however, the simulations shifted the temperature of both, the hot and the cold ends at the same time, maintaining a constant span and as a result, a faster degradation of the performance in the FOPT material, compared to that of the SOPT material was reported [94]. In my opinion, what Lei's work really shows is that FOPT materials are more sensitive to the ambient working temperature and may be unable to start the cooling process

if the ambient temperature is too far[22] from the hottest Curie temperature of the AMR's materials.

It must be emphasized that in real situations, the user has no idea whatsoever about the heat load being introduced in the cabinet. The user may be aware of the mass and temperature of the goods, but surely not of their heat capacity, and absolutely no calculations are going to be made by the end consumer. Also, as far as the end use of a magnetic refrigerator goes, its working point will always be a relative condition. The cooling power is normally determined by the continuous application of heat to the cold source until a steady state is reached, and then the span and applied power are registered, but this procedure does not really represent the real life use of the refrigerator. The baseline of the cooling power vs. temperature span characteristic curve—i.e., zero cooling power—is the equilibrium with the losses of the system under the test conditions used to obtain the curve. This means that in order for the graph to be really useful and comparable, the test conditions should be those of a commercial refrigerator—e.g., $T_{\text{cabinet}} = 5$ °C and $T_{\text{ambient}} = 32$ °C. The cooling power can then be different from zero when there is some parameter change from the test conditions. This change can be punctual—e.g. new food load at higher temperature—or kind of continuous over time—e.g. a change in ambient temperature. Hence, the return of the machine to the steady state after a punctual perturbation, brings the load line back to zero, and the return to a steady state after a more permanent perturbation like ambient temperature changes implies a change in the baseline, or it can also be interpreted as an additional heat load relative to the test conditions, marking hence a new working point in the graph, at a $\dot{Q}_c \neq 0$.

Going back to figure 1.9, in the case of SOPT multi-material AMRs, the curve is softened according to the soft typical shape of the MCE that the SOPT materials present. The shape approached is analogous to that of the pressure vs. flow rate characteristic curve of a centrifugal hydraulic pump, see figure 1.11. Following the reasoning presented previously for the nominal working point in FOPT multi-material AMRs, there is in this case, in general, no clearly preferred working area as far as temperature stability goes and, therefore, the obvious objective is to work around the point of maximum efficiency[23]. In the case of a centrifugal pump, this point is usually found in the upper half of the

[22] "Too far" here means only more than two degrees, due to the sharpness of the MCE in FOPT materials.

[23] However, from the temperature stability point of view, it probably would be preferred an operation below the point of maximum efficiency.

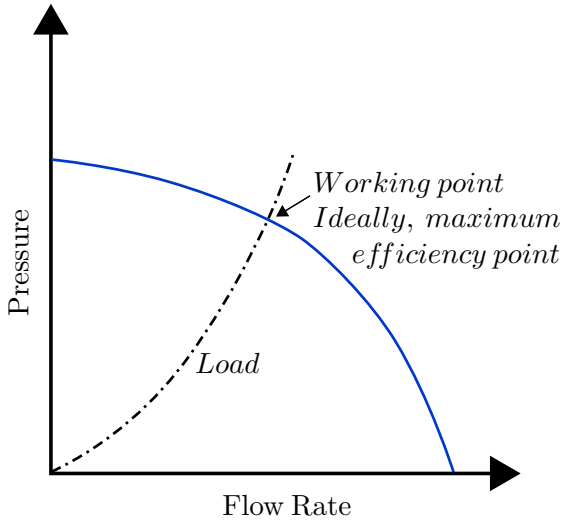

Figure 1.11: Pressure vs. flow rate characteristic curve of a centrifugal hydraulic pump. In an installation, the point of maximum efficiency is seeked as the nominal working condition, although the installation may have different working conditions that drive the pump to work in a different point of the curve. Due to the shape of the graph (this is only a typical graph), pressure and flow rate can change considerably with any perturbation but, again, if the perturbation is ceased, the system returns to the original working point automatically.

curve, with enough room to smoothly move sideways when the system's load changes. Isoefficient curves cross the graph at equidistant points on both sides of the maximum efficiency.

In summary, the behavior of a SOPT multi-material AMR does not support a stable temperature area, but due to the wide nature of SOPT materials' MCE, it should be easier to maintain a positive temperature span ($\Delta T = T_{ambient} - T_{cabinet}$) when a perturbation occurs.

An interesting possibility to try getting the best of both worlds, FOPT and SOPT materials, could be the use of combined multi-material AMRs, using layers of FOPT and SOPT materials. Lei et al. concluded in [94] that according to their simulations, mixing both types of MCM *helps to improve the system stability regarding deviations in the Curie temperature* of the materials. However, to the best of my knowledge, neither further simulations nor lab tests

with this approach have been reported.

1.7.2 Measuring the performance

The Coefficient of performance, or COP, is the most extended efficiency metric in refrigeration, and is defined as

$$COP = \frac{\dot{Q}_c}{\dot{W}}, \tag{1.22}$$

where $\dot{Q}_c$ is the cooling power—i.e. what we get—and $\dot{W}$ is the work power applied—i.e. what we provide, power consumed. COP has kind of a "personal" definition, because it depends on where I set the limits of the system, either including or neglecting power consumption in electronics, fans...

The effectiveness of energy devices may also be judged by its performance relative to that of a corresponding Carnot cycle machine, and is frequently expressed in terms of a percentage of the Carnot cycle efficiency. The theoretical maximum of COP is that of a Carnot cycle. Hence, the Carnot efficiency, or COP normalized to Carnot's COP, serves as a simple indicator to show how efficient an energy conversion device is, compared to the theoretical maximum of a corresponding ideal regenerative cycle. It is a seemingly easy way to compare, but care must be taken when choosing the temperatures of reference, since it is a source of misinterpretations when trying to compare results from different sources. The temperatures can be ambient and chamber temperatures, localized temperatures at some point of the heat exchangers or at source and sink, some kind of averaged temperatures at source and sink...

The COP of the ideal Carnot cycle operating between hot sink temperature, T_h and cold source temperature, T_c, can be expressed as a function of these two temperatures:

$$COP = \frac{\dot{Q}_c}{\dot{W}_{Carnot}} = \frac{T_{cold}}{|T_{hot} - T_{cold}|}, \tag{1.23}$$

and the Carnot efficiency as a percentage is then calculated applying,

$$\eta_{Carnot}\ [\%] = \frac{COP}{COP_{Carnot}}\ 100\%. \tag{1.24}$$

Exergy-equivalent cooling power, Ex_Q (exergy from now on), is also another way to measure the performance. It includes both, cooling power and temperature span and is the rate of exergy transfer, i.e. the work equivalent value of the heat flow or useful cooling power. The exergetic cooling power is then defined as,

$$Ex_Q = \dot{Q}_c\left(\frac{T_{hot}}{T_{cold}} - 1\right), \tag{1.25}$$

and in multi-material AMRs, the maximum value is typically found at the knee point of the cooling power vs. temperature span graph 1.9. In a single material AMR, the maximum exergy occurs at half the maximum cooling power, $\dot{Q}_{c,max}/2$.

As was mentioned above for the COP, it is also interesting to normalize Ex_Q. Rowe, proposed the exergy normalization to be done by volume of MCM, V_{MCM} and the applied magnetic field [104]. This proposal was later improved by Arnold et al. [105], using the magnetic field jump between the mean maximum and minimum fields during the fluid blow periods ($\bar{B}_{high} - \bar{B}_{low}$), obtaining a specific energy, μ_s, defined as

$$\mu_s = \frac{Ex_Q}{(\bar{B}_{high} - \bar{B}_{low})V_{MCM}}, \tag{1.26}$$

where

$$\bar{B} = \frac{1}{t_{blow}}\int_{t_\mathrm{i}}^{t_\mathrm{f}} B(t)\mathrm{d}t. \tag{1.27}$$

Since the COP does not include any information about the temperatures involved in the process, which turns the COP into a meaningless number for the home appliance industry[24], the efficiency of the device,η, can also be estimated mixing COP with exergy:

$$\eta = \frac{Ex_Q}{\dot{W}} = COP(\frac{T_{hot}}{T_{cold}} - 1). \tag{1.28}$$

Its value is restricted between zero and one, but it can also be expressed as a percentage.

[24]It is necessary to meet with regulatory standards and this means that, in order to be useful, the efficiency values should be given within the temperature windows established for each kind of appliance.

More details about commonly used performance metrics can be found, for example, in [1, 62, 104, 106]

As was explained in section 1.7.1, the knee point that appears in the cooling power vs. temperature span diagram of multi-material AMRs (figure 1.9), is mathematically defined as *that where the product of span and power is maximized* and, as explained above in this section, the maximum exergy is typically found at the knee point. Hence, it comes straightforward that the simple product of temperature span and heat load can also be used as an efficiency meter, at least for FOPT multi-material AMRs. However, this figure suffers once again from the same problem as the COP does, its lack of relation to the temperature range of the test.

According to EU regulation (EU 1060/2010), the international standard IEC[25] 62552 is used[26], through the energy efficiency index (EEI), which is used to define the Energy Efficiency Class that appears on the Energy Label of each appliance sold in the EU[27]. The EEI is expressed as a percentage, rounded to the first decimal place, and is determined as a function of the Annual Energy consumption (AE) and the Standard Annual Energy consumption (SAE):

$$EEI\ [\%] = \frac{AE}{SAE}\ 100\%. \tag{1.29}$$

The details about the calculation of AE and SAE can be found in EU 1060/2010 and EU 2019/2016[28], both available in the appendices A and B, respectively.

[25] International Electrotechnical Commission

[26] This standard has been recently revised in 2020.

[27] Energy Star Label in Australia, Canada or the U.S.A., for example.

[28] As already mentioned in section 1.7, EU 1060/2010 is to be completely substituted by EU 2019/2016 on March 1, 2021.

Part I

Building a Prototype

Presentation of Part I

Although the simulation of systems is a great tool to study their behavior, set starting points for prototype design and check the effects of modifications, prototypes are needed to check results in the real world, taking account for situations not foreseen in simulations (or too hard or computing time intensive to do so), often related with the clash between theoretical concepts and technical reality.

There was a desire to test a magnetic refrigeration device concept that, at the moment of starting the project and to the best of our knowledge, had not been used before. Basically, the concept involved the design of an improved version of a magnet previously reported by Eriksen et al. [107], and the use of solenoid valves as flow control devices with a continuous flow pumping system, avoiding the use of pistons, and rotary or poppet valves.

A rotary magnetic refrigeration prototype has been fully designed at ICMA (now INMA) (University of Zaragoza - CSIC) and built in collaboration with the company Dynatech Dynamics & Technology, S. L. U., and constitutes the first part of this thesis.

Chapter 2

A Rotative Magnetic Refrigeration Prototype

A magnetic refrigeration prototype has been constructed with the aim of testing the suitability of its concept and to allow the test of different MCMs and multilayer configurations. The concept of the prototype comprises a rotary magnet system with a modular AMR, a fluid flow control based on high speed solenoid valves and a rotary vane pumping station. The system is meant to hold an appreciable amount of MCM, with the expectation of obtaining a performance comparable to that of a commercial home refrigerator.

The purpose of this prototype follows the aimed goal of the project in which it is immersed, which is mainly to develop an understanding of magnetic refrigeration's capabilities and its sources of inefficiency. Although the previous experience in building magnetic cooling prototypes is of great help (see [108]) the concept and performance goal seeked, probably make this the most complicated magnetic refrigeration prototype conceived in our research group.

A rotary magnetic refrigeration prototype following Brayton-like thermal cycles has hence been fully designed at ICMA (now INMA) (University of

Zaragoza - CSIC), and built in collaboration with the company Dynatech Dynamics & Technology, S. L. U., being the last in charge of the assembly of the permanent magnet in a frame, and provide it with a traction system, power wiring, fluid pumps, high speed solenoid valves, programmable logic controller (PLC) based valves' aperture control, and power wiring.

2.1 Design specifications

The aim is to design a machine capable of holding an AMR with a large amount of MCM, and whose modularity allows it to hold from 1 to 6 MCMs, allowing the assembly of modular regenerators with exchangeable MCMs. This prototype is meant to test a specific machine concept which comprises a static regenerator block, in order to avoid the need of designing and using rotary valves for HTF flow control. The HTF flow control will be done by means of solenoid valves.

Additional requirements include a high inner MCM capacity, with eight regenerators for which cogging effects should be minimized for smooth magnet revolution, with a small and continuous demand of revolving torque. The phasing of the HTF blow through the regenerators and their magnetization should be adjustable $\pm$ 22.5° in steps of 2.5°.

The desired temperature span is of around 31 K and, ideally, with 45 W of cooling power, close to the temperature specification of the fresh-food storage compartment of a large built-in fridge, of an SN climate class appliance, and close to the upper limit cooling power of a T climate class. In order to achieve this, high MCM mass content and an improved magnet design are needed. Each pole of the magnet has to cover 45° (one regenerator), with a plateau at low field for enhanced performance of the AMR cycle, and a target rotating frequency of 1 Hz. This frequency regards the mechanical rotation of the magnet, since the regenerator is static as stated above, but the maximum frequency of the thermodynamic cycle is an integer multiple of this value, as will be later explained.

The desired 45 W of maximum cooling power, having in mind the considerations expressed in section 1.7, would not really correspond to the final figure when used in a commercial refrigerator. The actual figure would certainly be lower in an SN-appliance without freezer. Also, the maximum cooling power generated in a given MCM setup will depend on the final mass contained in the regenerators and the operation frequency and then, the system's losses will come into play. Hence, the cooling power finally obtained can differ substantially from the theoretically maximum achievable figure, and a similar reasoning can be followed with the maximum temperature span which, for a given MCM combination in an AMR, depends mainly on the separation of the T_C of the materials and the temperature range they cover, taking also into account the width of the MCE of the selected materials. It is therefore clear that, although the aim is to approach to the above mentioned values, the final result will depend on many design variables.

A home designed two pole magnet is used. This magnet is turned by a servo motor whose speed is controlled with a software provided by the supplier. The link between the motor and the magnet is achieved by means of a pinion and a slewing ring coupling. The assembly has a 1/20 reduction ratio, which means that in order to obtain 1 Hz of mechanical frequency in the magnet, the set value for the motor speed has to be 1200 rpm. Since each regenerator performs two thermodynamic cycles in every turn of the magnet, a motor speed of 1200 rpm will provide 2 Hz of thermodynamic frequency.

A further initial requirement is that the design of the prototype should be as compact as possible, trying not to exceed the width of a standard one door wide household refrigerator—600 cm.

These specifications, imply many others that often come into conflict with each other. A detailed analysis of the specifications' implications is discussed henceforth. The compromises taken, always pose a risk of failure in achieving the expected results.

Chapter 3

Magnetocaloric materials selection

The magnetocaloric material is the reason-to-be of a magnetic refrigerator and, therefore, the most important component. The selection of the MCMs includes not only their transition order (see section 1.4.3), but also, the family of materials and the way in which these materials are presented (e.g. plates, spherical beads, wires...) and the elections made, affect the design of the prototype and its operation. Deciding transition order and family of the materials, for example, determines the number of layers with different T_C that are needed for a desired temperature span. When the MCMs have the appropriate transition temperature spacing, they enlarge the temperature span of the device. As a drawback, if the spacing is too wide, the results turn bad because the whole fluid volume in the non acting layers is dead volume that spoils the regeneration effect. It has also to be considered that the family of materials chosen can sometimes limit the ways in which they are available.

There are no materials able to provide the large temperature change required for a household refrigerator using magnetic fields with a practical accesibility. The solution to enlarge the temperature span reached has been solved using an active magnetic regenerator (AMR), using different MCMs.

We need materials that, submitted to the action of a magnetic field, suffer a large adiabatic temperature change, ΔT_S, necessary to transfer heat between the acting materials in the cooling fluid. The cooling materials also need to have a high isothermal entropy change, ΔS_T, that affects the cooling power. Materials having high values of these two parameters are found in magnetic materials having a magnetic transition in the temperature range of interest. There are also some materials that, associated with the magnetic transition, can have a structural or an electronic transition that enhances the entropy change through the transition. Materials having a usual magnetic ordering transition show a second-order type of transition. These materials have a broad temperature range of cooling efficiency, moreover they do not suffer about thermal hysteresis problems, but their cooling power is not very high (they do not have the so-called giant magnetocaloric effect). The best material of this type is gadolinium (Gd), which is used as a benchmark for MCMs, though, being a rare earth, its high cost prevents its generalization for broad market devices.

A brief introduction to the MCM selection general criteria, and to some promising MCM families have been presented in section 1.4.3. I will focus now in the selection of the MCM family, the shape and other important considerations when selecting the materials for the AMR. It has to be emphasized that the selection process has to take into account different aspects which are linked with the design of other components of the prototype. I will henceforth remark the most relevant issues that have been considered in the design of the prototype and how they have been solved.

3.1 MCM family choice

The choice of the MCMs is usually done according to the characteristics of the MCE produced in them, but their availability, the shaping possibilities of the materials, and their mechanical integrity when used, have to be seriously taken into account.

It was a desire within our group to test two different families of materials, namely, one showing a SOPT and another presenting a FOPT, and due to the

relatively poor solid-fluid heat transfer observed in prior projects with parallel plates [108], it was decided to build the AMR with beds of spherical particles. Having all this in mind, Gadolinium and Gadolinium-Erbium compounds were chosen as the SOPT materials and the $La(Fe,Mn,Si)_{13}H_y$ family as the FOPT option. MCM characteristics of the materials and their availability were the deciding factors.

Gd and Gd-Er, and $La(Fe,Mn,Si)_{13}H_y$ compounds have been widely used and are very representative materials of SOPT materials, the first two, and of FOPT materials the last. $La(Fe,Mn,Si)_{13}H_y$ compounds (LaFeMnSi-H) are held as very promising materials for their application in magnetic cooling.

Each cavity of an AMR section has an effective volume of $10\,cm^3$, allowing for up to 0.35 kg of LaFeMnSi-H or 0.40 kg of Gd or GdEr spheres, which adds up to 2.1 and 2.4 kg of LaFeMnSi-H, and Gd or GdEr spheres, respectively, when using a six section AMR block.

3.2 The importance of being in shape

The shape of the materials has a definite impact in the design of the regenerator housing and the HTF pumping system. Materials used in plates need a design that holds blocks of several plates, in series. Machined MCM blocks in the shape of a fin heat exchanger is another option to obtain a plate-like MCM block. In these cases, the mass of MCM is fixed easily and with very high repeatability, and the void volume within the regenerator is fixed and easy to calculate, making this kind of presentation an easy choice for regenerators working in parallel, which should have a balanced flow—i.e., an identical pressure drop, see section 4.2—in order to maximize their performance [109]. Also, the use of plates implies a moderate pressure drop of the HTF as it is pushed through the regenerator, but the heat transfer between solid and fluid is rather poor [108], especially when using flat plates. However, the pressure drop is much lower than that obtained when spheres of MCM are used. The use of spherical beads brings about several design handicaps like a high pressure drop (the smaller the beads, the higher the drop), a habitual lack of sphericity of the beads, which are not mono-sized (with luck, a mono-modal dispersion of

sizes is obtained); finally, the mass of MCM lacks of a high repeatability and the figure of the void volume is not as easy to obtain as with plates, making it hard to construct pairs of twin regenerators to work in parallel. Another problem that arises from the use of particulate materials is the relative movement of the particles during the packing process, or when subjected to alternative magnetic and flow cycles if they are not very tightly packed. The relative movement produces heat losses and, especially, wearing of the particles, which means that the MCM ends up either clogging the porosity of the AMR, or being carried around the fluid system [110, 111]. As a preventive measure, a fine mesh filter has to be foreseen in the fluid installation in order to protect the pumping and valving subsystems, but this relative movement should be avoided at all cost, since having it, means that the voids are too big and will grow steadily to be transformed into dead volumes (see section 4.1), loosing MCM mass and diminishing the performance of the AMR [112].

Loose blocks of particles imply also problems of repeatability of the volume of fluid pushed through the AMR in every blow. In order to retain the MCM particles in separated blocks and, also, to avoid them from being carried out of the AMR by the HTF, some kind of containing method has to be devised. A common solution is the use of a nonmagnetic mesh with a pore size small enough to hold the particles inside their housing, while allowing an easy fluid flow at the same time. The exact shape of the MCM's particles and their size, related to the pore size of the mesh, can lead to the sudden and variable obturation of an important number of pores in the mesh if the particles are loose and can be moved by the magnetic forces and the HTF flow within the regenerator's compartment, changing thus the fluid dynamic resistance of the AMR. The flow may vary hence, according to different values of the pressure loss due to the uncontrollable disposition of the particles. This uncontrollable packing variation and possible movement of the particles first, added later to the brittle nature of certain MCM families that can turn the material into debris through repeated thermomagnetic cycling [111, 113], originated a search for a way to transform the beds of loose particles into a porous monolithic block. Although there are different techniques available to obtain a monolithic AMR—some of them published after the start of this project—like laser beam melting, powder extrusion, electrical discharge machining (EDM), polimer bonded powders, additive manufacturing processes, freeze-casting..., the most used techniques at the time of choosing the MCMs for this prototype were EDM shaped MCM blocks, and the use of a thin layer of epoxy to cover MCM particles and glue them together [23, 102, 111, 114–118]. For this last solution, the amount of epoxy has to be carefully controlled to be enough to produce a thin layer that provides a relatively flexible mechanical reinforce-

ment around the particles, thin enough not to be a serious hindrance for the solid-fluid heat transfer, but thick enough to glue the particles together in a high porosity block. Although it is a general opinion that a thin layer of a plain epoxy[1] increases interfacial heat transfer resistance acting as a parasitic mass, and risks the clogging of the bed's porosity (which would increase the pressure drop), according to Jacobs et al., the use of epoxy as binder in particle beds can sometimes also help to lower the pressure drop of the fluid flow, since the binder produces a smooth surface around the particles, providing a lower resistance to the flow [102]. The price to pay should be a poorer solid-fluid heat transfer performance due to the decrease in the heat transfer surface of the particles and the added polymer's heat resistance; however, it is my believe that the benefits and hindrances of this epoxy bound AMR blocks remain controversial. Results reported in literature depend much on the material's initial shape characteristics, the characteristics of the epoxy, the processing conditions, the care taken during the conformation process and, of course, on the nature of the HTF used [102, 111, 114, 115, 119]. An important issue seldom accounted for is that epoxy resins are usually mixed with additives which somehow modify the behavior of the polymer for different purposes, although the manufacturers do not always provide this information. Especially in the case of small sized end consumer presentations, the precise composition of the resin is often unknown. The use of some very common additives in epoxy resins like calcium carbonate are discouraged in applications were corrosion resistance is needed, and they often increase the epoxy's hygroscopicity which results in an increase of the polymer's volume and a major change in its mechanical performance due to water absorption. Other common additives are meant to increase the electrical or thermal conduction of the polymer. This information should be known and provided when reporting research results to allow proper comparison with other published results.

The use of EDM shaped MCM blocks is an interesting technique which results in very easy to assemble regenerators. EDM is used due to its precision in machining very small gaps without subjecting the material to high mechanical stress, although a casting technique for example, would certainly produce cheaper blocks. Some important drawbacks of this technique come alight especially when using it with FOPT materials:

[1] So far, the epoxy glue reported as used in this kind of application has, to the best of my knowledge, no additives to increase their thermal conductivity. The use of such an epoxy could minimize or even avoid this problem.

1. The cycling stresses typical from FOPT materials are still a problem and measures need to be undertaken to avoid their consequences.

2. Many FOPT materials, like those of the La-Fe-Si family, are brittle, having limited machining possibilities and increasing the minimum advisable thickness. This, limits the shaping options to an extent that does not allow obtaining a thin enough structure in certain areas of the block.

3. The thickness that the blocks present in certain spots, limit the heat transfer between the core of the solid and the HTF, enhancing the heat transfer limitations present in the use of flat MCM plates.

The possibility of using in-house EDM shaped blocks was investigated and a test pattern was designed to be machined in a small block of a LaFeCoSi sample; however, the results proved rather disappointing since the thin fins needed broke very easily during the process and, also, the surfaces of the block showed important signs of corrosion. Commercial EDM shaped blocks were out of the question since, in addition to the problems pointed out above, due to the AMR's shape being handled, it would be necessary to order specially shaped blocks out of catalog, with an increased cost and lead time, if possible at all.

3.3 A bit of beds of beads modelling

When considering the shape of the magnetocaloric material (MCM) to be placed in the regenerator, different issues have to be taken into account. Once it has been decided which MCM family or families are of interest to be placed in the machine, several questions arise: price, availability of the material, supply forms available, machinability, specific considerations regarding the material, heat transfer considerations of the material's shape, etc.

An implicit common ground of MCM shape studies is that there is always a trade-off between good heat transfer and pressure drop. For example, parallel plate shapes, result in laminar flows with negligible heat buildup due to viscous friction and very low pressure drops, but mediocre heat transfer rates between the MCM and the HTF. By contrast, packed bed systems usually show good

solid-fluid heat transfer, but the trade off comes in the form of high pressures and turbulent flows that generate viscous friction.

Simulation of packed bed systems has a higher complexity than of parallel plate systems and this is due to the flow regime, the geometry of the MCM, the voids of the bed, and the shape of the bed's particles. All this brings about a handful of heat transfer an shape considerations within the governing equations, intended to take into account as many of these different aspects, that affect the final results, as possible. One of the aspects that appears in the governing equations which is physically important, is that of the size and shape of the bed's particles. Particle technology, and packed and fluidized beds research are the main resources to enlighten the path when addressing a packed bed configuration.

When a simulation or a theoretical calculation is made, one is prone to use a simple number for the size of the particle and consider it and its shape constant. Spherical particles of an exact diameter specification are almost invariably the goals when designing a packed bed AMR. However, these two characteristics, size and shape, are probably the most annoying ones when you get to the real world. A material sample can very rarely be represented by a unique shape, i.e. a sphere, or a unique size, i.e. the diameter. The sphericity of the particles can vary due to the manufacturing process and inherent characteristics of the material. In this context, the word 'diameter' may not make much sense. Also, the size is never going to be unique. The particles within the batch will have many different sizes, and the supplier can sieve them in order to provide a batch with a controlled distribution of sizes. A good supplier should be able to provide a batch with a narrow distribution of sizes, hopefully uni-modal. There are ways of addressing the problem of characterizing the particles' size and shape distributions with equivalent single numbers. They are statistic solutions of common use in particle technology as can be found in [120].

It should be noted that not only the size and shape of the particles are of utmost importance, but also, their distribution is very important. Size and shape distributions of the particles affect the bed's final porosity and from it, the pressure work needed to push the fluid through it. They also affect the effective heat transfer between the solid bed and the heat transfer fluid.

3.3.1 Pressure drop in a packed bed

A recurrent issue in the management of the heat transfer fluid in any magnetic refrigerator is the pressure work needed to push the fluid through the AMR. The amount of work needed to push the fluid while the machine is working is, of course, one of the big numbers to control if you want to achieve a machine that has a good overall Coefficient of Performance (COP); but this problem is trickier than it seems, because the fluid pressures and speeds, i.e. the flow regime used, affects also the heat transfer performance and can be the origin of an unwanted heat buildup within the AMR. This unwanted heat buildup can became relevant when there is a turbulent regime within the regenerator, which is the case when using a packed bed of MCM in the AMR.

In the present prototype, there are two groups of regenerators working at any one time. Each one of these groups consists of two regenerators working in parallel, connected in series through the cold spot of the refrigerator.

We can use the modified Ergun equation (3.1), to make calculations that bring some light to the implications of using a packed bed of spherical beads of MCM.

Verifying the relationship between the pressure drop in one AMR, and the pressure drop within the complete group of regenerators is interesting in order to have a proper idea of the implications of the chosen combination of AMR. The modified Ergun's equation used in this work is:

$$-\frac{dp}{dx} = \frac{180\mu_f(1-\varepsilon)^2}{d_p^2\varepsilon^3}v_d + \frac{1,8\rho_f(1-\varepsilon)}{d_p\varepsilon^3}v_d^2\,. \tag{3.1}$$

Under laminar conditions, the first term of equation (3.1) is dominant and it reduces to a modified Carman-Kozeny equation. The second term accounts for the pressure drop under turbulent conditions, where it becomes dominant and the modified Ergun equation then reduces to a modified Blake-Plummer equation [120, 121].

Ergun's equation, as is written in (3.1), is valid for mono-sized beds of spherical particles, which is very rarely the case, and Newtonian fluids. In order to use this equation with a distribution of non-spherical particles, corrections have to be made in the diameter, d_p.

Taking into account the lack of sphericity, the diameter of the sphere has to be replaced by the surface to volume diameter, d_{sv} (see equation (3.2)), which is the diameter of a sphere having the same surface to volume ratio as one of the non-spherical particles in question [120].

$$d_{sv} = \frac{\text{Volume of particle}}{\text{Surface area of particle}} \tag{3.2}$$

However, for a distribution of particles, the correct value to use is the surface to volume mean:

$$\bar{d}_{sv} = \frac{\int_0^1 x^3 dF_N}{\int_0^1 x^2 dF_N} \,, \tag{3.3}$$

where F_N is the number of particles per unit volume of the container.

Starting now from the modified Ergun's equation (3.1), we can extract the common factors obtaining the following expression:

$$-\frac{dp}{dx} = \frac{v_d(1-\varepsilon)}{d_p \varepsilon^3}\left(\frac{180\mu_f(1-\varepsilon)}{d_p} + 1,8\rho_f v_d\right) . \tag{3.4}$$

We can now make $v_d = \mathcal{Q}/A$, being $\mathcal{Q}$ the volumetric flow rate and A the cross section area of the regenerator bed, and at constant $\mathcal{Q}$ and μ_f:

$$-\frac{dp}{dx} = \frac{\mathcal{Q}(1-\varepsilon)}{S d_p \varepsilon^3}\left(\frac{180\mu_f(1-\varepsilon)}{d_p} + 1,8\rho_f \frac{\mathcal{Q}}{A}\right) \Rightarrow \tag{3.5}$$

$$\Rightarrow dp = -\frac{\mathcal{Q}}{A}\frac{(1-\varepsilon)dx}{d_p\varepsilon^3}\left(\frac{180\mu_f(1-\varepsilon)}{d_p} + 1,8\rho_f\frac{\mathcal{Q}}{A}\right). \tag{3.6}$$

Making a change of variables, equation (3.6) is transformed into:

$$dp = -\frac{\mathcal{Q}}{A}dx\left(\mathcal{A} + \mathcal{B}\frac{\mathcal{Q}}{A}\right). \tag{3.7}$$

Similarly, we can duplicate the section, $A' = 2A$ obtaining:

$$dp' = -\frac{\mathcal{Q}}{2A}dx\left(\mathcal{A} + \mathcal{B}\frac{\mathcal{Q}}{2A}\right). \tag{3.8}$$

Equation (3.8) shows that the pressure loss is not only reduced by a half, but also, that it halves its quadratic term in speed.

Following the same procedure, duplicating now the length by making $dx' = 2dx$:

$$dp'' = -\frac{\mathcal{Q}}{2A}2dx\left(\mathcal{A} + \mathcal{B}\frac{\mathcal{Q}}{2A}\right) \Rightarrow \tag{3.9}$$

$$\Rightarrow dp'' = -\frac{\mathcal{Q}}{A}dx\left(\mathcal{A} + \mathcal{B}\frac{\mathcal{Q}}{2A}\right) = 2dp'. \tag{3.10}$$

Now, equation (3.10) shows that when the length is doubled, the pressure loss doubles, also. As a result, a single regenerator with double the section and simple length (or even smaller) can be physically tested, in order to lower the pressure loss within the model, and later multiply the pressure drop obtained by the length reduction factor that has been applied.

On the other hand, if we pay attention to the diameter of the bed's spherical beads, starting from equation (3.6), we can see that when increasing the

spheres' diameter, the pressure loss diminishes and viceversa. The result of this is that we can introduce a scaling factor, ϕ, in the diameter of the particles (it could be the sphericity, shape factor or just a change in the nominal diameter):

$$dp''' = -\frac{\mathcal{Q}}{A}\frac{(1-\varepsilon)dx}{\phi d_p \varepsilon^3}\left(\frac{180\mu_f(1-\varepsilon)}{\phi d_p} + 1,8\rho_f\frac{\mathcal{Q}}{A}\right), \tag{3.11}$$

which can be rewritten as follows at equal porosity, flow rate, section, viscosity, density and length:

$$dp''' = -\left(\frac{\mathcal{A}}{\phi^2} + \frac{\mathcal{B}}{\phi}\right). \tag{3.12}$$

Equation (3.12) is an interesting result since it shows that if we obtain the pressure loss for a given bead diameter (or shape factor), we can calculate the pressure loss for another bead diameter or shape factor, under the same conditions of porosity, flow rate, section, viscosity, density and length, by applying the scale factor to the terms of Ergun's equation (3.1). Equation (3.12) also implies that a change in the shape of the particles that makes them less spherical, will significantly increase the pressure loss, since the factor ϕ is 1 for a perfect sphere and it decreases as the particles' shape departs from the ideal contour.

An example of the application of these results further shows their interest. Let us assume a bed of spherically shaped beads of 0.5 mm of diameter and a porosity of 36%. Let us assume also that the flow rate, cross section, viscosity, density and the length of the bed with a value of 1 in the international measurement system. Under these conditions, applying (3.11), once transformed from Pa into bar, we obtain:

$$dp'''_{0.5} = -\frac{(1-0.36)}{0.5\times10^{-3}\times0.36^3}\left(\frac{180\times(1-0.36)}{0.5\times10^{-3}} + 1.8\right) \approx 6.32\times10^4 \text{ bar}. \tag{3.13}$$

In this case, from (3.11) and (3.12) and transforming the result into bar,

we obtain

$$\mathcal{A} = \frac{\mathcal{Q}}{A}\frac{(1-\varepsilon)dx}{d_p\varepsilon^3} \approx 6.32 \times 10^9 \ , \tag{3.14}$$

$$\mathcal{B} = \frac{(1-\varepsilon)dx}{\phi d_p\varepsilon^3}1.8\rho_f\frac{\mathcal{Q}}{A} \approx 4.94 \times 10^4 \ . \tag{3.15}$$

Now, if we want to know how a change in the diameter of the balls, let us say to 0.8 mm, will affect the pressure loss in the system, we can simply apply $\phi = 0.8/0.5 = 1.6$ to (3.12) obtaining, transformed into bar,

$$dp'''_{0.8} = -\left(\frac{6.32 \times 10^9}{1.6^2} + \frac{4.94 \times 10^4}{1.6}\right) \approx 2.47 \times 10^4 \text{ bar.} \tag{3.16}$$

These figures show that just by changing the diameter of the balls from 0.5 to 0.8 mm, a reduction of the pressure loss by a factor of 2.56 is achieved.

3.3.2 Particle Diameter and Heat Exchange: a simple model

The study of the heat transfer between a bed of spheres of MCM and the HTF is of great importance, since we can extract from it information to decide the diameter of the spheres that will result in a good heat transfer, without unnecessarily increasing the pressure drop in the regenerator. The quality of the heat transfer can be measured taking into account the temperature decay time of a heat pulse within the sphere. For this purpose, a 1D dynamic model of a bed of MCM spheres has been developed in Fortran and the data obtained processed in order to have an approximation of the temperature decay times for different diameters of the spheres and fluid flow speeds. Actually, the result at a low flow speed is what is relevant.

For the sake of user clarity, and in order to save some pre-processing and computing time, an Excel spreadsheet is used as user interface to introduce the basic parameters of the simulation such as AMR size, initial temperature, basic MCM and HTF physical data, heat pulse introduced, porosity of the bed, MCM sphere diameters set, HTF volume per blow set, and mesh and time step

values. The spatial mesh for fluid and solid is unified in a common step size. The spreasheet makes the basic calculations which are not field, temperature or time dependent for all cases—i.e., parameters for the combinations of sphere diameter and HTF speed—and builds through a routine programmed in Visual Basic for Applications (VBA) the input text file for the finite differences calculations program, made in FORTRAN. Incompressible fluid approximation and, due to the small temperature range used in the calculations, constant thermal conductivities and fluid viscosity are used, for which some typical values are introduced (table 3.1).

Although the worst case is when the speed of the fluid is zero, the model can be set to make the calculations for different flow speeds. The flow speed is set by establishing the fraction of the void volume of the container that it is pushed through. This model was used as a preliminary approach, before the AMR block had its final design, to see how the size of the MCM particles really affects the heat transfer from the MCM to the fluid. Most physical parameters of the MCM and HTF have therefore been used with constant and typical values. Only the heat capacity of the MCM has been modeled to show a realistic behavior.

In order to build a model to do some calculations, several aspects need to be mathematically defined: the bed has to be characterized (shape, size, bed characteristics including MCE), the fluid flow, the pressure loss (Ergun's equation (3.1)), the heat transfer between solid and fluid, and the calculation procedure (dimension of the model and mathematical approach).

Material model and governing equations

The model simulates the heat transfer taking place along the longitudinal axis of a bed of MCM spheres to the fluid flowing through the bed. Since this is meant to be a simple model, several approximations have been used in order to develop the program in a short time and, also, to speed up the calculations.

The fluid is considered incompressible, the flow is constant and the MCM particles are considered mono-sized perfect spheres. Another approximation is

related to the way the MCM gets excited, to increase its temperature due to the MCE. A sudden heat pulse within the material is introduced as excitation of the system, which is similar to the real effect, but no calculation regarding the excitation of the material and its MCE response has to be carried out. The use of a heat pulse could actually have been changed for a fixed initial temperature in the solid of about 3 °C higher than that of the fluid—e.g., about 12.5 °C, which is an aproximate value of the ΔT_S of the MCM used in this simulation for a field change from 0 to 1.5 T, if the initial temperature is of about 9.5 °C.

The MCM used in the simulation is a $LaFe_{13-x-y}Co_xSi_y$ sample available in our laboratory. This election was done because the heat conduction of this material is rather low (i.e. worst case), compared to other considered MCMs. Actually, $La_{1.005}Fe_{11.086}Co_{0.871}Si_{1.044}$ batch MPS 1175 provided by the company Vacuumschmelze GmbH & Co. KG. (VAC) was the material used in the model, of which I had direct measured MCE data available. Further, the initial temperature and the temperature of the fluid entering the bed, is set to 9.5 °C, which is approximately, its value at the peak of the heat capacity of the MCM, c_p, at a field of 1.5 T.

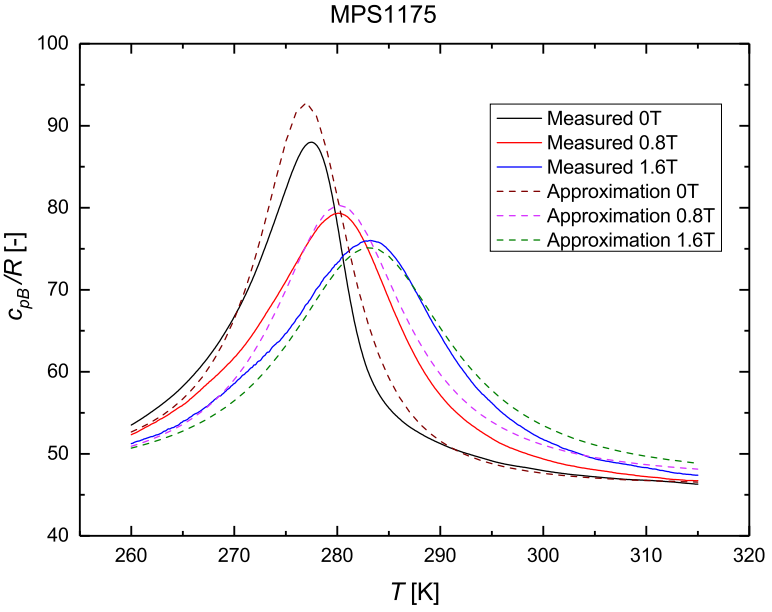

Figure 3.1: Graphs obtained from measurements compared with the asymmetric Lorentz equation (3.17). Although the approximation is a bit crude for 0 T, it is enough for the purpose.

Even though I published a modeling method for FOPT materials based on LaFeCoSi compounds [122, 123], it ended with data interpolation tables, which are costly in terms of computing time. If the thermodynamic parameter can be approximated by means of an equation, the programming turns easier and the computing time ends up being shorter.

Taking the data of the $c_p(T)$ at 0, 0.8, 1.6 and 3 T, it can be observed that they are fairly well approximated by an asymmetric Lorentz equation as long as we do not move very far from the peak temperature (see figure 3.1). The expression obtained is a function of the temperature and the field:

$$c_{p,B}(B,T) = \left(y_0 + \frac{A(B)w(B) - b(B)(T - T_0(B))}{4(T - T_0(B))^2 + w^2(B)}\right) \frac{R}{M_m \times 10^{-3}} \,, \quad (3.17)$$

where B is the magnetic field intensity in Tesla, T is the temperature in Kelvin, R is the molar gas constant in J/(mol K), M_m is the molar mass of the material in g/mol and then, $c_{p,B}$ is given in J/(kg K) and according to the fitting carried out with the software OriginPro from OriginLab Corporation:

$$y_0 = 46.5, \quad (3.18a)$$
$$T_0(B) = 277.31 + 3.623B, \quad (3.18b)$$
$$w(B) = 11.095 + 6.3678B - 0.85048B^2, \quad (3.18c)$$
$$A(B) = 511.65 + 22.732B \quad (3.18d)$$

and,

$$b(B) = 142.16 + 38.955B - 10.764B^2. \quad (3.18e)$$

Since the simulated MCE is only a pulse, the value of the magnetic field, B, is set to 1.5 T at the pulse and then reset to 0 T for the rest of the simulation, leaving the heat capacity as a function of temperature, only. A summary of the physical parameters used for the MCM and the HTF, is available in table 3.1.

The length of the packed bed is set to 150 mm. This size corresponds to six sections of MCM, each one of 25 mm of height, which is the size that was being handled in the design at the time of programming the model. The final design comprises a section height of 30 mm, which adds up to 180 mm when six sections of MCM are used in the AMR block. Also, the shape of the AMR was set to match a cylinder with the cross section area of an AMR as was obtained from the preliminary design handled at the time ($6.62 \times 10^{-4}\,\mathrm{m}^2$). The cross

Table 3.1: Summary of the fixed MCM and HTF physical parameters, initial temperature and heat pulse used in the simulation. Although the value of the heat pulse may seem very large, it is applied only in a timestep, resulting in a small energy pulse.

T_{ini}	9.5	°C			
Q_{MMC}	10	MW			
FLUID			SOLID		
ρ_f	997.13	$\mathrm{kg\,m^{-3}}$	ρ_s	7100	$\mathrm{kg\,m^{-3}}$
k_f	0.570	$\mathrm{W\,m^{-1}\,K^{-1}}$	k_s	7	$\mathrm{W\,m^{-1}\,K^{-1}}$
$C_{p,f}$	4180	$\mathrm{J\,kg^{-1}\,K^{-1}}$			
μ_f	8.91×10^{-4}	Pa s			

sectional area of two parallel regenerators in the final design ended up being $6.67 \times 10^{-4}\,\mathrm{m^2}$, which is a very close figure.

The governing equations are based on a model that arises from applying the first law of Thermodynamics to the solid bed and to the fluid flowing through it, resulting in two equations coupled by the convective term of the heat transfer.

$$-(1-\varepsilon)\,\rho_s\,T_s\,\frac{\partial s}{\partial B}\,\frac{\partial B}{\partial t} = -k_{e,s}\,\frac{\partial^2 T_s}{\partial x^2} - h_{s,f}\,a\,(T_f - T_s) + (1-\varepsilon)\,\rho_s\,c_s\,\frac{\partial T_s}{\partial t}\,, \tag{3.19a}$$

$$\frac{dP}{dx}\,v_d = \rho_f\,v_d\,c_f\,\frac{\partial T_f}{\partial x} - k_{e,f}\,\frac{\partial^2 T_f}{\partial x^2} - h_{s,f}\,a\,(T_f - T_s) + \varepsilon\,\rho_f\,c_f\,\frac{\partial T_f}{\partial t}\,. \tag{3.19b}$$

This model is well-established and widely used by other authors [102, 124, 125]; however, it must be clarified that defining the MCE in terms of $(\partial s/\partial B)_T$ is not correct when dealing with hysteretic FOPT materials and should be transformed in terms of $(\partial/T\partial B)_S$. The reason for this is that in a first order transition, the values of $(\partial s/\partial B)_T$ and c_{pB} tend to infinity, leading to an indeterminate form of the type (∞/∞). Besides, unlike the form in terms of $(\partial T/\partial B)_S$, the expression of the MCE in terms of $(\partial s/\partial B)_T$ has not been demonstrated for the case of irreversible thermodynamics. Nevertheless, since the MCE in this case is going to be substituted by a heat pulse (equation (3.27)), no calculation regarding the MCE in terms of $(\partial s/\partial B)_T$ is performed.

The different parameters present in equations (3.19a) and (3.19b) are determined following Monfared and Palm [124], who summarized in their work

the necessary equations extracted from different sources. These parameters are obtained with equations (3.20) (valid as long as $Re_d < 8500$), (3.23), (3.24), and (3.25) [126]. Also, as it is done in the referred work, the pressure drop along the MCM packed bed is obtained using the modified Ergun equation (3.1) [121].

$$h_{s,f} = \frac{k_f}{d_p}\left(2 + 1.1\, Pr^{1/3}\, Re_d^{0.6}\right) \tag{3.20}$$

where:

$$Pr = \frac{c_f\, \mu_f}{k_f}\ , \tag{3.21}$$

$$Re_d = \frac{\rho_f\, v_d\, d_p}{\mu_f}\ , \tag{3.22}$$

$$k_{e,f} = k_f\left(\varepsilon + 0.5\, Re_d\, Pr\right)\ , \tag{3.23}$$

$$k_{e,s} = (1-\varepsilon)\, k_s\ , \tag{3.24}$$

and,

$$a = \frac{6\,(1-\varepsilon)}{d_p}\ . \tag{3.25}$$

If the excitation of the system is to be introduced by means of a heat pulse, equation (3.19a) has to be rearranged. First, the time derivatives have to be grouped together and then, a substitution of the MCE by a heat term is necessary. Rearranging then equation (3.19a),

$$(1-\varepsilon)\,\rho_s\Big[\overbrace{c_s\frac{\partial T_s}{\partial t}}^{Sensible\ heat} + \underbrace{T_s\frac{\partial s}{\partial B}\frac{\partial B}{\partial t}}_{MCE}\Big] = \overbrace{k_{e,s}\,\frac{\partial^2 T_s}{\partial x^2}}^{Conduction} + \underbrace{h_{s,f}\,a\,(T_f - T_s)}_{Convection}\ . \tag{3.26}$$

The MCE term in equation (3.26) is now substituted by a variable that resembles the heat change produced by MCE. After doing this and rearranging, the equation is transformed into:

$$\frac{\partial T_s}{\partial t} = \underbrace{\frac{k_{e,s}}{(1-\varepsilon)\,\rho_s\, c_s}}_{A_1(T,B)}\,\frac{\partial^2 T_s}{\partial x^2} + \underbrace{\frac{h_{s,f}a}{(1-\varepsilon)\,\rho_s\, c_s}}_{C_1(T,B)}\,(T_f - T_s) - \underbrace{\frac{Q_{MCE}}{\rho_s\, c_s}}_{D_1(T,B)}\ , \tag{3.27}$$

where Q_{MCE} has to be expressed in $\mathrm{W\,m^{-3}}$.

The equation above can be simplified using the variable changes shown in the underbrackets, obtaining:

$$\frac{\partial T_s}{\partial t} = A_1(T,B)\,\frac{\partial^2 T_s}{\partial x^2} + C_1(T,B)\,(T_f - T_s) - D_1(T,B) \tag{3.28}$$

The terms of equation (3.19b), which can also be simplified in a similar way, are as follows:

$$\overbrace{\frac{dP}{dx}}^{Pressure\ term} v_d = \underbrace{\rho_f\, v_d\, c_f\, \frac{\partial T_f}{\partial x}}_{Advection} - \overbrace{k_{e,f}\, \frac{\partial^2 T_f}{\partial x^2}}^{Conduction} - \underbrace{h_{s,f}\, a\, (T_f - T_s)}_{Convection} + \overbrace{\varepsilon\, \rho_f\, c_f\, \frac{\partial T_f}{\partial t}}^{Fluid\ energy\ change}\ , \quad (3.29)$$

where the pressure derivative is obtained by means of the modified Ergun equation (3.1).

We obtain the simplified equation by introducing the following variable changes:

$$\frac{\partial T_f}{\partial t} = \underbrace{\frac{k_{e,f}}{\varepsilon\, \rho_f\, c_f}\, \frac{\partial^2 T_f}{\partial x^2}}_{A_2(T,B)} - \underbrace{\frac{v_d}{\varepsilon}\, \frac{\partial T_f}{\partial x}}_{B_2} + \underbrace{\frac{h_{s,f}\, a}{\varepsilon\, \rho_f\, c_f}\, (T_f - T_s)}_{C_2(T,B)} + \underbrace{\frac{dP}{dx}\, \frac{v_d}{\varepsilon\, \rho_f\, c_f}}_{D_2(T,B)}\ . \quad (3.30)$$

The simplified equation results:

$$\frac{\partial T_f}{\partial t} = A_2(T,B)\, \frac{\partial^2 T_f}{\partial x^2} - B_2\, \frac{\partial T_f}{\partial x} + C_2(T,B)\, (T_f - T_s) + D_2(T,B)\ . \quad (3.31)$$

Discretization

The process shown in section 3.3.2 results in a simplified system of equations. equation (3.28) describes the energy balance of the solid and equation (3.31), describes the energy balance of the fluid, while the convective terms that appear in both equations establish the coupling between both sub-models—i.e. solid and fluid sub-models.

Ideally, Crank-Nicolson and Gauss-Seidel methods combined should be used for a system like the proposed one, due to its precision and avoidance of convergence problems. However, being this the first time this author used FORTRAN as programming language, I decided to start making a much simpler program with an explicit method as a starting point and, if necessary, transform it to a Crank-Nicolson afterwards. The explicit finite element method can be very problematic due to its convergence restrictions, it is also less accurate than Crank-Nicolson and forces the use of very small time steps, being

hence a risky bet. Fortunately, a convenient convergence was soon obtained with the explicit method, and there was no real need to program the implicit one.

The discretization of the explicit mode has been done with the numeric approximations in table 3.2.

Table 3.2: Differences used in the discretization for the explicit method.

First time derivative	$\longrightarrow$	Forward difference
First space derivative	$\longrightarrow$	Backward difference, three steps upstream (to increase precission)
Second space derivative	$\longrightarrow$	Central difference

Taking then the simplified equations obtained above,

$$\begin{cases} \dfrac{\partial T_s}{\partial t} = A_1(T,B)\,\dfrac{\partial^2 T_s}{\partial x^2} + C_1(T,B)\,(T_f - T_s) - D_1(T,B)\ , \\ \dfrac{\partial T_f}{\partial t} = A_2(T,B)\,\dfrac{\partial^2 T_f}{\partial x^2} - B_2\dfrac{\partial T_f}{\partial x} + C_2(T,B)\,(T_f - T_s) + D_2(T,B)\ , \end{cases}$$

after discretizing, these equations turn into:

$$\frac{T^i_{s_2} - T^i_{s_1}}{\Delta t} = A_1(T,B)\left[\frac{T^{i+1}_{s_1} - 2\,T^i_{s_1} + T^{i-1}_{s_1}}{(\Delta x)^2}\right] + C_1(T,B)\left[T^i_{f_1} - T^i_{s_1}\right] - D_1(T,B)\ , \tag{3.32a}$$

$$\begin{aligned} \frac{T^i_{f_2} - T^i_{f_1}}{\Delta t} = {} & A_2(T,B)\left[\frac{T^{i+1}_{f_1} - 2\,T^i_{f_1} + T^{i-1}_{f_1}}{(\Delta x)^2}\right] + \\ & - B_2\left[\frac{3\,T^i_{f_1} - 4\,T^{i-1}_{f_1} + T^{i-2}_{f_1}}{2\,\Delta x}\right] + C_2(T,B)\left[T_f - T_s\right] + D_2(T,B)\ , \end{aligned} \tag{3.32b}$$

Solving for the variables of the next timestep (with subscript " 2"), the

equations to be used in the simulation program are:

$$T_{s_2}^i = T_{s_1}^i + \frac{A_1(T,B)\,\Delta t}{(\Delta x)^2}\left[T_{s_1}^{i+1} - 2\,T_{s_1}^i + T_{s_1}^{i-1}\right] + \\ + C_1(T,B)\,\Delta t\left[T_{f_1}^i - T_{s_1}^i\right] - D_1(T,B)\,\Delta t\,, \tag{3.33a}$$

$$T_{f_2}^i = T_{f_1}^i + \frac{A_2(T,B)\,\Delta t}{(\Delta x)^2}\left[T_{f_1}^{i+1} - 2\,T_{f_1}^i + T_{f_1}^{i-1}\right] + \\ - \frac{B_2\,\Delta t}{2\Delta x}\left[3T_{f_1}^i - 4T_{f_1}^{i-1} + T_{f_1}^{i-2}\right] + C_2(T,B)\,\Delta t\,[T_f - T_s] + D_2(T,B)\,\Delta t\,, \tag{3.33b}$$

where the subscripts "1" and "2" stand for the actual and the next time values, respectively[2].

After carrying out a batch of sensitivity tests, it was determined that a step size, Δx of 5×10^{-4} m and a time step of 1×10^{-4} s was a good combination of discretization parameters to run the simulations. The chosen spatial step size resulted in 300 elements for the solid and the same for the fluid meshes.

Simulation results

The simulation results are output in text format files and are post-processed using the software OriginPro. Attention is paid to the fluid speed values that result in a lower heat transfer ratio—i.e., zero or low speed cases. The main goal of the collected data is to draw a comparison graph of the thermal relaxation times of the different input sphere diameters, obtaining at the same time a curve fit that allows the direct calculation of the relaxation time for any sphere diameter. The relaxation process involves two phases:

1. a fast relaxation, with which the temperatures of solid and liquid balance their temperatures, and,

[2] Another more formal way to express this would be to change subscript "1" for a variable—e.g. "j"—and acordingly, subscript "2" for "$j+1$"

2. a slow relaxation of the common temperature of both, solid and liquid, to that of ambient.

Only the fast relaxation process is of interest to us in this case, and the relaxation times are calculated for temperatures in the mid-length of the bed. The basic AMR geometric and device working assumptions used in the simulations are summarized in table 3.4.

As a result, the graph obtained for a no-flow case is shown in figure 3.2, the exponential fit data of the curve is presented in table 3.3 and a summary of the relevant points of the curve are available in table 3.6. From the data of table 3.3, the relation between the particle diameter and the relaxation time for the no-flow case can be calculated using:

$$[t_{rel}]_{0\%} = 74.88977\, e^{d_p/0.66117} - 96.80479\ , \tag{3.34}$$

where the subindex "0%" stands for a fluid blow of 0% of the interstitial volume of the bed, and t_{rel} is obtained in ms if d_p is stated in mm.

Table 3.3: Exponential fit data of figure 3.2 (stagnant fluid). The particle diameter has to be given in mm and the relaxation time is obtained in ms.

Model	One-phase exponential growth		
Equation	$t_{rel} = A_1 e^{d_p/t_1} + t_0$		
Reduced Chi-Sqr	2.35716		
Adj. R-Square	0.99961		
		Value	Standard Error
Relaxation time in solid	t_0	-96.80479	10.73866
	A_1	74.88977	7.98294
	t_1	0.66117	0.03389

The above presented information and the fit data contained in table 3.3 regard the worst possible heat transfer case between the solid and the fluid, which is with stagnant liquid—i.e., no flow. The relaxation times experiment a great change when some speed is given to the fluid. The fluid used in this simulations is water, and water is known for having a rather low thermal conductivity, relying most of its heat exchange capacity in convection. As an example, we can take a look at the difference when only 5% of the AMR's void volume is pushed through the bed in each blow (void regenerator fraction blow, or V_{frac}).

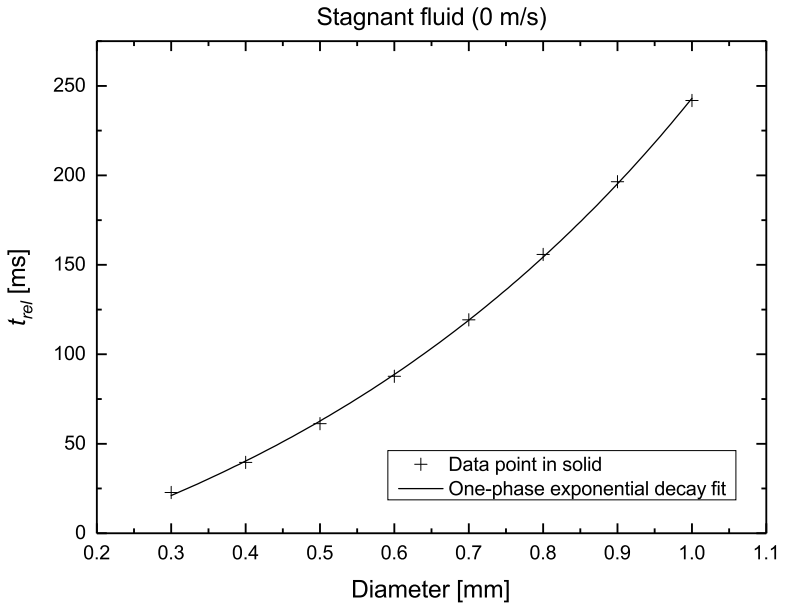

Figure 3.2: Relaxation times of MCM vs. diameter of the spheres at no fluid flow. A summary of the data points is in table 3.6. The details of the data fit are shown in table 3.3.

In order to evaluate the flow rate that corresponds to any V_{frac}, first a thermal operating frequency has to be set, and this value is linked to the mechanical frequency of the machine. In this prototype, the thermodynamic frequency is twice the mechanical frequency ($f_{th} = 2\, f_{mec}$), since any regenerator undergoes two complete thermodynamic cycles in each turn of the two-pole-magnet. Hence, applying this relation and knowing that the machine has eight AMRs working in parallel couples, the blow time can be estimated:

$$t_{ap} = \frac{Thermal\ period}{AMR\ parallel\ couple\ count} = \frac{1}{8\, f_{mec}} \tag{3.35}$$

The estimated cross section of an AMR at the time of these simulations is $A_{AMR} \simeq 6.62 \times 10^{-4}\,\mathrm{m}^2$ and the length of the AMR is $L_{ARM} = 150\,\mathrm{mm}$. With these figures, the volume of the AMR results $V_{AMR} = A_{AMR}\, L_{AMR} \simeq 9.94 \times 10^{-5}\,\mathrm{m}^3 \simeq 0.0991$ and its void volume is then:

$$V_f = \varepsilon\, V_{AMR}\ . \tag{3.36}$$

Assuming that the bed is perfectly compacted, the porosity is $\varepsilon = 0.36$.

equation (3.36) allows obtaining the flow through the AMR as,

$$\mathcal{Q} = V_{frac}\frac{V_f}{t_{ap}} \tag{3.37}$$

and from the flow, calculating the average speed of the fluid, $\bar{v}_d$, is straightforward:

$$\bar{v}_d = \frac{\mathcal{Q}}{A_{AMR}} \tag{3.38}$$

Table 3.4: Summary of the basic regenerator geometry parameters and device working frequency assumed for the bed simulations.

Parameter	Value	Units
f_{mec}	1.5	Hz
$AMR\ count$	4	couples
ε	0.36	-
L	0.15	m
A	6.62×10^{-4}	m^2

With the figures from table 3.4 we can calculate hence the average fluid speed for the case of $V_{frac} = 0.05$ (i.e. 5%) obtaining $\bar{v}_d \simeq 3.24 \times 10^{-2}\,\mathrm{m\,s^{-1}}$. This speed is combined with the diameter of the spheres of MCM, and the materials and HTF parameters, to supply the finite difference program with the information necessary to carry out the calculations using equations 3.1 and 3.20 to 3.25, which the program introduces in the discretized model (equations 3.33a and 3.33b).

This procedure is followed for any other desired pushed fraction of AMR's void volume per blow. A separate data file is obtained from the simulation program, for each diameter and average flow speed combination introduced. The main information extracted is the set of time vs. temperature in solid and fluid at the center of the bed, and the bed's pressure drop. Figures 3.3 and 3.6 sumarize the results for the $V_{frac} = 0.05$ case. Figure 3.4 is an example of the output obtained for this fluid regime and a sphere diameter of 0.8 mm. Also, table 3.5 exhibits the data of the exponential fit of t_{rel} vs. d_p, which corresponds to the equation:

$$[t_{rel}]_{5\%} = 24.0313\, e^{d_p/1.3625} - 26.04352\ , \tag{3.39}$$

where t_{rel} comes out in ms and d_p has to be given in mm. Also, figure 3.5 shows the different evolution of the temperatures as the flow speed is increased. In

this figure, it can be noticed after a close inspection that the fits introduce a small error in the graphs, which is evident seeing that the fluid and solid temperature lines for the same diameter cross each other slightly. This happens when the fits of either fluid or solid (or both) are not very precise and have an adjusted R-square lower than 1, a problem that is enhanced as the speed of the fluid increases. The increasing speeds shown correspond to fluid blows equivalent to pushing a volume equivalent to a bed's percentage of interstitial volume of 5%, 10% and 30%, respectively.

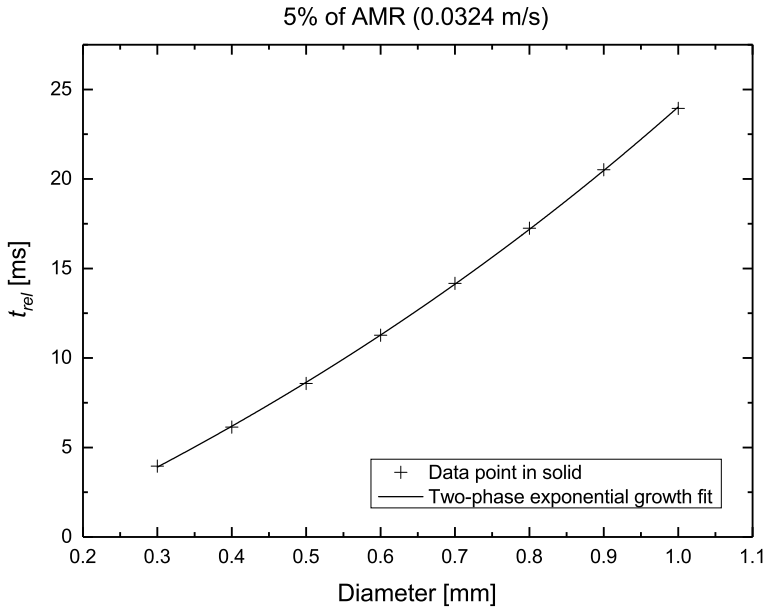

Figure 3.3: Relaxation times of MCM vs. diameter of the spheres at $0.0324\,\mathrm{m\,s^{-1}}$ fluid flow. A summary of the data points is in table 3.6. The details of the data fit are shown in table 3.5.

From the simulation results, other interesting information can also be obtained, like the expected pressure drop along the bed at a given flow regime (for example, at the lowest non-zero speed of the set), for any diameter. Figure 3.6 shows the results for $V_{frac} = 0.05$ and d_p =0.8 mm. The two-phase fit obtained of this pressure drop vs. sphere diameter graph, summarized in table 3.7, results in equation:

$$dP = 9.104e^{-d_p/0.09253} + 1.2303e^{-d_p/0.3185} + 0.05389\ . \qquad (3.40)$$

The simulations show that the diameter of the spheres does not necessarily

Table 3.5: Exponential fit data of figure 3.3 (low fluid speed). The particle diameter has to be given in mm and the relaxation time is obtained in ms.

Model	One-phase exponential growth		
Equation	$t_{rel} = A_1 e^{d_p/t_1} + t_0$		
Reduced Chi-Sqr	5.75208E-6		
Adj. R-Square	1		
		Value	Standard Error
Relaxation time in solid	t_0	-26.04352	1.97121
	A_1	24.0313	1.82969
	t_1	1.3625	0.07011

Table 3.6: Summary of figures 3.2, stagnant fluid, and 3.3, at low speed, pushing 5% of AMR's void volume.

	Stagnant fluid	5% AMR per blow
Diameter	Relaxation time	Relaxation time
d_p (mm)	t_{rel} (ms)	t_{rel} (ms)
0.3	22.79	3.96
0.4	39.58	6.14
0.5	61.21	8.58
0.6	87.74	11.27
0.7	119.27	14.17
0.8	155.82	17.25
0.9	196.46	20.52
1	241.85	23.94

have to be as small as it is often reported in prototypes using packed beds [127–131]. The use of bigger spheres would lead to lower pressure drops along the regenerator, with the resulting design advantages regarding the resistance of the constructive materials, the water tightness of the system and the pumping power needed to operate the device. The timing of each blow is obtained with equation (3.35). In the case of operating the prototype at a mechanical frequency of 1.5 Hz, each blow would last around 83.3 ms, and in the event of reaching a mechanical frequency of 2 Hz, this figure would go down to 62.5 ms. In both cases, the relaxation times for spheres from 0.3 mm to 1 mm are lower than the aperture time resulting from the operation at 2 Hz or lower mechanical frequency. As a result, according to the results of the simulations, even

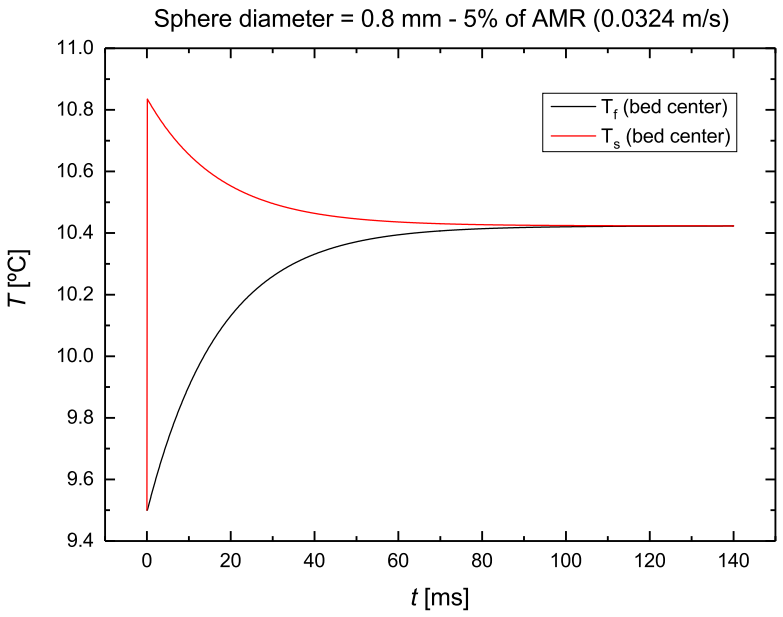

Figure 3.4: Direct simulation output of temperatures for spheres of diameter 0.8 mm, at a speed equivalent to a fluid blow of 5% of the bed's interstitial volume.

Table 3.7: Exponential fit data of figure 3.6. The particle diameter has to be given in mm and the pressure is obtained in bar.

Model	Two-phase exponential decay		
Equation	$dP = A_1 e^{-d_p/t_1} + A_2 e^{-d_p/t_2} + dP_0$		
Reduced Chi-Sqr	6.6937E-8		
Adj. R-Square	1		
		Value	Standard Error
Relaxation time in solid	dP_0	0.05389	0.00261
	A_1	9.104	0.51849
	t_1	0.09253	0.00286
	A_2	1.2303	0.07485
	t_2	0.3185	0.01069

$LaFe_{13-x-y}Co_xSi_y$ spheres as large as of 1 mm of diameter would be suitable for the device under working parameters close to the ones used in the model.

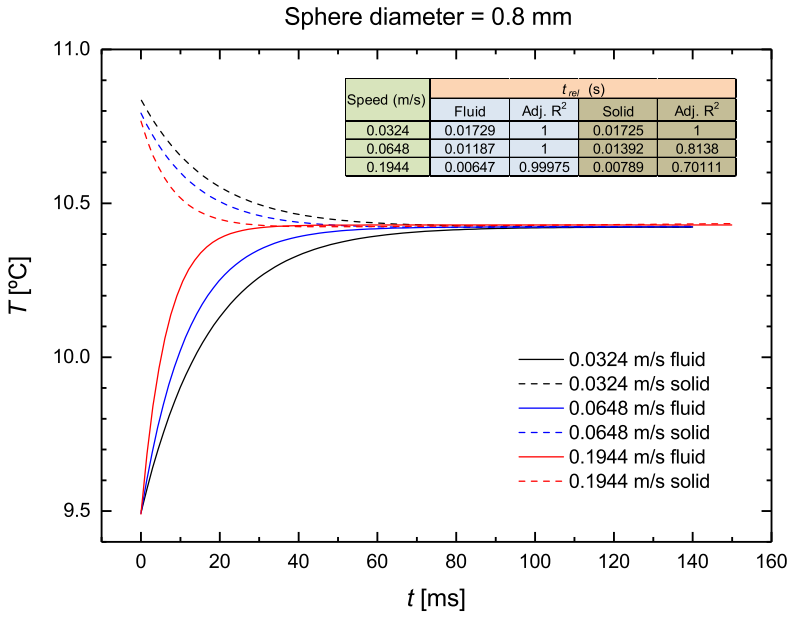

Figure 3.5: Comparison of the fitted temperatures evolution of the fast relaxation process at different fluid speeds, for MCM spheres of 0.8 mm of diameter. Flow speeds are determined by the desired AMR interstitial volume pushed in a blow. The quality of the fits is shown in the table insert.

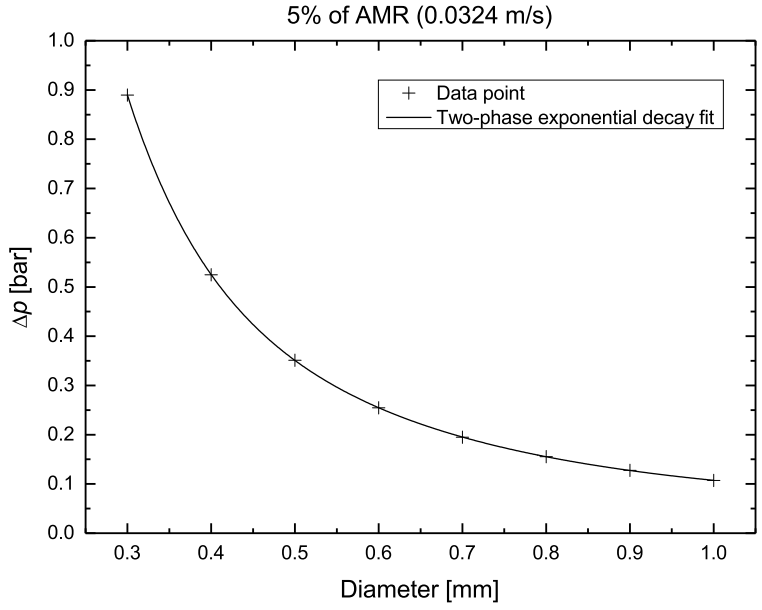

Figure 3.6: Pressure drop along the bed produced by the $V_{frac} = 0.05$ flow with different sphere diameters. A two-phase fit has been done and its data are shown in table 3.7.

3.3.3 Verifying the pressure drop

In order to confirm that the model explained in previous section 3.3 does not result in unfavorable errors in the pressure drop values obtained from the simulation, I designed and assembled a simple setup to measure the pressure drop in packed bed samples.

Two aluminum canisters were designed to hold the sample packed bed. Their geometric characteristics are summarized in table 3.9. These canisters were designed to be attached at the end of a copper pipe system, whose flow was controlled by means of an on-off circuit consisting of a solenoid valve, powered through a manual switch, and a pressurized fluid reservoir (see figures 3.7 and 3.8). The pressure of the reservoir is set using a pressurized dry air bottle with a regulator, which introduces pressurized air at the top of the reservoir that contains water with anti-corrosion additives, with the relevant parameters of table 3.8. The pressure is also monitored by a pressure sensor close to the top of the packed bed container. The pressure gauge 4 to 20 mA signal is measured with a Keithley Instruments 196 System DMM microvoltmeter connected to a computer through a GPIB-USB-HS controller. A simple Labview program acts as data acquisition system. The volume of fluid pushed through the packed bed is dumped in a 1000 ml beaker and measured after a set flow time to be registered in an Excel spreadsheet. This simple method offers a limited precision, but enough for the purpose sought.

Table 3.8: Relevant physical characteristics of the fluid used in the tests (diluted Luzar™ to 25%).

ρ_f [kg m^{-3}]	μ_f [Pa·s]
1035	3.33×10^{-4}

Table 3.9: Geometric parameters of the packed bed canisters.

For batch	Inner diameter [mm]	Length [mm]	Aperture width [µm]
Coarse	22.5	22.5	300
Fine	28	22.5	300

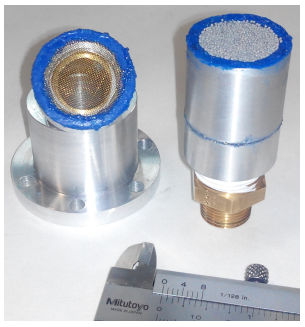

(a) Open canister assembly with spheres. A brass mesh was used to hold the spheres in the canister. A blue colored "form in place" silicon sealant gasket maker product from Krafft™ was used to seal the cylinders and hold the mesh in place.

(b) Half mounted canister assembly. The central disposition of the packed bed allows for a symmetric assembly. The sealant forms a gasket that glues the surfaces together with the mesh.

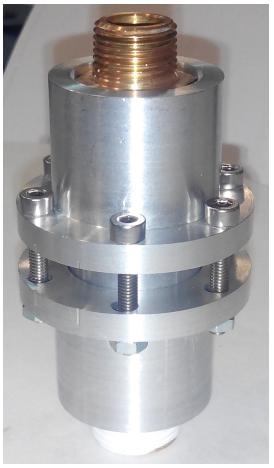

(c) Completely mounted canister assembly. The canister cylinders are pressed together to form a watertight assembly. Teflon tape is applied to the thread to avoid leaks.

Figure 3.7: Packed bed step-by-step assembly.

Two batches of LaFeMnSi-H spheres of different average diameter were obtained from the company VAC to carry out these pressure tests. The characteristics of both batches are summarized in table 3.10. The MCM beads of this batches are not ideal and would need a correction within Ergun's equation in order to take into account their deviation from the ideal spherical beads' pack. As has been addressed in section 3.3.1, these deviations include non-monosized beads, non-perfect spherical shape and rough surface (see figure 3.9). The size deviation can be approximated using a proper average value and the shape deviation can be compensated using a sphericity parameter. In the calculations that lead to the theoretical pressure drops shown in figures 3.11, the sphericity was held as perfectly spherical, with a value of one, and the average diameter of the batch has been used; the lack of information about the size distribution did not allow to consider a more representative diameter approximation.

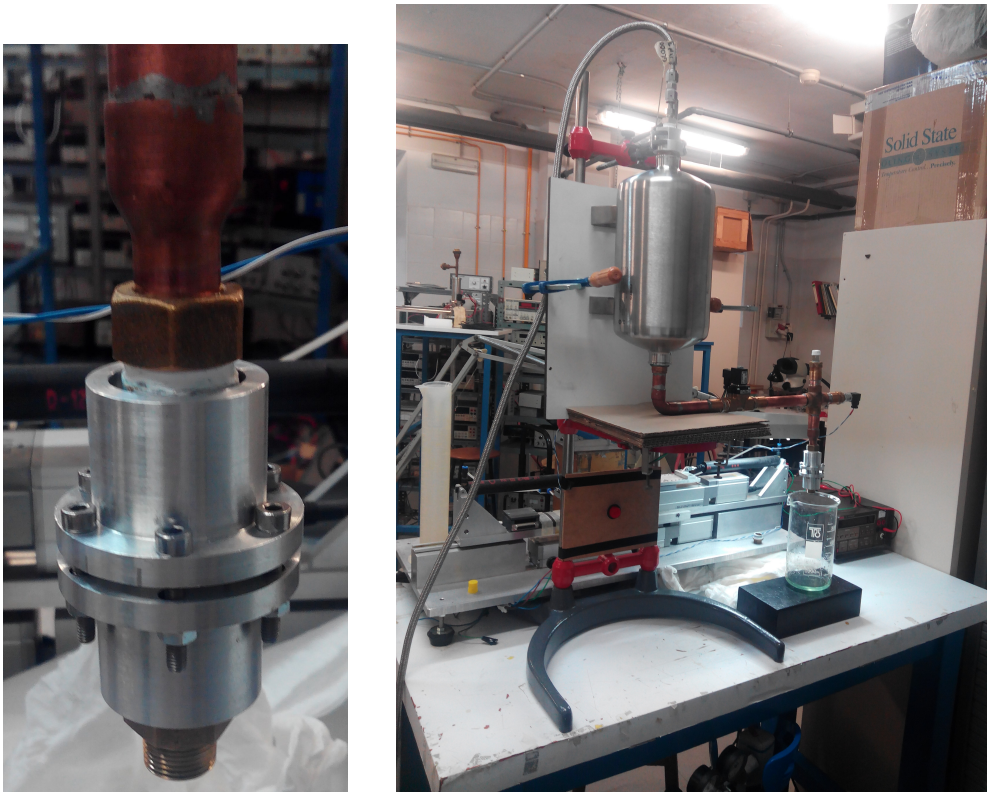

(a) (b)

Figure 3.8: (a) Packed bed assembly ready for testing. The packed bed assembly is screwed at the end of the installation's pipe. (b) Overall test assembly image.

Several measurements were performed with both batches, which are different sphere size samples. For a small set of pressures, measurements were made with different flow times. The measured volume and the flow time allows the obtention of the volumetric flow, and the pressure sensor gives the manometric pressure after the post-processing.

By regulating the pressure of the reservoir, only an approximate initial value of the test is set. The pressure at the packed bed's inlet suffers a decay as the air expands within the reservoir, while the fluid is pushed out through the pipes and the packed bed (see figure 3.10). As a result, the average of the measured pressure of this process is used for post-processing. Also, the flow time has a manual control and, hence, the timing precision cannot rely on the nominal time value, which only serves as a differentiation tag of the measurement. In order to eliminate most of the timing error, the real time

Table 3.10: Characteristics of the LaFeMnSi-H batches provided by VAC. The mass shown here is the mass fitted in the testing canister. Note that the canister used for the coarse batch was shorter than that used for the fine batch.

Batch	Diameter [µm]	mass [g]	Density [$kg\,cm^{-3}$]	Resulting porosity [-]
Coarse	710 to 900	40.34	7.2	0.374
Fine	400 to 630	43.618	7.2	0.456

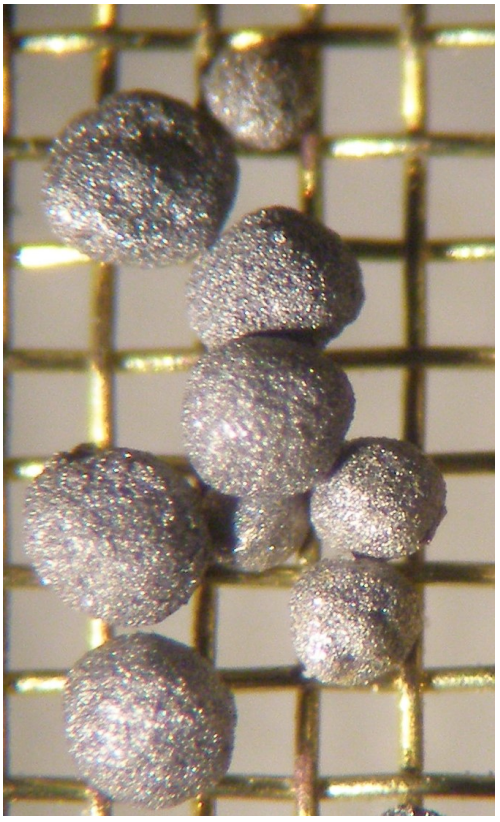

Figure 3.9: Spheres of one of the batches provided by VAC, over the brass mesh. It can be observed that the beads are not perfectly spherical, they show a size distribution and their surface is rough. These characteristics affect the real pressure drop through the bed and can be characterized in Ergun's equation with a correction parameter if more precise numerical figures are desired.

value is obtained once again during post-processing from the pressure gauge current signal. The initial time is taken at the leftmost upper point of the graph and the final time is set at the midpoint of the pressure drop line, to compensate for the error produced by the small volume that exits the container while the valve opens and closes.

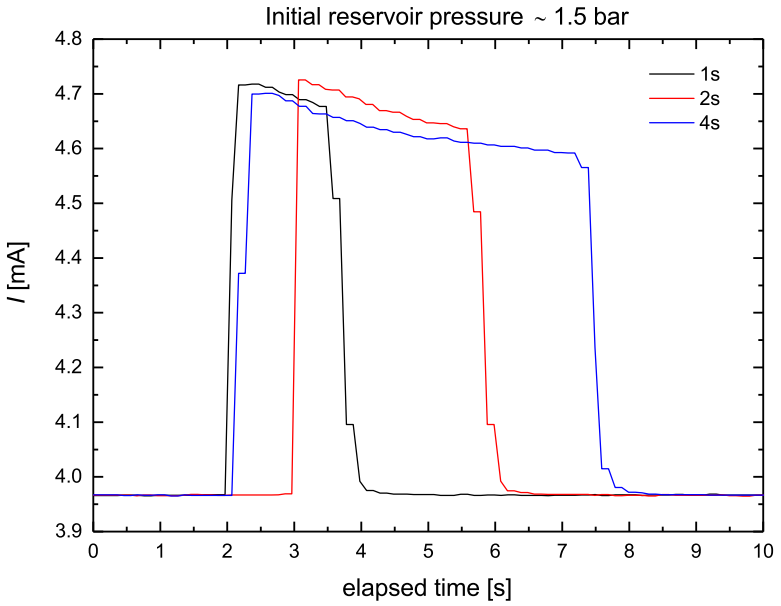

Figure 3.10: Pressure sensor current output for tests with the coarse batch with nominal reservoir pressure of 1.5 bar at nominal flow times around 1, 2 and 4 s.

The measurements results are shown in figure 3.11a and 3.11b. Although the measurements of the fine batch of beads match better with the theoretical lines (the wider size distribution of the fine batch helps), in general, the values registered are in fair accordance with Ergun's modified equation (3.1) and the deviations observed are on the side of security. This proves that Ergun's equation can be trusted when calculating the pressure drop in packed beds under conditions similar to those of the tests carried out, and serves as a partial validation of the model described in 3.3.1.

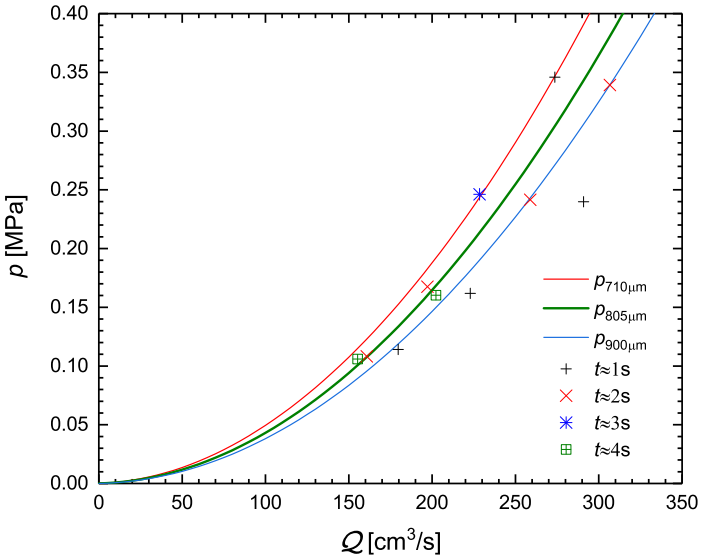

(a) According to the supplier, the batch consisted of spherical particles of diameters 710 µm to 900 µm, but no information about the size distribution; therefore, the theoretical pressure drop for the average diameter of 805 µm is shown (green line).

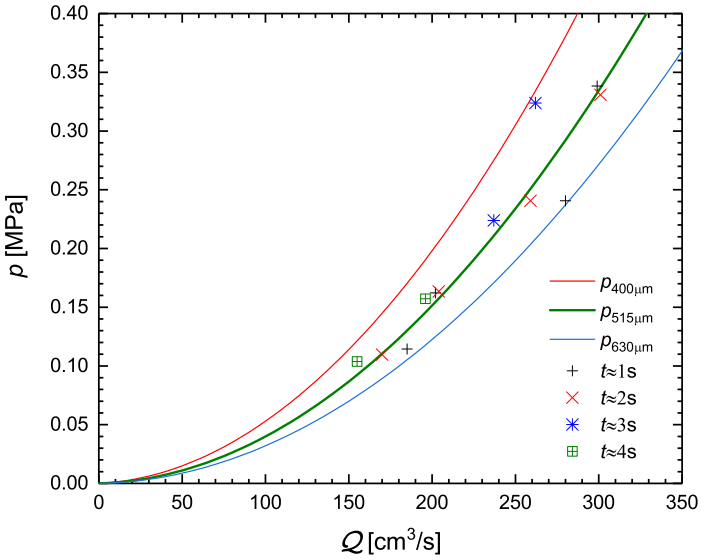

(b) According to the supplier, the batch consisted of spherical particles of diameters 400 µm to 630 µm, but no information about the size distribution; therefore, the theoretical pressure drop for the average diameter of 515 µm is shown (green line).

Figure 3.11: Theoretical pressure drop for the extreme and average diameters of the coarse (a) and fine spheres (b), resulting from the modified Ergun equation (3.1). The pressure drop expected for the upper size of the batch is shown in blue and that of the lower size in red. The measurements made in the tests are depicted as single points.

Chapter 4

Building an AMR

In this chapter, I will analyze and comment some important issues regarding physical requirements for the design of an active magnetic regenerator (AMR) and also, how these requirements clash with reality as you want to build a real AMR.

Being the AMR the heart of a magnetic refrigerator, a good design is of utmost importance for the performance of the complete system. An important early decision has to be whether the refrigerator is going to be a materials testing system or an overall system performance test machine. This can really make a difference in the design and the results finally obtained, due to the awful lot of different requirements to meet. Also, a very important issue that really can turn the design into a very challenging issue is the decision as to whether building a reusable, modular regenerator, variable in size, or a more fixed system that can be interchangeable (change the regenerator for another filled with a different material). This last kind of system decreases the design requirements regarding the ease to build, extract and disassemble the AMR, as well as its final size and MCM capacity.

The casing of an AMR is a very challenging component and its design is linked to the shape of the magnetocaloric material (MCM) that it has to hold inside. A regenerator casing meant to hold a porous bed of spherical beads

is very different from one meant to hold blocks of flat plates; also, the ease of the design differs greatly if we deal with a multimaterial AMR instead of a single material one. The requirements for this component come from different aspects, including fabrication process related issues, and build together a complex multidisciplinary problem.

At the beginning of this chapter I will present the design solutions adopted, aimed to avoid or minimize some known AMR design problems. I will follow then with how other design issues have been faced, to end presenting the final design adopted.

4.1 Avoiding dead volumes

Dead volumes are fluid volumes between the regenerator and the heat exchangers which move back and forth with the fluid. Other volumes of material contained in the AMR block which present no MCE can also be considered as dead volumes. Mesh screens can have a very small volume and their effect can often be disregarded. In fluid dead volumes, inlet and outlet fluids can mix and a fraction of the cooling load is lost as the cold outlet fluid gains heat from the inlet fluid before reaching the cold spot, degrading the system performance.

Simulations reported by Jacobs [109] made with five layer $La(Fe_{1-x}Si_x)_{13}H_z$ and single-layer Gd beds show that *"as long as the dead volume is less than ∼6% of the fluid volume in the active portion of the bed, its effect on the performance of the multilayer design is minimal"*. This sensitivity is even lower in materials that provide a *" significantly smaller cooling load"* like in single-layer Gd beds, because the temperature difference between inlet and outlet fluids on the cold side is smaller and the effect of the mixing temperatures represents hence a smaller degradation.

Solution adopted

In order to avoid having any significant dead volume, the design of the AMR discourages the mixture of cold and hot flows by using separate paths for each flow. The AMR has two inserts on each end, one for hot flow and the other for cold blow. Also, the flows outside the regenerator blocks are unidirectional. The MCM containers are hence filled to the top, covered with a wire mesh and the AMR block is closed on both sides with specific cover rings in which inlet and outlet are physically separated by a wall, reducing the possibility of cold and hot blows mix as much as possible (see figures 4.1 and 4.2). The check-valves located in the fluid circuit outside the regenerator block, combined by the action of the solenoid valves, prevents unwanted returns of fluid to the AMR block that can result in dead volumes. The unidirectional design of the fluid circuit outside the AMR and the inner separation of flows at the AMR top and bottom cover rings, are the main warrants to avoid dead volumes. A complete schematic drawing of the fluid circuit can be found in section 6.2, figure 6.4, on page 151.

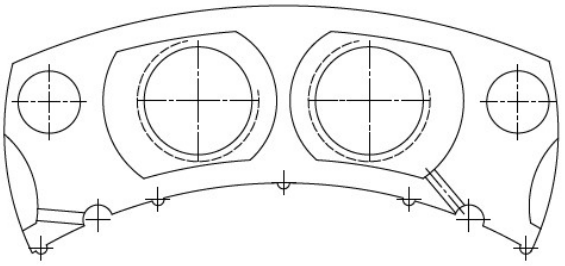

Figure 4.1: Detail of the design of the top cover of the AMR. The two small circles on both sides of the image are the allocate the threaded rod that holds the regenerator block together and constitute the azimutal limit of the AMR. The bigger circles are the flow inlet and outlet where fittings are screwed. A mesh is installed covering the wider hollows around the inlet and outlet, on the inner side of the cover. Note that there is a wall separating inlet and outlet.

Figure 4.2: Perspective of the complete top cover.

4.2 Avoiding flow imbalance

Magnetic refrigeration fluid systems with several beds working in parallel are commonly used as a means to maximize the use of the magnetic field and the cold and hot blows are distributed among different regenerators.

The construction of fluid systems with elements working in parallel, requires the hydraulic balancing of the parallel branches of the fluid circuit in order to avoid unwanted counterflows through the lines with higher flow resistance. The same principle applies in the design of magnetic refrigeration systems that have regenerators working in parallel. In order to assure that the flow is equally diverted through parallel regenerators, their flow resistance has to be matched.

Also, a flow imbalance occurs when the flow rate through a regenerator bed during hot-to-cold blows differs form the rate during the cold-to-hot blows. This happens when the fluid circuits of both flow directions have sensibly different flow resistances.

According to Jacobs [109], multilayer designs are quite sensitive to flow imbalance, which can be quantified using the flow imbalance ratio, defined as

$$R_{\Delta\Phi} = \frac{\Delta\Phi}{\Phi}, \tag{4.1}$$

where Φ is the ideally balanced flow and $\Delta\Phi$ is its deviation. 1D simulations show that a flow imbalance ratio of only 5% in a 5 layer $La(Fe_{1-x}Si_x)_{13}H_z$ bed degrades the cooling power by 37%, and up to 100% with a 12% flow imbalance ratio [109]. Also, *COP* and cooling power degradations by 30% and 50%, respectively, with a 5% deviation in flow resistances were reported in other 1D simulations carried out by Eriksen et al. [132].

Due to this sensitivity of the performance to flow imbalance, the piping systems must be designed to produce equal flow rates in either direction. This can be achieved by means of regulating valves inserted in the circuit, but care must be taken not to introduce a significant pressure drop.

Solution adopted

Trying to avoid the flow imbalance problem, regulating valves have been inserted in the paths of both flow directions, for each regenerator (see figure 4.3).

Availability, size restrictions, adjustment indicator presence, tubing compatibility and the use of low thermally conductive materials were taken into account in the selection of these valves.

Solving the flow imbalance problem brings the need of measuring the flow through each separate subcircuit that is active whenever a couple of solenoid valves open it. This complicates the design of the fluid circuit even further. Depending on the amount of the flow meters available in the prototype, a complete set of tubes and manual valves have to be inserted in the circuit. The precision of the flow measurement is also very relevant, due to the great sensitivity of the final performance to the flow imbalance.

Figure 4.3: Regulation valves meant to compensate the possible flow imbalance.

This is a real problem in this prototype, mainly due to two facts: the nature of the pumping system and the precision of the flow meters available. Further discussions about this subject follow in section 6.2.1.

4.3 Avoiding magnetic cogging

The fact that the regenerator block housed within a cylindrical gap cannot present a continuous magnetic permeability as the magnetic field revolves, constitutes a sink of energy in the form of work to be provided to overcome the differential forces that arise from this discontinuous permeability. The walls that divide the cylindrical regenerator block into different parallel AMRs are areas of magnetic flow disturbance. The additional torque needed to pass from a position with high permeability to the next one (from an AMR filled with MCM in ferromagnetic state, aligned with a pole of the magnet, to the next one) is known as cogging torque. The desirable operation of the prototype should involve a continuous relative revolving torque of the magnetic field and the regenerator block, in order to minimize the power demanded by the motor that provides the revolving torque.

An additional possible contribution to cogging effect is related to the different temperatures of the MCMs within the regenerators, around which the magnet revolves. The magnetic susceptibility of the MCM changes with its temperature. The temperature of the MCM increases when increasing the magnetic field to which it is subjected, and decreases while decreasing the field. To this we have to add, that the flow of HTF also produces changes in

the MCM temperature, inevitably changing the material's susceptibility and, thus, the force with which the regenerators are attracted to the pole of the magnet. This induces a differential force, and a torque as a result, between the entry of an AMR in the high field area of the pole and its exit.

Solution adopted

Minimization cogging effects can be addressed with a good continuity and symmetry management. The magnet should "see" a susceptibility in its gap, as continuous as possible; even with the temperature differences already mentioned, the evolution of the susceptibility should be continuous. Additionally, symmetry in the disposition of the MCM around the core contributes to a continuous susceptibility. The inherent symmetry of the rotating operation makes that whenever an AMR is entering the high field zone, there is another one leaving it and the susceptibility of both can be expected to compensate greatly since the derivative of the field in symmetric positions with respect to the maximum field point has, in principle, the same absolute value. However, this compensation is not perfect and cannot be relied on, because a completely symmetric behavior of the MCM regarding its magnetic and thermal parameters cannot be accounted for, affecting the evolution of the susceptibility differently at field increase and decrease. A differential force is therefore to be expected, resulting in a torque that the magnet's drive will have to overcome, as an addition to traditional mechanical transmission losses.

The magnet is thus designed as a "uniform" cylindrical surface (no protruding poles, see figure 5.3 in section 5.4), eight AMRs that cover almost 45° each are built around the magnet´s core, and the design of the AMR housing provides a shape that lowers the size of the low permeability areas, making them also smoother. To achieve this, a lobed design of the cross section of the AMR puts part of the MCM volume behind the threaded rods that hold the regenerators' sections together (figure 4.4).

The end result is that at a "constant" temperature, the magnet can be revolved by hand with no noticeable cogging torque to overcome in the prototype.

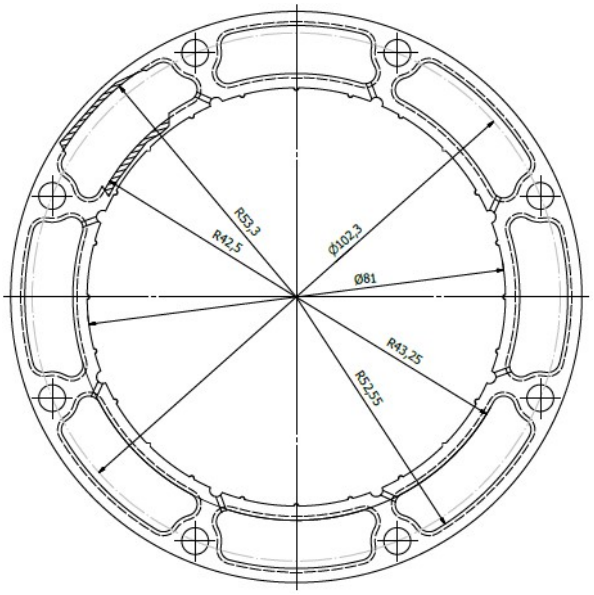

Figure 4.4: Design of the AMR section. The lobed design contributes to a smoother transition between regenerators while avoiding stress concentration points.

4.4 Ensuring pressure resistance and low deformations

The main concerns when designing a container that is going to hold moving pressurized fluid are its mechanical resistance and the water tightness of the assembly. The water tightness requires certain design solutions, but first, it has to be assured that the material, the thicknesses and the shapes of the container can withstand the stress to which it will be subjected, and that the strain produced in the material will produce no undesired effects, like interferences with parts that have a relative movement with respect to the container.

A major milestone in the design of the container is choosing the material with which it is going to be built. Choosing the material is not a minor task, since the requirements are contradictory and there are non physical issues that really make up a series of relevant determinants that condition the decision in a very important way. Some of the most relevant questions addressed when choosing the material were:

- non-magnetic material,
- thermal insulator,
- electrical insulator,
- mechanically resistant,
- resistance reliability,
- rigidity,
- easily available,
- fabrication ease,
- affordable cost.

Most of these characteristics match well with certain polymeric materials. However, handling polymeric materials in small quantities, with severe mechanical requirements is quite difficult. Suppliers provide data sheets with expected mechanical data, and the real values change from batch to batch and this information is not easily obtained unless you get the material directly from the manufacturer and ask for specific tests to be carried out for the batch. This is really the case with any commercial material, but the variability of the parameters (manufacturers produce a slightly different composition for known polymeric materials, although under different brands), together with strict requirements, very limited accessibility to producers, limited timing of the project and very limited financial resources, makes trying to obtain reliable and precise technical data of polymeric materials a nonsense unless samples are obtained and in house resistance tests are made. Since this would imply a large amount of time and economic dispense, this route was out of the question. The reliability of manufacturers' or distributors' technical data turns even more important when thinking about non-homogeneous materials, like fiber reinforced polymers. This kind of polymers are known for very high mechanical strength and, also, high Young's Modulus, however, these materials are very anisotropic and it is hard to assure that the fibers' alignment within the polymer matrix will, after the product's manufacturing process, match that of the principal stress of the application seeked. Also, polymeric materials with high mechanical characteristics, are extremely expensive and very hard to obtain. Although other materials were briefly considered to build the AMR block structure, like non-magnetic stainless steel, FGRP + epoxi composite or ceramic materials, they were soon discarded mainly due to fabrication process difficulties and

other issues (e.g., AISI 304 or 316 steels have a thermal conductivity of around $12.1\,\mathrm{W\,m^{-1}\,K^{-1}}$ at 20 °C, very large compared to polymeric candidates shown in table 4.4).

Taking into account that the materials family that looks better positioned to be used is the polymeric materials one, I carried out simulations with 3D finite element models in Comsol™. Simulations were done with two models: one modeling a single regenerator, to check the stress and strain to which it would be subjected with the maximum expected working pressure, and a second model comprising the whole assembly with six blocks of MCM per regenerator to check the behavior of the assembly, although due to the symmetry of the design and the pressures applied, no great changes were expected, this last model helped to double check results. The models were also used to compare different material candidates and check the effectiveness of introducing exterior AISI 316 reinforcement bands to improve the resistance, and lower the stress and the strain of the polymer. An example of results obtained from Comsol for the complete AMR block is found in figure 4.5.

The first polymeric material held as a candidate was Polyoxymethylene (POM), also known as acetal, polyacetal and polyformaldehyde[1]. This material was previously used in our group to build a regenerator for another prototype and has several advantages:

- high stiffness,
- machinable,
- fair dimensional stability,
- low friction coefficient,
- low water absorption,
- good mechanical strength,
- readily available,

[1] This material was first produced by DuPont in the 1950s, but is now produced by many companies with slightly different formulations under different commercial names. The best known is Delrin™ from DuPont, but it can also be fount under the names of Celcon™, Duracon™, Hostaform™, Kocetal™, Ultraform™, Ramtal™, Kepital™or Polypenco™, for example.

- reasonable price.

However, certain concerns were held about the mechanical resistance for the design being made. POM is not a fiber reinforced polymer and has isotropic characteristics[2]. It therefore relies its performance on its tensile strength (i.e., yield strength) and Young's modulus (E) mainly, which have a typical value of around 70 MPa and 3.1 GPa, respectively, although some in-house measurements of E carried out in our group, with samples provided by our supplier, showed values as high as 5.8 GPa. As a result, POM was the first natural choice, but it had to be verified with simulations, and it could be compared with other possible materials just by changing in the model the values of density, tensile strength, Young's modulus and Poisson coefficient of the material (see table 4.2 for a non exhaustive list of materials that were checked with the models). However, the above mentioned technical specification problem strikes here again. Apart from density, mechanically isotropic materials just have one global value for the already mentioned mechanical parameters, but anisotropic materials need at least two values for these parameters to be fully specified and it is often found that only the most favorable values that the manufacturer can assure are specified, but not always in the perpendicular direction—i.e. the highest value of tensile strength and E are specified, which correspond to the values expected in the nominal direction of the fibers in the case of fiber reinforced materials. The values used in these cases have to be properly approximated and the results interpreted with care on behalf of security of operation.

The empty gap between the moving magnet and the static regenerator block is obtained from the worst case outer radius of the regenerator block (which includes an outer 0.15 mm thick inox steel band) and the worst case inner radius of the magnet (see table 4.1). Counting with a minimum gap to account for a possible minor misalignment of the central core's axis and vibrations, and avoiding contact between parts in relative motion, a maximum deformation limit was established for the regenerator block using the equations:

$$\delta_{gap} = R_{int}^{magnet} - R_{ext}^{AMR\,block} \tag{4.2}$$

$$\delta_{lim} = \delta_{gap} - \delta_{min} \tag{4.3}$$

[2]Some characteristics may be affected by the manufacturing process. For example, extrusion tends to align molecules and may introduce some anisotropy in thermal conductivity or other characteristics.

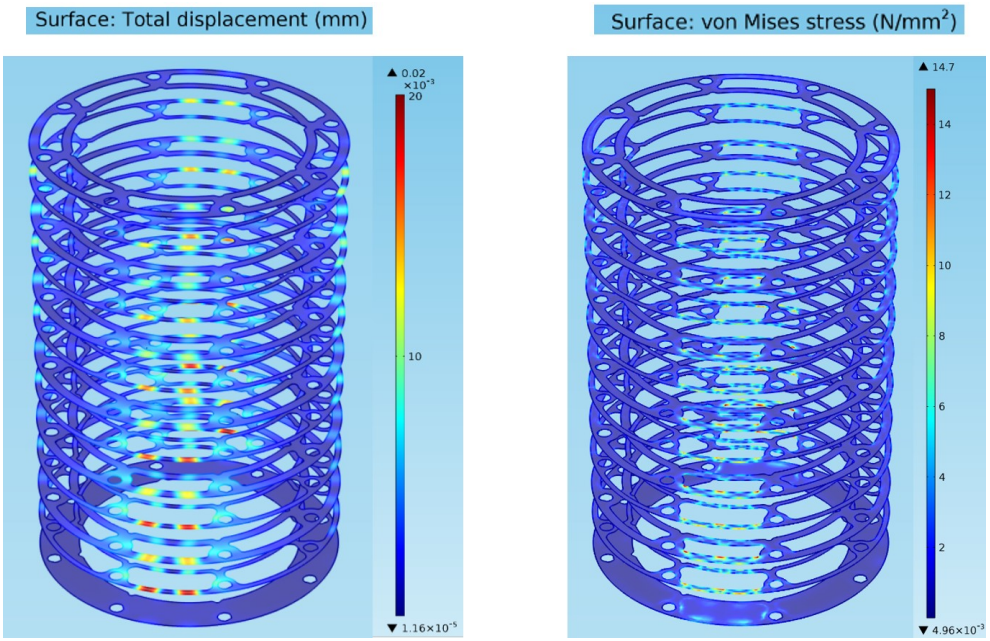

Figure 4.5: Example of finite element model results images, representing transversal slices of the AMRs made of one of the materials tested. Displacements on the left and stress on the right. A pressure ramp was applied and, thus, maximum displacements and stresses (marked in red) are located around the cavities subjected to highest pressure.

Table 4.1: Worst case radii and resultant gap between the moving magnet and the static regenerator block.

Parameter	[mm]
R_{int}^{magnet}	56.75
$R_{ext}^{AMR\,block}$	55.45
δ_{gap}	1.3

With the figures from table 4.1, it was decided allowing for a maximum deformation in the radial direction of 0.4 mm, leaving a real minimum gap of only 0.9 mm. This minimum gap goes down to 0.6 mm at the point were the steel band extremes overlap to be welded together. As a result, the limiting values to validate the use of a specific material are:

$$\delta_{max} \leq 0.4\,\text{mm} \tag{4.4}$$

and

$$\sigma_{max} \leq \sigma_s, \tag{4.5}$$

being δ_{max} the maximum deformation of the material, σ_{max} its maximum stress and σ_s, the resistance of the material.

In the model, the regenerator block is subjected to a static pressure that decreases linearly along the regenerator length from 8 to 0.1 bar. In the case of the model of the complete assembly, the maximum pressure is set at one end of a confronted couple of regenerators and also, at the opposite end of another couple situated at 90° from the first.

Table 4.2: Sample list of simulated materials (non exhaustive).The elastic modulus and tensile strength shown in the case of fiber glass reinforced polymers (FGRP), correspond to the values in the direction of the fibers, which are its maximum value.

Commercial denomination	Polymer	E [GPa]	σ_s [MPa]	Observations
	POM	3.1	70	Typical value
	POM	5.8	70	In-house measurement of E and typical σ_s value
Duratron U1000	PEI	3.5	129	Manufacturer data
Torlon 5030	PAI	14.6	221	FGRP 30%, manufacturer data
Torlon 5030	PAI	6.9	159	FGRP 30%, extruded, extruder data
Duratron T5530	PAI	8.275	152	FGRP 30%, distributor data
Ketron LSG	PEEK	4.6	115	Manufacturer data
Udel GF-130	PSU	8.69	107.6	FGRP 30%, manufacturer data

As expected, the results of the simulations clearly confirm that using the

exterior steel bands reduces the polymer's stress and strain significantly. The results show that POM does not meet the mechanical requirements with the design proposed, requiring at least doubling the walls' thickness, specially due the stress; however, when using the steel bands, the stress and strain values comply with ease. High-end polymers checked with the models, like those in table 4.2, show that they can comply with the mechanical requirements without using steel reinforcements. Some present stress and deformation security coefficients that surpass the value of two when using FGRPs. Deformation security is easily reached in all cases without steel bands, but not in the case of using POM with $E = 3.1\,\text{GPa}$. Stress security is found without steel bands in all FGRPs; however, the steel bands are needed to meet the stress requirements when using POM. A summary of the simulation results obtained for some polymers is presented in table 4.3.

Table 4.3: Samples of simulation results for some polymers with, and without AISI 316 steel bands. The figures under n_σ and n_δ are the security coefficients obtained for stress and deformation, respectively. The values under one, printed in red figures, mean that the requirement is not met and the material is not suitable under the simulated conditions.

Polymer	E [GPa]	σ_s [MPa]	Steel band	σ_max [MPa]	δ_max [mm]	n_σ	n_δ
POM	3.1	70	without	102.31	0.446	0.68	0.90
			with	26.9	0.03	2.60	16
	5.8		without	102.31	0.238	0.68	1.68
			with	26.9	0.01	2.60	30.77
Duratron U1000	3.5	129	without	102.31	0.40	1.26	1.01
			with	26.9	0.02	4.80	18.18
Torlon 5030	6.9	159	without	91.24	0.19	1.74	2.15
			with	22.46	0.01	7.08	38.10
Torlon 5030	14.6	221	without	91.24	0.08	2.42	4.55
			with	22.46	0.00	9.84	80.65

Solutions adopted

The results obtained from simulations, once checked the thermal conductivity (see table 4.4) of the material, allow to make a material choice for the AMR block. The first polymeric candidate, POM, proved to be the best choice

when combined with the use of the non-ferromagnetic AISI 316 steel bands. Within the polymeric candidates, once the mechanical requirements have been met, availability, characteristics' reliability, ease of fabrication and price, are the main selection concerns that POM complies with, and as a result, POM was selected to construct the AMR block structure. The different parts of the regenerator block structure were machined from a POM cylinder with high precision numeric control machining tools from the engineering company Dynatech Dynamics & Technology, S.L.U. An image of the design of the AMR sections is shown in figure 4.6 and a photograph of a six-section AMR assembled onf the magnet's core can be seen in figure 4.7.

Table 4.4: Thermal conductivity of some polymeric materials. POM has a typical value that sits below the midpoint between the minimum and the maximum values of this table.

Thermal conductivity		
Denomination	Source	$\frac{\mathrm{W}}{\mathrm{m\,K}}$
Ketron™ 1000 PEEK	QUADRANT	0.25
Ketron™ LSG PEEK	QUADRANT	0.25
Udel™ PSU GF-130	SOLVAY	0.26
Duratron™ T4203 PAI	BRONYMEC	0.26
Duratron™ T5530 PAI	BRONYMEC	0.36
Torlon™ 7130 PAI	SOLVAY	0.52
Torlon™ 5030 PAI	SOLVAY	0.36
Duratron™ U1000 PEI	BRONYMEC	0.24
Delrin™ POM	Typical	0.31

Figure 4.6: Perspective of the design of the AMR sections . The lobed design contributes to a smoother transition between regenerators while avoiding stress concentration points. The core of the magnet is inserted in the central hole and the regenerator makes contact only with the small vertical protruting ribs shown, creating a small air chamber acting as thermal insulation.

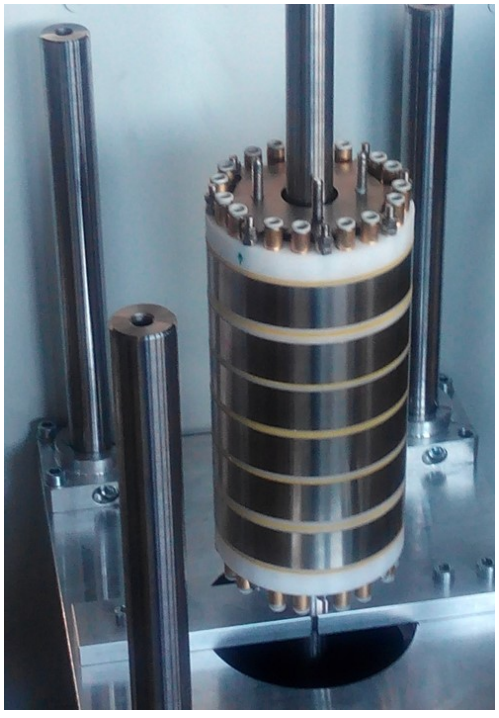

Figure 4.7: AMR block mounted with six sections on the magnet´s core.

4.5 AMR block assembly and watertightness

Each section of the regenerator block is stacked and their contact surfaces have to provide a watertight seal, capable of withstanding 8 bar of pressure. ARM sections have a design that accounts for longitudinal holes where threaded rods are inserted. These rods are provided with nuts and washers to provide sealing pressure to the assembly and a gasket is inserted between sections and between the end sections and the AMR block end covers. Also, a special home designed laser cut washer is introduced at the top and bottom ends of the AMR block. This washer, laser cut at Instituto Tecnológico de Aragón (ITA), is made of non magnetic AISI 316 stainless steel and it is meant to distribute more uniformly the stress produced when the AMR block is compressed with the nuts of the rods. However, this seemingly simple system only works if certain technical requirements are met, and here is one of the main design problems that had to be faced.

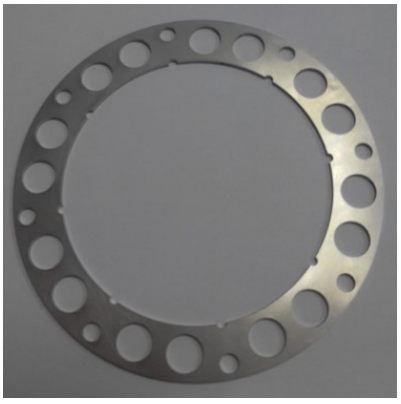

Figure 4.8: Home designed laser cut pressure washer meant to distribute the closing pressure of the nuts and threaded rods more homogeneously. This washer can be seen once assembled in figure 4.10b.

The search for a large cooling power pushes researchers to introduce as much MCM as possible in the regenerator and, once the gap of the magnet has been set, this means thinning the walls of the container, and this brings about major problems like lower mechanical performance of the container's material, lower thermal insulation of the AMR and, in this case also, narrower contact surfaces to form a watertight union. An additional problem is the fact that what is to be compressed to be watertight is a polymeric structure and, although POM is fairly rigid, it still is quite flexible, specially in certain areas

due to the thin walls of the design.

The compression stress to which the block is subjected has to be as uniform as possible, and the home designed washer introduced in the block contributes to this; however, the torque with which the nuts are tightened has to be uniform also, and the value of the torque has to be enough to provide sealing, but not so much as to produce a plastic deformation in the block.

Tests were carried out to check the watertightness of the assembly. A three section regenerator was assembled and introduced in a transparent container with water. Plugs are placed at the bottom ends of the empty regenerators, while pressurized air is connected to the top part of the block in four diametrically opposed regenerators. Due to the design and the flexibility of the material, a POM cylinder of the size of the magnet´s iron core has to be introduced in the assembly where it should be placed when used in the prototype, before the nuts are tightened.

The air pressure is increased by means of a regulator until it either reaches 8 bar or leaks showing air bubbles. Different gaskets were tested and different torques were applied to the nuts of the assembly to find the right material for the gasket and the correct torque.

Leaks were detected during the tests and it was finally determined that with an assembly torque of 3 N m, the leaks were located in the thermocouple insertion holes of certain sections. In these holes, the thermocouple wires enter the AMR and the void volume is filled with epoxy glue. After close inspection, it was found that the adhesive unions of the epoxy glue with the POM and, also with the PFA[3] wire sleeves of the thermocouples did not have enough strength and the air leaked through the interfaces. Thermocouple wires with this sleeves were selected because it was the only option found for such thin wires which was actually waterproof, knowing that gluing was going to be a problem.

Another problem found with these tests is that the glue[4] used to hold

[3] A polymer very similar to polytetrafluoroethylene (PTFE).
[4] Plastobond™ modified cyanoacrylate from Würth.

the meshes placed between the MCM particles of the different sections was too rigid, and did not adapt to the deformation that the regenerator block structure suffers when assembled and pressurized. The adhesive union with the POM walls ended up breaking and the meshes were finally loose at certain areas of the cavity walls.

Solutions adopted

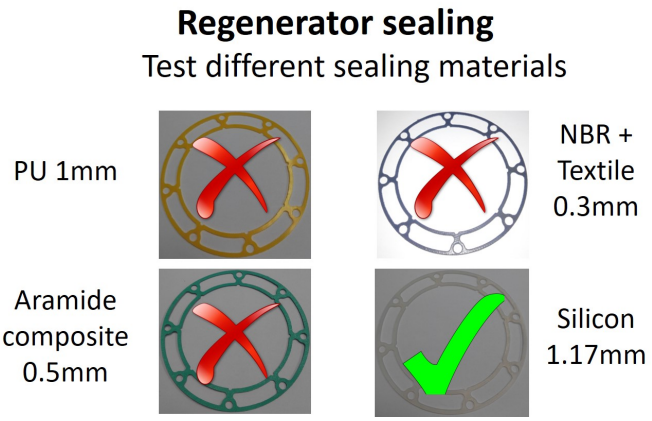

Figure 4.9: Sealing gaskets made of different materials were considered. PU gaskets are too hard and did not adapt well to the contact surfaces evenness flaws and they also presented some chemical compatibility issues with the HTF. Aramide and NBR gaskests are too thin to adapt to the mentioned contact flaws. Silicon gaskets showed a good behavior.

Figure 4.9 presents gaskets made of different material candidates. As is displayed, evaluations and tests showed that the best gaskets were those made of silicon. These gaskets have an initial thickness of 1.17 mm and their flexibility allow the leveling of the interfaces between the different sections. Also, in order to minimize the extrusion that the gasket suffers due to the assembling pressure and the small flat contact surfaces of the adjacent parts (figure 4.10a), the reinforcement steel bands were moved from their original position, centered in each section, to cover the interface area were the gaskets lay. This avoids the outwards extrusion of the gasket (figure 4.10b). The extrusion towards the

magnet's iron core is avoided by the core itself.

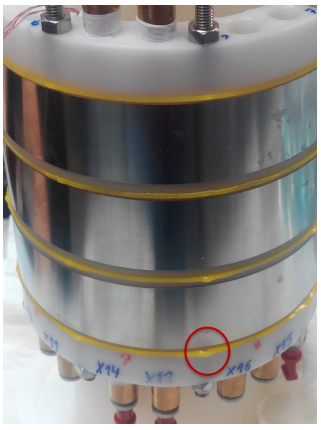

(a) Outwards extrusion of the gasket in one of the tests, marked in a maroon circle.

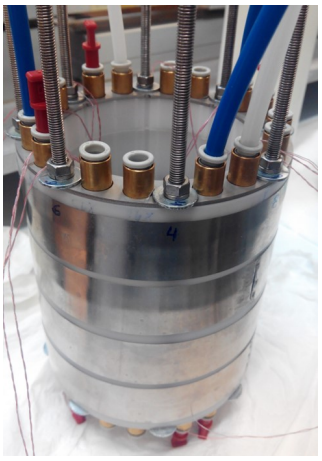

(b) Moving the steel reinforcement bands to cover the interfaces between sections forces the gasket to stay in place.

Figure 4.10: Solving the outward extrusion problem.

From the tests, a torque of 3 N m was considered enough to seal the block. Also, it was determined that once tightened, the nuts' torque had to be checked at least once after 24 hours, in order to assure its value, since the polymeric material may present a small stress relaxation. The nuts were combined with split-lock washers to avoid their loosening (figure 4.11). It has to be remarked that no magnetic components are used in the AMR assembly.

Figure 4.11: Split-lock washer used to avoid loosening of the AMR block. This special washer is placed between the nut and a normal flat washer. This last washer has a bigger diameter and has a smooth surface, protecting thus the surface of the home designed pressure leveling washer while helping in the pressure distribution.

The adhesion problem was solved by testing different epoxy glues and modifying the surface preparation procedure. Since, due to the small size, no suitable corona treatment was available, a surface mechanical preparation was performed. On POM, the process was started with the cleaning of the surface with ethanol, surface mechanical abrasion, cleaning again with ethanol and applying a primer for gluing difficult polymers from the company Ceys, before gluing with Fast Araldite™ epoxy from Ceys also. With the thermocouple PFA sleeve, only the primer application at the area that is going to be located in the insertion channel is used. This system proved to provide a better adhesion and was pressure tested with good results. Again, the lack of flexibility of the adhesive used to hold the mesh screen in place was solved by changing to the Fast Araldit™ epoxy glue and using the already mentioned procedure in those areas, too.

4.6 Providing inner temperature measurement

In order to have information about what is really happening in the regenerator while the refrigerator is running, a set of homemade E type thermocouples was installed in the interfaces between sections and at the cold side cover of four diametrically opposed regenerators. The tip of the sensor in placed at the center of each regenerator cavity mesh. Type E was chosen because its components are not ferromagnetic.

Type E 0.12 mm thermocouple wires (Omega TFCC-005-100 and TFCH-005-100) were used and their union made by spark welding the ends of both wires together in a Dentaurum Master 3000 welding unit. This procedure allowed to weld the wire tips without using any solder, obtaining a very small butt-welded union with no additional metals that can be a source of errors in the thermocouple readings. These sensors were placed only in four diametrically opposed AMRs. In this way, if a thermocouple happens to malfunction, an equivalent replacement will be readily available.

The thermocouples are used in contact with the HTF, and the metallic screens and particles; therefore, the bare wire tips of the sensors have to be coated in order to avoid electrical contact with the MCM and the HTF. It was

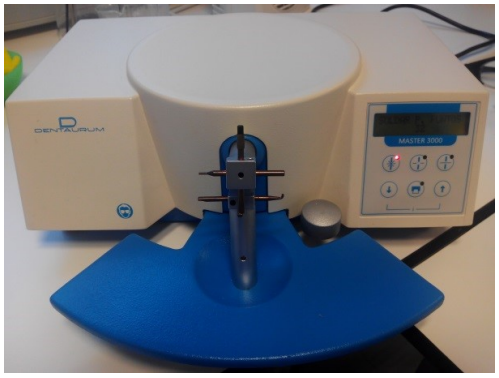

Figure 4.12: Dentaurum Master 3000 welding unit.

decided to use a thin cyanoacrylate layer for this purpose. Although this glue is not a good thermal conductor, the layer is very thin and the response time will not be sensibly affected. After many tests, a procedure was established, the coating was performed by hand under a microscope and the results checked with an ohmmeter. Some details about the manufacturing process are shown in figure 4.13. The wires of the thermocouples are twisted to diminish noise coupling effects, specific type E thermocouple connectors are installed at their ends, and they are later placed in the regenerator sections and the top cover ring of the AMR block, in the middle point of the cross section and on the rib between the inlet and outlet port of the cover ring (see figure 4.14).

Thermocouple wires are connected to a data acquisition module (DAQ) (Omega OMB-DAQ-2416) which is connected to a computer. Different Labview programs have been made for different tasks related to the machine setup and testing, including the acquisition of temperature readings from the regenerator block and other parts of the prototype, as well as other necessary data. Since the DAQ module can only host 16 thermocouples, not all the temperature sensors available in the prototype can be monitored at any one time. More details about the DAQ system are available in chapter 7.

The thermocouples have been calibrated using the cold spot's PT100 sensor as a reference, using a mechanized aluminum block as common temperature mass (figure 4.15).

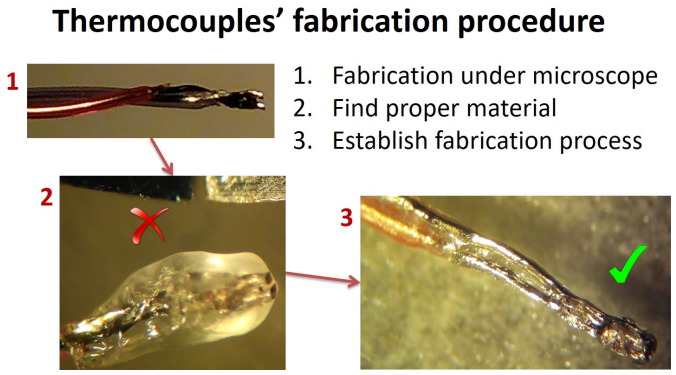

Figure 4.13: Thermocouple fabrication process definition. A butt-welded thermocouple can be seen in image 1, taken under a microscope. Image 2 shows a cyanoacrylate covered thermocouple tip with a caliper tip open 0.1 mm. In this case, the cyanoacrylate layer at the tip was too thick and the wire tips protruding from the weld posed a glue wetting problem. Image 3 shows a finished thermocouple after improvements were introduced in the fabrication process.

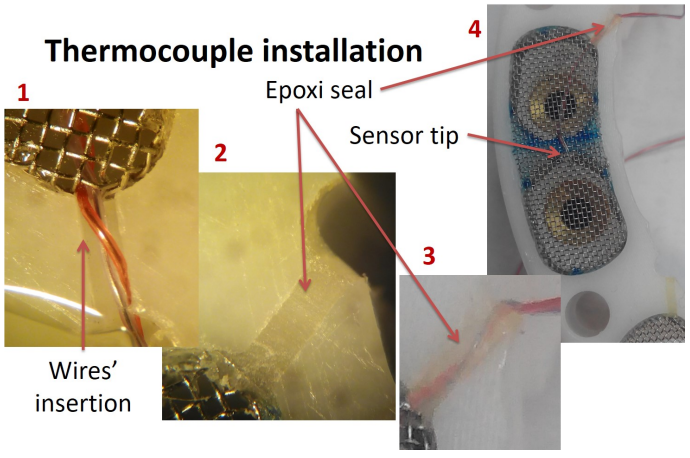

Figure 4.14: Thermocouple installation. Image 1, presents the entry channel of the regenerator section with the thermocouple wires entering the wire mesh. Image 2 shows an unused entry channel of the AMR section sealed with epoxi, while in image 3, a used channel sealed with epoxi can be seen. Image 4 presents a thermocouple installed at the top cover ring of the AMR block.

Figure 4.15: Thermocouple calibration setup. The thermocouples were calibrated against the readings of the Pt100 sensor of the cold spot using an aluminum block as common temperature mass.

4.7 Screen mesh fabrication

Mesh screens are located at the ends of each section of the regenerator block to hold the MCM particles and prevent them from mixing and being washed away by the fluid and carried to other areas of the refrigerator. Also, the meshes prevent the particles from falling out of place when manipulating the AMR sections while assembling or dismounting the regenerator block. Figure 4.17 shows a section with its meshes glued in place, and in figure 4.18 the different mesh versions used are shown.

Meshes had to accomodate to the shape of the AMR housing's cross section and, therefore, the mesh had to be shaped before its insertion. In order to shape the mesh, two cold stamping dies with different shapes were designed: one with the shape of the AMR sections' cross section and another with the shape of the inlet/outlet areas of the AMR cover rings. Renders of the tools' designs are shown in figure 4.16. The dies were used by hand, since the closing pressure to conform the wire cloth was low, due to its malleability.

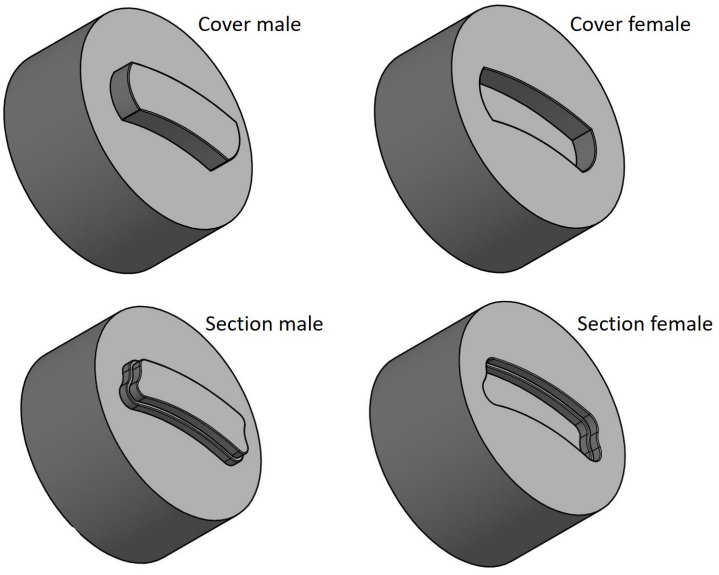

Figure 4.16: Renders of the designs of the cold stamping dies for both types of meshes.

The mesh used for these purposes was a plain wave woven wire cloth made of non magnetic stainless steel AISI 304, with an aperture width of 410 µm and

a wire diameter of 0.14 mm.

Some minor modifications are needed in the meshes of the cover rings to finally accommodate them in place. This was done with the help of small scissors. All the mesh screens were finally secured in place with fast Araldit™ epoxy glue.

Figure 4.17: An AMR section with its meshes glued in place.

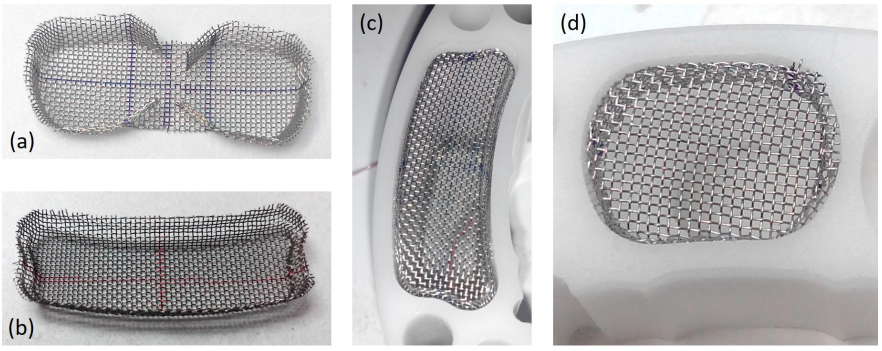

Figure 4.18: Meshes before being glued in their positions: figure (a) shows the first version of the stamped mesh for the top cover of the AMR block. A single piece covers both entries in each AMR. Figure (b) shows the conformed mesh for the bottom of a section's cavity, and in (c) one of these meshes is shown in place, before glue is applied. In (d), the second version of the mesh for the top cover of the AMR block can be seen. This time the mesh covers a single hole of the entries to each AMR, but it is held better in place and leaves more room for the MCM.

Chapter 5

Magnet design

Being the magnetic field source the most expensive element of a magnetic refrigeration device, the design of an efficient magnet with high and low field regions, using reduced volumes of permanent magnets, is of great importance for the practical application of this new technology. What follows is an abstract of a published paper authored by Beltrán-López, Palacios, Velázquez and Burriel [133].

A two-pole rotary magnet formed by sectors of oriented hard magnets and soft iron pieces was optimized in angular width and magnetization direction of each sector. A quadratic approximation was used for the optimization of the defining angles, providing the parameters that result in extreme values of a given functional F, defined as an efficiency variable of the working device. The procedure also gives the correlation between parameters and the relative importance of the deviations with respect to their mathematical optimal values. The optimized magnet has been built, and the resulting calculated fields compared with experimental measurements in the real system.

The efficiency of a magnet was quantified by Björk et al. [134] with an expression that applied to the present magnet results in

$$\Lambda_{cool} = \left(\langle B_{high}^{2/3} \rangle - \langle B_{low}^{2/3} \rangle \right) \frac{V_{field}}{V_{mag}} P_{field} \,, \tag{5.1}$$

where $\langle B_{high}^{2/3} \rangle$ is the average of $B_{high}^{2/3}$ in the high field region (similarly, $\langle B_{low}^{2/3} \rangle$ in the low flux density region), being B the flux density in Tesla. V_{field} is the volume of the high field region, V_{mag} the volume of the permanent magnets and P_{field} the time fraction in which the AMR is in the high flux region. The power $2/3$ arises from the dependence of the magnetocaloric effect in typical materials, on a second-order magnetic transition near the Curie temperature. From expression 5.1 it results that, for a given design, a near zero field in the low field region is more important than reaching a very high field in the high field region.

Although the Λ_{cool} parameter has been increasing since the early 2000's from $\Lambda_{cool} = 0.05$, [135] to $\Lambda_{cool} = 0.21$ with a four-pole magnet [136]. A further derivation of this last design by Eriksen et al. [107], replaces almost one half of the permament magnet material with soft iron, with only a small reduction of the maximum field, but achieving a high increase of Λ_{cool}. However, this design has small regions with magnets' demagnetization risk, i.e., regions of the permanent magnets where $\mathbf{B}$ is small or even opposite to the magnetization $\mathbf{M}$. In order to avoid the possible consequences of this problem, these regions should be made of a harder magnetic material, which usually implies a lower magnetization. This design can also be improved by optimizing the angular thickness and magnetization directions of the NdFeB sectors. As a result, a new magnet design is made through the optimization of these parameters. For this purpose, a functional $F(x_i)$ of the optimizable parameters x_i is defined with a view to its application in this magnetic refrigeration prototype.

5.1 Design and model definition

Based on the two-pole magnet reported by Eriksen et al. [107], several variable parameters are introduced as summarized in table 5.1 and shown in figure 5.1. These values are introduced in a 2D FEM model to proceed with their optimization. The model was made in 2D to save computing time, considering that this simplification has no relevant effect on the parameters to be optimized.

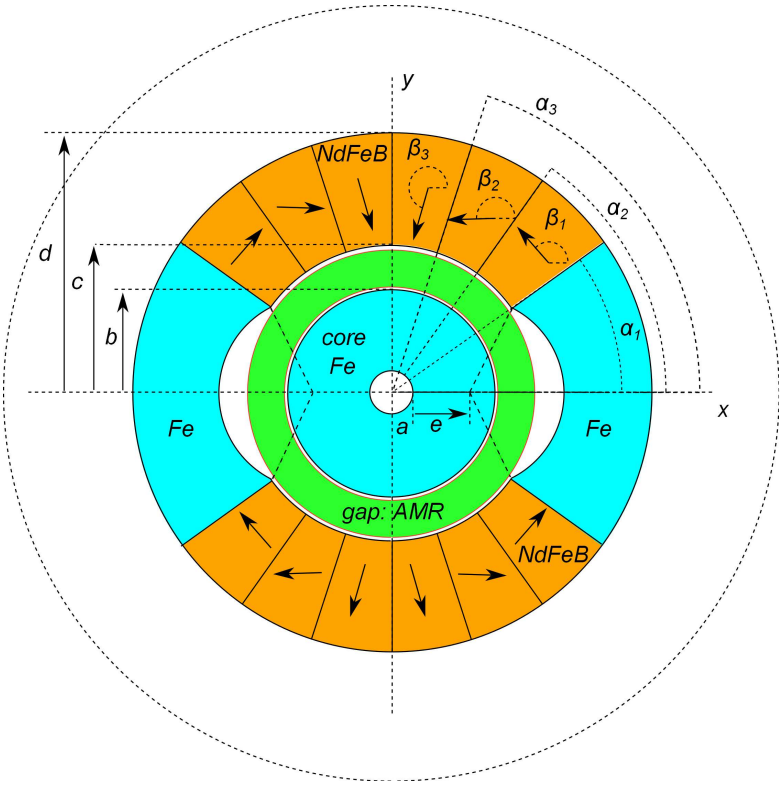

Figure 5.1: Cross-section of the magnet's initial design, following the model of Eriksen et al. [107] with the definition of the variable parameters. The outer dashed circle marks the limit for the FEM calculation ($1.5 \cdot d = 150\,\text{mm}$), where the radial component of $\mathbf{B}$ has been fixed to zero.

Table 5.1: Magnet's defining parameters involved in the optimization with the 2D finite element model (not all of them can be optimized). The parameters are graphically shown in figure 5.1.

Parameter	Variable
Radii	a, b, c, d
Azimut angles of iron-magnet and magnet-magnet interfaces	$\alpha_1, \alpha_2, \alpha_3$
Sector's magnetization angles	$\beta_1, \beta_2, \beta_3$
Meniscus center point displacement	e

The central blue zone (core), shown in figure 5.1, is made of a magnetically soft iron with negligible anisotropy and hysteresis. The lateral iron sectors are under a nearly static magnetic field. The empty meniscus between the AMR block and each iron sector has circular boundaries, one of them with the center

at $x = a + e$, $y = 0$, being e another adjustable parameter. In the model, the fields $\mathbf{B}, \mathbf{H}$, and $\mathbf{M}$ are symmetric with respect to the y-axis and antisymmetric with respect the x-axis, both shown in figure 5.1.

The green region in figure 5.1 (gap) is filled with an MCM divided in eight sectors, covering an angle of 45° each. Every sector acts as an AMR along the axial direction, z-axis, perpendicular to the plane of figure 5.1. The outer part of the magnet assembly, which includes permanent magnets and iron sectors, rotates during the operation of the magnetic cooler around the z-axis.

The magnetic behavior of the materials has been modeled as follows. All permanent magnets were assumed as having the same constant M, changing only the direction from one sector to another, which turns M into a scale factor. When far enough from reaching the coercive field, the permanent magnets of NdFeB alloys behave very accurately as media with constant magnetization $\mathbf{M}$. The core and the two iron sectors are made of soft iron and low-carbon steel, respectively. For the calculations, iron is assumed to have a linear dependence $\mathbf{B} = \mu(\text{Fe})\mathbf{H}$ with relative permeability $\mu_r(\text{Fe}) = \mu/\mu_0 = 200$ (provided that $\mu_r(\text{Fe}) >> 1$, this parameter has a small effect on the field). The actual values of $\mu_r(\text{Fe})$ exceed safely 200, adding a negligible reluctance to the magnetic circuit. The magnetization of the AMR depends on temperature and field in a non-trivial way. In reality, the magnetic work received by an AMR per cycle and unit volume,

$$W_m = \oint \mathbf{M} \cdot d\mathbf{B}\,, \tag{5.2}$$

comes explicitly from the dependence of μ on temperature. Although the $B(H)$ dependence of the AMR is neither always linear nor simple and it has some measurable effect on the field, this effect is not decisive [137]. Hence, a linear dependence with constant $\mu = 2\mu_0$—typical average value for an MCM near its Curie temperature—has been assumed for the sake of simplicity. The permeability of air is taken as μ_0. Under these conditions, $\mathbf{M}$ is assumed to be a constant vector in the permanent magnets,

$$\bigtriangledown \cdot \mathbf{H} = \bigtriangledown \cdot \mathbf{B}/\mu_0 - \bigtriangledown \cdot \mathbf{M} = 0\,. \tag{5.3}$$

In linear homogeneous media,

$$\mathbf{B} = \mu\mathbf{H} \Rightarrow \bigtriangledown \cdot \mathbf{H} = \bigtriangledown(1/\mu) \cdot \mathbf{B} + \bigtriangledown \cdot \mathbf{B}/\mu = 0 \tag{5.4}$$

In both cases, the magnetic field,

$$\mathbf{H} = -\bigtriangledown \phi\,, \tag{5.5}$$

derives from a scalar potential ϕ following the Laplace equation in every region, with the boundary conditions of continuity of the normal components of **B** and the parallel components of **H** at every interface. This scalar potential has been determined by the FEM model with triangular meshing, using the software GMESH,[138] and GETDP[139] for solving the system of equations. Resulting flux density data are given as the dimensionless quantity $B/\mu_0 M$.

5.2 Optimization

An initial FEM calculation was made with a mesh of 8473 nodes and 16752 triangles. It has to be pointed out, that the mesher does not return exactly the same mesh when varying the different parameters and, although close to these figures, the number of nodes and triangles may change slightly with every modification in the system's parameters.

The results of the initial calculation show that B is intense near the corners of the regions. Theoretically $B \to \infty$ with the logarithm of the distance to any corner, but the assumption of constant **M** is not realistic near a corner and, thus, the physical corners are not mathematical vertices. These initial results show that when the regenerators are empty (making $\mu_{AMR} = \mu_0$), and the same geometry and NdFeB material described in this reference are used, the average $B(\theta)$ over the radius of the gap region agrees with the calculation of Eriksen et al.[107].

Using the above mentioned typical average value for an MCM near its Curie temperature, $\mu_{AMR} = 2\mu_0$ (see section 5.1), the maximum field in the gap increases significantly. B is very small, meaning that $\mathbf{H} \simeq -\mathbf{M}$, near the top and bottom of the magnet's cross section, shown in figure 5.2, being these the only regions with risk of demagnetization. Also, the high field shown near the central hole of figure 5.1 could pose a risk of iron core saturation. This can be reduced by decreasing the diameter a.

Instead of the ususal maximum gradient method, a quasi-Newton method was used to find the zero of the gradient of a functional, given by a quadratic

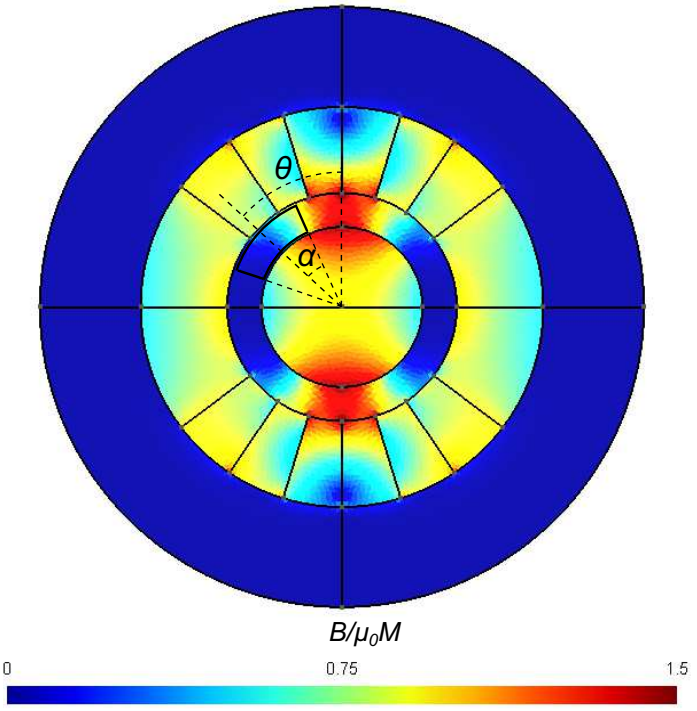

Figure 5.2: $B/\mu_0 M$ for a typical FEM calculation. The sector limited by a solid black line in the gap's area represents one of the eight AMRs, in a position determined by the polar angle θ between the center of this AMR and that of maximum field. Each AMR covers an angle 2α =45°.

approximation [137]. The optimized functional $F(x_i)$, which has N adjustable parameters x_i $(i = 1, 2, ..., N)$, is defined according to the specifications of the physical system. $F(x_i)$ is minimized or maximized for the values of x_i. This procedure, not only gives the optimal parameters, but also the relative importance of each parameter, and tells whether a given parameter can be optimized or not.

Near a critical point (maximum, minimum, or saddle point), $F(x_i)$ can be expanded in a Taylor series of several variables up to second order as:

$$\begin{aligned} F \quad (x_i) &= F(x_{i0}) + \sum_{i=1}^{N} \left(\frac{\partial F}{\partial x_i} \right)_{x_{i0}} (x_i - x_{i0}) + \\ & \frac{1}{2} \sum_{i=1}^{N} \sum_{j=1}^{N} \left(\frac{\partial^2 F}{\partial x_i \partial x_j} \right)_{x_{i0}} (x_i - x_{i0})(x_j - x_{j0}) + ... = \\ F \quad (x_{i0}) &+ \sum_{i=1}^{N} B_i (x_i - x_{i0}) + \frac{1}{2} \sum_{i=1}^{N} \sum_{j=1}^{N} A_{ij} (x_i - x_{i0})(x_j - x_{j0}) + ..., \end{aligned} \tag{5.6}$$

where the vector (x_{i0}) is an arbitrary point in the parameter space. With a method to evaluate $F(x_i)$ for any set of parameters, the first and second derivatives can be evaluated taking small increments Δx_i using finite-difference approximations, with errors proportional to Δx_i^3. Defining, for each pair of increments $\Delta x_i = x_i - x_{i0}$ and $\Delta x_j = x_j - x_{j0}$,
$F_0 = F(x_{10}, ..., x_{i0}, ..., x_{j0}, ..., x_{N0})$,
$F_1 = F(x_{10}, ..., x_{i0} - \Delta x_i, ..., x_{j0}, ..., x_{N0})$,
$F_2 = F(x_{10}, ..., x_{i0} + \Delta x_i, ..., x_{j0}, ..., x_{N0})$,
$F_3 = F(x_{10}, ..., x_{i0} - \Delta x_i, ..., x_{j0} - \Delta x_j, ..., x_{N0})$,
$F_4 = F(x_{10}, ..., x_{i0} + \Delta x_i, ..., x_{j0} - \Delta x_j, ..., x_{N0})$,
$F_5 = F(x_{10}, ..., x_{i0} - \Delta x_i, ..., x_{j0} + \Delta x_j, ..., x_{N0})$,
$F_6 \equiv F(x_{10}, ..., x_{i0} + \Delta x_i, ..., x_{j0} + \Delta x_j, ..., x_{N0})$,
we have, up to second order in the increments,

$$\left(\frac{\partial F}{\partial x_i} \right)_{x_{i0}} = B_i \cong \frac{F_2 - F_1}{2\Delta x_i} \tag{5.7}$$

$$\left(\frac{\partial^2 F}{\partial x_i^2} \right)_{x_{i0}} = A_{ii} \cong \frac{F_2 + F_1 - 2F_0}{\Delta x_i^2} \tag{5.8}$$

$$\left(\frac{\partial^2 F}{\partial x_i \partial x_j} \right)_{x_{i0}} = A_{ij} \cong \frac{F_6 - F_5 - F_4 + F_3}{4\Delta x_i \Delta x_j}. \tag{5.9}$$

The expression obtained replacing the derivatives with the finite differences, is not just an approximation of the Taylor series, but an interpolation formula

that matches the exact functional $F(x_i)$ at (x_{i0}) and at points obtained from it by the increment of a single variable to $x_{i0} \pm \Delta x_i$, i.e., it matches exactly the F_0, F_1, F_2 values for each variable. The value of $F_6 - F_5 - F_4 + F_3$ for every pair of increments Δx_i, Δx_j is also exactly represented. A critical point $(x_{i,cr})$ is defined as obeying $\left(\frac{\partial F}{\partial x_i}\right)_{x_{i,cr}} = 0$, $\forall i = 1, ..., N$.

From the use of the quadratic approximation, we obtain the following linear system of equations:

$$\sum_{j=1}^{N} A_{ij}(x_{j,cr} - x_{j0}) + B_i = 0, \qquad i = 1, ..., N\,. \tag{5.10}$$

The solution $(x_{j,cr}, j = 1, ..., N)$ surely corresponds to a minimum if the matrix A is positive definite, to a maximum if negative definite, and to a saddle point if it has some positive and some negative eigenvalues. If an eigenvalue is zero, the corresponding eigenvector is a linear combination of increments which makes $F(x_i)$ locally invariant near $(x_{i,cr})$, up to third order in the increments. Like in a least squares optimization, which is a particular case of functional F, the approximation would be more accurate if (x_{i0}) is near the critical point, but the obtained solution $(x_{i,cr})$ can be taken as a new (x_{i0}) for iteration, until the convergence is reached within some allowed error.

In principle, this procedure can be used to optimize the working parameters of a real system or a simulation, being F either an experimental result or a result from a computer simulation of a complete system. In such cases, as in a 3D FEM calculation, reducing the number of evaluations of F is vital. In each iteration, this procedure needs $2N + 1$ evaluations of $F(x_i)$ to obtain the first-order and direct second-order derivatives, and $2N(N-1)$ evaluations for the mixed second-order derivatives, $2N^2 + 1$ evaluations in total. Each evaluation involves meshing, finite elements solution for the field, and numerical evaluation of $F(x_i)$ from the results. Note that a quadratic function of N variables has only $(N + 1)(N + 2)/2$ coefficients to be determined, this is hence the minimum number of evaluations of F to determine the critical point, i.e., the critical point of the unique hyper-paraboloid passing exactly through $(N+1)(N+2)/2$ given points. This means that we are using an approximation involving more evaluations, but giving the derivatives with a higher order of approximation. For small deviations with respect to (x_{i0}) and for the present approximation, the error in $F(x_i)$ is a combination of cubic terms in $x_i - x_{i0}$,

$x_j - x_{j0}$, $x_k - x_{k0}$ $(i, j, k = 1, ...N)$. The error in the first and second derivatives is quadratic since, for the first derivatives, the even terms of the Taylor expansion cancel in $F_2 - F_1$. The error in $F_2 - F_1$ is therefore cubic, and in $(F_2 - F_1)/\Delta x_i$ is quadratic. Similarly, for the second derivatives, the cubic terms cancel in the expansion of $F_1 + F_2 - 2F_0$, and also in $F_6 - F_5 - F_4 + F_3$. The ratio of the number of parameters used with respect to the minimum is $f = 2(2N^2 + 1)/[(N + 1)(N + 2)]$, being $1 \leq f < 4$. This means that in the optimization of the magnet described in 5.2, $N = 6$, $f = 2.61$.

Extending the Taylor series to higher order terms has no practical interest with many variables because the number of partial derivatives to be determined increases quickly. The general conditions for convergence of this procedure will not be discussed here, but will only mention that it leads to a maximum of $F(x_i)$, in the present problem of optimizing a magnet, if the initial point is close enough to the maximum, that is, if the B_i vector is small, and especially if the hyper-ellipsoid centered at (x_{i0}) and with half-axes (Δx_i) contains the critical point. A detailed discussion of the convergence of the quasi-Newton method is given in [140].

Once the critical point $(x_{j,cr})$ has been found, the functional F can be expressed in terms of the increments with respect to $(x_{j,cr})$. That is, defining $x'_i = x_i - x_{i,cr}$, we have

$$F - F_0 \simeq \frac{1}{2} \sum_{i,j=1}^{N} A_{ij} x'_i x'_j \,, \tag{5.11}$$

where the linear terms have vanished, since the first derivatives are zero at a critical point. As any symmetric matrix, A can be diagonalized as an orthogonal matrix O, made with the eigenvectors of A written in columns, in such a way that the diagonal elements of $A_d = O^t A O$ are the eigenvalues, λ_i. Using the new coordinates $y_i = \sum_j^N O^t_{ij} x'_j$ near the critical point, the quadratic approximation results in

$$F - F_0 \simeq \frac{1}{2} \sum_{i=1}^{N} \lambda_i y_i^2 \,. \tag{5.12}$$

Therefore, the eigenvectors of A (columns of O) indicate the independent combinations of increments x'_i, in such a way that the change of F with respect to the critical value produced by one single increment y_i is independent of any other y_j. The eigenvalues indicate how large an increment of F is produced

by a given y_i. If every $\lambda_i > 0$, F is a minimum at $(x_{i,cr})$, if every $\lambda_i < 0$, F is a maximum, and if $\lambda_i > 0$ and $\lambda_j < 0$ for some i and j, it is a saddle point. If one $\lambda_i = 0$, F is locally invariant, indicating that F does not vary for small changes of this particular parameter y_i, up to second order in y_i.

The magnet is intended for a magnetic refrigerator. The eight independent AMRs are placed in the green region of figure 5.1, covering an angle of 45° each. The outer part of the magnet assembly rotates counterclockwise around the z-axis, perpendicular to 5.1. To analyze the case, let us suppose that the AMRs rotate clockwise with constant angular speed and the outer part of the magnetic circuit is fixed. The liquid starts flowing when the right end of the analyzed AMR sector reaches the maximum field point, this is, when $\theta = \alpha$ in figure 5.2, and stops flowing when the left end leaves the maximum field point ($\theta = -\alpha$). Similarly, for the minimum field region (dark blue region of the gap, near the x-axis), with cold liquid flowing to the cold source. The same thing happens in the AMRs at their opposite positions, at 180°+θ. For these four AMRs there is a dead time without flow between the high and low field regions (while the AMR turns 90°-2α), allowing the field to change from high to low values. During this dead time the other four AMRs are active, with liquid flow, in the maximum or minimum field regions.

Regarding the application to this problem, the important quantity is the average field over one AMR. The field profile is symmetric with respect to the maximum and minimum, therefore the average effective field, when the center of an AMR is near the position $\theta_0 = 0$ or 90°, is given by

$$\langle B \rangle = \frac{1}{\alpha(c^2 - b^2)} \int_b^c r dr \int_{\theta_0 - \alpha}^{\theta_0 + \alpha} B(r, \theta) d\theta \tag{5.13}$$

Computing $\langle B \rangle$ for the highest and lowest field zones, the maximum magnetocaloric effect will be obtained for the largest difference. Consequently, the quantity to be maximized is $F = (\langle B_{high} \rangle - \langle B_{low} \rangle)/\mu_0 M$, computing $\langle B_{high} \rangle$ and $\langle B_{low} \rangle$ with equation (5.13) for the values θ_0 =0° and 90°, respectively.

Not all the parameters in figure 5.1 can be optimized. The fields **B** and **H** are invariant under the application of a scale factor to all lengths. The maximum flux density increases if the gap, $c - b$, decreases (the maximum F occurs for $c - b = 0$, which is obviously useless), but it has to be determined by the desired volume of the AMRs. For a magnetic circuit made with permanent magnets having a constant M, taking a closed line along the circuit, Ampere's

law states

$$\oint \mathbf{H} \cdot d\mathbf{l} = 0 \Rightarrow \int_{mag} \mathbf{M} \cdot d\mathbf{l} = \int_{mag} (B/\mu_0) dl + \int_{AMR} (B/\mu_{AMR}) dl + \int_{Fe} (B/\mu_{Fe}) dl \qquad (5.14)$$

where the subscripts mag, AMR, and Fe refer to the parts of the circuit line of each material. The magnetic flux through the closed circuit, Φ, is constant. Taking the circuit with average cross-sections for the different materials, A_{mag}, A_{AMR}, and A_{Fe}, one can write the total flux as a function of the average field in each region,

$$\Phi = \langle B_{mag} \rangle A_{mag} = \langle B_{AMR} \rangle A_{AMR} = \langle B_{Fe} \rangle A_{Fe} \qquad (5.15)$$

This allows to determine approximately the flux Φ and the average fields in each region by substituting B in equation (5.14) with its average value in each term, taken from equation (5.15). Thus, using $\Phi = \langle B_{AMR} \rangle A_{AMR}$ and the values taken for μ_{AMR} and μ_{Fe}, results in

$$\langle B_{AMR} \rangle = \frac{\mu_0 \int_{mag} \mathbf{M} \cdot d\mathbf{l}}{A_{AMR} \left(\frac{l_{mag}}{A_{mag}} + \frac{l_{AMR}}{2A_{AMR}} + \frac{l_{Fe}}{200 A_{Fe}} \right)}, \qquad (5.16)$$

where the parenthesis in the denominator is the reluctance of the magnetic circuit. For the dimensions of figure 5.1, the reluctance of the iron parts of the magnetic circuit happens to be negligible and $l_{AMR} << l_{mag}$, all cross-sections being of similar magnitude. Then, as a quick and simple estimate, the flux is roughly determined by the magnetization M, the alignment of the vector $\mathbf{M}$ with the flux lines, and the length l_{mag} of the flux lines in the magnets. This means that $l_{AMR} = 2(c-b)$ can be increased to values compatible with a small decrease of the magnetic flux (e.g., for $l_{AMR}/l_{mag} = 0.1$, a 5% decrease is expected with respect to the case $c - b = 0$).

The a parameter is also not optimizable, since the optimal value is zero. However, F is quite insensitive to a, since the core reluctance is negligible anyway. This parameter can be increased to save material but it should not be too high, in order to prevent saturation of the iron core, since B reaches high values right next to the central hole, near the x-axis.

5.3 Numerical results

Let us consider for the initial parameters the approximate values deduced from the figures given by Eriksen et al., [107] taking the lengths $a = 20\,\text{mm}$, $b = 50\,\text{mm}$, $c = 65\,\text{mm}$, $d = 110\,\text{mm}$, $e = 6\,\text{mm}$, and angles $\alpha_1 = 33°$, $\alpha_2 = 52°$, $\alpha_3 = 71°$, $\beta_1 = 140°$, $\beta_2 = 195°$, and $\beta_3 = 250°$. With these parameters, the calculation of $B/\mu_0 M$ in an empty AMR of 45°, using the FEM method, gives $F = \langle B_{high}/\mu_0 M\rangle - \langle B_{low}/\mu_0 M\rangle = 1.014$. The first derivatives B_i are high and the quadratic approximation is not necessarily good. Moreover, we find that the field on the iron sectors can be near the saturation.

Calculations with and without meniscus have been made and they show that, within the model, the meniscus has only a small effect on the total flux. On one hand, it reduces the field in the gap near $\theta = 90°$, but it also reduces the cross section of the iron sector, increasing B where it can already be near saturation. The reluctance of the iron gets dangerously close to saturation when the flux flows out of it. Moreover the material saving is not so important, since the iron sectors are not made of any critical material, the real amount of material necessary to manufacture the part depends on the manufacturing process used and, in all cases, the absence of meniscus makes their construction cheaper and easier.

These parameters were changed slightly to $a = 0$, $b = 40\,\text{mm}$, $c = 57\,\text{mm}$, $d = 100\,\text{mm}$, and canceled the meniscus according to our specifications for the size of the magnet and the available volume for magnetocaloric material. Canceling the meniscus is a substantial improvement of this design. With these new parameters and keeping the same angles, we found $F = 0.974$ for a gap without any magnetocaloric material (the calculation for an empty gap is useful for a further comparison with measurements in the actual magnet) and $F = 1.162$ for a filled gap with a material having $\mu_r = 2$.

To optimize the magnet, an initial FEM calculation of F with single variations of the angles, one by one, was made, taking the increments Δx_i and Δx_j in equations 5.7 to 5.9 as 5°. A significant increase of the optimized functional value to $F = 1.236$ for $\mu_r = 2$ and the following parameters $x_1, ..., x_6$: $\alpha_1 = 35°$, $\alpha_2 = 55°$, $\alpha_3 = 75°$, $\beta_1 = 125°$, $\beta_2 = 170°$, and $\beta_3 = 235°$ was found. These first optimized parameters were used as a starting point for the final op-

timization of the magnet. The complete optimization, following the procedure previously described, gave the final angles $\alpha_1 = 28.5°$, $\alpha_2 = 56.6°$, $\alpha_3 = 72.6°$, $\beta_1 = 128.9°$, $\beta_2 = 167.3°$, and $\beta_3 = 234.9°$, resulting in a value $F = 1.251$ for the functional.

Table 5.2: Matrix A and vector B as defined in equation (5.10), eigenvalues of A, λ_i (in decreasing absolute values), normalized eigenvectors, (v_i) (in columns), and solution of the system $A(x - x_0) = -B$ for the optimal increments. All matrix elements and eigenvalues in the table must be multiplied by 10^{-4}. Maximum and minimum average fields $\langle B_{high} \rangle$, $\langle B_{low} \rangle$ for $\theta_0 = 0$ and 90°, respectively, in units of $\mu_0 M$, defined in equation (5.13), and values of the functional $F = \langle B_{high} \rangle - \langle B_{low} \rangle$, for the initial and the optimized parameters.

	α_1	α_2	α_3	β_1	β_2	β_3	
x_{j0}	35	55	75	125	170	235	
	A_{i1}	A_{i2}	A_{i3}	A_{i4}	A_{i5}	A_{i6}	B_i
A_{1j}	-4.072	-0.957	-0.073	0.685	0.704	-0.015	-25.80
A_{2j}	-0.957	-6.693	0.297	1.004	1.144	-0.044	4.269
A_{3j}	-0.073	0.297	-25.72	-0.118	3.129	0.6073	-52.28
A_{4j}	0.685	1.004	-0.118	-0.884	0.031	0.013	6.066
A_{5j}	0.704	1.144	3.129	0.031	-1.293	0.056	6.607
A_{6j}	-0.015	-0.044	0.6073	0.013	0.056	-34.86	9.164
λ_i	-37.94	-23.06	-7.48	-3.81	-0.90	-0.34	
	v_1	v_2	v_3	v_4	v_5	v_6	
v_{1j}	-0.0012	0.0080	0.3289	0.9233	0.0177	0.1972	
v_{2j}	0.0042	-0.0057	0.9079	-0.3665	-0.0105	0.2030	
v_{3j}	-0.4525	0.8820	-0.0209	-0.0182	-0.0917	0.0898	
v_{4j}	-0.0019	0.0046	-0.1718	-0.0905	0.7405	0.6433	
v_{5j}	0.0372	-0.1279	-0.1938	-0.0678	-0.6652	0.7054	
v_{6j}	0.8910	0.4533	-0.0067	-0.0037	-0.0172	0.0168	
$\Delta x_{j,opt}$	-6.480	1.580	-2.376	3.856	-2.682	-0.153	
$x_{j,opt}$	28.52	56.58	72.62	128.86	167.32	234.85	
		$\langle B_{high} \rangle$		$\langle B_{low} \rangle$		F	
x_{j0}		1.247		0.011		1.236	
$x_{j,opt}$		1.266		0.014		1.251	

Table 5.2 gives the initially optimized parameters x_{j0}, the vector of the first derivatives, (B_i), the symmetric Hessian matrix A and the values of F obtained from the initial parameters x_{j0} and from the final $x_{j,opt}$ values for the maximum F. It also reveals that the A matrix is negative definite, indicating

that the critical point found is a maximum of F. The highest eigenvalue λ_1, in absolute value, corresponds mainly to β_3 variations combined with α_3. Both of them are by far the most influential parameters for the optimization of F, as can be seen from equation (5.12). On the other hand, the influence of α_1 deviations from the optimum value is one order of magnitud below. This detail will be considered for the construction of the actual system and can be understood in the framework of the magnetic circuit. When the iron and gap reluctances are negligible, an increment of α_1 produces a decrease of $l_{mag} \simeq 2\,(90 - \alpha_1)(\pi/180)(c + d)/2$, which results in approximately the same factor in the numerator and denominator of equation (5.16). F is then insensitive to α_1. Actually $l_{mag} \simeq 4.3\,l_{AMR}$ making such a simplification a bit crude. Also small changes in β_1 and β_2 are almost irrelevant. The optimum F for the functional defined in this work is about 8% higher than the value obtained with the original parameters α_1 to β_3 of Eriksen et al., [107]. A calculation of the optimized F has also been done for a system made with 16 sectors of permanent magnets (i.e., with parameters $\alpha_1, ..., \alpha_4, \beta_1, ..., \beta_4$) but the value of F only improves a mere 2%. As a result, the actual design was made with only 12 sectors of permanent magnets. Finally, the optimization of the e parameter, defining the center of the meniscus line, gave a very small difference of only 0.2% in F. As discussed above, the meniscus increases the reluctance of the gap for direct flux between the core and the iron sectors, reducing $\langle B_{low} \rangle$, but the effect is small since B radial is already zero at the x-axis due to the symmetry. Additionally, the calculated flux density in the iron sectors is near the limit of the linear dependence of $B = \mu(Fe)H$ and the meniscus reduces its cross section, increasing B inside. In this region of the $B(H)$ curve of iron, a small increase of B would produce a large increase of H, expelling the flux lines, due to the continuity of the parallel components of H at the iron-air interface.

5.4 Experimental measurements in the built magnet

The magnet was finally constructed with the initial FEM calculations, using single variations of the parameters and a further step forward looking to optimize the functional with each parameter. The effect of the non zero susceptibility of the magnetocaloric material in the AMRs was also included. Moreover, the meniscus was finally not built, considering its small effect and the resulting easier construction without it. The final parameters were slightly

different from the results of the full optimization described above. For this magnet, the radii were scaled to have a fairly small system, but with enough volume for the AMR to test different magnetocaloric materials with a good cooling power. Table 5.3 summarizes the final constructive measurements and angles of the magnet. The main difference with the optimal values previously calculated is the increase of α_1, that saves expensive material. This can be expressed in terms of Λ_{cool} (see equation (5.1)), considering the important reduction of V_{mag}, against a small decrease of $\langle B_{high}^{2/3} \rangle - \langle B_{low}^{2/3} \rangle$. A summary of the materials finally used for the construction of the magnet is available in table 5.4. An image of the magnet can be seen in figure 5.3.

Table 5.3: Actual constructive values of the magnet after optimization.

Angle	Value	Diameter	Value [mm]
α_1	37°	$a = -e$	12.5
α_2	56°	b	40
α_3	73°	c	57
β_1	133°	d	100
β_2	180°	Length	200
β_3	237	(z-axis)	

Table 5.4: Summary of the materials used for the construction of the magnet. The intrinsic coercivity of the magnet sectors prevents the risk of demagnetization for $B > -0.10$ T in the **M** direction. The stack of insulated perpendicular to the z-axis sheets, that forms the core, reduces eddy currents' dissipation.

Part	Material	Characteristic values
Magnet sectors	NdFeB N48H	$B_\mu \mu_0 M = 1.41$ T $\mu_0 H_c = 1.70$ T
Iron sectors	Unalloyed steel 5235JR	
Core	Soft magnetic iron M600-50A (stack of insulated sheets)	$\mu_r = 1660$

The magnetocaloric material filling the AMR increases the relative permeability of the gap from 1 to 2, which produces an important increase of the flux. For the given radii and lengths, the optimized values for the angles, $\alpha_1, ..., \beta_3$, considering the AMR space full of magnetocaloric material with $\mu_r = 2$, resulted in a functional value $F = 1.251$. The built magnet keeps close to the optimized values the three most influential parameters, β_3, α_3, and α_2. The angle α_1 is markedly higher than the optimized value, but this deviation has a

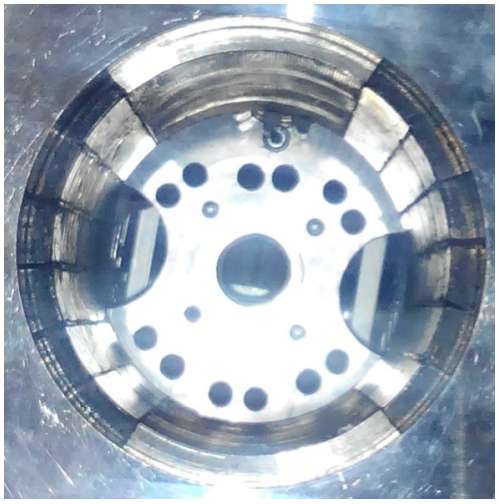

Figure 5.3: A top view of the magnet already installed in the prototype's frame without its core. The NdFeB sectors of the magnet can be seen in black and the iron sectors in gray.

small influence on F, reducing, on the other hand, the amount of permanent magnet used, and the also sizable deviations of β_1 and β_2 are even less important, as seen above. The resulting functional F, with the actual geometric parameters, decreases only to 1.234. Considering the dimensions of the magnet, the volume of the high field region restricted to its use in each AMR with $2\alpha = 45°$, and $\langle B^{2/3} \rangle$ calculated in the high and low field regions, the resulting figure of merit of equation (5.1) is $\Lambda_{cool} = 0.16$.

From an analysis of the resulting magnetic circuit, a 26% increase in the maximum field is expected when the AMR is completely filled with the MCM (see [133]), similar to the 21% increase given by the FEM calculations.

Measurements of the actual field were taken on the gap of the empty magnet using calibrated Hall probes for the longitudinal and transverse components, at different radial, angular and longitudinal positions, r, θ, $0\,\text{mm} \leq z \leq 200\,\text{mm}$, taking the center at $z = 100\,\text{mm}$. figure 5.4 shows these measured values at $z = 100\,\text{mm}$, along the circle with the average radius of the AMRs region. The high and low field regions have values around $B_{max} = 1.50\,\text{T}$ for $\theta = 0°$ and $B_{min} = 0.00\,\text{T}$ for $\theta = 90°$. Measurements taken in the gap, at 10 mm from the ends ($z = 10\,\text{mm}$ and 190 mm), showed a decrease of the radial component of 20% from the maximum field and a longitudinal component $B_z < 0.3\,\text{T}$. The

calculated values, using $\mu_r = 1$ to take into account that the measured region is empty of MCM, are also shown. A good agreement was found between the measured and calculated fields, using a value for the magnetization of the NdFeB sectors $\mu_0 M \simeq 1.33\,\mathrm{T}$, which is slightly lower than the reported typical value for the material used.

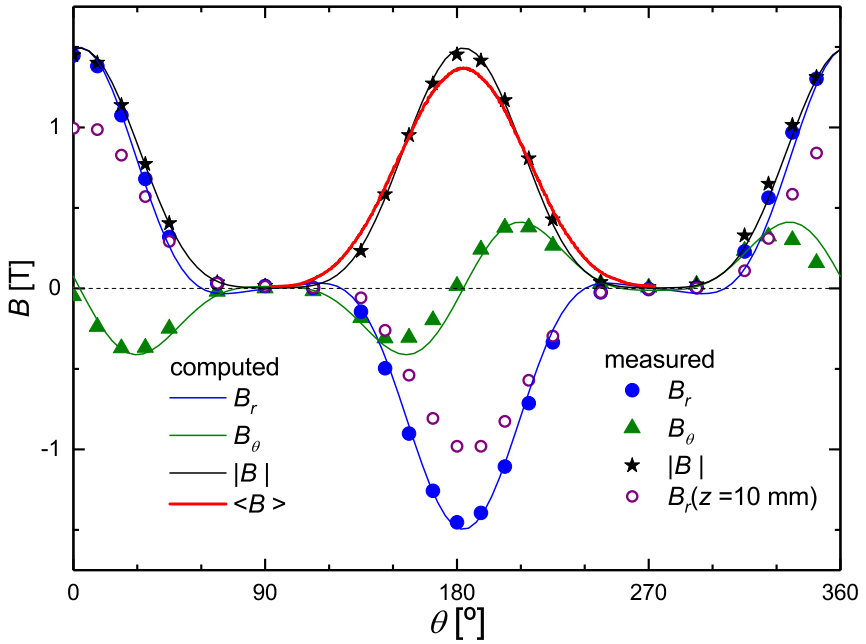

Figure 5.4: Experimental measurements of the magnetic field at different points of the gap, compared with the calculated ones. A 183° shift has been applied to accommodate the computed values to the experiment. The magnetization value M is a scale factor in the calculations. The calculated and measured values agree for $\mu_0 M \simeq 1.33$ T. Hollow circles: Measured B_r at 10 mm from the end, show the field decay.

As a summary, the magnetic field measured in the actual magnet built with optimized parameters agrees very well with the expected values from the calculations. The built magnet minimized the use of expensive hard magnets and gave a high volume for cooling material. The radial thickness of the gap for the AMRs allows an available volume for MCM over 40% of the volume of NdFeB, and more than 50% of the magnet was completed with soft iron.

Chapter 6

Fluid circuit

Traditional magnetic coolers use a heat transfer fluid (HTF) to carry the heat from the cold source to the regenerator and from the regenerator to the hot sink of the system. The desire of the research community to use water as HTF often clashes with the need to avoid corrosion in the MCM and, unless other measures are taken, the usual solution is using a mixture of water with some kind of corrosion inhibitor.

Velázquez et al. presented in THERMAG VI corrosion tests of different HTF candidates on $La(Fe,Co,Si)_{13}$ plates [141]. This work's conclusion was that a 1%vol. ENTEK FNE® corrosion inhibitor diluted in demineralized water was a good choice, but a dilution 30%vol. of Luzar® organic antifreeze showed even better results and did not present any supply issues like the former product.

The availability and good results obtained with $La(Fe,Co,Si)_{13}$ plates made Luzar® organic antifreeze the natural choice. However, since the planned MCMs were Gd, and GdEr and LaFeMnSi-H compounds, and a more diluted mixture was desired, a double check was advisable. The shape of the materials is now spherical particles instead of flat plates and, in order to get the viscosity of the HTF closer to that of water (lowering thus the work needed to maintain the flow through the system), testing the behavior of a 20%vol.

dilution of Luzar® in demineralized water was needed, since this is the most diluted mixture recommended by the manufacturer in order to maintain its corrosion protection. Although the aim of the tests was just to confirm that a 20%vol. dilution showed no signs of corrosion, other HTF candidates were also checked to anticipate possible inconveniences. Several spheres of each different compound were immersed and maintained in different HTF candidates at room temperature. The results after a very long time of observation was that the 20%vol. dilution of Luzar® in demineralized water showed no sign of corrosion in any case (figure 6.1, and was therefore the HTF of choice. A summary of the most relevant physical characteristics of Luzar 20%vol. at 20 °C is available in table 6.1.

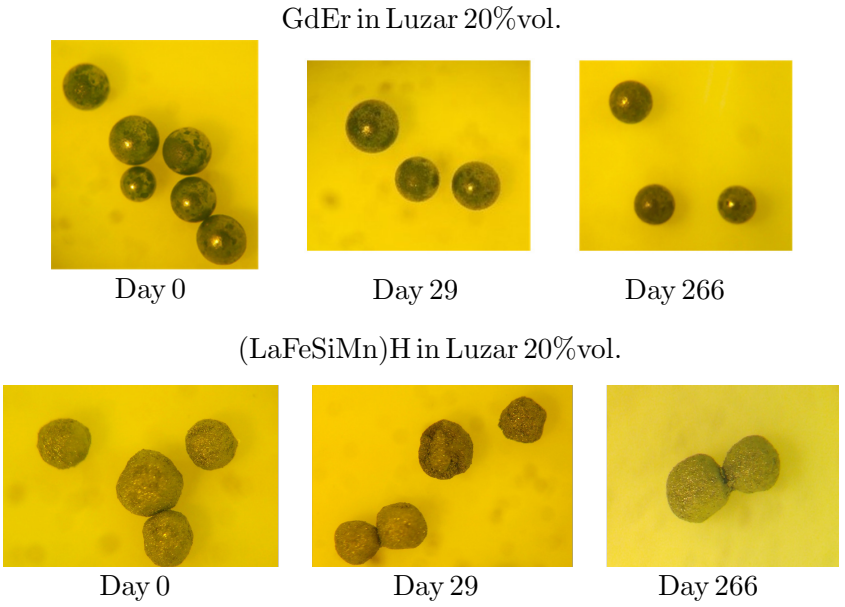

Figure 6.1: Images of the corrosion tests with GdEr and (LaFeSiMn)H compounds in Luzar 20%vol. at different days. After 266 days there is no visible sign of corrosion.

Table 6.1: Physical characteristics of Luzar 20%vol. at 20 °C. Source: Aguidrovert S. L.

Magnitude	Value	Units
μ	1.59×10^{-3}	Pa s
k	0.52	$\mathrm{W\,m^{-1}\,K^{-1}}$
ρ	1027	$\mathrm{kg\,m^{-3}}$
c_p	3850	$\mathrm{J\,kg^{-1}\,K^{-1}}$

6.1 Piping

The tubing of the prototype's fluid system has been made using Linear Low Density Polyethylene (LLDPE) tubing from John Guest® for cold and intermittent hot water applications. Two different sizes of tubing have been used as shown in table 6.2. The thinner tube has been used whenever a space availability problem is found, like in the tubes that connect the regenerator with other external areas, or when the flow that the tubes have to carry is sensibly reduced from the main general flow.

Table 6.2: Sizes and pressure resistance of the LLDPE tubes according to the manufacturer's information.

Tube kind	Outer diameter [mm]	Inner diameter [mm]	Maximum pressure at 20 °C [bar]
Thick	8	6	10
Thin	6	4	16

This kind of piping has several advantages like:

- thermally insulating material (see table 6.3, although the walls are only 1 mm thick,
- easy manipulation, cutting, connection and replacement,
- many configuration options, flexibility in design, no exact measurements needed,
- ready made connections,
- hand made piping modifications on the run.

On the other hand, this solution has also some drawbacks like the large curvature of the tubes, which forces the use of fittings (figure 6.2) to achieve more controlled, small curvatures in the installation and, hence, the options are limited to 90° turns in most cases which add higher losses to the system. The connections require also the use of fittings, which are relatively expensive and have to be chosen well in advance in order to keep up with the assembly

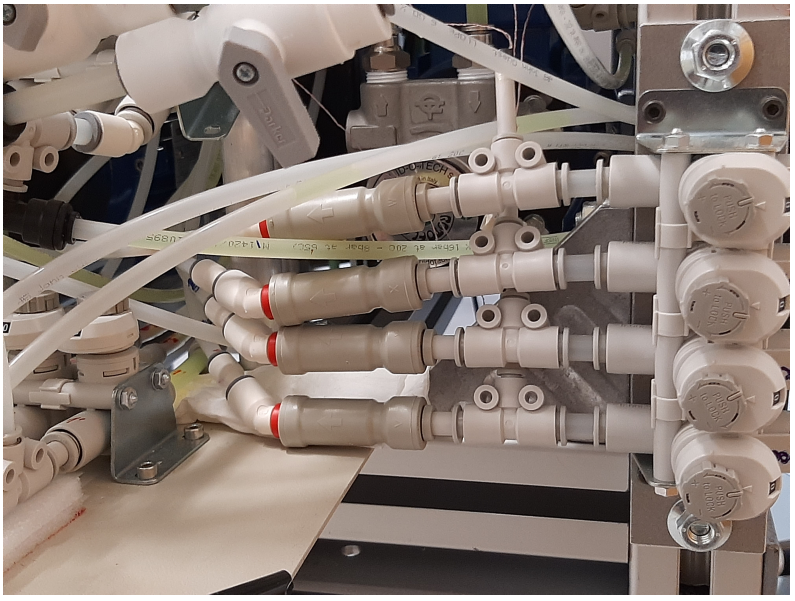

Figure 6.2: Tube fittings are used for easy connection in element with different purposes. Standardized sizes allow the use of elements from different brands. From right to left we can see adjustment valves, "T" connectors with thermocouple inserts and check valves followed by 45° fittings. A ball valve can be seen at on the top left.

process without stock outs of specific parts. Most fittings of small size are meant to be used with air, although some are specifically designed for liquids; nevertheless, most work fine with liquids also.

Table 6.3: Typical values of some thermically relevant physical characteristics of LLDPE.

ρ $[\mathrm{kg\,m^{-3}}]$	c_p $[\mathrm{J\,kg^{-1}\,K^{-1}}]$	k $[\mathrm{W\,m^{-1}\,K^{-1}}]$
920	2100	0.3

The fittings used for the connections were chosen from different manufacturers, namely, John Guest, SMC and Legris. Whenever possible, polymeric fittings for specific liquid applications were selected, but in some cases, compressed air and metal threaded fittings had to be used. The use of fittings with polymeric bodies had the goal to improve the insulation of the piping system, although they may be a bit bulkier than their metallic counterparts.

6.1.1 Inserting thermocouples in the circuit

In order to obtain temperature data in certain spots of the fluid circuit, thermocouples are inserted. Since the thermocouples are self-made, a procedure to insert them safely in the tubing had to be developed. The easiest way to do this avoiding leakage problems is to use a stem from the fittings' catalogs of the diameter of the tube in which the sensor is to be inserted. The thermocouple wire is passed through the stem and through a small piece of plastic drilled in its center. This small piece, cut a bit smaller than the inner diameter of the stem, serves as plug and this ensemble is secured with fast epoxi glue from both sides of the stem. The stem with the mounted thermocouple is easily inserted in a "T"-fitting and no further sealing is needed (see figure 6.3).

(a) **(b)**

Figure 6.3: (a) Thermocouple mounted in a stem. Some glue excess is needed around the tip to avoid excessive bending of the tip due to the force exerted by the flow. Fortunately, the flow is unidirectional. (b) View of the thermocouple tip from the tube entrance. The tip of the sensor sticks out of the stem just enough to be as close as possible to the center of the flow.

6.2 Fluid flow distribution

The fluid circuit is characterized by the use of one-way loops outside the regenerator, maintaining four separated flows with thermal contact among them in the cold spot. The fluid flow is diverted to the different groups of regenerators acting two parallel couples in series, as the magnet revolves, using eight high speed solenoid valves. These valves are commanded with a programmable logic controller (PLC) that has a zeroing electronic cam and an encoder which are read to determine the angular position of the magnet with respect to the regenerator block, in order to decide the precise moment to open and close the different sets of valves. This moment can be shifted by changing the zero position of the system, introducing thus an angular phase change between the magnetization of an AMR and the fluid flow through it, that can be set from zero to $\pm 22.5°$ in steps of $0.5°$.

A scheme of the fluid system is presented in figure 6.4. The fluid is moved by means of two rotary vane pumps which can be used in parallel when there is a need of very high flow rates. A single pump has a maximum flow rate of about $400\,\mathrm{l\,h^{-1}}$ at 0 bar exhaust pressure and 1450 rpm, which is equivalent to almost $7.1\,\mathrm{l\,min^{-1}}$ at 1370 rpm[1]. The flow needed to push 100% of the void volume of a six section high regenerator at maximum operating speed is expected to be close to 12 l, depending on the porosity finally achieved in the beds, two pumps like the above mentioned ones are installed in parallel. These pumps include as a security measure an internal adjustable pressure activated relief valve. This valve has been adjusted to avoid pressures above 9.5 bar at maximum pump speed, which is regulated with a frequency converter.

From the pumps, the flow is driven through the hot heat exchanger, where it can be cooled to a controlled temperature with a flow provided by a chiller unit. This flow can now either be driven through a flow meter or, bypassing this meter, it can run directly to four solenoid valves that control towards which regenerator set the fluid flows at any one time. From the control valves, the flow is diverted and passed through regulation valves meant to minimize the flow imbalances between regenerator parallel couples, due to the differences in the flow's resistance of unequal fluid circuits working in parallel, when the hot blow takes place—i.e., from the bottom to the top of the AMR block in this

[1] The maximum speed of the motors attached to the pumps is 1370 rpm.

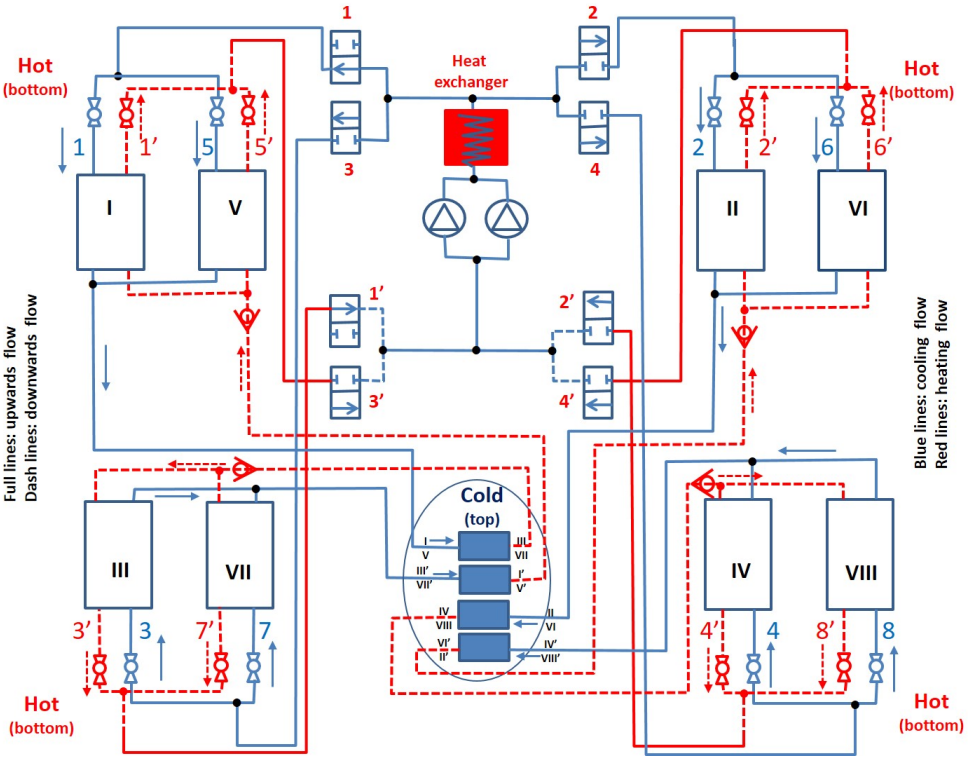

Figure 6.4: Fluid circuit´s concept design scheme of the prototype. To this circuit, additional elements had to be added in order to complete a functional system, including flow adjustment valves, check, drainage and bleed valves, pressure and flow sensors, filters, a chiller to control the hot spot's temperature and a reservoir tank.

refrigerator. After passing through a parallel AMR couple, the fluid flows to the cold spot of the cooler to return through another parallel couple of AMRs situated at 90° (cold blow), exiting from the bottom towards another set of regulation valves that minimize the imbalance of the returning flows from the AMRs. From this point, the flows are driven through 400 µm strainers and then towards the solenoid valves that control the returning flows to the pumping units. The pumping units are protected with a 10 µm filtering unit.

A bypass system is used between the hot spot and the electrical valves, right after the flow meter, going directly to the reservoir tank. This bypass is used to eliminate air bubbles from the circuit after filling it with the HTF. The tank returns the flow to the pumping system's suction side. Additional bypasses have been implemented to measure independently the flow through the different circuits operating in the refrigerator, diverting those flows to one of the two magnetic-inductive flow meters available.

The flow switching of the fluid in the different circuits and directions is activated with high speed solenoid valves, with an optical activation linked to the angular position of the magnet. The distribution of fluid flow in the regenerator channels allows approximating the desired Brayton cycles. Alternating the activation and deactivation of the AMR channels improves the heat transfer between MCM and fluid with resting steps within each cycle period. Fast solenoid magnetic valves drive and distribute the fluid through the circuit. The rotating magnet gives a high mechanical frequency, which is multiplied by eight in cooling cycles due to the channel distribution.

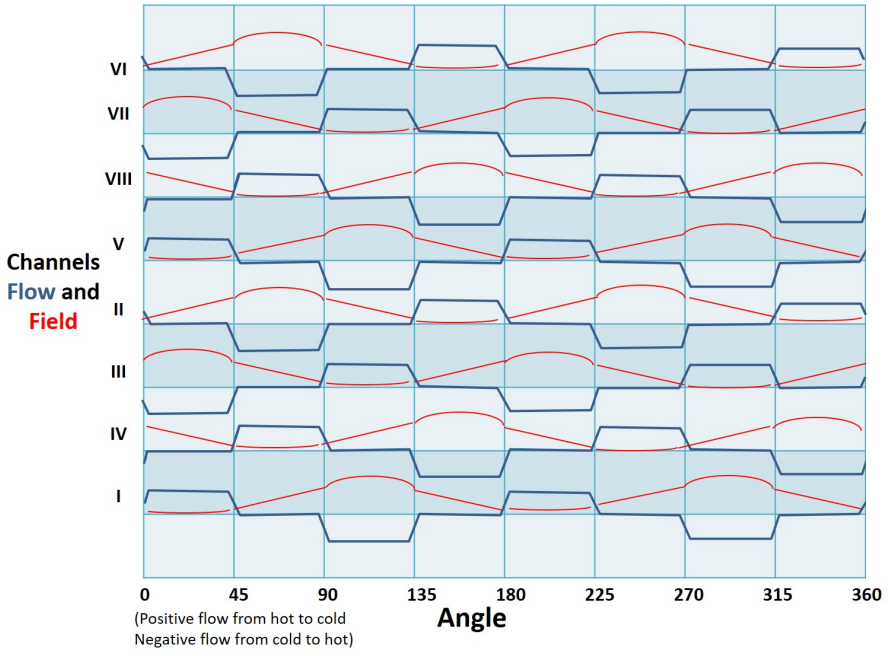

Figure 6.5: Flow activation and magnetization of the eight regenerators. The regenerators are numbered in Roman figures as in figure 6.4. The fluid flow is shown in blue lines while the red lines represent the evolution of the field with respect to each AMR. It can be observed how two AMRs are working in parallel and two in antiparallel at any one time,

6.2.1 Knowing how much you push

Rotary vane pumps, although they are positive displacement machines and provide fluid packages while rotating, are meant to continuously push discrete fluid volumes through the pump's outlet. These packages of fluid increase the pressure of the circuit and force the fluid flow. As a result, the movement of the fluid through the packed beds is pressure-to-load driven (i.e. pressure against flow resistance driven), rather than single packet pushed volume driven like in the case of systems using pistons. This working condition makes a very important difference, because assuring the volume that flows through the packed bed in every working regime turns out to be, by far, more complicated. The first problem is that the same pump working at a specific speed, is meant to supply pressure to different regenerators that can be formed with a variable number of sections[2] filled with somewhat spherical particles. This means that an ideal condition is that all the cavities of the section have a common porosity figure, and that this figure is as closely matched as possible in the rest of the sections used to form the AMR block. Under these conditions, an average porosity value can be used with some confidence to find the void volume of each section and, thus, that of every AMR (which in this case can all be held as having the same porosity). If the void volume value is under control, pressure-to-load driven flow behaves alike with every AMR and the volume of fluid that runs through any AMR can be known with a high certainty.

The volume of fluid that flows through an AMR depends on the speed at which the pump pushes the fluid packets and the flow resistance of the AMR (which is the main hydraulic load by far). The speed of the pumps is set with the manual rotating knob of a frequency converter. This knob regulates the frequency of the pump's motor power supply and has no automatic feedback control and raises the need to manually check the flow meter and correct the frequency until the right value is achieved.

A further issue comes into play when setting the speed of the pump to push a specific fraction of the void volume of each AMR (which we now assume of equal porosity).This issue regards the revolving speed of the magnet which is what marks the valves' open time window and, as a result, the volume of fluid pushed through the AMR. As a fact, every time that the rotating speed of the

[2] All regenerators in any specific assembly have the same length, but this length can be changed when setting up another regenerator block.

magnet changes, if the volume pushed through the regenerator has to remain constant, the setpoint of the pump's frequency converter has to be readjusted to change the speed of the pump and, consequently, the pressure of the system.

To put some order and facilitate the work of setting the machine in the desired work regime, some preliminary experimental work had to be done. For example, knowing the equivalence of flow and pressure of the cooler as a function of the set-point of the frequency converter and the load to pump $p(\mathcal{Q})$ relationship, is of great help. Also, knowing the fluid flow needed to push a certain fraction of void volume in the regenerator at different speeds of the magnet is also important. So, tests were made to characterize the fluid system, in order to be able to make testing the machine a bit easier. The only problem with this is that the characterization is valid as long as the porosity figure of the regenerators is established with certainty and reliability, and as long as the regenerator is not replaced. A wrong porosity value leads to non valid characterizations and a change of regenerator alters the porosity and the hydraulic load of the AMRs. Of course, the reliability of the graphs obtained depends also on the quality of the flow, frequency and pressure measurements used. Graphs obtained in the characterization of the hydraulic system are presented in figures 6.6, 6.7 and 6.8.

Apart from the phase between magnetic field and fluid flow, which is established by moving a screw from one hole to another from the set drilled every 2.5°, the only parameters needed to set the machine's working condition are the flow provided by the pumps and the revolving speed of the magnet; however, the difficulty lies in determining the combination of speeds of magnet and pump to obtain a flow that matches the desired AMR void volume fraction to be pushed through the AMR.

The graphs shown in figures 6.6, 6.7 and 6.8 are of much help to set the machine in a desired working condition; however, since the fluid flow is set manually and the pump's speed setpoint control is analogic, there is still a need to manually check and adjust as close as possible. The rotating speed of the magnet can be set digitally by means of the software provided by its drive's manufacturer (Infranor). The software permits to write down an rpm setpoint and the control unit performs the regulation loop to maintain the correct speed of the magnet´s drive.

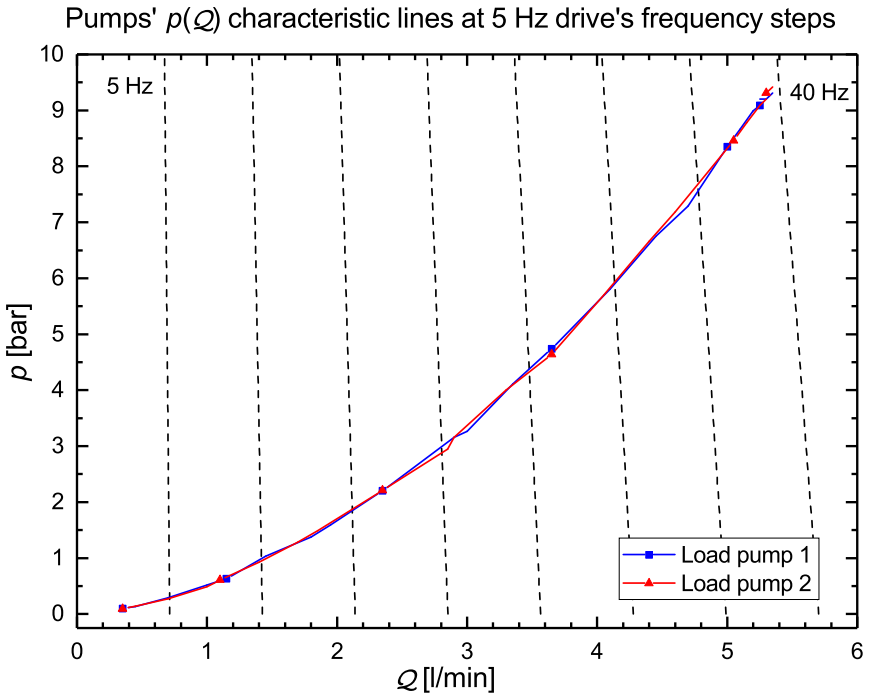

Figure 6.6: The operation point of the cooler can be determined with this graph that superimposes the load curve of the circuit, over the characteristic graph of a pump (dashed lines which mark 5Hz increments in the frequency converter). The refrigerator had a 43% porosity single gadolinium bed installed.

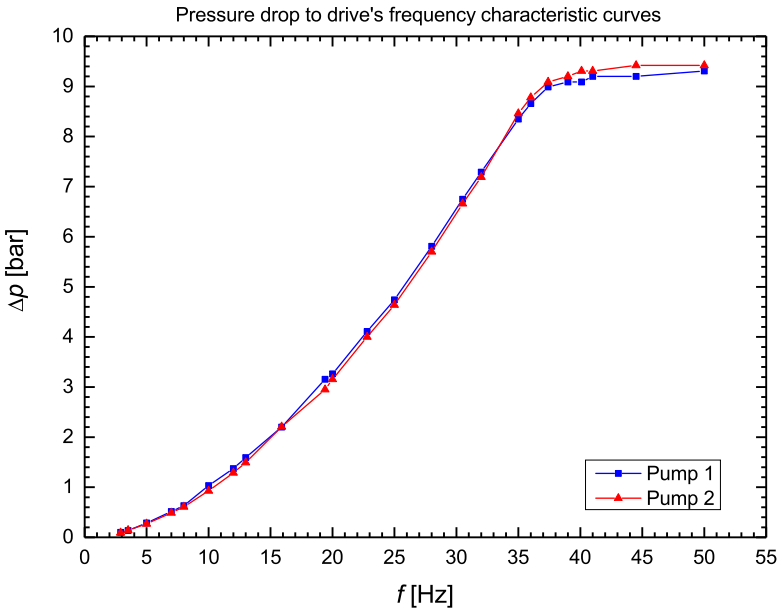

(a) Graph showing the pressure difference induced in the system. The curve starts with the typical parabolic shape provoked by hydraulic loads.

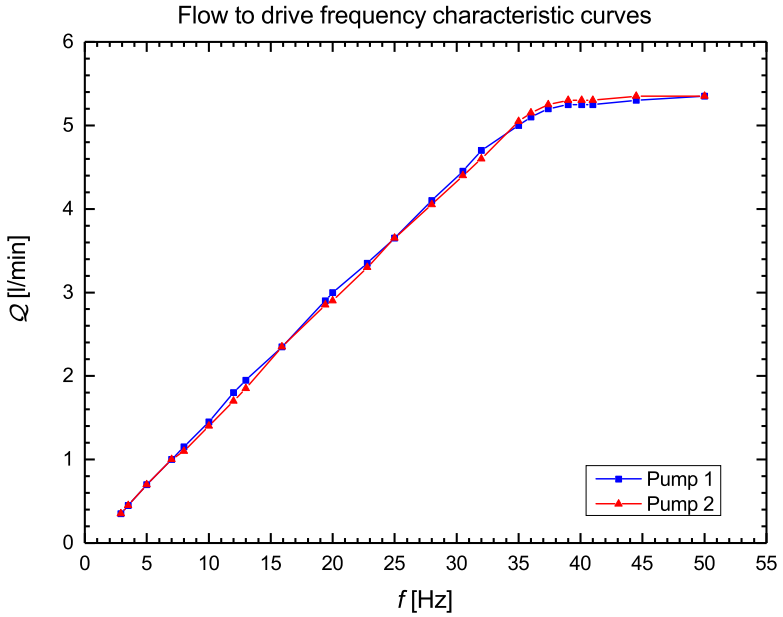

(b) Graph showing the volumetric flow of the system. The flow shows a linear dependence with the frequency, with a slope $\sim 0.14\,\mathrm{l\,min^{-1}\,Hz^{-1}}$.

Figure 6.7: Graphs resulting from the characterization of the hydraulic system of the prototype at different frequency setpoints of both pumps of the prototype while operating independently. The graphs were obtained with a single section AMR filled with gadolinium particles and its average porosity was estimated to be 43%. The asymptotes in the high pressure and high flow areas of the graphs are due to the action of the relief valves.

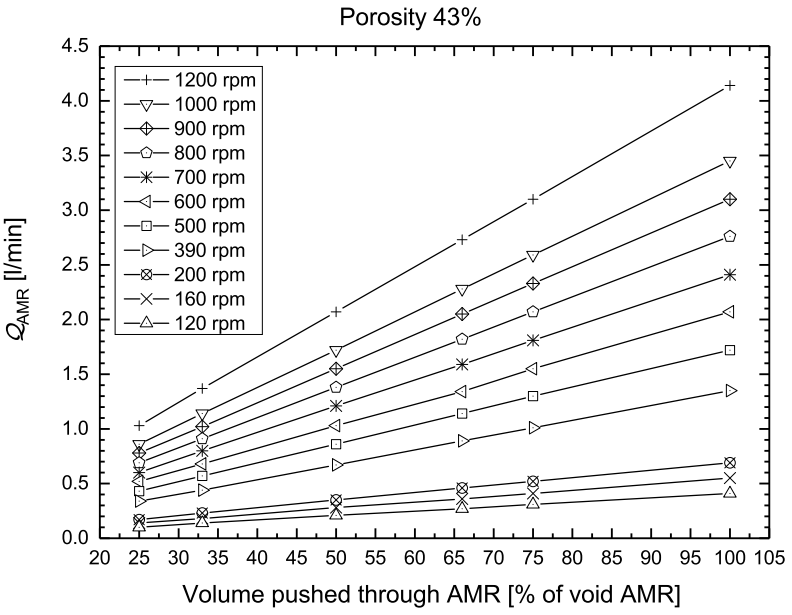

Figure 6.8: This chart was constructed to find the volumetric flow needed in order to set a certain pushed volume fraction of void AMR for different speeds of the magnet´s drive. This chart was made for a 43% porosity single gadolinium bed installed. The existing gap from 200 to 390 rpm is due to the vibration problems that appear in the machine when trying to operate the cooler at those speeds, which have been avoided for the sake of safety.

6.3 Cold spot design

Many prototypes reported use a very small cold spot. Often just a temperature sensor. This prototype goes a step further. On the one hand, the cold spot design includes physical separation of the four fluid channels that come out of the regenerator to cool the cold spot and return to the AMR block. There is only a thermal contact between the fluid channels, but no mixture of flows among them. On the other hand, the cold spot has some mass, which means that it has some thermal inertia, poses a small initial heat load[3], and a bigger thermal contact with the environment, likely to produce noticeable losses.

[3]In reality, the whole machine structure in thermal contact with the HTF or the MCM and any other thermal loss regarding a poor insulation can be considered as a heat load.

Three different designs were made for the cold spot (see figures 6.9, 6.10 and 6.11. This was done because the initial design finally showed an unsolvable channel communication problem during assembly and had to be discarded. Finding a manufacturer for the second design was initially not possible, which triggered the third design. The second design was simple, but the small and long drills in it were difficult to mechanize.

The first version was ordered with some modifications introduced upon the suggestions of the supplier, in order to facilitate the manufacturing process with copper[4], which resulted in many small parts to be soldered and later proved to be a bad solution regarding the assembly process.

The third version was designed as a backup. Fortunately, when the construction of the third was going to start, a manufacturer for the second version was found. This was the best solution since the second version was designed in one single piece from a small block of aluminum through which, four groups of small conduits were drilled from side to side. Both ends of the groups of conduits were provided with threads, in order to screw in fittings suitable for docking the tubes of the four circuits that run through the aluminum block. All three designs were provided with a housing for the insertion of an electrical resistor (heater) that, connected to a programmable power supply, can provide adjustable thermal loads for testing purposes.

The final version installed in the prototype (figure 6.9), has an hexagonal pattern of 19 holes of 1.8 mm of diameter, inscribed in a circle just a bit smaller than the female connection thread of the end. The pattern has a length of 30 mm and adding the threads for the fittings at both ends, the total length of the block is 56 mm. A heating resistor housing is drilled in the center point of one of the faces where the tubes are connected, and a small hole is provided at the opposite face for two purposes: first, to allow pushing with a pin to extract the resistor and second, to introduce a Pt100 sensor to measure the temperature of the cold spot.

[4]Copper machining is problematic, since it tends to produce a continuous plastic chip that affects the surface quality of the machined parts.

(a) Inner structure of the subchannels.

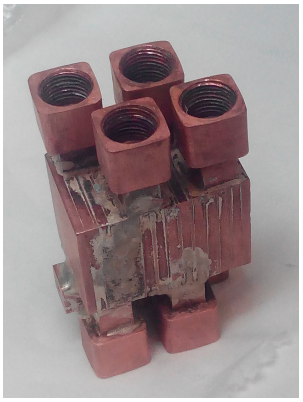

(b) Fully assembled version one cold spot.

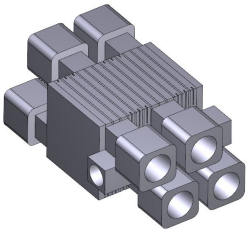

(c) Drawing of fully assembled cold spot.

Figure 6.9: Cold spot version one. Several parts were mechanized in copper to be assembled with silver soldering. The design had to be discarded due to watertightness problems provoked by the succesive heating of the soldering process during assembly.

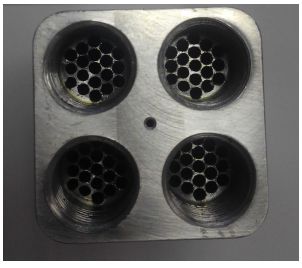

(a) Structure of the small conduits in each circuit.

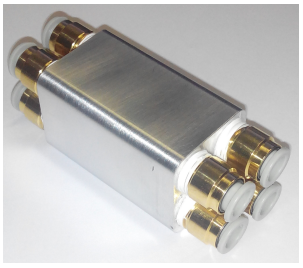

(b) Fully mounted version two cold spot.

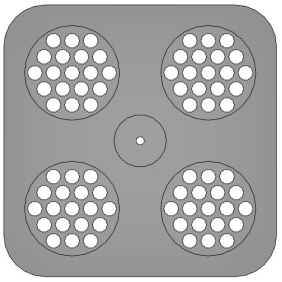

(c) Drawing front detail of the channels and resistor housing.

Figure 6.10: Cold spot version two. Mechanized in one block. This is the cold spot finally used in the magnetic refrigerator.

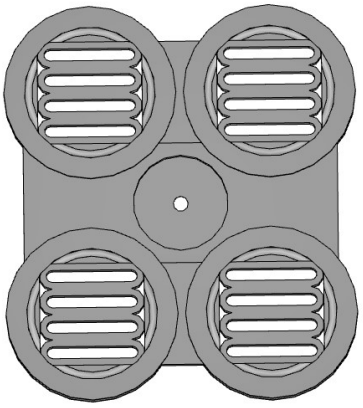

(a) Drawing of the structure of the subchannels and heater housing. Note that some open areas are covered in the soldering process.

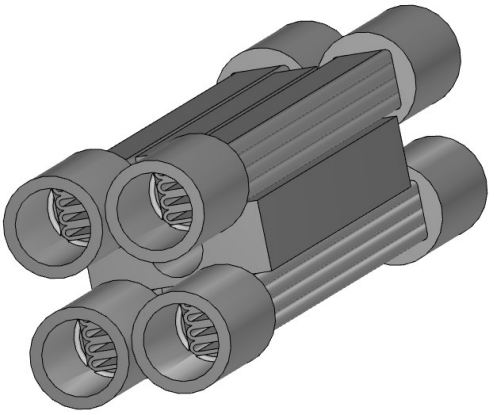

(b) Drawing of fully assembled version three cold spot.

Figure 6.11: Cold spot version three. Several simple to mechanize parts made in copper are to be assembled with silver soldering. In this case, the HTF conduits are made with calendered copper tubes which are then stacked to complete the size of the circuits' tubes.

Chapter 7

Data acquisition

The Data Acquisition System (DAQ) comprises several sensors, a signal emitter, an electronic temperature acquisition system, a scanner, digital a multimeter and a dedicated PC with Labview that retrieves the measurements. Some of the retrieved values are graphically represented on screen, and all are logged in one or more computer files that can be later used for data analysis. The signals managed by the DAQ system are presented in table 7.2. Data are kept as raw as possible in the data logging programs in order to save computing time and retrieve as many data points as possible.

7.1 Thermocouple DAQ

There was a special interest in our group to measure temperatures as fast as possible with the objective of getting a precise graphical reproduction of the thermodynamic cycle within the AMRs. This forced me to put speed on top of the thermocouple reading demands and was the main reason to use homemade thermocouples as explained in section 4.6. High speed reading of the thermocouples is problematic since, apart from the inherent error of the thermocouple itself, the faster you read, the higher the typical accuracy error and the noise you get from the DAQ electronic board. Also, the specifications

of the DAQ board about the scanning speed are to be taken with care, because manufacturers very often specify the speed of the muxtiplexing system of the board—i.e., the figure given by the manufacturer has to be divided into the number of channels to be read. Besides, the maximum scan speed is not a synonym of the maximum throughput of the measurements. The scan speed selected and the number of input channels determine the maximum throughput of the measurements. As a result, for the DAQ board used in this magnetic cooler (OMB-DAQ-2416 from Omega[1]), the maximum throughput rate in Hz is given by

$$\text{Maximum throughput} = \frac{1}{\sum_{1}^{n}\left(\frac{1}{\text{Data rate}} + 640 \times 10^{-6}\right)}, \tag{7.1}$$

where the data rate is selected from the values available for the DAQ board in Hz and n is the number of thermocouples to read. Reducing the data rate, increases the averaging of the samples, and noise drops correspondingly.

Thermocouples can pick up noise from environment and it is advisable to select a data rate based on the primary noise frequency. Hence, it is a common choice in countries with a 50 Hz power supply to select a data rate of that frequency or a sub-multiple. It was found after some tests that the primary source of noise came from the solenoid valves and after building a Faraday box around them, using aluminum foil, the noise dropped considerably (see figure 7.1).

A compromise had to be reached between speed, noise, throughput and number of thermocouples to be read, to obtain fast, low noise measurements. After many tests it was decided that a 100 Hz would be a good compromise, leaving the maximum throughput when reading the 16 thermocouple channels, using equation (7.1), in about 5.87 Hz. Whenever a more realistic graph of the thermal evolution within a regenerator is desired, a special setup of the software can be made to measure a limited number of thermocouples and, if necessary, at a higher sampling rate[2].

[1] This board can read up to 16 thermocouples in differential mode.

[2] The maximum selectable sampling rate for this DAQ electronic board is 3750 scans per second.

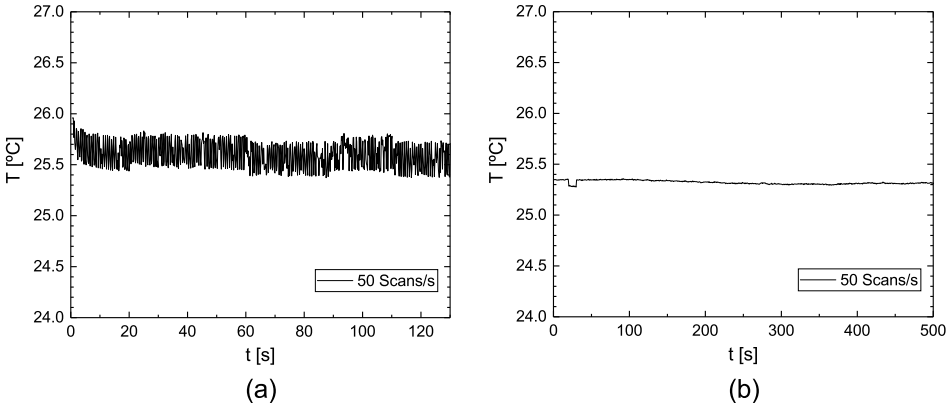

Figure 7.1: Comparison of temperature readings at the same sampling rate, before (a) and after (b) noise reduction measures were taken.

7.2 Other measurements

Not all data logged with the Labview programs come from thermocouples. The temperature of the cold spot of the machine is measured using a Pt100 plugged to a 4-20 mA transmitter. Also, two pressure gauges and two flow meters send their measurements to the computer. These measurements are transformed into voltage signals which are passed through a scanner and then, a multimeter. This multimeter sends the readings to the computer using an IEEE-488 (GPIB) connection, to which the scanner is also plugged in. Hence, using the GPIB, the Labview program can control the scanner channel selected and the working parameters and readings of the multimeter. Thinking about the timing of the measurement cycle, it had to be considered that scanner channel switching and multimeter magnitude reading changes introduce delays and they should be kept to a minimum. In order to improve the data acquisition speed of the Labview program, it is desirable that the multimeter measures only one physical magnitude (either current or voltage). Transitory periods due to switching in current loops and precision issues make the measurement of voltage the proper option.

Fluid flow, pressure and cold spot´s Pt100 values are read using the scanner-multimeter combination. In order to transform the current loop signals into voltage signals, a set of resistors is introduced in the circuit. For this purpose, an electronic board with resistors was prepared. The resistors were measured

with a four-point procedure in order to have more precision at the time of programming the conversion factors for the different measurements (see 7.1).

Table 7.1: Values measured of the resistors used to transform the 4-20 mA loop signals into voltage signals. R_{Pt100} is a resistor with a low temperature drift.

Resistor	R [Ω]
R_{P1}	215.5825
R_{P2}	218.4985
R_{Pt100}	123.7365

A Pt100 RTD is placed in the cold spot in order to log the temperature of its metallic block. Since the signal that is obtained is a voltage signal and it has to be taken all the way to the scanner and the multimeter, a specific two wire 4-20 mA transducer (LKM 103) is used to make the signal as interference safe as possible and transmit it to the current-to-voltage resistor board located in the electrical cabinet of the machine. From the cabinet, shielded cable was used to avoid the introduction of noise in the signals. The two wire Pt100 has a circular cross-section and 2.18 mm in diameter (Honeywell HEL-705-T-0-12-00). The size and shape if this sensor allows inserting it in the end drain hole of the cold spot's heater housing without direct contact with the resistor.

Two pressure sensors are installed in the prototype to measure its value at different points. The sensors are two high output pressure transducers and transmitters, providing a 4-20 mA current output capable of being used in control and indicating loops without further amplification (GEMS 310-00-B-0016G-01-B-000). The measurement range of the pressure sensors is 0 to 16 bar. These sensors are connected to the fluid circuit in such a way that they can be used to measure either the global pressure drop of the fluid circuit, from the pumps' suction side to the pumps' outlet, or the pressure drop in one of the regenerators. This is changed manually operating ball valves inserted in the fluid circuit. The connection of the pressure gauges to the computer is done from the resistor board to the computer as described for the Pt100.

Two magnetic-inductive flow meters are used in the refrigerator and they are meant to be used to achieve flow compensation between couples of regenerators that work in parallel. Also, one of them can be used to measure the

global flow of the prototype. Both meters have a measuring range from 0.1 to 25 l min^{-1} with a resolution of 0.05 l min^{-1} and have analogue outputs of 4-20 mA and 0-10 V. Since the cable of these flow meters is shielded and the computer is close to the prototype, it was decided to use the voltage loop to transfer the measurements to the computer. Magnetic-inductive flow meters were selected with the mind set on avoiding mechanical problems present in other traditional flow measuring systems.

The above mentioned signals are transferred to a scanner in order to measure all the current signals with only one multimeter. The scanner (Keithley 705) has a switching rate of 100 channels per second (10 ms per channel) and it can be operated remotely using GPIB protocol. The scanner multiplexes the signals to a multimeter which reads the values provided by the different transducers associated with the different sensors. The multimeter (Keithley 196 System DMM) is software configurable via GPIB protocol.

A chiller (Solid State Cooling Systems Thermocube 10-200-2G-2-R2) is used to control the temperature of the hot spot of the refrigerator. This allows establishing a more controlled test condition. The chiller has an RS-232 communication port which allows the automatic control and reading its operational data. This equipment sends a temperature controlled liquid flow to a heat exchanger (Lytron LL520G12) that assures a good heat exchange with the prototype's fluid circuit on its hot side. The heat exchanger is connected as a counterflow exchanger to improve its efficiency and it is insulated in order to minimize the impact of ambient temperature in the tests' results, assuring a stable and controlled temperature at the exit of this hot spot. Also, a thermocouple is installed at the exit of the main flow from the exchanger, which constitutes in fact the hot spot.

7.3 Labview programs

As a result of the resistor values presented in table 7.1, the conversion equations for pressure and Pt100 readings can be obtained. For the 4-20 mA current loops, the measurements are obtained considering the current ramp

from the minimum to the maximum value and the equivalence of these points.

$$I = I_{min} + \frac{I_{max} - I_{min}}{p_{max} - p_{min}} \left(p - p_{min}\right), \tag{7.2}$$

were $I_{min}, I_{max}, p_{min}$ and p_{max} are the minimum and maximum current and pressure values of the equivalence. Considering that the range of the pressure sensors is 0 to 16 bar and the current loop has a range 4 to 20 mA, equation (7.2) turns out,

$$p = I - 4\,, \quad \text{and using Ohm's law,} \quad p = \frac{V}{R} - 4\,. \tag{7.3}$$

In the case of the Pt100, a temperature equivalent equation to 7.2 is

$$I = I_{min} + \frac{I_{max} - I_{min}}{T_{max} - T_{min}} \left(T - T_{min}\right), \tag{7.4}$$

and since the emitter of the Pt100 has a range of 0 °C to 200 °C, it is derived that

$$T = I\,\frac{10^5}{8} - 50\,, \quad \text{and using Ohm's law,} \quad T = V\,\frac{12500}{R} - 50\,. \tag{7.5}$$

Using equations 7.3 and 7.5 with the values of table 7.1, the relationships for the pressure and Pt100 variables (see table 7.2) are obtained as:

$$P1 = \frac{V_{p_1}}{215.5825} - 4 \tag{7.6}$$

$$P2 = \frac{V_{p_1}}{218.4985} - 4 \tag{7.7}$$

$$PT100 = V_{PT100}\,\frac{12500}{123.7365} - 50\,. \tag{7.8}$$

Minor corrections are finally added to the pressure measurements to take into account the manometric differences introduced in the measurements by the location in height of the pressure sensors, with respect to the point were the measurement is directed to.

In a similar manner, we can obtain the values of the variables from the measurements of the flow meters, but taking into account that the maximum

value of the measurement range can be programmed. The maximum value for this range is set to $14\,\mathrm{l\,min^{-1}}$ and the voltage values go from 0 to 10V obtaining hence the same equation for both flow meters,

$$Q_i = \frac{7}{5} V_i\,, \quad \text{with } i = 1, 2. \tag{7.9}$$

In this case, Q_i refers to the DAQ flow registered variable from flowmeter "i" (see table 7.2) and not to a generic flow, and hence, the font used here is not that of the variable for "flow" ($\mathcal{Q}$).

Equations (7.2) to (7.9) are used in Labview to obtain the readings of the sensors. Programs were made in Labview, not only to log data from the tests, but also as tools for the setup of the machine—e.g. flow balancing of parallel AMRs or flow and pressure monitoring.

The scheme of the data acquisition (DAQ) program has to take into account the limitations of the hardware and the software available to carry out this task. The desirable top working frequencies force to try to reach a compromise between the acquisition speed and the number of channels to log. Also, the speed and processor cores available will affect the performance of the data acquisition program.

Taking into account the speed limitations of the DAQ system and the number of channels to log and show on screen, an evaluation of the real need of the information available in each data channel and its acquisition frequency needed, has to be done. The values of the temperature at the cold and hot spots, which give in turn the value of the temperature span of the refrigerator, do not need to be checked at a high frequency, although their values are indispensable since they represent the main goal of the refrigerator, which is to obtain a temperature span. On the contrary, the temperature within the regenerator is only useful, but since it varies greatly with the different steps of the cycle, its variation depends much on the working frequency of the machine and, if a very precise picture of the temperature waves is desired, a very high logging frequency would be needed as the refrigerator's working frequency is increased. Also, it has to be taken into account, that the throughput rate of the DAQ board is lowered when a lower scanning frequency is set for any of the channels to be read.

The runtime of the program, and thus, the data logging process can be speeded up if the acquisition can be run in parallel, separating the acquisition of temperatures from the thermocouples from the other data acquisition tasks, for example. Hence, the two main acquisition tasks run in parallel—i.e., DAQ board and multimeter reading—trying to take advantage of the two cores pf the computer's processor.

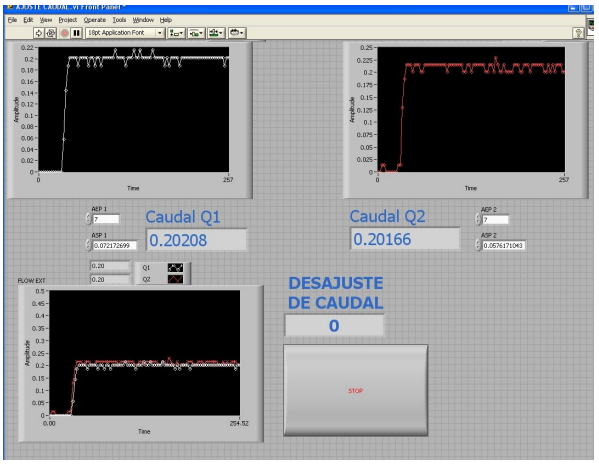

Figure 7.2: Screenshot of the flow balancing program. The program shows the evolution and reading of both flow meters, the evolution of both in a single graph, and the value of the difference between both flow values.

The main goal of the Labview programs is to build temperature logs with enough additional data about the recorded test as to determine the working conditions under which it was performed. Due to the temperature DAQ system considerations discussed in section 7.1, I decided to separate different specialized tasks in smaller programs that can be run separately when they are needed. This means that there is a small collection of Labview programs related to the prototype:

1. a flow balancing program focused only on the retrieval of the flow values of both meters (a screenshot can be seen in figure 7.2),
2. a chiller setup program which can be used to introduce the setpoint of the chiller and monitor the evolution of the temperature in its internal fluid tank,
3. a flow and pressure data logging program,
4. a temperature recording program, which is the core of the data logging used while testing.

The flow balancing program is very useful when adjusting the parallel flows of the regenerators. The chiller setup program is just useful to start the chiller and monitor the temperature until it has reached the setpoint. After this, it is not really necessary and memory and processor time can be freed. The flow and the pressure measurements are really not needed all the time. The values are to be repeated during the whole test and it is only necessary to run the program for a short period of time to record the values while the machine is working. What is really necessary is to use the temperature logging program during the whole test, if the full evolution of the recorded temperatures is to be logged to be post-processed.

The temperature logging program can actually be adjusted to record only a certain number of thermocouples; no need to record all 16 channels and, if no other values are considered necessary, one can select only the hot spot channel. Finally, the only measurement that comes from the multimeter is the temperature of the cold spot (variable $PT100$). The rest of the measurements come from the DAQ board and there is no need to spend time in changing the scanner channel, obtaining thus a faster program.

7.3.1 Stop criterion

Least squares linear fittings of arrays of the last temperature readings of cold and hot spots are performed. Since the throughput of the DAQ board that reads the thermocouples is fixed once selected, the size of these arrays are varied depending on the rotation speed of the magnet and the closest number of complete thermodynamic cycles of the AMR performed at a time specified by the user (typically 20 s). The actual values of both fittings, made when the arrays are full of data, are subtracted to obtain a span value, which is stored. From the last five fittings obtained, the maximum and minimum values of their slope are subtracted and compared with a user preset value (typically 0.05 °C), which constitutes the stop condition when the difference is smaller than this preset value.

Table 7.2: Working variables managed by the data acquisition system of the prototype.

LIST OF PROTOTYPE'S WORKING VARIABLES					
Name	Variable	Notes	Register	Signal	Protocol
Pressure 1	$P1$	Pumps' impeller side or AMR input pressure.	Automatic	4-20 mA	GPIB
Pressure 2	$P2$	Pumps' suction side or AMR output pressure.	Automatic	4-20 mA	GPIB
Pt100	$PT100$	Pt100 Emitter	Automatic	4-20 mA	GPIB
Thermocouple 1...16	$T1 \ldots T16$	Omega DAQ	Automatic	BUS	USB
Flow1	$Q1$	Pumps' frequency converters' potentiometers. Global or Channels' flow adjustment.	Automatic	4-20 mA	GPIB
Flow 2	$Q2$	Pumps' frequency converters' potentiometers. Channels' flow adjustment.	Automatic	4-20 mA	GPIB
Frequency	f	Speed of magnet's drive. Dedicated control software in PC.	Manual	-	-
Chiller Set Point	TSP	User given value sent to the chiller.	Manual	RS232	RS232
Chiller Temperature	TCH	To be read and displayed on screen.	Automatic	RS232	RS232
Phase Advance	PA	Mechanical setup.	Manual	-	-

Chapter 8

Results and discussion

The prototype was assembled according to the specifications, design and of course, using all the adjustments necessary to transform an idea "on paper" into a working machine, getting over limitations that came from different areas like supply chain, commercial availability of specific solutions, manpower, lab resources, financing and other unexpected problems. Pictures of the finished prototype are presented in figure 8.1.

After assembly, the machine was set in working condition, first by introducing the core of the magnet in the AMR block and then both, in the magnet. As a start, a regenerator block with only one section filled with Gadolinium spheres is assembled. Before, the AMR block was tested for pressure resistance by mounting a special fluid supply setup outside the machine. The core with the AMR block was introduced in a transparent container and tubing was provided to supply the AMRs with fluid flow from the machine. After checking that at maximum pressure there was no apparent leak, the setup was dismounted and the AMR block and the core were introduced in the magnet. The fluid circuits were balanced in flow, the pump's relief valves adjusted and graphs to help setting the right operation conditions were obtained, as described in section 6.2.1.

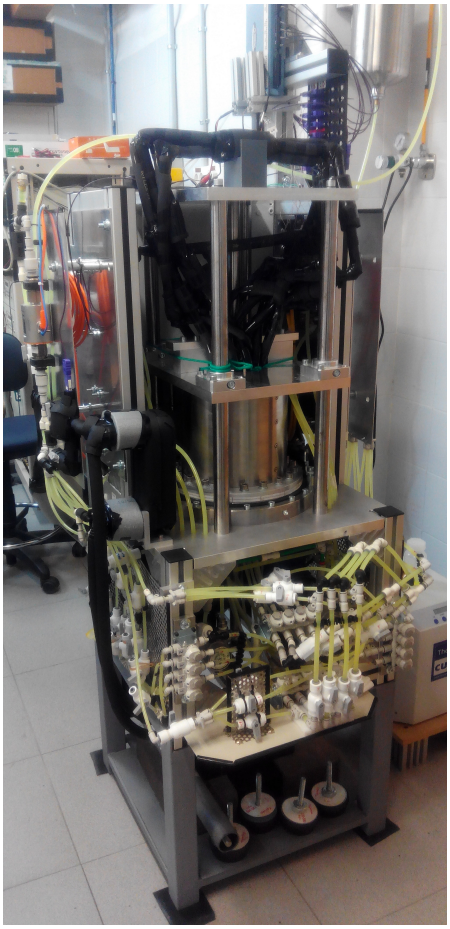

(a) Finished prototype with the first regenerator block (single Gd section). Note the black insulated tubes going to the cold spot at the top of the machine, on a gray PVC stand.

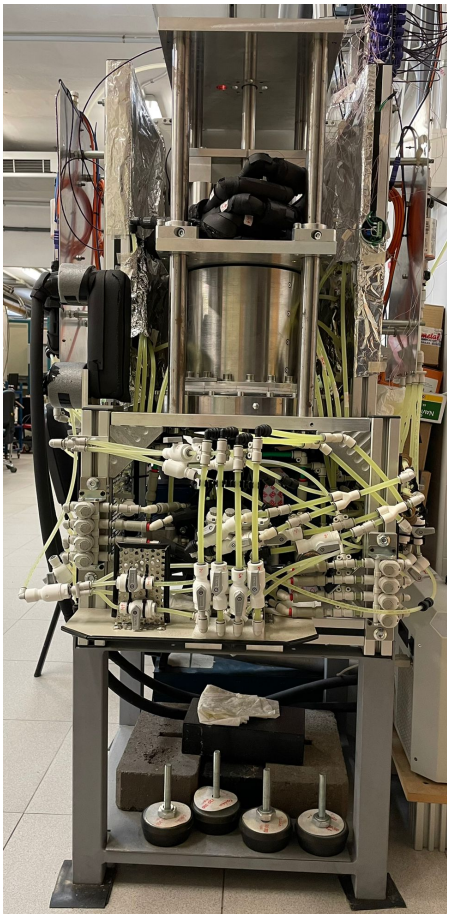

(b) Finished prototype with the second regenerator block (Three sections of Gd and GdEr alloys). Note that the black insulated tubes of the cold side are now much closer to the regenerator block.

Figure 8.1: Finished prototype with the two AMR assemblies tested. The cold side on figure 8.1b has a much shorter length and the tubes on this side were insulated all the way to the AMR block.

8.1 Testing procedure and tests

The procedure followed to find a point of maximum temperature span followed four steps:

1. pushing 50% of the AMRs void volume, a steady state at different revolving speeds of the magnet is searched,
2. at the speed at which the maximum temperature span is obtained, the pushed volume is varied, obtaining a new maximum span,
3. using the speed and pushed volume obtained, now the magnetic field to fluid flow phasing is varied from $-22.5°$ to $22.5°$ in steps of $5°$, obtaining a new maximum[1],
4. verify the condition of maximum by varying the revolving speed to both sides of it, to check whether it really is a maximum; repeat by changing the pushed volume to both sides of the maximum.

Following this procedure with the single layered Gd AMR block, the results shown in figures 8.2 8.3 and 8.4, are obtained. The spans are low and the results are not very repeatable. The maximum span obtained in this first tests is of only 2.1 °C with no load applied. This value was obtained at 700 rpm of the magnet's motor—i.e., ∼0.79 Hz mechanical frequency and ∼6.32 Hz of overall thermal frequency of the device[2]—a pushed volume of 100% of the AMR void volume and a phase of 20°. This means that the flow is applied to the AMR 20° later than the magnetic field, being the regenerator's central radial line very close to be aligned with the maximum field.

[1] Actually, a negative phase means that the fluid is pushed before the AMR is fully magnetized/demagnetized. As a result, it is of common sense expecting a bad performance with a negative phase.

[2] In reality, the eight regenerators work in couples and, therefore, it could be also considered that the machine's thermal frequency is of only four times the mechanical frequency, but performed by a double-sized regenerator.

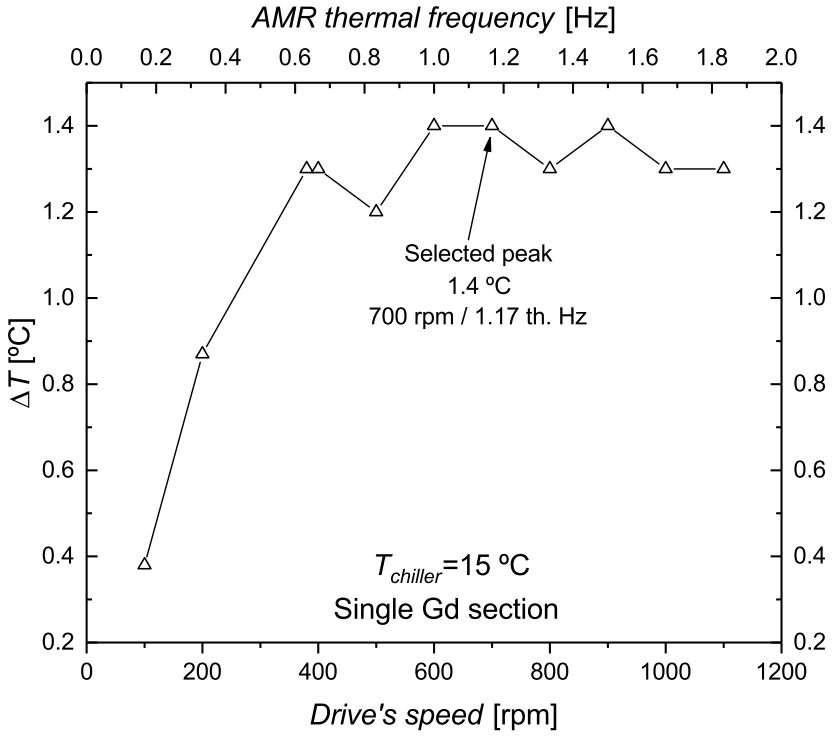

Figure 8.2: Optimization process of a one Gd section AMR. Results of rotating speed optimization. The AMR thermal frequency makes reference to the speed of the thermodynamic cycle in each AMR.

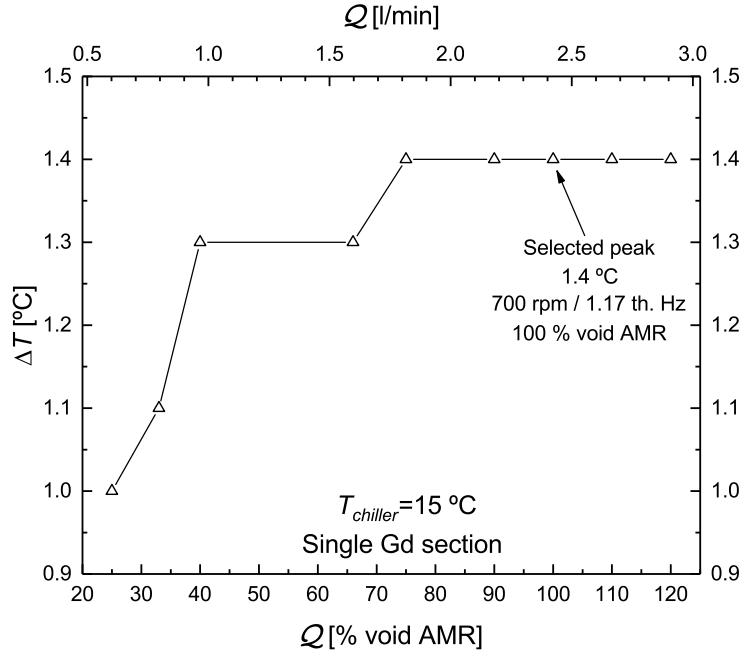

Figure 8.3: Optimization process of a one Gd section AMR. Results of flow optimization.

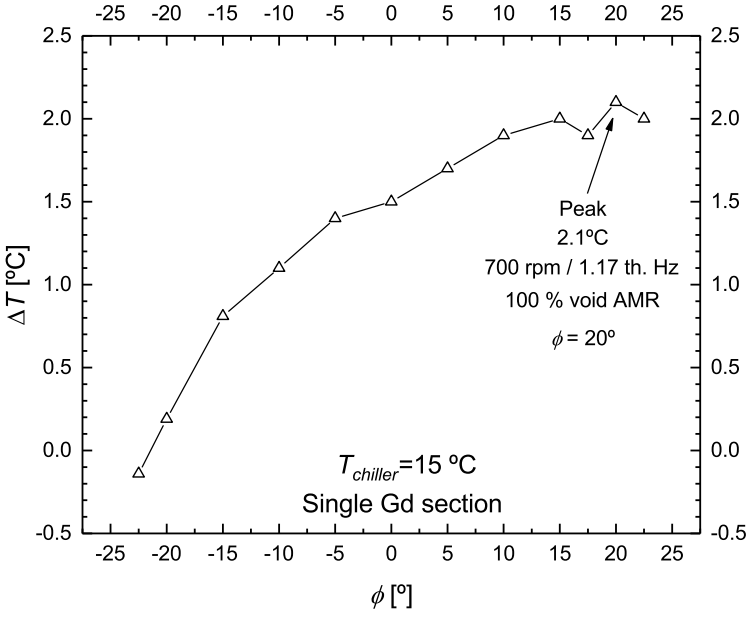

Figure 8.4: Optimization process of a one Gd section AMR. Results of field to flow phase optimization.

Many verifications were done trying to find the origin of this bad result and they are discussed in section 8.2. However, it all pointed out to an excess of losses due to thermal inputs from the machine itself and from the ambient.

With not enough time left to do much more due to the end of the project among other reasons, the regenerator block was changed for another one built with three sections of Gd and GdEr alloys. This gave the opportunity to insert new thermocouples and redo the cold side of the machine, making the piping shorter and improve the thermal insulation. This time, the average porosity of the AMRs was 42%, and new graphs had to be made as tools for the machine setup.

At the first start, without seeking an optimization, a span of 3.4 °C with no load applied was obtained (figure 8.5). This happened at 50 rpm of the magnet's motor—i.e., ∼0.04 Hz mechanical frequency and ∼0.67 Hz of overall thermal frequency of the device—a pushed volume of 35% of the AMR void volume and a phase of 0°. However, this result could not be replicated.

Only a few tests were conducted with the three section AMR block and no methodological optimization was performed. A temperature span of 3 °C with no load applied was obtained. This happened again at 50 rpm of the magnet's motor—i.e., ∼0.04 Hz mechanical frequency and ∼0.32 Hz of overall thermal frequency of the device a pushed volume of ∼33% of the AMR void volume and a phase of 0°. Due to the end of the project, the corona virus crisis and tight academic deadlines, no further works could be done with the prototype.

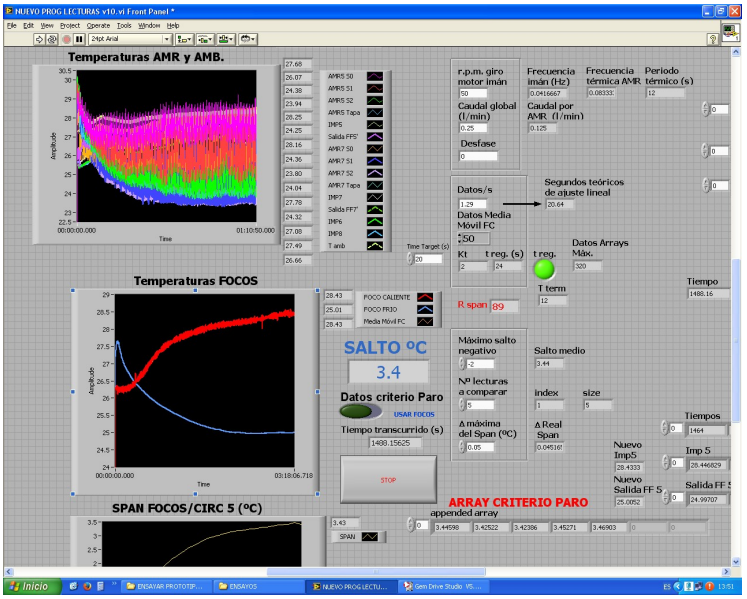

Figure 8.5: Screenshot of the test program with the best results obtained with the AMR block built with three sections of Gd ans GdEr alloys. Unfortunately, this result could not be replicated.

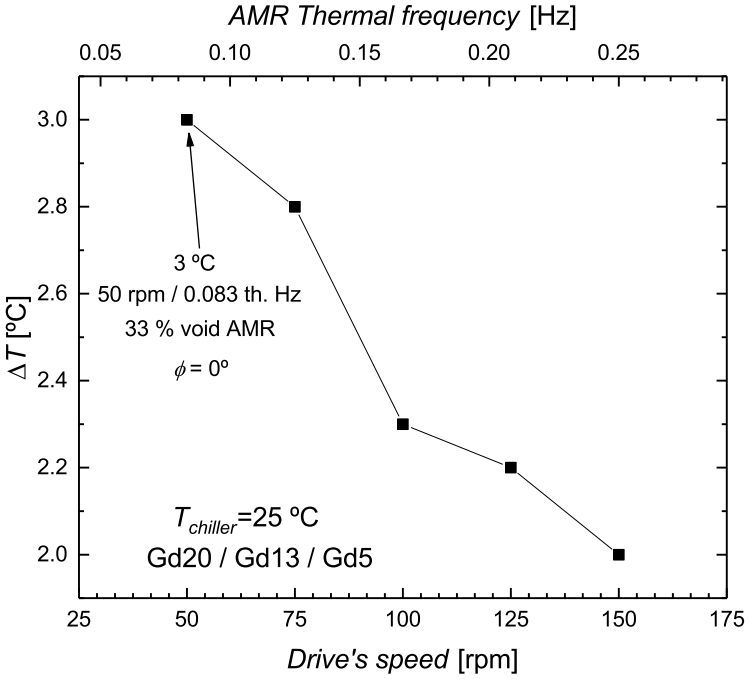

Figure 8.6: Test results corresponding to a speed sweep of a three section AMR filled with Gd20, Gd13 and Gd5 (see table 8.1). The pushed volume was fixed at 33% of void AMR and the phase was set to 0°.

8.2 Discussion

Several possible combined reasons could be the origin of the poor performance of the prototype. A discussion about possible them follows.

8.2.1 Magnetocaloric materials

Initially, it was foreseen the use of Gd and GdEr compounds, as well as $(LaFeMnSi)_{13}$-H alloys. Soon after reception, the materials were tested to verify their transition temperatures using a Differential Scanning Calorimeter (TA instruments Q2000).

The $(LaFeMnSi)_{13}$-H alloys supplied by Vacuumschmelze in spherical particles of 0.6 to 0.8 mm in diameter, were close to the ordered transition temperatures. Nevertheless, the supplier stated that the precision with which they could tune the alloys at that time had an error window of ± 2 K. Even having this in mind, some higher differences could be seen (see table 8.1). In these compounds the differences are below 4 °C and could be caused to the inherent error in the tuning process, added to the different experimental technique used in its determination.

Table 8.1: Differences between the T_C values of the ordered materials. None of them presents the T_C ordered.

Material Coded name	Ordered T_C [°C]	Received T_C [°C]	Composition
La2	2	-1.7	$LaFe_{11.23}Mn_{0.46}Si_{1.32}H_{1.65}$
La7	7	4.41	$LaFe_{11.26}Mn_{0.43}Si_{1.31}H_{1.65}$
La12	12	9.28	$LaFe_{11.29}Mn_{0.4}Si_{1.31}H_{1.65}$
La17	17	13.99	$LaFe_{11.29}Mn_{0.39}Si_{1.32}H_{1.65}$
La21	21	18.91	$LaFe_{11.32}Mn_{0.37}Si_{1.31}H_{1.65}$
La26	26	24.13	$LaFe_{11.32}Mn_{0.36}Si_{1.32}H_{1.65}$
Gd5	5	-2.81	$Gd_{0.915}Er_{0.085}$
Gd13	13	3.88	$Gd_{0.955}Er_{0.045}$
Gd20	20	9.75	Gd

The Gd and the Gd compounds, supplied in spherical particles of 0.6 to 0.84 mm in diameter by Baotou Research Institute of Rare Earths, showed a very important deviation from the ordered value. The DSC measurements are presented in figure 8.7. Magnetization tests were performed with these materials, using a Physical Properties Measurement System (PPMS) from Quantum Design Inc. from the Servicio General de Apoyo a la Investigación (SAI) of the University of Zaragoza, in order to confirm the important shifts observed in the Curie temperatures. The results confirmed these shifts. Trying to find the reason of this deviations, a fluorescence analysis performed also at the SAI, with a secuential fluorescence x-ray spectrometer (Thermoelectron ARL ADVANT?XP), showed no relevant signs of contamination. However, assuming that the tuning of the T_C in the GdEr alloys has the required stoichiometry, and taking into account that the "pure" Gd also presents a shift in the T_C, the only possibility left is assuming that there is some small amount of contamination that causes the shift[3]. It can be observed from literature that the T_C of Gd varies depending on the purity of the sample and the experimental technique used in its determination, [71], and this can surely be extrapolated to any MCM. In Gd, according to Dan'kov et al. [71], a sample with a 99.9 wt.% purity sees its T_C lowered, and its temperature range of the paramagnetic$\longleftrightarrow$ferromagnetic transition broadened. In these cases, the shift is too big to be due just to the different determination technique used.

Since the gadolinium based materials present such a high T_C shift, making them work in a non controlled temperature environment turns harder due to the different room temperatures which are usually sensibly higher than the actual T_C of the Gd spherical particles used.

Knowing the tendency of $(LaFeMnSi)_{13}$-H alloys to break when subjected to thermomagnetic cycling, the company Vacuumschmelze was contacted to transform the loose spherical beads into epoxy glued blocks. Due to the experience of the first regenerator assembled in the prototype, Vacuumschmelze was asked to do the transformation also with the gadolinium based materials. Although the company had previous experience in this procedure, the resulting blocks for which AMR sections were used as molds, turned out partially clogged with epoxy and, also, the glue was unstable, allowing the detachment of the particles. Under these circumstances, the blocks can not be used in the refrigeration prototype and the materials were useless. Fortunately, enough

[3]The other possibility is that the Chinese supplier sent a different batch by mistake. There was no chance to obtain a substitution in a reasonable time.

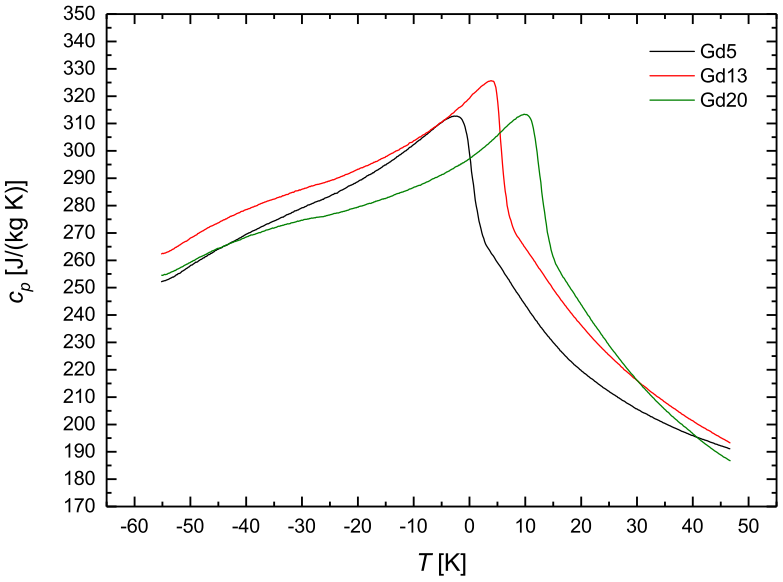

Figure 8.7: DSC measurements of Gd (Gd20) and GdEr (Gd13 and Gd5). The Gd20 sample corresponds to "pure" Gd has a T_C shift of $-10.25\,\mathrm{K}$. GdEr compounds are coded as Gd13 and Gd5 (the numbers correspond to the ordered T_C of each compound). Both show shifts of -9.12 and $-7.81\,\mathrm{K}$, respectively.

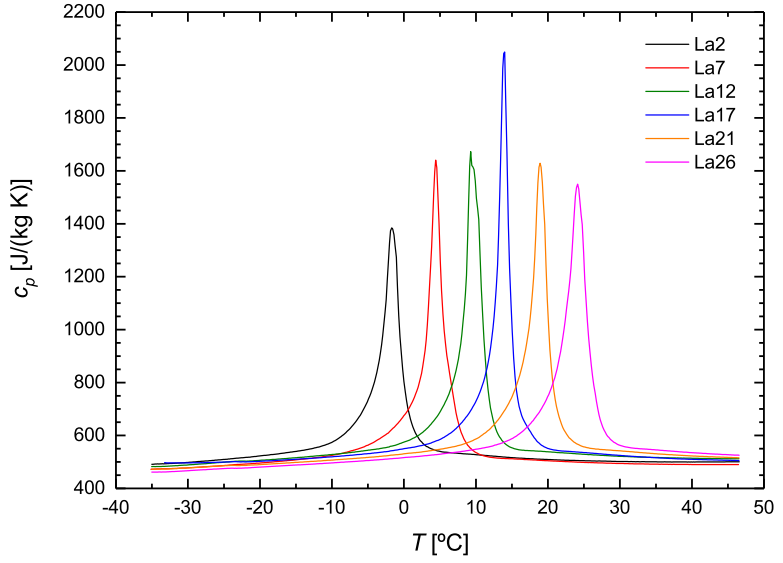

Figure 8.8: DSC measurements of $(LaFeMnSi)_{13}$-H alloys. The numbers of their codes correspond to the ordered T_C of each compound. All materials show a shift between 1.8 and 3.7 °C.

Gd and GdEr spherical particles were still available to fill some regenerator sections and, I was hence forced to use loose packed beds of Gd and GdEr.

Measurements of the temperature evolution on thermocouples situated in contact with the MCM where checked to find that they gave good values, compatible with the field change effect on the Gd spheres. Figure 8.9a shows the temperature change upon a slow field rotation without any fluid flow. The shape of the cyclic curve follows practically the shape of the field given by the magnet and shown in Figure 5.4, with the broad and flat low temperature section and a sharper high temperature side. When adding some fluid flow to the changing field, we can see in Figure 8.9b the cooling section of the cycles due to the cold blow and the heating part of the hot blow with an intermediate stable temperature. The corresponding amplitude of the temperature oscillation goes up to 2.2 K, which is about the span obtained from the cold and hot sinks, but the regenerators are unable to create a temperature gradient along the MCM.

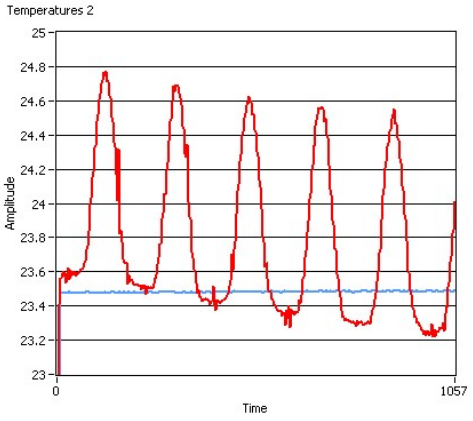

(a) Screenshot of the temperature evolution at one end of an AMR at low rotational speed, without fluid flow.

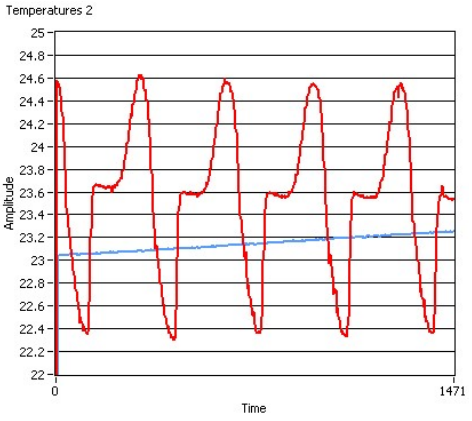

(b) Screenshot of the temperature evolution at one end of an AMR at low rotational speed, with fluid flow.

Figure 8.9: Temperature evolution of a thermocouple at the border of one of the regenerators under a low rotational frequency of the magnet. The blue lines correspond to the cold source temperature.

A more detailed analysis of the origin of the poor behavior of the system was not possible without having temperature sensors in different positions of the circuit. One possible reason is the heat losses through the long fluid pipes,

part of them uninsulated, due to the space limitations with the number of tubes going to the regenerator.

Also, according to Nielsen and Engelbrecht [65] the optimal thermal conductivity of the MCM applied in a parallel-plate AMR strongly depends on the length of the AMR and the operating frequency. They showed that in the case of a long AMR of 200 mm the thermal conductivity should be as high as possible (up to $30\,\mathrm{W\,m^{-1}\,K^{-1}}$, independent of the operating frequency, up to 4 Hz, and the temperature span, while in the case of a shorter AMR of 50 mm the optimal thermal conductivity depends on the operating frequency (the higher the frequency the higher the optimal thermal conductivity will be: around 10 mm at 1 Hz and 30 mm at 4 Hz). For example, Gd and its alloys with Er have a typical thermal conductivity around $10\,\mathrm{W\,m^{-1}\,K^{-1}}$ and La–Fe–Co–Si alloys, around $8\,\mathrm{W\,m^{-1}\,K^{-1}}$. Nevertheless, these values are inherent to the MCM and cannot be changed easily in a controlled manner, out of their natural variation with temperature.

8.2.2 Thermal insulation

As explained in section 4.4, the AMR block is constructed in POM, which has a typical thermal conductivity of $0.31\,\mathrm{W\,m^{-1}\,K^{-1}}$, which is a low value in comparison with most alternative materials; however, due to the greed of volume for the MMC, the walls have a thickness of only 2 mm. The vertical ribs designed in the center hole of the AMR sections as contact lines with the core, provide only an 0.5 mm air gap between the inner wall of the AMR section and the core of the magnet (figures 8.10 and 4.6). Moreover, this air gap is not closed at the ends, allowing for air flow and, hence, a small convection to appear. Unfortunately, there is no room in the magnet's gaps to use any additional thermal insulation covering the regenerators block.

Also, the holes for the threaded rods that run the AMR block longitudinally to close it, have a similar wall thickness in the direction to the nearby AMR cavities. The transmission of heat to or from the rods to the nearby regenerators, although small, could also happen and the heat could be transported by the nonmagnetic stainless steel thermal highway longitudinally ($k \approx 16\,\mathrm{W\,m^{-1}\,K^{-1}}$ at 20 °C), to or from their anchors on the magnet's core.

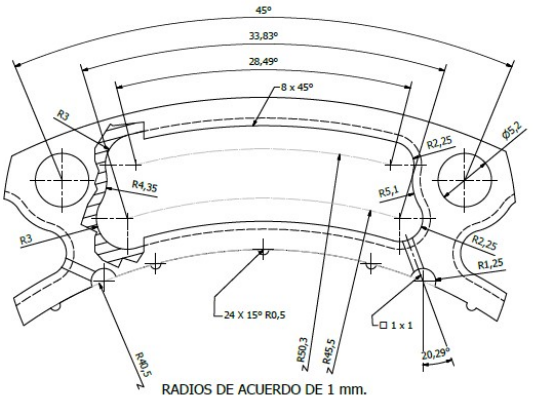

Figure 8.10: Detail of the design of the sections of the AMR. The two small circles on both sides of the image are the allocate the threaded rod that holds the regenerator block together and constitute the azimutal limit of the AMR. The outer and inner walls of the ring are 2 mm thick and the small semicircles of a radius of 0.5 mm are the ribs that make contact with the core of the magnet. The two holes on each side of the regenerator cavity are where the threaded rods that close the AMR block are housed in.

The LLDPE tubes have a thermal conductivity of $0.3\,\mathrm{W\,m^{-1}\,K^{-1}}$, according to the manufacturer, which is a similar value to that of POM. This means that, since the thickness of the walls is half of that of the AMR, the heat loses basically double under equivalent conditions. As a result, it is very important to use additional insulation to avoid excessive heat transfer from ambient (usually hotter) and the inner walls of the device's elements; specially on the cold side, but also in certain areas of the hot side, to avoid that the heat from other heat generating components of the prototype, warm up the HTF within the tubes that run from the hot side to the AMR. For this purpose, insulating sleeves and adhesive tape have been used in tubing and other elements like the cold and hot spots (temperature controlled with a chiller), to lower the heat transfer with the ambient. The sleeves were 6 mm thick, with a heat transfer coefficient of $0.035\,\mathrm{W\,m^{-1}\,K^{-1}}$ at 20 °C and the tape was 3 mm thick, with a heat transfer coefficient of $0.04\,\mathrm{W\,m^{-1}\,K^{-1}}$ at 40 °C. It must be clarified that the tubes cannot be insulated in the length that lies between the bottom duralumin plate and the top extreme of the magnet due to the lack of space and the risk of being worn out by the rotating magnet, or even trapped in the pinion and slewing ring responsible for the magnet's spin. This is specially relevant in the case of short regenerator blocks, like the first one assembled, consisting of a single section, leaving a longer length of unprotected tubes carrying HTF at different temperatures in an antiparallel flow and very close to each other.

The ball valves in the fluid circuit are made of fiber glass reinforced (FGR) polypropylene, with a typical thermal conductivity of $0.2\,\mathrm{W\,m^{-1}\,K^{-1}}$. These valves are covered with insulating material as far as it is possible without compromising their handling, whenever insulation is required.

In the second regenerator block installed, the cold side of the setup was refurbished, increasing the insulation and cutting down the average length of the tubing around 50%, and the length of unprotected tubes inside the gap of the magnet was also shorter, due to the increased length of the regenerator block (30 mm longer). However, there was no change that could be possibly made about the insulation of the AMR block, which presented this time an increased surface with 2 mm thick walls, being prone to increased losses due to heat transfer with ambient and with the magnet's core.

Thermal relaxation

While the first regenerator block was installed, thermal relaxation tests were performed. For this, a cold fluid is circulated in the refrigerator until a constant temperature near 16 °C is reached, while the room temperature is about 24 °C. At this moment, the fluid flow is stopped and the temperatures of the device and the room are recorded. Figure 8.11 shows a scheme of a tube with insulation, used as basis for relaxation calculations.

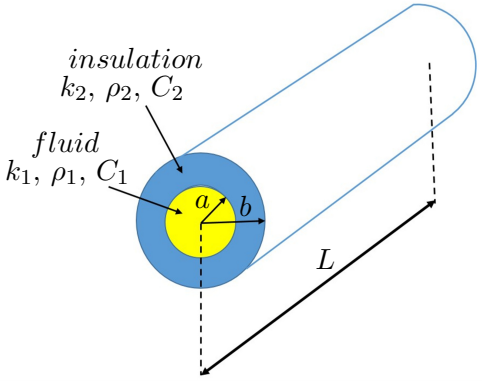

Figure 8.11: Scheme of a tube with insulation. Model used for relaxation calculations.

A simple model is used for the calculations. The thermal transfer between a tube with liquid at rest and the atmosphere is composed of four parts:

1. pure conduction in the liquid,
2. pure conduction through the tube wall,
3. pure conduction to the insulator,
4. conduction/convection from the external insulator wall to the atmosphere.

Let us first consider the radial conduction in a cylinder of internal radius a, and external radius b. The insulation diffusivity is much smaller than that of the fluid during the transient after the fluid stops, as a quasi-steady state is reached, but with the fluid temperature (almost uniform) varying slowly with time.

During the quasi-steady state time the insulator temperature T(r) follows the Laplace equation:

$$\nabla^2 T(r) = 0 \Rightarrow \frac{1}{r}\frac{\partial}{\partial r}\left(r\,\frac{\partial T}{\partial r}\right) = 0 \Rightarrow T(r) = A\ln r + B\,, \tag{8.1}$$

were A and B are two constants.

The boundary conditions are: $T(a) = T_a = T(fluid)$ and $T(b) = T_b$; hence, we can transform equation (8.1) into:

$$T(r) = T_b + \frac{T_b - T_a}{\ln(b/a)}\,\ln\frac{r}{b}\,. \tag{8.2}$$

Under these conditions, the heat flux density is radial and is:

$$J_Q(r) = -k_2\nabla T(r) = k_2\,\frac{T_a - T_b}{\ln(b/a)}\,\frac{1}{r}\,, \tag{8.3}$$

and the total radial heat flow through the tube is then

$$\frac{\mathrm{d}Q}{\mathrm{d}t} = J_Q(r)\,2\,\pi\,r,\; L = 2\,\pi\,L\,k_2\,\frac{T_a - T_b}{\ln(b/a)}\,. \tag{8.4}$$

As a result, the pure conduction follows rigorously the law:

$$\frac{\mathrm{d}Q}{\mathrm{d}t} = L\,h'(T_a - T_b)\ ,\ \text{being:}\ h' = \frac{2\,\pi\,k_2}{\ln\,(b/a)}\,. \tag{8.5}$$

Secondly, let us consider the conduction/convection through the air, which is a complex fluid dynamics problem but, for the sake of simplicity, we can assume that the same law is followed (equation (8.5)) becoming:

$$\frac{\mathrm{d}Q}{\mathrm{d}t} = L\,h_{air}(T_b - T_{room})\,, \tag{8.6}$$

where T_{room} is the temperature at a long distance from the tube. Actually, h_{air} depends on the difference temperature with some power and the heat flow is proportional to $(T_a - T_b)^{\alpha}$, with $\alpha > 1$.

In the experimental case the conduction/convection is very slow and the temperature of the liquid is very approximately uniform and equal to T_a. After a short transient time, a quasi-steady state is reached in which the fluid temperature varies slowly.

The heat flow relates to the fluid temperature with

$$\frac{\mathrm{d}Q}{\mathrm{d}t} = -\pi\,a^2 L\,\rho_1\,C_1\,\frac{\mathrm{d}T_a}{\mathrm{d}t} = L\,h'(T_a - T_b) = L\,h_{air}(T_b - T_{room}) = L\,h\,(T_a - T_{room})\,, \tag{8.7}$$

being ρ and C_1 the density in $\mathrm{kg\,m^{-3}}$ and the heat capacity in $\mathrm{J\,kg^{-1}\,K^{-1}}$ of the liquid, respectively. equation (8.7) determines the temperature of the tube-air interphase

$$T_b = \frac{h' T_a + h_{air} T_{room}}{h' + h_{air}} \tag{8.8}$$

and the coefficient,

$$h = \frac{h'\,h_{air}}{h' + h_{air}}\,. \tag{8.9}$$

Considering $h_{air} \cong \textit{constant}$, in the quasi-steady state, the evolution of the temperature of the liquid is given by

$$\ln \frac{T_a(t) - T_{room}}{T_a(0) - T_{room}} = -\,\frac{h}{a^2 \rho_1 C_1}\,t = -\,\frac{1}{t} \tag{8.10}$$

and after a short transient time, the temperature of the fluid relaxes exponentially with a characteristic time:

$$\tau = \frac{a^2 \rho_1 C_1}{h} \,. \tag{8.11}$$

As a result, an experimental measurement of the relaxation time gives the transfer coefficient.

Following this model, the temperature evolution at different spots can be used to obtain the transfer coefficients at relevant areas of the prototype. The results obtained are summarized in table 8.2, showing that, of the different spots tested, the main source of losses lays in the regenerator block. The relaxation tests were performed with a sationary magnet and, hence, the coefficients of the regenerators can be expected to increase when the magnet is rotating and generating air flow within the gap of the magnet.

Table 8.2: Summary of the relaxation test results. The relaxation times and thermal transfer coefficients in different areas of the prototype are given. The higher values of the regenerators' thermal transfer coefficients point out that there resides the main area of losses. Since the relaxation tests were performed with a sationary magnet, the coefficients of the regenerators can be expected to increase when the magnet is rotating and generating air flow within the gap of the magnet.

Location	τ [s]	h [$\mathrm{W\,m^{-1}\,K^{-1}}$]
Insulated tube near output of cold spot	823	0.021
Insulated tube near input of cold spot	830	0.020
Cold spot	4286	0.0356
Naked tube	592	0.029
Regenerator 1	5263	0.17
Regenerator 2	5047	0.18

The prototype lacks of a thermally controlled enclosure, and this affects the repeatability of the tests, since the room temperature was also uncontrolled and its variations clearly affected the results. Such an enclosure was not provided for the prototype for several main reasons:

- need of access to all sides of the prototype during setup and operation,
- availability of space in the lab,

- increased complexity,
- cost.

8.2.3 Solenoid valves

Different kinds of high speed dosing systems were considered. The main difficulty was finding a system comprising high speed operation with small and reliable time response delays, and a high flow capacity while withstanding pressures up to 16 bar. Finally, it was decided to use Bürkert 0255/053188 solenoid valves (see figure 8.12). This decision was fundamentally based on the response times claimed by the manufacturer which are presented in table 8.3. Operating the refrigerator at maximum rotating frequency of the magnet (1 Hz) would mean aperture times of 125 ms apertures every 500 ms. Even being high speed valves, an analysis of the best and worst case timings from table 8.3 results in aperture timing deviations ranging from 0 to to 16%. As a result, comparable flow imbalances can be expected and, as was explained in section 4.2, according to simulations, a 5% flow imbalance degrades the cooling power by 37%, and up to 100% with a 12% flow imbalance. Also, it has to be understood that even a zero timing deviation as described above has consequences, since there is a minimum opening time delay, a shift in the phase between the magnetic field and the flow within the AMR is introduced.

It has to be taken into account that there are two solenoid valves controlling the cold blow (e.g. 1 and 1' in Figure 6.4) and two other valves controlling the hot blow (e.g. 3 and 3'). Differences in these activation times on the different solenoid valves can have an important effect in the cooling efficiency. The prototype's flow meters cannot take measurements fast enough to detect the real flow in such short periods. Another source of possible flow difference, depending of the direction, is the existence of check valves in non-symmetrical positions for each direction when the sigle Gd section AMR block was used, which can give differences in their opening times. In fact, the different amplitude of the positive and negative temperature oscillations shown in Figure 8.9b give an indication of this lack of flow symmetry in the measured regenerator. Substitution of each pair of solenoid valves 1-3, 2-4, 1'-3', and 2'-4' by a single two-way valve would be advisable to have the same fluid flow in the cold and hot blows, but appropriate two-way valves with the needed short activation times could not be found.

The selected valves can work at the required maximum pressure with a reasonable flow coefficient K_v[4] of $0.5\,\mathrm{m^3\,h^{-1}}$. The K_v coefficient accounts for the pressure drop produced by the valve in the fluid circuit following the equation:

$$\Delta p = S_g(\frac{\mathcal{Q}}{K_v})^2\,, \tag{8.12}$$

where S_g is the specific gravity of the fluid (one in the case of water), Δp the pressure drop and $\mathcal{Q}$ is the volumetric flow through the valve.

Table 8.3: Response times of the selected solenoid valves (Bürkert 0255/053188). Note that in the case of solenoid valves, these timings are given in windows, which introduces an uncertainty in the real value and, therefore in the real flow time (and HTF volume). This makes impossible assuring that the fluid volumes pushed through the regenerators are always exactly the same, allowing the possibility of a flow imbalance that cannot be fully avoided.

Opening [ms]	Closing [ms]
10 to 20	20 to 30

This dynamic flow imbalance produces a de facto flow-magnetization phase change that cannot be controlled with a simple shift of the angular position of the magnet with respect to the regenerator. Only a small part of this dynamic imbalance can be compensated if the valves manufacturer's data are trusted. There is a minimum delay in the opening response time of 10 ms. A shift of an angle equivalent to a 10 ms advance in the opening signal to the valve would cancel this delay and, hence, the fluid-field phase change. However, this shift in the angle is not as easy to achieve as it seems, since the angular shift needed changes with the speed of the magnet and, unless the magnetic cooler has a fixed field rotation speed, the system to achieve this shift should provide a continuous regulation if the speed is varied continuously, or a matching discrete system if the speed is set in discrete values, rather than the discrete system available in this prototype for a continuously variable speed.

It has to be emphasized, that time delay duration is not as much of a problem as having a fixed and reliable value of it, since the time delay can be

[4] K_v is defined as the water flow at 16 °C, measured in $\mathrm{m^3\,h^{-1}}$, that results in a pressure drop through the valve of 1 bar. This means that at a flow of $10\,\mathrm{l\,min^{-1}}$, a pressure drop of about 1.44 bar through the valve can be expected if the fluid is water.

compensated via software, for example, but this cannot be properly done if the timing of this delay is variable and a risky approximation has to be used.

Table 8.4: Power consumption of the solenoid valves as reported by manufacturer. Since no information about the power factor of the inrush coil is available, no straight conversion can be made to obtain its power consumption in Watts.

Power consumption	
Inrush	Hold (hot coil)
[VA]	[VA/W]
35 to 40	16/10

An additional hindrance provoked by the solenoid valves is parasitic heating of the fluid. Apart from the heating produced by the activation current of the valve (the inrush peak consumption can go up to 25 W) the valve maintains a constant 10 W consumption while the valve is held open. A simple approximation to the heat load added can be done considering that two valves are acting at any one time, but only one is upstream of the regenerator and the cold side of the cooler. Using the average opening delay ($\bar{t}_{open}$ =15 ms) as equivalent to the inrush period of the valve, and using the shortest opening time required, which happens at maximum rotating speed of the magnet (worst case, 125 ms), it follows that the heat load from the valves (Q_{valves}) can be approximated as

$$Q_{valves} \simeq \frac{P_{in}\bar{t}_{open} + P_{hold}t_{hold}}{\bar{t}_{open} + t_{hold}} \approx 11.6W\,, \tag{8.13}$$

where P_{in} and P_{hold} are the powers consumed during inrush and hold periods, respectively, and t_{hold} is the holding time required to complete the opening time of the valve. Therefore, it can be considered that there is a constant maximum power load in the refrigerator due to the operation of the valves of 11.6 W, with a realistic minimum of 10 W. This load heats the HTF after it has passed through the hot sink and this heating is pointed out by thermocouple readings located between the solenoid valves and the regenerator, which show readings of higher temperature than that of the hot sink.

These AC solenoid valves turned out to be quite noisy. If a DC version could be used, the noise would probably decrease, but unfortunately, they are slower. DC coils are quieter, show less wear on the plunger or core tube and demonstrate a high holding force whereas an AC coil, displays faster switching

times, but can hum, requiring a shading ring and facing a risk of burn-out if the plunger is ever jammed.

Figure 8.12: Solenoid valve during installation.

8.2.4 Concluding remaks

As it has been discussed along this chapter, there are different sources of losses affecting the performance of the prototype. The heat transfer through the thin walls of the regenerator is the main loss source found, and to this, we can add the losses in long tubes (some not insulated), the losses in the old spot, and the heat buildup coming from the solenoid valves. Also, the shift in the MCE of the MCMs used, towards sensibly lower temperatures, further encourages a low performance of the materials at room temperature, which may find very hard to build the temperature ramp in the AMR if any other losses like those already mentioned are added.

Additional losses seem to come from the asymmetry in the cold and hot fluid blows through the regenerator. It can be affected by the positions of the check valves and this was partly corrected adding four new check valves. But there is another possible influence due to small differences in the activation times of the solenoid valves which give different fluid blows depending on the direction. The problem can be in the range of the milliseconds of opening times and cannot be checked or corrected easily.

Other problematic issues that can also affect the results lie on the low precision of the setup system of the prototype. The selection and assurance of the fluid flow with an analogic turning knob, the low precision of the flow readings, added to the nature of the pumping system and the variability of the conditions of the regenerator filling (i.e. uniform porosity and full filling assurance of the regenerator cavities), turn the device into a really hard system to control. A symptom is the fact that flow measurements under unchanged conditions obtained sometimes different values. The device can therefore be held as of unstable behavior.

The impossibility of ensuring a proper reaction timing of the solenoid valves, as well as the noise and power consumption, are not a good presentation card for this kind of solution in magnetic refrigerators aimed for household applications.

It is obvious from the scenario presented, that no indepth study of the

optimal performance of the prototype has finally been considered. The construction of the machine and the DAQ system, with all the problems suffered in supplies, the bad performance observed, the work done to find its sources and, finally, the covid-19 crisis turned impossible any further works in the prototype.

Part II

Solid State Magnetic Cooling

Presentation of Part II

One of the most evident handicaps of traditional magnetic cooling devices is their high dependence on the use of heat transfer fluids (HTF). Managing the heat transfers involved in these devices introduces a great deal of inefficiency sources, requiring the use of fluid pumping systems, turning the devices bulky, noisy and energy consuming, and transforming the prototyping process into a complex multidisciplinary task. Conventional heat transfer mechanisms are very limited by the heat transfer surface and HTF properties and the power density obtained in devices is thus rather low. Boosting the power density of magnetocaloric devices by orders of magnitude requires looking to other directions, getting out of the scope of the conventional AMR, which is fundamentally based on forced heat convection. The possibility of using magnetic cooling while avoiding most of the inconvenient problems that HTF management brings about, is well worth to be researched. While this does not necessarily mean being fully independent from HTF use, relegating it to the minimum is always an interesting option to be tested.

Different special heat transfer mechanisms have been proposed, and research in many of the proposals has been and is being carried out, however, to the best of my knowledge, very few of these systems have been translated to real prototypes. A good review about these special mechanisms can be found in the book of Kitanovski et al. [1]. One of the most interesting options is the introduction of thermal diodes, an idea first introduced by Kitanovski and Egolf in 2010 [17] in the domains of solid-state and of microfluidic thermal diodes. Most work regarding this idea has been focused on solid-state Peltier thermal diodes and, although some works show the great potential of this kind of systems [16, 18–20], the benefits one of such real devices remains controversial [21, 22].

In this part of the thesis, the simulation of single hybrid thermoelectric-magnetocaloric sandwiches is addressed, and their results are presented.

Chapter 9

What is the difference?

A very simple hybrid thermoelectric-magnetocaloric (TE-MC) system is analytically and numerically simulated using the working parameters of commercial Peltier cells and the properties of a material with a first-order magnetostructural phase transition, as $La(Fe,Si)_{13}H_{1.65}$. The results are compared with those corresponding to a pure TE system and a pure magnetocaloric (MC) one with ideal thermal diodes. At the same cooling power, the realistic hybrid system has higher efficiency than the pure Peltier method and similar to the pure MC with ideal diodes. An original master equation is introduced to deal with materials with a first-order transition.

As it has been explained in chapter 1, the Montreal (1987) and Kyoto(1997) protocols were designed to reduce the emission of gases depleting the ozone layer and the greenhouse effect, respectively. Consequently, alternative more efficient systems, and avoiding the use of such gases, have been researched. Among them the most relevant systems are those based on the thermoelectric (TE) or Peltier effect and those based on the magnetocaloric effect (MCE). The former is based on the fact that in type P and type N semiconductors the charge carriers, also heat carriers, move in opposite directions when a given electric current flows through them. A thermoelectric cell is formed by a couple of such semiconductors connected electrically in series and thermally in parallel. The heat flows from the central junction, the extreme contacts of both semiconductors. This is an extremely simple conception, since it has no

moving parts, it avoids the use of fluids, and can work on very small devices (e.g. electronic components) or in spacecrafts. Moreover, they can work also as thermal electric generators, when a hot source and a cold sink are available (e.g. TE generation for solar energy conversion [142]).

The weak point of the TE refrigerators is their low coefficient of performance (COP), defined as the ratio between the heat extracted from a cold source to the work made to do so, $COP = Q_c/W$. This is a consequence of three conflicting properties. A good TE material should have high Seebeck coefficient ϵ, high electrical conductivity σ, and low thermal conductivity k (a TE couple with materials with $\sigma \to \infty$ and $k = 0$ has the maximum or Carnot's COP). But a high Seebeck coefficient needs high effective mass and low carriers density (Mott's formula), what implies low conductivity. On the other hand high σ implies usually high k also (Wiedemann-Franz law). But this law is not necessarily obeyed by semiconductors and in the practical TE materials, the phonon heat conduction is more important than the electron or hole conduction. A way to reduce the phonon contribution to k is the use of semiconductors of high molar mass, like Bi_2Te_3. A practical index to characterize the efficiency of a TE material is the figure of merit $ZT = \sigma\epsilon^2/k$. The maximum COP of a TE refrigerator working between a cold heat source at temperature T_{cold} and a hot heat sink at T_{hot} is

$$COP_{max} = \frac{T_{cold}}{T_{hot} - T_{cold}} \frac{\sqrt{1+ZT} - T_{hot}/T_{cold}}{\sqrt{1+ZT}+1} \tag{9.1}$$

where $ZT \to \infty$ corresponds to the Carnot efficiency. Today, the maximum $ZT \simeq 3$ for Bi-doped PbSeTe/PbTe [**?**], but commercial TE materials usually have $ZT \simeq 1$. This means as an example, that near room temperature (RT), at $T_{hot} = 300$ K, and for a temperature interval of 20 K (i.e. $T_{cold} = 280$ K), COP_{max} cannot be higher than 31% of the Carnot efficiency with the most advanced TE materials, but with commercial Peltier cells $COP_{max} \simeq 14\%$ of Carnot, at most. For a revision of the TE materials, references [143] and [144] are suggested.

On the other hand, since the discovery of the so-called "giant magnetocaloric effect" [59] the MC refrigeration has become a real alternative to traditional systems. From the thermodynamic point of view, this method is highly efficient (even 60% of Carnot [23]), but there are also several difficulties with these systems. First, the limited temperature span achieved with magnetocaloric materials (MCMs). This is solved via regeneration, which is essentially a battery or a continuum of systems working in series, one deliver-

ing heat to the next one at higher temperature. Second, a way of transferring heat from the cold heat source to the MCM, and from this one to the hot heat sink. Some thermal diodes or switches have been proposed [145], but in most prototypes the heat transfer is made with a fluid consisting of water and anti-corrosion additives. This fluid involves new problems: slow thermal contact (and then low frequency and low cooling power), pressure to move the fluid, viscous dissipation, leakages, and so on. A revision of materials and systems for magnetocaloric refrigeration can be seen in the book by Tishin and Spichkin [23]. For a recent review, among many, reference [118] is suggested.

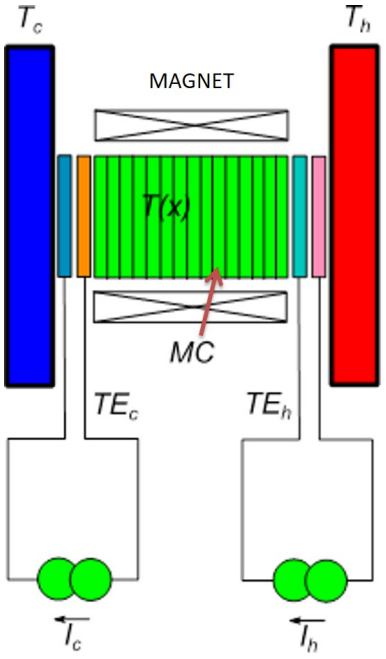

Figure 9.1: A "sandwich" formed by a magnetocaloric material and two thermoelectric or Peltier cells between a cold heat source at temperature T_{cold} and a hot heat sink at T_{hot}.

A possibility of combining the strengths of TE and MC methods is a hybrid system. The Peltier method has low efficiency for high temperature span $\Delta T = T_{hot} - T_{cold}$, but it increases strongly for low or even negative ΔT. This procedure was proposed by Tomc et al. [16] and Egolf et al. [146]. As sketched in figure 9.1, a TE-MC-TE sandwich is placed between a cold heat source at temperature T_{cold} and a hot heat sink at T_{hot}. An alternate magnetic field is applied to the MCM. When the magnetic field is on, the MCM is at its highest temperature, near to T_{hot}. Then the right side TE cell is activated and pumps

heat from the MCM to the hot sink. When the magnetic field is off the MCM is cold, eventually near or colder than T_{cold}. The left side TE cell is activated transferring heat from the cold source to the MCM. In 2017, de Vries and van der Meer [22] reported a simulation of a similar system, concluding that the cooling capacity is similar to that of Peltier cells alone, but this system uses a fluid as regenerator.

Some preliminary results of the simulation of a single sandwich were presented at the THERMAG VII conference [147], concluding that the TE-MC hybrid system is an interesting device, but there were many variables to be optimized. Reference [148] simulates a battery of sandwiches, designed to reach a higher temperature span. This work deals mainly with the properties of the TE materials, but it was found that the properties and dimensions of the MCM should be correlated with the TE cells to get an optimum performance in COP or in cooling power.

Chapter 10

Simulation of a hybrid system

In this work, the properties of a TE cell are simplified, characterizing with only three parameters: the effective Seebeck coefficient ϵ, the electrical resistance R_0, and the thermal conductance, C. The simulations take into account the properties of modern commercial TE cells.

For the MCM, the experimental properties of several materials are tested, including doped La(Fe,Si)$_{13}$ alloys, $Gd_{1-x}Er_x$, and theoretical MCM obeying the mean field theory. This point is interesting because the experimental errors in the heat capacity at constant magnetic field, C_B could lead to an unphysical behavior in a simulation. Also a master equation is derived for a MCM with a FOPT. The output of the simulation program (COP, magnetocaloric and thermoelectric works, extracted and released heats, etc.) is monitored for continuous variation of many working parameters. To simplify the case, only one element is studied, considering that a battery is essentially a superposition of sandwiches.

10.1 Model

10.1.1 Thermoelectric cells

The properties of most commercial Peltier modules can be modeled with only three parameters, the effective Seebeck coefficient, ϵ, the electric resistance R_0 and the thermal conductance C[1]. These are effective values for a module consisting of many thermoelectric elements. The modelization has been tested against the reported curves of extracted heat $\dot{Q}_c$ against temperature difference ΔT for several electric current supplies I, and against the voltage V against ΔT for different I values. In particular, the data of cells from TE Technology Inc. (Traverse City, Michigan USA) and from RMT Ltd. (Moscow, Russia) have been tested against the model.

From first principles of irreversible Thermodynamics [149], assuming a constant Seebeck coefficient, the voltage in a Peltier cell connected between two heat sources/sinks at temperatures T_1 and T_2 is,

$$V = \epsilon(T_2 - T_1) + R_0 I \,. \tag{10.1}$$

The extracted heat power from the side 1 (let us assume cold side), which is released to side 2 ("hot side") and the work supplied by the cell are given by

$$\dot{Q}_1 = T_1 \epsilon I + C(T_1 - T_2) - \frac{1}{2} R_0 I^2 \tag{10.2}$$

$$\dot{Q}_2 = T_2 \epsilon I + C(T_1 - T_2) + \frac{1}{2} R_0 I^2 \tag{10.3}$$

$$\dot{W} = \dot{Q}_2 - \dot{Q}_1 = (T_2 - T_1)\epsilon I + R_0 I^2 = VI \,. \tag{10.4}$$

From these equations, it follows that if $R_0 \to 0$ and $C \to 0$, then the Carnot efficiency for a Peltier Cell is $COP = \dot{Q}_1/\dot{W} \simeq (T_2 - T_1)/T_1$. Also, a very important detail is that for small temperature differences, the conduction term can be neglected and it results,

$$COP(\Delta T \to 0) \simeq \frac{T_1 - 0.5 R_0 I/\epsilon}{T_2 - T_1 + R_0 I/\epsilon} \,. \tag{10.5}$$

[1] In this part of the thesis, C will stand for thermal conductance, instead of heat capacity.

The fixed parameters for the cell 1ML07-050-15AN from RMT Ltd. at a temperature of T_1 =298 K, are presented in table 10.1. For $T_2 - T_1 = 0$, $COP = 4.47\text{A}/I - 1/2$, giving an enormous value for low current. For instance, for I =0.1 A, $COP = 44.2$. For a negative temperature difference $T_2 - T_1$ =−1 K, and I =0.1 A, $COP = 52$. However, for higher positive differences the performance decays quickly and this cell hardly can transfer heat to the hot side if $T_2 - T_1$ >8 K ($\dot{Q}_1 = 0$) with that same current. Nevertheless, it is able to stop heat leakage from the hot side to the cold side. A MCM (i.e. a LaFeSi alloy) can easily increase the temperature by $\Delta T_{MC} \simeq 4$ K upon application of a magnetic field, making heat transfer possible, and very efficiently for $T_2 - T_1 < \Delta T_{MC}$. Consequently, the statement of reference [22] that the hybrid system has the same performance as a TE alone can be valid for a particular but not very happy choice of parameters; however, this is not generalizable. Most probably, in the simulation of that reference the Peltier subsystem is much more powerful than the MC subsystem, exhausting its possibilities. Both subsystems should be adequately dimensioned.

Table 10.1: Fixed parameters of the cell 1ML07-050-15AN from RMT Ltd. The cell is a combination of many TE elemental couples.

ϵ $[mVK^{-1}]$	C $[mWK^{-1}]$	R_0 $[\Omega]$
15	55	1

10.1.2 Simple model for a sandwich with FOPT MCM

Let us assume that there is a heat reservoir, representing the MCM, that we assume of infinite heat capacity and temperature, T, externally regulated by a magnetic field. An MCM with FOPT fulfills these conditions in phase coexistence. As a simple case, let us consider that T has a constant lower value T_1 for a time τ and a higher one T_2 for the same time, the period being 2τ. Let us assume that we apply some electrical current to the high and low temperature cells I_h, I_c in the following way

$$0 < t < \tau : \; T = T_1; \; I_h = I_{1h}, \; I_c = I_{1c} \tag{10.6}$$

$$\tau < t < 2\tau : \; T = T_2; \; I_h = I_{2h}, \; I_c = I_{2c} \tag{10.7}$$

with constant values of I_{1c}, I_{2c}, I_{1h}, and I_{2h}. I_{2c} is intended to prevent heat leakage to the cold source at T_{cold}, through the TE cell on the left side (cold TE cell), when the MCM is at its highest temperature T_2. During this time the cold TE cell plays the role of a thermal diode, but it needs a small electric work supply to achieve this purpose. I_{1c} is intense enough to extract heat from the cold source when the MC is at its lower temperature T_1, and the transfer can be made efficiently. Similarly, in the hot TE cell, I_{1h} prevents heat leakage to the MC when it is at T_1 and I_{2h} transfers heat from the MCM, when it is at T_2, to the hot sink at T_{hot}. We assume also that the change between T_1 and T_2 takes a negligible time. In that interim, the magnetic subsystem performs an adiabatic process from T_1 to T_2 or vice versa. This assumption is ideal but not far from the real case. Equations, (10.2) to (10.4) give the instantaneous heat power extracted from the cold source ($\dot{Q}_c$), released to the intermediate system ($\dot{Q}_i$), extracted from the intermediate system by the hot TE cell ($\dot{Q}_f$), released to the hot source ($\dot{Q}_h$), and the work power made by each cell, $\dot{W}_c$ and $\dot{W}_h$, replacing the temperatures by those at the ends of each cell. The quantities have subscript 1 or 2, according to the temperature of the intermediate system, that is:

$$0 < t < \tau \qquad (T = T_1):$$

$$\left.\begin{aligned} \dot{Q}_{1c} &= T_{cold}\,\epsilon\,I_{1c} + C(T_{cold} - T_1) - \frac{1}{2}R_0\,I_{1c}^2 \\ \dot{Q}_{1h} &= T_{hot}\,\epsilon\,I_{1h} + C(T_1 - T_{hot}) + \frac{1}{2}R_0\,I_{1h}^2 \end{aligned}\right\} \tag{10.8}$$

$$\left.\begin{aligned} \dot{Q}_{1i} &= T_1\,\epsilon\,I_{1c} + C(T_{cold} - T_1) + \frac{1}{2}R_0\,I_{1c}^2 \\ \dot{Q}_{1f} &= T_1\,\epsilon\,I_{1h} + C(T_1 - T_{hot}) - \frac{1}{2}R_0\,I_{1h}^2 \end{aligned}\right\} \tag{10.9}$$

$$\left.\begin{aligned} \dot{W}_{1c} &= (T_1 - T_{cold})\,\epsilon\,I_{1c} + R_0\,I_{1c}^2 \\ \dot{W}_{1h} &= (T_{hot} - T_1)\,\epsilon\,I_{1h} + R_0\,I_{1h}^2 \end{aligned}\right\} \tag{10.10}$$

$$\tau < t < 2\tau \qquad (T = T_2):$$

$$\left.\begin{aligned} \dot{Q}_{2c} &= T_{cold}\,\epsilon\,I_{2c} + C(T_{cold} - T_2) - \frac{1}{2}R_0\,I_{2c}^2 \\ \dot{Q}_{2h} &= T_{hot}\,\epsilon\,I_{2h} + C(T_2 - T_{hot}) + \frac{1}{2}R_0\,I_{2h}^2 \end{aligned}\right\} \tag{10.11}$$

$$\left.\begin{aligned} \dot{Q}_{2i} &= T_2\,\epsilon\,I_{2c} + C(T_{cold} - T_2) + \frac{1}{2}R_0\,I_{2c}^2 \\ \dot{Q}_{2f} &= T_2\,\epsilon\,I_{2h} + C(T_2 - T_{hot}) - \frac{1}{2}R_0\,I_{2h}^2 \end{aligned}\right\} \tag{10.12}$$

$$\left.\begin{aligned} \dot{W}_{2c} &= (T_2 - T_{cold})\,\epsilon\,I_{2c} + R_0\,I_{2c}^2 \\ \dot{W}_{2h} &= (T_{hot} - T_2)\,\epsilon\,I_{2h} + R_0\,I_{2h}^2 \end{aligned}\right\} \tag{10.13}$$

These equations are trivially integrated to give the extracted and released heats in every subsystem, and the thermoelectric work in a cycle.

$$Q_c = \tau\left[\epsilon\,T_{cold}(I_{1c} + I_{2c}) + C(2T_{cold} - T_1 - T_2) - \frac{1}{2}R_0(I_{1c}^2 + I_{2c}^2)\right] \tag{10.14}$$

$$Q_h = \tau\left[\epsilon\,T_{hot}(I_{1h} + I_{2h}) + C(T_1 + T_2 - 2T_{hot}) + \frac{1}{2}R_0(I_{1h}^2 + I_{2h}^2)\right] \tag{10.15}$$

$$Q_i = \tau\left[T_1\,\epsilon\,I_{2c} + T_2\,\epsilon\,I_{1c} + C(2T_{cold} - T_1 - T_2) + \frac{1}{2}R_0(I_{1c}^2 + I_{2c}^2)\right] \tag{10.16}$$

$$Q_f = \tau\left[T_1\,\epsilon\,I_{1h} + T_2\,\epsilon\,I_{2h} + C(T_1 + T_2 - 2T_{hot}) - \frac{1}{2}R_0(I_{1h}^2 + I_{2h}^2)\right] \tag{10.17}$$

$$W_c = \tau\left[(T_1 - T_{cold})\,\epsilon\,I_{2c} + (T_2 - T_{cold})\,\epsilon\,I_{1c} + R_0(I_{1c}^2 + I_{2c}^2)\right] \tag{10.18}$$

$$W_h = \tau\left[(T_{hot} - T_1)\,\epsilon\,I_{1h} + (T_{hot} - T_2)\,\epsilon\,I_{2h} + R_0(I_{1h}^2 + I_{2h}^2)\right]\,. \tag{10.19}$$

The intermediate "reservoir" should actually be a thermodynamic heat pump that obtains $\dot{Q}_i$ at a temperature T_1 or T_2 and transfers $\dot{Q}_f$, making a work W_M in a cycle. We assume that the intermediate system works cyclically, without any thermal connection with the environment (in a real device this point is not fulfilled since the magnetic subsystem has a weak thermal leakage to or from the environment). In this case, the work made by the magnetic subsystem us $W_M = Q_f - Q_i$ and the total work $W = W_c + W_h + W_M = Q_h - Q_c$. For compatibility with the Second Law of Thermodynamics the entropy released by the intermediate device should be higher than that extracted, resulting in

$$\tau\alpha\left(\frac{\dot{Q}_{1i}}{T_1} + \frac{\dot{Q}_{2i}}{T_2}\right) = \tau\left(\frac{\dot{Q}_{1f}}{T_1} + \frac{\dot{Q}_{2f}}{T_2}\right)\,, \tag{10.20}$$

with $\alpha \geq 1$. The value $\alpha = 1$ holds for an ideal Carnot device, working without entropy production.

Moreover, the value of W_M is determined by the properties of the MCM for T_1 and T_2 given (i.e., W_M is the area of the thermodynamic cycle in the magnetization/field or entropy/temperature diagrams for that substance) which imposes another relation between Q_i and Q_f. This pair of relations involving T_1, T_2, I_{1c}, I_{2c}, I_{1h}, and I_{2h} indicates that four of these six quantities can be chosen arbitrarily. Let us assume that $\alpha = 1$ and the four currents through the TE cells are fixed. Then the intermediate system must adapt its maximum and minimum temperatures T_1 and T_2 to get the Carnot efficiency since the extracted and released heats are determined by the currents at the TE cells. If the MCM is a usual ferromagnet without a phase transition (strictly, only a second-order transition at zero field and the Curie temperature occurs, but there is no transition for any other field in a usual ferromagnet) the steady-state is reached when equation (10.20) is fulfilled and $W_M = Q_f - Q_i$.

In a MCM with a FOPT, like $La(Fe,Si)_{13}$, working in phase coexistence state, the temperatures T_1 and T_2 are both determined by the minimum and maximum magnetic fields (this is a requirement of the Gibbs' phase rule, i.e., the state of the MCM is a point of the coexistence line in a B/T diagram and B determines the temperature). However, if the relation 10.20 is not fulfilled, the MCM will gain or lose net heat every cycle, and then $W_M \neq Q_f - Q_i$. This net heat will transform one phase into another, and the material will leave the coexistence state when one phase disappears and the material goes into a single-phase state. After this, one of the extreme temperatures, T_1 or T_2, will change slowly until relation 10.20 is satisfied, reaching thus a steady state. It is desirable to have the MCM in coexistence state as long a time as possible, when the MCE is much higher. Most usually, the lowest magnetic field is zero, being then T_1 the transition temperature at zero field, T_0, (frequently referred to as "Curie temperature", but its character differs strongly from a usual ferromagnet). On the other hand the coexistence line is very approximately a straight line $T = T_0 + \beta B$ and T_2 is determined by the maximum applied field. Therefore, for a MCM with a FOPT and maximum applied field B, only three parameters can be chosen among I_{1c}, I_{2c}, I_{1h}, and I_{2h}, if we want to work in steady-state and always in phase coexistence. For instance, if we apply equal currents to both TE cells, making $I_{1c} = I_{1h}$ and $I_{2c} = I_{2h}$ (two constraints), the MCM will leave surely the coexistence state prior to the steady-state, except for the precise value of the magnetic field B, that determines T_2 so as the relation 10.20 is satisfied.

A natural working hypothesis is to take I_{2c} and I_{1h} as the minimum values that prevent thermal leakage from the MCM to the cold source and from the hot sink to the MCM. This is achieved making $\dot{Q}_{2c} = 0$ in equation (10.11) and $\dot{Q}_{1f} = 0$ in equation (10.9), i.e., choosing the currents according to:

$$0 = T_{cold}\,\epsilon\,I_{2c} + C(T_{cold} - T_2) - \frac{1}{2}R_0\,I_{2c}^2 \tag{10.21}$$

$$0 = T_1\,\epsilon\,I_{1h} + C(T_1 - T_{hot}) - \frac{1}{2}R_0\,I_{1h}^2 \tag{10.22}$$

These relations determine the two low currents. We can choose arbitrarily the higher current at the cold cell, I_{1c}, that determines the heat power extracted from the cold source, according to equation (10.14). With T_1 and T_2 given, and I_{1c}, I_{2c} and I_{1h} chosen, equation (10.20) gives the value of I_{1h} for steady regime. The cooling power, $Q_c/(2\tau)$, and other heats and works are obtained via eqs. (10.14)-(10.19). Finally the COP in steady regime is computed as

$$COP = \frac{Q_c}{W} = \frac{Q_c}{Q_h - Q_c}\,. \tag{10.23}$$

As said before, a good approximation for a MCM with FOPT gives the transition line for a moderate magnetic field B as

$$T(B) = T_0 + \beta B\,, \tag{10.24}$$

where T_0 can be tailored playing with the chemical composition of several MC alloys. For typical alloys derived from $La(Fe,Si)_{13}$, $\beta \simeq 4\,\mathrm{K\,T^{-1}}$. Let us assume that the magnetic subsystem follows a Carnot cycle between the magnetic fields 0 and B. Then, the temperatures of the MC system are $T_1 = T_0$, $T_2 = T_0 + \beta B$. The steady-state, while keeping the MCM in coexistence state, imposes the fulfillment of equation (10.20). The fixed parameters of the TE cells 1ML07-050-15-AN25 are shown in table 10.2.

Table 10.2: Fixed parameters of the cell 1ML07-050-15-AN25 from RMT Ltd.

ϵ $[mVK^{-1}]$	C $[mWK^{-1}]$	R_0 $[\Omega]$
25	55	1

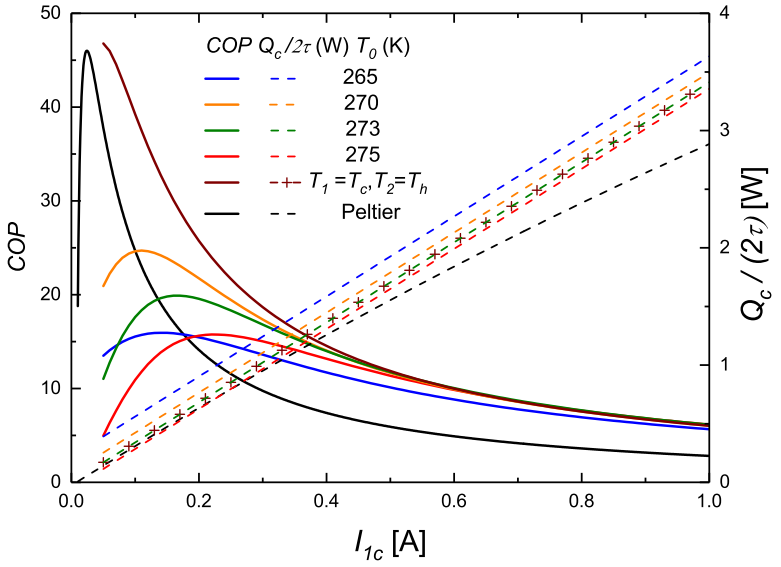

(a) COP and cooling power $Q_c/(2\tau)$ of the sandwich for T_{cold} =273 K, T_{hot} =278 K, maximum field B =2 T ($T_2 = T_1 + 8$K), and $\alpha = 1$ (Carnot efficiency of the MC subsystem), for several values of the characteristic temperature T_0 of the MCM. Also the data for a pure Peltier system with the same extreme temperatures T_{cold}, T_{hot}, and equal constant currents $I = I_{1c}$. The cooling power is divided by 2 for comparison since the hybrid system is extracting heat only for a half of the period.

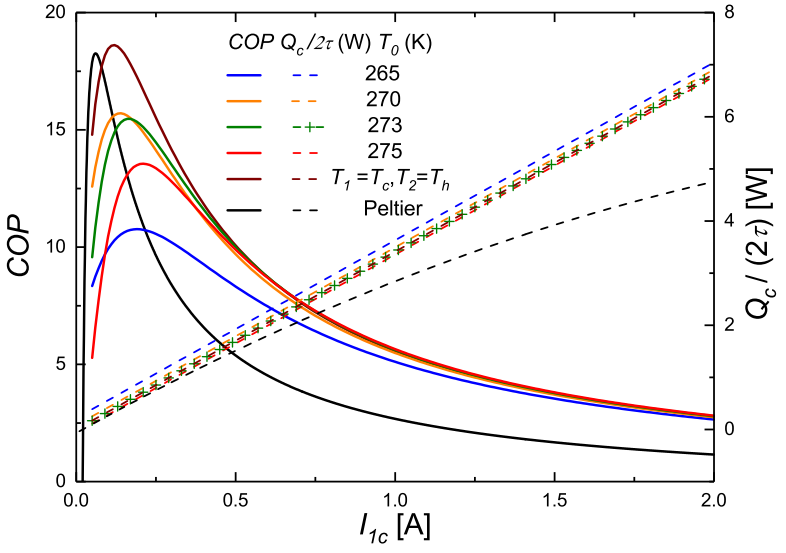

(b) Plot for T_{cold} =273 K and T_{hot} =278 K, for the same parameters.

Figure 10.1: COP and cooling power with ΔT =2 K for several characteristic temperatures of the MCM and a fixed increment $T_2 - T_1 = \beta B$ =8 K, and pure Peltier heat transfer simulation (two Peltier cells in series).

Figure 10.1a shows the COP and the cooling power $Q_c/(2\tau)$ for T_{cold} =273 K, T_{hot} =275 K (ΔT =2 K), for several characteristic temperatures of the MCM and a fixed increment $T_2 - T_1 = \beta B$ =8 K. This figure shows also the data for pure Peltier heat transfer, that is two Peltier cells in series, working continuously, with the same current I_{1c}, without any intermediate system. To compare with the hybrid system, the power of the pure Peltier method is divided by 2, because in the hybrid system each cell is working actively only during one half of period. Figure 10.1 shows the results for T_{cold} =273 K, T_{hot} =278 K. Except for very weak currents, the COP is clearly higher for the hybrid method, even more than a twofold in most of the current range, and the cooling power is more than one half of the pure Peltier method. The COP of the hybrid system decreases if $T_1 > T_{cold}$ (e.g., for $T_1 = T_0$ =275 K) or $T_2 < T_{hot}$ (e.g., for $T_1 = T_0$ =265 K, $T_2 = T_0$+8 K=273 K). The highest COP occurs if the MCM and the magnetic field are chosen to have $T_1 = T_{cold}$ and $T_2 = T_{hot}$ (brown curves in figure 10.1).

A hybrid system can be composed of two sandwiches in parallel in antiphase, which is easy to implement in a single rotating magnet when there is at least one region of high field and a region of nearly zero field. Just as an example, although a much smaller device would suffice, the cylindrical magnet designed for the pure magnetic refrigeration prototype presented in I, and published in [133] has two regions of high field ($B \simeq 1.5$ T), two of nearly zero field, and four with B changing from the maximum to the minimum or vice versa. Depending on the distribution of the sandwiches, this magnet is adequate, for example, for four sandwiches working in series around the central core, and many of these blocks in parallel, repeating the scheme along the length of the magnet. There are also magnet designs with four poles, adequate to contain eight sandwiches in series. In this case, the combined system would extract continuously more than twice as much heat as a pure Peltier system with the same work. As the main conclusion of this study, a hybrid sandwich in which the MCM has a first-order transition improves the efficiency with respect to a pure thermoelectric system if working in coexistence state, but the working parameters must be carefully chosen.

10.1.3 Magnetocaloric material with SOPT

A common ferromagnet has a SOPT with the critical point at zero field and temperature T_C ("Curie temperature"). Its temperature is not determined by the magnetic field alone, since it varies when the material gains or loses heat even at constant field B, due to the finite heat capacity $C_{p,B}$. Therefore, T_1 and T_2 are no longer constant, but depending on the heat flux and the properties of the material. For instance, for $B = 0$, if T_1 varies between $T_{1,ini}$ and $T_{1,fin}$, then

$$Q_{1c} + Q_{1h} = N \int_{T_{1,ini}}^{T_{1,fin}} C_{p,B}\, dT\,, \tag{10.25}$$

being N the molar number. Similarly at the maximum field, but even that is too crude since the finite thermal conductivity of the material makes the temperature non-uniform, that is $T(\dot{r}, t)$ is determined by an equation similar to that of heat conduction but including the magnetocaloric effect. It has to be solved numerically as a function of space an time for a given initial temperature distribution and the heat fluxes $\dot{Q}_{1i}$, $\dot{Q}_{1f}$, $\dot{Q}_{2i}$ and $\dot{Q}_{2f}$ as boundary conditions imposed by the currents at the TE cells.

Experimental data of adiabatic temperature change $(\partial T/\partial B)_S$, heat capacity at constant field $C_B = T(\partial S/\partial T)_B$, and thermal conductivity $k = -J_Q/\nabla T$, where J_Q is the heat current density, are used for the simulation. However, using a theoretical material that follows exactly the mean-field equations (usually an approximation to real materials) is also an interesting option. Although this is less realistic, it results in values of C_B and $(\partial T/\partial B)_S$ which agree exactly with the fundamental laws of Thermodynamics, allowing thus testing if the numerical errors of the simulation can produce unphysical results, before using the program with a real MCM. Moreover, for a real material, the calculation of C_B and $(\partial T/\partial B)_S$—which change orders of magnitude both spatially and temporarily—from a data table at every point of the mesh and at every time instant, usually requires long computing times which can be shortened by using a theoretical material. This procedure allows to test the results with many combinations of the working parameters. Furthermore, simulating a material allows monitoring many difficult to access properties in a real material (e.g. M/B diagrams, or a direct evaluation of the magnetocaloric work, that can be compared with the net heat output to check the energy conservation in the simulation).

In the mean field approximation, the magnetic entropy is

$$S_M(T,B) = NR \left[\ln \frac{\sin \dfrac{2J+1}{2J} y}{\sin \dfrac{y}{2J}} - y B_J(y) \right] , \tag{10.26}$$

where N is the number of moles, and there is a molecular field proportional to the magnetization M and the mean field is

$$B_m = B + \lambda M \, , \tag{10.27}$$

y is given by

$$y = N_A \, g \, J \, \mu_B \, (B + \lambda M)/RT \, , \tag{10.28}$$

being N_A the Avogadro constant, g is the gyro-magnetic ratio, μ_B Bohr's magneton and λ is a constant, proportional to the exchange interaction parameter. The magnetization is given by the mean field equation

$$M = N_A \, g \, \mu_B \, J B_J(y) = M_s B_J(y) \, , \tag{10.29}$$

being M_s the saturation magnetization and B_J the Brillouin function for spin J. Curie's constant is defined as

$$C_J = (N_A \, g \, \mu_B)^2 J(J+1)/(3R) \tag{10.30}$$

and the ordering temperature is given by

$$T_C = \lambda C_J = \lambda (N_A \, g \, \mu_B)^2 J(J+1)/(3R) \, . \tag{10.31}$$

The transcendental equation (10.29) can be readily solved by iteration or by the Newton method, giving M, y and then the entropy for any temperature and field. Nevertheless, to get some physical insight without complicated calculations, a useful approximation can be derived for $T > T_C$ and weak field,

i.e. $0 \leq y << 1$

$$M = \frac{C_J}{T - T_C} B \qquad ; \qquad B_m = \frac{T}{T - T_C} B \tag{10.32}$$

$$S_M = NR \left[\ln(2J+1) - \frac{C_J B_m^2}{2R^2 T^2} \right] = NR \left[\ln(2J+1) - \frac{C_J B^2}{2R^2 (T - T_C)^2} \right] \tag{10.33}$$

$$C_B = C_L(T) + \frac{T}{N} \left(\frac{\partial S_M}{\partial T} \right)_B = C_L(T) + \frac{T C_J B^2}{R(T - T_C)^3} \tag{10.34}$$

$$\left(\frac{\partial S_M}{\partial B} \right)_T = -N \frac{C_J B}{R(T - T_C)^2} \,. \tag{10.35}$$

Here, C_L is the lattice heat capacity, including phonon and electron contributions. Near room temperature, we can consider C_L as constant. As a result, the lattice entropy is $S_L = C_L \ln(T/T_0)$, with T_0 being some reference temperature at which the lattice entropy is arbitrarily taken as zero. The total entropy is then,

$$S = S_L + S_M = N C_L \ln(T/T_0) + NR \left[\ln(2J+1) - \frac{C_J B^2}{2R^2 (T - T_C)^2} \right] \tag{10.36}$$

and finally, differentiating this expression at constant S it results

$$\left(\frac{\partial T}{\partial B} \right)_S = \frac{C_J B \, T (T - T_C)}{C_L R (T - T_C)^3 + C_J B^2 \, T} \,. \tag{10.37}$$

This set of equations gives explicitly the thermodynamic quantities of an ideal magnetocaloric material. The set can be computed very quickly millions of times in a simulation, allowing testing the system with many different working parameters in an acceptable computing time with a fair approximation for the behavior of a real material. Moreover, and very important, an ideal material obeying exactly this set of equations obeys also exactly the Laws of Thermodynamics (but the Third Law, due to the lattice entropy). C_L does not have to be constant at low temperatures but tending to zero. However, the model is valid only for $T > T_C$). Actually this set of equations corresponds to an ideal thermodynamic system with fundamental molar equation (i.e. equation involving all and only extensive parameters)

$$U(S, \mu, N) = N C_L T_0 \exp\left(\frac{S - NR \ln(2J+1)}{N C_L} + \frac{\mu^2}{2 C_L C_J N^2} \right) - \frac{N T_C \mu^2}{2 \, C_J N^2} \tag{10.38}$$

where $\mu = NM = (\partial U/\partial B)_{S,N}$ is the total magnetic moment or extensive parameter conjugate with the external field B. This fundamental equation is that given in Callen's book (reference [149], equation 3.66) for a paramagnet with the addition of the exchange energy in the mean field approximation, $U_{exch} = -T_C\mu^2/(2NC_J)$. Also the molar lattice heat capacity is allowed to take any constant value C_L, instead of $C_L = R$, taken in that reference.

10.2 Master equation

The following equation is used for the heat transfer in the MCM:

$$\frac{\partial T}{\partial t} = \frac{P_m}{\rho\, C_B}\vec{\nabla}\cdot(k\vec{\nabla}T) + \left(\frac{\partial T}{\partial B}\right)_{ad}\frac{dB}{dt}\,, \tag{10.39}$$

where P_m is the molar mass and ρ the density of the MCM. This equation is slightly different to that widely used equation 2 of reference [148], where $(-T/C_B)\,(\partial S/\partial B)_T$ replaces the adiabatic temperature change with field—i.e., $(\partial T/\partial B)_{ad}$. It should remarked that the heat capacity is at constant field, very different from C_M, which equals C_L in the ideal ferromagnet model, while pressure is neither necessarily constant, nor relevant indeed for a solid. Actually, both expressions are equivalent in equilibrium Thermodynamics, but not necessarily in the case of a material with a hysteretic FOPT. More important, in a FOPT $(T/C_B)\,(\partial S/\partial B)_T$ involves an ∞/∞ indetermination, when both $C_B \to \infty$ and $(\partial S/\partial B)_T \to \infty$. Using experimental data, these quantities are not infinite, but produce an ill–conditioned value (i.e., at T_C, C_B can change enormously from a sample to another of the same compound, and from determinations in a single crystal or in powder, or even in different thermal cycles of the same material). On the other hand, in a FOPT, $(\partial T/\partial B)_{ad}$ is the slope of the transition line in a T/B diagram and is very well determined. By the way, $(\partial T/\partial B)_{ad}$ can be constant only if it is zero or $C_B \to \infty$, as happens in a FOPT while two phases coexist.

A 1D finite difference approximation has been done for equation (10.39) using the Crank-Nicolson (CN) method [150]. The position $0 \le x \le L$ of $Nx{+}1$ discrete points of the MCM is considered at $x_i = i\Delta x$, $i =, 0, 1, ...Nx$, $\Delta x = L/Nx$ and the time at instants $t_i = n\Delta t$, $n = 0, 1, 2, ...$ Assuming k as

constant, the master equation is replaced by the approximate system,

$$T_i^{n+1} = T_i^n + \frac{1}{2} D_i^n (T_{i-1}^n + T_{i+1}^n - 2T_i^n) + \\ + \frac{1}{2} D_i^{n+1} (T_{i-1}^{n+1} + T_{i+1}^{n+1} - 2T_i^{n+1}) + \frac{1}{2}\,\tau_i^n \frac{dB(t_n)}{dt} + \frac{1}{2}\,\tau_i^{n+1} \frac{dB(t_{n+1})}{dt}\,, \quad (10.40)$$

with the definitions,

$$D_i^n = \frac{P_m\, k\, \Delta t}{\rho\, C_B(T_i^n, B^n)\, \Delta x^2}\,, \quad (10.41)$$

$$B^n = B(t_n)\,, \quad (10.42)$$

and

$$\tau_i^n = \Delta t \left(\frac{\partial T(x_i, t_n)}{\partial B} \right)_{ad}\,. \quad (10.43)$$

The error of this approximation of the order of Δt^2 for the time derivative and of Δx^2 for the second derivative with respect x. That is one order of approximation better than the explicit or implicit Euler methods. Moreover, the CN method converges always and there is no restriction to the values of parameters D_i^n of τ_i^n, other than the desired precision of the calculation.

The boundary conditions are imposed by the energy conservation at the ends of the MCM, according to the heat flux input and output to the MC caused by the TE cells:

$$x = 0; \qquad kA(T_0^n - T_1^n) = T_0^n\, \epsilon\, I_c + C(T_{cold} - T_0^n) + \tfrac{1}{2} R_0\, I_c^2\,,$$

$$x = L; \qquad kA(T_{Nx-1}^n - T_{Nx}^n) = T_{Nx}^n\, \epsilon\, I_h + C(T_{Nx} - T_{hot}^n) - \tfrac{1}{2} R_0\, I_h^2\,, \quad (10.44)$$

being A the section of the MCM, and I_c and I_h, the currents trough the TE cells at the cold and hot sides, respectively.

The set of equations (10.40) and (10.44) form a non-linear system since D_i^n and τ_i^n depends on the instantaneous temperature and magnetic field at every point. From the temperatures T_i^n at any time t_n, the solution of the system gives them at the next step, t_{n+1}. The solution can be obtained by iteration. The first iteration takes $T_i^{n+1} = T_i^n$, $D_i^{n+1} = D_i^n$ and $\tau_i^{n+1} = \tau_i^n$ at the right side of equations 10.40, obtaining explicitly a new set of values for the time t_{n+1}. The calculation is then repeated inserting the new values in the right side of the equation, until a desired convergence is reached. The whole procedure has been achieved with a home-made FORTRAN code.

10.3 Results of the simulation

10.3.1 Typical parameters

The set of parameters used for each simulation will be specified in the corresponding sub-section. Here, typical values that apply are given, when not explicitly specified otherwise. Most usually, the simulation keeps constant all parameters for a given simulated time $t_{start} = 100$ s to reach a steady (usually sinusoidal) regime. After this time, one or a few parameters are continuously but very slowly varied to get a continuous plot of the results as functions of the varied parameter in a quasi-steady-state. There are slight differences respect to the results at true steady-state (that can be observed clearly upon passing from steady to quasi-steady) but this procedure saves computation time, avoiding having to wait for the steady state for each value of the varied parameter.

The cold source is at fixed temperature $T_{cold} = 0\,°\text{C} = 273.15\,\text{K}$, while the hot sink is at variable or constant $T_{hot}(= \Delta T) \simeq 1\,°\text{C}$, considering the sandwich as a single element in a battery. The most frequently simulated Peltier cells are 1ML07-050-15-AN25 from RMT Ltd. (Moscow, Russia) and some simulations have been made for the cell TE-35-0.6-1.0 from TE Technology Inc.; both can be parameterized according to the data from table 10.3.

Table 10.3: Fixed parameters of the cells from RMT Ltd. (1ML07-050-15-AN25) and TE Technologies Inc. (TE-35-0.6-1.0).

Model	ϵ $[mVK^{-1}]$	C $[mWK^{-1}]$	R_0 $[\Omega]$
1ML07-050-15-AN25	25	55	1
TE-35-0.6-1.0	15	65	2.46

For the MCMs, the experimental data tables for $C_B(T, B)$ and $(\partial T/\partial B)_{ad}$ of some $La(Fe,Si)_{13}H_{1.65}$ alloys have been used. The interpolation procedure to obtain these properties for every value of T and B from the experimental data tables is not a trivial task (e.g., when $C_B(T)$ is proportional to a Dirac delta-like function centered at the transition temperature for every field, for an intermediate field it is not the average, but a a delta-like function picked

at an intermediate temperature) are explained in reference [151]. The density $\rho \simeq 7200\,\mathrm{kg\,m^{-3}}$ is taken as a typical value for these alloys. The thermal conductivity is enhanced to values about $k = 100\,\mathrm{W\,m^{-1}\,K^{-1}}$. That means that in a real device, sheets of the MCM would have to be intercalated with copper sheets. As the most simple property a value of $dT/dB \simeq 4\,\mathrm{K\,T^{-1}}$ for the coexistence line was used. Also the properties of GdEr alloys have been used. In most simulations, the "ideal ferromagnetic" model sketched in subsection 10.1.3 has been used with T_C =250 K, $J = 7/2$, $g = 2$ and $C_L = 3R$, $\rho = 7260\,\mathrm{kg\,m^{-3}}$, $P_m = 0.157\,25\,\mathrm{kg\,mol^{-1}}$, and $k = 400\,\mathrm{W\,m^{-1}\,K^{-1}}$. With these parameters $(\partial T/\partial B)_{ad} = 1.5\,\mathrm{K\,T^{-1}}$ at $T = 0\,^{\circ}\mathrm{C}$ and $B = 1\,\mathrm{T}$. Typical dimensions of the MCM are, section $A = 1\,\mathrm{cm^2}$, length $L = 2.5\,\mathrm{mm}$.

The magnetic field B is varied in a quasi-square wave shape between 0 and $B_0 \simeq 2\,\mathrm{T}$ with frequency $f = 1\,\mathrm{Hz}$, period $p = 2\pi/f$, but many simulations have been made with other frequencies. That is,

$$0 < t < 0.2p\,,\ B = 0 \tag{10.45}$$

$$0.2p < t < 0.3p\,,\ B = B_0(t/p - 0.2)/0.1 \tag{10.46}$$

$$0.3p < t < 0.7p\,,\ B = B_0 \tag{10.47}$$

$$0.7p < t < 0.8p\,,\ B = B_0(0.8 - t/p)/0.1 \tag{10.48}$$

and

$$0.8p < t < p\,,\ B = 0\,. \tag{10.49}$$

Also, sinusoidal dependence has been used in some simulations. The discretization parameters have been taken smaller and smaller until no substantial differences have been found. Finally, typical values are:

$$\Delta x = 0.156\,\mathrm{mm} = L/16,\ \Delta t = 10^{-4}/f = 1 \times 10^{-4}\,\mathrm{s}\,.$$

With these parameters, other typical values are:

$$D_i^n \simeq 0.16 \text{ and } \tau_i^n \simeq 1.5 \times 10^{-4}\,\mathrm{K\,s\,T^{-1}}\,.$$

D_i^n does not need to be below 1/2 for convergence but better precision is reached if $D_i^n << 1$).

The temperatures are obtained solving iteratively the set of equations 10.40 and 10.44 with some initial condition $T_i^0 = const.$ From the T_i^n values the instantaneous heat and work powers are computed as $\dot{Q}_c$, $\dot{Q}_h$, and $\dot{W}_{TE}$ by

equations 10.2, 10.3, and 10.4, applied to the cold and the hot Peltier cells, respectively. The heat power released by the MCM is:

$$\dot{Q}_{MC} = kA\,\frac{T_1 - T_0 + T_{Nx-1} - T_{Nx}}{\Delta x}\,. \tag{10.50}$$

These powers are integrated over a cycle go get integrated heats and works, being the magnetic work $W_{MC} = Q_{MC}$ in a cycle. For the "ideal ferromagnet" the magnetic work is computed also as $W_{MC} = N \oint BdM$ to check the energy conservation in the simulation. The total work is $W = Q_h - Q_c$ in steady-state. Finally, the performance coefficient is:

$$COP = \frac{Q_c}{W_{TE} + W_{MC}} = \frac{Q_c}{Q_h - Q_c}\,. \tag{10.51}$$

A typical simulation covering 2000 s of simulated time takes a CPU time about 3000 s on a desktop personal computer.

10.3.2 Pure thermoelectric cooling

Figure 10.2a, shows the temperature of the MCM at five different points, namely, $x = 0, L/4, L/2, 3L/4, L$, on increasing current supply $I_h = I_c$ through the TE cells, for $T_{hot} - T_{cold} = 1\,\mathrm{K}$. At the instant $t = 138\,\mathrm{s}$, when $I_h = 0.023\,\mathrm{A}$, this weak current is enough to avoid heat leakage from the hot side to the cold side, since the T–gradient is nearly zero in the MCM. For higher current the Peltier cells transfer heat from the cold side to the hot side.

Figure 10.2b shows that $\dot{Q}_c$ increases with I_h reaching a maximum out of the figure. The maximum $COP_{max} = 82 = 30\%\,COP_{Carnot}$ occurs for $I_h = 0.011\,\mathrm{A}$, a very high value but less than that obtained for the same ΔT without the MC. This is due to the relatively low thermal conductivity of the MC. The heat flow by conduction imposes a large temperature gradient, making the thermal jump greater than $(T_{hot} - T_{cold})/2$ on each TE cell, which reduces its efficiency. Therefore, if the MC is not playing its role, it is not indifferent, but a hindrance for the system's performance. A high conductivity of the MCM becomes vital. It can be increased alternating copper sheets ($k \simeq$

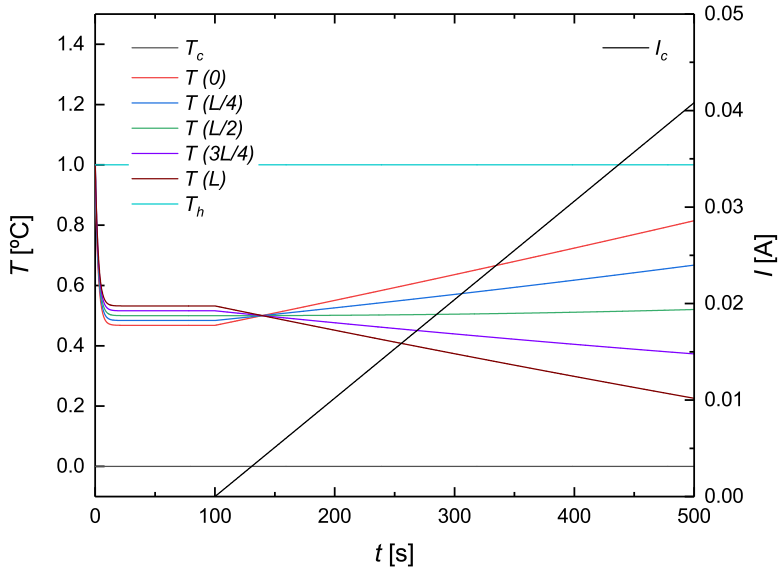

(a) Temperatures at different points of the MCM for constant temperature difference $\Delta T = T_{hot} - T_{cold}$ and increasing current (right scale) at the TE cells $T_{hot} = T_{cold}$, without magnetic field.

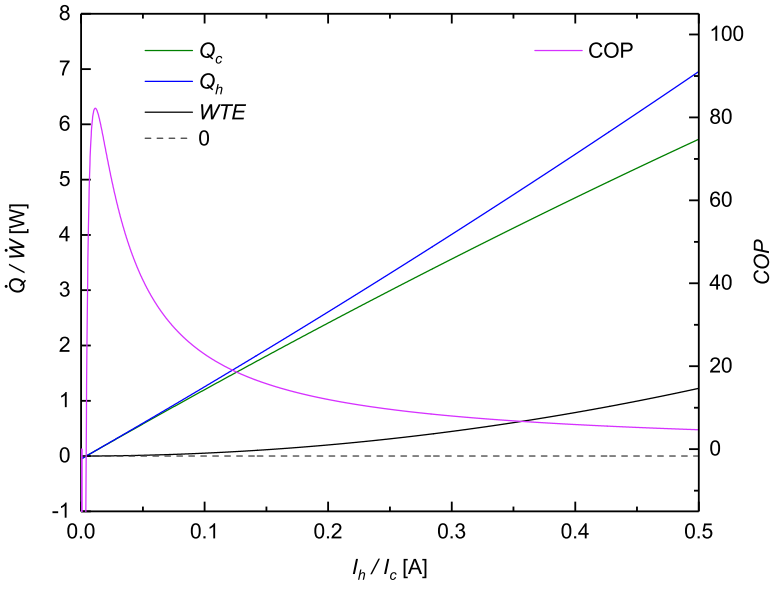

(b) Left scale: Extracted heat power $\dot{Q}_c$, released heat power $\dot{Q}_h$ and thermoelectric work power against current at the TE cells. Right scale: COP.

Figure 10.2: Results of the simulation of pure thermoelectric cooling.

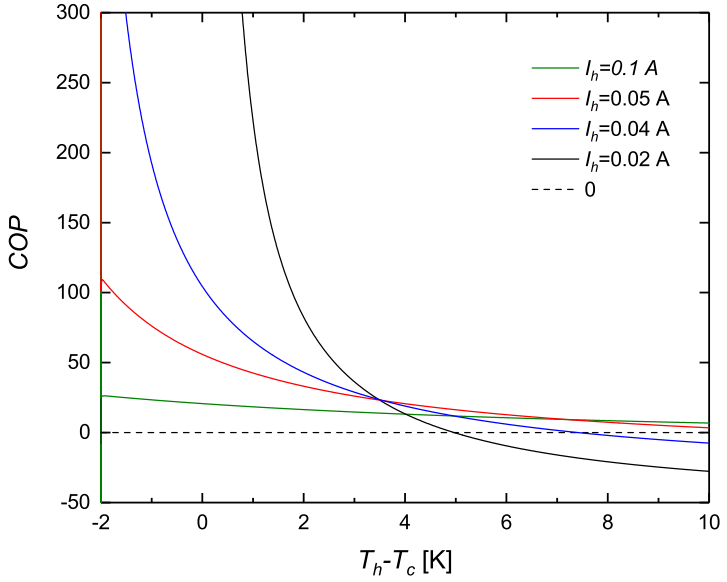

(a) COP of the sandwich on increasing $\Delta T = T_{hot} - T_{cold}$ at $B = 0$, for several current supplies $I_h = I_c$.

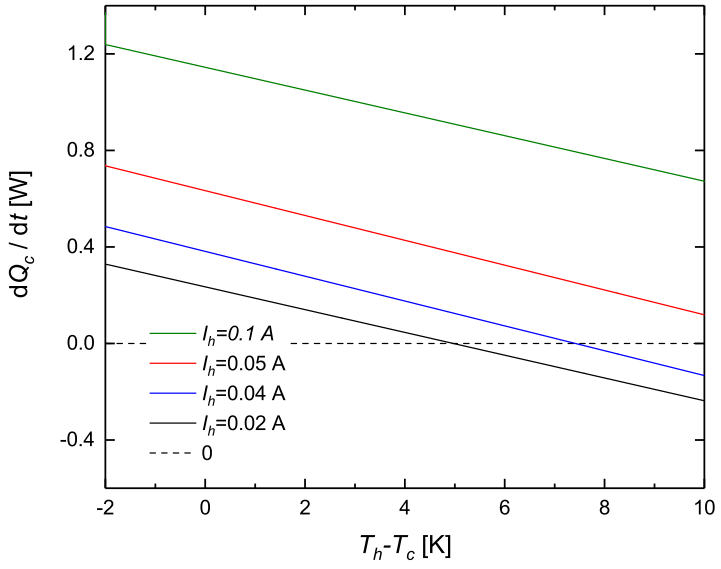

(b) Heat power extracted from the cold source.

Figure 10.3: Results of the simulation of pure thermoelectric cooling.

$400\,\mathrm{W\,m^{-1}\,K^{-1}}$, 40 times higher than that of LaFeSi) parallel to the heat flow. For higher I_h, the COP decreases quickly as usual in a TE refrigerator.

Figure 10.3a shows the COP of the pure TE system with increasing temperature difference $\Delta T = T_{hot} - T_{cold}$ and several current supplies, $I_h = I_c$, to both TE cells. For very weak currents, the COP reaches very high values at small or negative ΔT (For negative ΔT the Carnot COP is also negative since the system transfers heat from T_{hot} (lower) to T_{cold} (higher) and produces work). For higher currents the system can pump heat across higher ΔT but with low efficiency.

Figure 10.3b shows how, for low currents, the cooling power $\dot{Q}_c$, decreases with δT and increases with the current. In particular, it is clear that for $I_h = I_c = 0.02\,\mathrm{A}$ the Peltier cells can transfer heat with high efficiency for $\Delta T < 2\,\mathrm{K}$ and are yet able to stop leakage for $\Delta T < 5\,\mathrm{K}$. On the other hand, it is also clear that a Peltier system supplied with high current ($I_h = I_c > 0.1\,\mathrm{A}$) is not of much benefit with of a small or negative temperature difference. This is probably the cause of the small effect of the MC in reference [22], where currents of $0.01\,\mathrm{A}$ may be too strong given the size of the Peltier cells used in that reference.

10.3.3 Pure magnetocaloric cooling with passive thermal diodes

Pure magnetocaloric cooling using thermal diodes can be simulated with the same program, fixing $I_h = I_c = 0$ but imposing different conductance in both directions for the TE cells. Let C_r be the conductance towards the right side and C_l towards the left side. Let us assume $C_l = 55\,\mathrm{mW\,K^{-1}}$ to be equal to the real conductance of the Peltier cell 1ML07-050-15-AN25 and $C_r = 100 C_l$. This high rectification power is difficult to achieve with real thermal diodes (or they should be too sophisticated) but serves to evaluate the pure MC refrigeration.

Figure 10.4 shows the evolution of the temperatures at five points of the MCM, namely at $x = 0, L/4, L/2, 3L/4, L$, while the magnetic field oscillates

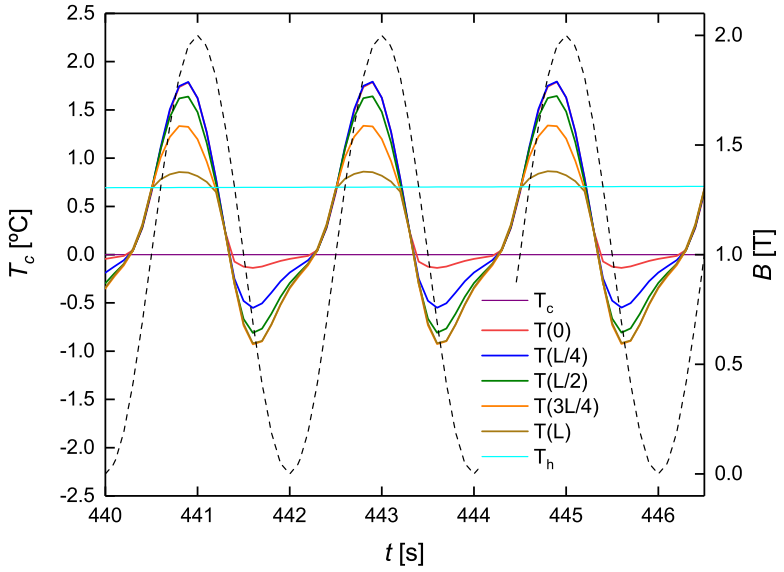

Figure 10.4: Pure MC refrigeration with thermal diodes. Left scale: Time evolution of temperatures at different points of the MCM along with the temperatures of the cold source, T_{cold}, and the hot sink, T_{hot}. T_{hot} is forced to increase slowly with time. Right scale: Magnetic field B varying with frequency $f = 0.5\,\mathrm{Hz}$.

sinusoidally between 0 and 2 T with frequency $f = 0.5\,\mathrm{Hz}$. The hot side temperature is forced to increase slowly with time (this variation cannot be noticed in the time range plotted in figure 10.4), from the instant $t_{start} = 100\,\mathrm{s}$ to the end of calculation $t_{end} = 5000\,\mathrm{s}$ as

$$T_{hot} = T_{cold} + 3\,\mathrm{K} \times \frac{t - t_{start}}{t_{end} - t_{start}}\,. \tag{10.52}$$

Due to the high conductance of the TE cells to the right side $T(0)$ is slightly higher than T_{cold} when the field is low, and $T(L)$ slightly higher than T_{hot} when the field is high. For this relatively low frequency there is a high temperature gradient at the MC—and hence, high heat transfer—only just before the maximum and minimum of B, but there is large fraction of the period (e.g. for $442\,\mathrm{s} < t < 442.6\,\mathrm{s}$, and so on every period) where the gradient is low, which reduces the power cooling of the system.

Figure 10.5 shows the cooling power $\dot{Q}_c$ and COP as functions of the temperature for the ideal magnetocaloric with B oscillating between 0 and 2 T, for several frequencies. This system can cool for $\Delta T < 2\,\mathrm{K}$ (i.e. $\Delta T_{max} \simeq B_{max}(\partial T/\partial B)_{ad}$), but the COP is above 30 for $\Delta T \simeq 1.5\,\mathrm{K}$. The cooling power decreases with increasing ΔT. For low ΔT, $\dot{Q}_c$ is mainly determined by the MC thermal conductance and increases with the frequency but not linearly. The MCM acts as an "elevator" for heat and also as heat reservoir. For low frequency, during each cycle a larger amount of heat is transferred from the cold source to the hot sink, but that reduces the temperature difference with respect to the MC, and then also, the transferred power. For very high frequency there is no time in a cycle for this reduction, and $\dot{Q}_c$ is independent of the frequency. Therefore, the frequency is limited by the conductance of the MC. Approximately, the relaxation time of the MC is

$$\tau_{relax} = \frac{\rho L^2 C_B}{P_m k} > 1/f\,. \tag{10.53}$$

A value above this maximum does not obtain any advantage and has technical problems. For the simulated parameters we get $\tau_{relax} \simeq 0.3\,\mathrm{s}$ which imposes a maximum frequency $f_{max} \simeq 3\,\mathrm{Hz}$, what is clearly indicated by the simulation. Obviously, the rate of heat transfer is proportional to k, what makes this parameter crucial. It can be increased inserting copper plates in parallel to the MCM.

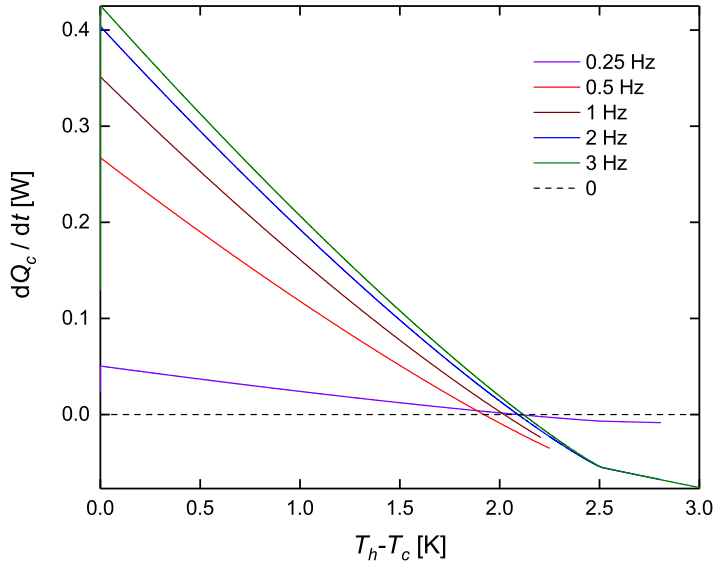

(a) COP of the sandwich on increasing $\Delta T = T_{hot} - T_{cold}$ at $B = 0$, for several current supplies $I_h = I_c$.

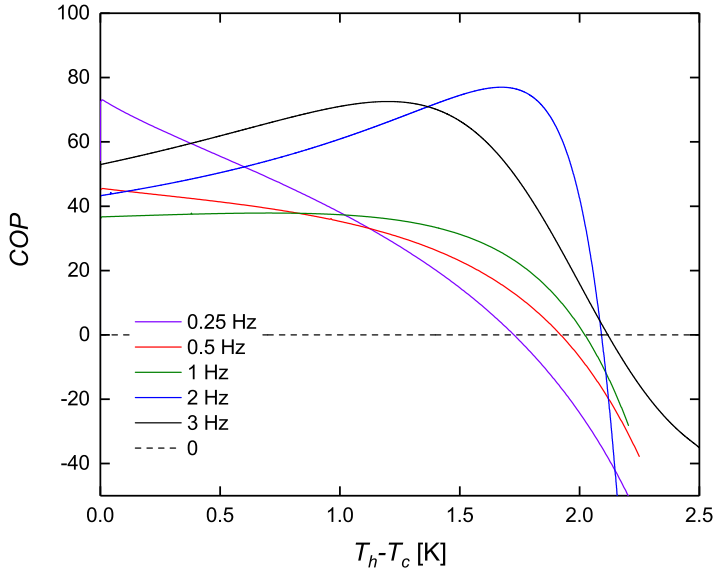

(b) Heat power extracted from the cold source.

Figure 10.5: Results for pure magnetocaloric cooling using passive thermal diodes.

10.3.4 Hybrid MC-TE cooling with La(Fe,Si)$_{13}$H

Figure 10.6a shows a few periods of the evolution of the temperatures at five points of the MCM along its length for a simulation where the currents at the TE cells are varying as a quasi-square wave, like the magnetic field $B(t)$. The current amplitudes increase very slowly with time (after 400 s for steady regime) from 0.04 A (estimated to prevent heat leakage) up to 1 A, always with constant magnetic field amplitude $B_0 = 1.5$ T and fixed temperatures of the cold source and the hot sink, $T_{cold} = 0$ °C, $T_{hot} = 2$ °C. The quasi-steady-state can be always assumed. The characteristic temperature (transition at zero field) of the MCM is $T_0 = -5$ °C. As shown in figure 10.6a, where the currents are low ($I_c = I_h \simeq 0.093$ A as maximum), when the field is increasing from 0 to B_0 the temperatures increase also, reaching the maximum, $T_{2,ini} > T_{hot}$, just when the maximum field is reached. After that the hot TE cell is activated, transferring heat to the hot sink.

Contrarily to an ideal system in phase coexistence, $T_2(t)$ depends on time (it has also a negative gradient allowing the heat to diffuse towards the right side end, symbolized by the red dotted line) and decreases slowly down to $T_{2,fin}$. Then the hot TE cell is deactivated (i.e., reduced to $I_h = 0.04$ A) and the field is quickly reduced to zero. The temperatures drop down to a value $T_{1,ini} < T_{cold}$. At this point, the cold cell is activated and $T_1(t)$ increases slowly up to $T_{1,fin}$ as the heat is transferred from the cold source to the MCM. Finally, the cold TE is deactivated and the magnetic field increased again, to repeat the process quasi-periodically (the applied currents are very slowly increasing). For the low currents featured in figure 10.6a, $T_{2,fin} > T_{hot}$ and $T_{1,fin} < T_{cold}$. As sketched in section 10.1.2 in the ideal working condition $T_1 \simeq T_{cold}$ and $T_2 \simeq T_{hot}$, which is not fulfilled by the simulated system for so low currents. A too wide temperature interval with the field means a too high W_{MC} that is not compensated by the increase of the TE cells efficiency. Using the "elevator" analogy, the elevator does not stay long enough at the "upper floor" to allow "all the passengers" to get out. Neither does the "elevator" remain enough time at the "ground floor" to fill its capacity. Thus, for this low currents, the frequency should be reduced.

Figure 10.6b shows the same data for $I_c = I_h \simeq 0.50$ A. In this case, T_1 and T_2 decrease more pronouncedly during the constant field phase. The interval

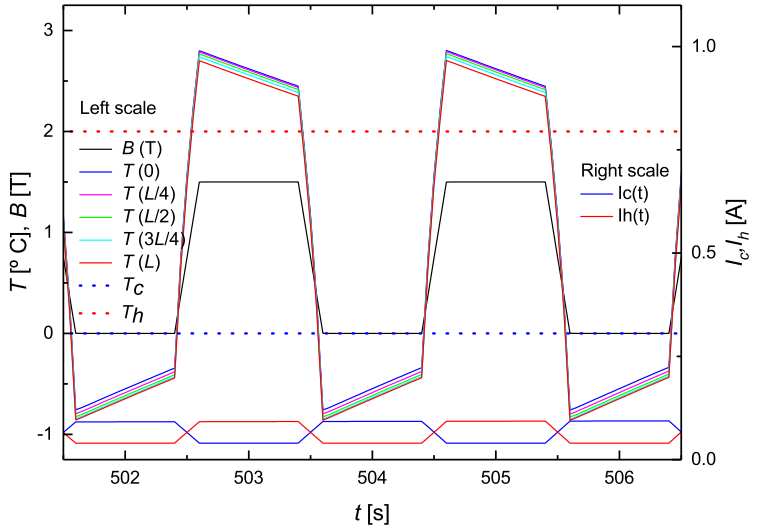

(a) Left scale: Magnetic field $B(t)$ and temperatures at several points of MC material for low, equal currents at the TE cells. Temperatures are of the cold source T_{cold} and the hot sink T_{hot}. Right side scale: Currents at the TE cells, $I_c(t)$, $I_h(t)$. The current amplitudes are slowly increasing with time.

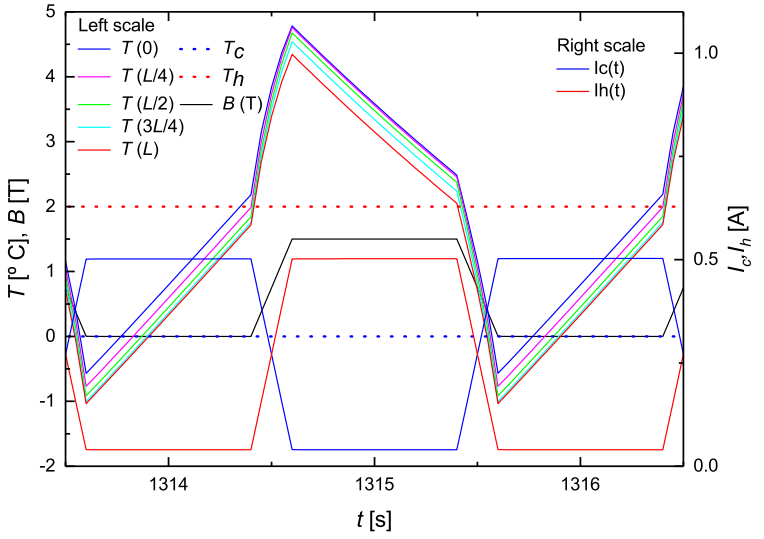

(b) As in 10.6a, but for medium currents, $I_c = I_h \simeq 0.5$ A.

is adequate to $T_{hot} - T_{cold}$ but the averages $\langle T_1 \rangle > T_{cold}$ and $\langle T_2 \rangle > T_{hot}$. As explained in section 10.1.2 the MC temperatures adapt themselves until the net heat flow to or from the MCM cancels in a cycle.

Figure 10.7a shows the instantaneous heat powers extracted from the cold source and released to the hot sink. Here, it is evident that when the magnetic field is high, the hot TE cell transfers heat to the hot sink and the cold TE cell extracts a small heat power from the cold source. Oppositely, when the field is zero. The lowest currents are just enough to avoid heat leakage. The right side panel shows the COP, the cooling power and the average power work made, along with for pure Peltier cooling. In this last case, the powers are divided by two taking into account that in the combined method, each cell is working less than one half of period.

As a conclusion, the parameters of the system have to be chosen with care, since the parameters of the MCM and those of the TE are correlated. Choosing well the parameters, the COP and the cooling power are higher for the combined method, but lower than for an ideal Carnot device for the MC subsystem. Particularly, for low currents the COP can have a big increase. For instance, for $I_{c,max} = I_{h,max} = 0.1\,\mathrm{A}$ the COP increases from 24 to 31. However, there is still the question whether the improvement obtained is worth the effort of building a TE-MC hybrid cooling device.

It must be also remarked, that there is the additional possibility, and to my knowledge it has not attracted much attention yet, of using energy harvesting techniques as power supply for the thermal diodes (i.e. Peltier modules). The presence of a rotating magnetic field points to the possibility of using it to produce small currents. Additionally, the presence of an unwanted heat source in the hot sink, although the temperature difference with ambient would be small, is also a possible target for energy harvesting. If the use of energy harvesting techniques is possible, an increase in the efficiency of these systems can be expected.

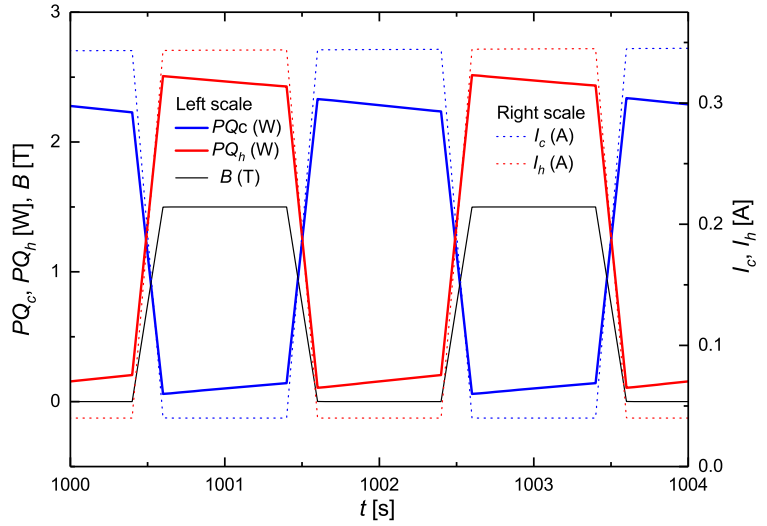

(a) Left scale: A small portion of the instantaneous heat power extracted from the cold source, $\dot{Q}_c$, and released to the hot sink, $\dot{Q}_h$, as well as the magnetic field. Right scale: instantaneous currents, through the cold an hot Peltier cells, $I_c(t)$, $I_h(t)$, respectively.

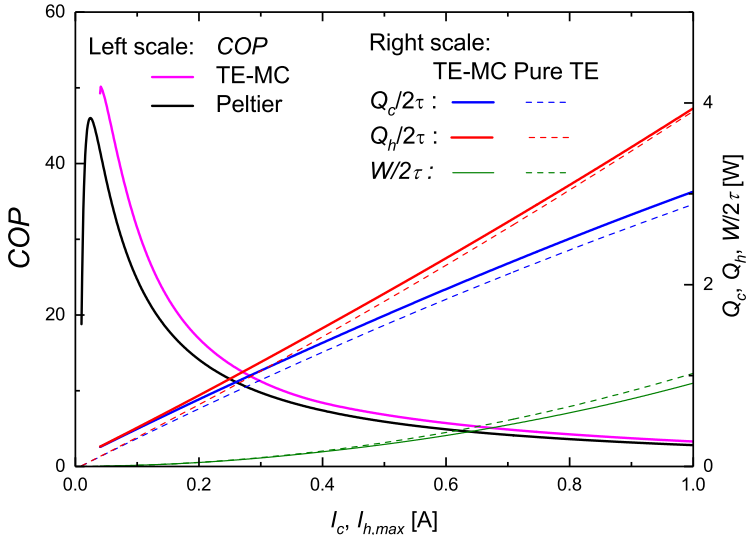

(b) Left scale: COP of the sandwich on increasing amplitude of I_c and I_h. Data for pure Peltier heat transfer. Right scale: Average heat power extracted from the cold source $Q_c/2\tau$, released to the hot sink, $Q_c/2\tau$, and work $W/2\tau = (Q_h - Q_c)/2\tau$. The heats and work are averaged over a period.

Figure 10.7: Results for a hybrid MC-TE system.

Conclusions

A good deal of this thesis was developed within the scope of a project aimed to gain understanding of magnetic refrigeration technology, in order to bring it closer to commercial applications at room temperature. The final part of this work, although out of the scope of the previous project, was addressed to test, by means of computer modeling, the use of thermoelectric-magnetocaloric (TE-MC) hybrid devices as building bricks for a not-in-kind cooling device. As a result, the present thesis is composed of two fundamental parts: first, the design and construction of a rotary magnetic refrigerator, using a concept design that, at the beginning of the project and to the best of our knowledge, had not been reported before, and second, the simulation of a not-in-kind cooling concept consisting in the use of TE-MC hybrid devices.

The introduction of this thesis, not only provides a brief overview of the basic foundations of magnetic refrigeration technology, but most importantly, presents a personal view of the different implications of the so-called “green technologies" and, more specifically, magnetic refrigeration. This introduction to the thesis states the need of being aware of the economic, ecologic and strategic consequences of the introduction of this technology, as well as its weak points and the related industrial developments that would be necessary to assure the viability of a widespread large-scale production. Some important conclusions within the introduction of this thesis follow below.

- The economic and health implications of the appearance of modern refrigeration technologies are undoubtedly beneficial, and the importance of reducing their high energy consumption and the ecologic implications that they represent is an issue of great relevance in a world with a growing

refrigeration demand. This is where magnetic cooling has been claimed to prove beneficial and could be an alternative. However, these already old claims have to be confronted with reality in an industrial scenario dominated by a mature vapor compression technology, which is still introducing improvements that make the chances of obtaining a surpassing technology everyday harder. In the mean time, magnetic cooling technology development seems to be a bit stagnant in the last years and the answer to the question as to whether this technology would ever make it to the home appliance market remains uncertain.

- Some personal considerations and analysis about the operation point and test conditions of a magnetic refrigerator in real environments, according to industrial specifications and common practices, are presented in section 1.7. This considerations may be summarized stating that magnetic refrigeration research works very rarely take into account realistic working conditions of commercial refrigerators. They are often focused in maximum or minimum results, disregarding other important industrial issues like perturbation stability and the corresponding response of the systems. This leads the academic research to focus on working points of maximum COP without further considerations. From the operational point of view (and thus, the device's maximum cooling power calculations), it may be better to focus on operational stability, since operation at maximum COP can be unstable, leading to broad temperature oscillations. Working at the maximum COP with some materials means a design too tight to the operational specifications of the device, leaving not enough spare power to compensate for sudden cooling power demands that can emerge, taking the machine out of the positive temperature span area. This is specially important in the case of FOPT materials and it should also be kept in mind when designing the regenerator—materials and mass—with SOPT materials. The cooling power vs. span graphs that very often appear in magnetic refrigeration literature should be interpreted from a more functional point of view.

In part I of this work, a description of the design and construction of a rotary magnetic refrigeration prototype, based on the use of an improved magnet design, and a continuous pumping system provided with solenoid valves for fluid flow control, has been presented. Due to the difficulties encountered and the results obtained, this part constitutes more a construction guideline than a presentation of test results obtained with the prototype. Challenges faced, lessons learned, solutions adopted, results obtained and possible explanations for these results are presented. However, some relevant lessons can be

extracted from the overwhelming work this part represents.

- A rotary magnetic refrigeration prototype has been fully designed at ICMA (now INMA) (University of Zaragoza - CSIC) and built in collaboration with the company Dynatech Dynamics & Technology, S. L. U., who was in charge of the assembly of the permanent magnet in a frame, and provide it with a rotary mechanism, fluid pumps, high speed solenoid valves and a programmable logic controller based valves' control. The rest of the device, fluid tubing, magnet, AMR, data acquisition system, etc. have been designed and implemented at the University of Zaragoza.

- A remarkable improvement of a previous two pole compact magnet design was achieved using an original optimization procedure that not only finds the optimum values for the defined design parameters, but also provides information about the sensibility upon their variation. The magnet was finally designed and built, using only a small amount of hard magnetic material, having a large volume for the magnetocaloric materials (MCMs). This optimized design improves the original magnet:

  1. it increases the final maximum measured field to 1.50 T, compared to the value of 1.13 T reported by Eriksen et al., [107], (over a 7% increase) with a measured low field of 0.00 T,
  2. it lowers the risks of demagnetization and saturation, thanks to the orientation of the field in the magnetic sectors of each pole, the proper selection of the materials and the elimination of the meniscus in the low field iron area,
  3. it has a lower manufacturing cost, since the elimination of the meniscus diminishes the necessary steps,
  4. according to the values of the functional F the overall improvement is above 8%.

- The distribution of the MCM in the regenerator ring is well equilibrated, allowing an easy rotation with a small torque.

- The distribution of field regions and the eight independent cavities of the regenerator ring allow having an overall thermal frequency of the cooling cycle eight times higher than the magnet's rotation mechanical one, acting simultaneously in two channels.

- The regenerator block of the prototype has a very large volume which can contain up to 2.1 kg of granules of LaFeMnSi-H materials or 2.4 kg of

Gd and GdEr alloys. It has a great versatility in the number of graded materials that can contain, which can either be FOPT or SOPT materials.

Conclusions from the operation of the prototype follow.

- Preliminary results with a one Gd section AMR block showed a maximum span of 2.1 °C with no load applied, at 700 rpm of the magnet's motor—i.e., ∼0.79 Hz mechanical frequency and ∼6.32 Hz of overall thermal frequency of the device—a pushed volume of 100% of the AMR void volume and a flow to magnetization phase of 20°.
- Tests with a three section AMR block filled with Gd and GdEr compounds show a span of 3 °C with no load applied at 50 rpm of the magnet's motor—i.e., ∼0.04 Hz mechanical frequency and ∼0.67 Hz of overall thermal frequency of the device—a pushed volume of 33% of the AMR void volume and a flow to magnetization phase phase of 0°.
- With the one section regenerator block, measurements of the evolution of temperatures on thermocouples in contact with the MCM gave values compatible with the field change effect on the Gd spheres. Following the shape of its cyclic curve the shape of the field given by the magnet. The temperature oscillation goes up to 2.2 K, which is a bit higher than the span obtained from the cold source and the hot sink; however, the regenerators are unable to create a temperature gradient along the MCM.
- Temperature relaxation measurements of internal points of regenerator, pipes, and cold source to the external temperature which, in the case of the regenerator, is the temperature of the magnet and, for the pipes and cold source, is room temperature, indicate important heat losses in the system.
- Other possible non-excluding explanations for the low performance observed are:

  1. lack of equivalence of hot and cold blows due to the uncertainty in the real opening and closing timings of the solenoid valves,
  2. heat build up from the solenoid valves,
  3. low resolution and precision of the measurement and setup systems of the prototype, in relation to the real needs,

4. variability in the packing of the MCM within the regenerator sections, which can provoke differential working conditions among the AMRs.

- Solenoid valves are too noisy and power consuming for any use in home appliances.

In part II of this thesis, a very simple hybrid thermoelectric-magnetocaloric (TE-MC) system is simulated using the working parameters of commercial Peltier cells and the properties of a material with a first-order magnetostructural phase transition, as $La(Fe,Si)_{13}H_{1.65}$. The results are compared with those corresponding to a pure TE system and a pure magnetocaloric one with ideal thermal diodes.

A TE-MC is formed with a MCM plate inserted between two thermoelectric cells with the idea of combining the best parts of both technologies—i.e. magnetic refrigeration and thermal diode behavior with very high COP at very low heat pumping conditions. The conclusions of this study are presented henceforth.

- An original master equation has been introduced that models the heat transfer for FOPT MCMs. This equation has been successfully used to model the TE-MC-TE sandwich.
- The analytic procedure presented demonstrates that the inclusion of the MCM can improve a lot the efficiency of the TE alone if the proper calculations are done to determine the working conditions of the sandwich for the given MCM.
- The parameters of the system have to be chosen with care, since the parameters of the MCM and of the TE are correlated. The TE currents are also related and fixing three of them, the fourth is also fixed. Choosing well the figures, the COP and the cooling power are higher for the hybrid system. The absence of these considerations, with the use of non correlated parameters seem to be the origin of the poor behavior observed by de Vries and van der Meer in [22], leading them to an erroneous negative conclusion.
- For low currents (e.g. 0.1 A) the COP of the Peltier cell presented increases from 24, in the pure thermoelectric case, to 31 in the case of the

hybrid device.

- At the same cooling power, the realistic hybrid system has higher efficiency than the pure Peltier method, and similar to the pure MC with ideal diodes.
- TE-MC hybrid devices are worth to be given further consideration.

Conclusiones

Buena parte de esta tesis se ha desarrollado en el marco de un proyecto destinado a incrementar la comprensión de la tecnología de refrigeración magnética, con el fin de acercarla a las aplicaciones comerciales a temperatura ambiente. La parte final de este trabajo, aunque fuera del alcance del proyecto anterior, ha estado dirigida a probar, mediante modelado informático, el uso de dispositivos híbridos termoeléctrico-magnetocalóricos (TE-MC) como elementos de construcción para un tipo alternativo de dispositivo de enfriamiento. Como resultado, la presente tesis se compone de dos partes fundamentales: la primera, el diseño y construcción de un refrigerador magnético rotatorio, utilizando un diseño conceptual que, al inicio del proyecto y hasta donde sabemos, no había sido publicado, y la segunda parte comprende la simulación de un concepto de refrigeración alternativo consistente en el uso de dispositivos híbridos TE-MC.

La introducción de esta tesis, no solo proporciona una breve descripción de los fundamentos básicos de la tecnología de refrigeración magnética sino que, lo que es más importante, presenta una visión personal de las diferentes implicaciones de las llamadas "tecnologías verdes" y, más específicamente, de la refrigeración magnética. En esta introducción a la tesis se plantea la necesidad de conocer las consecuencias económicas, ecológicas y estratégicas de la introducción de esta tecnología, así como sus puntos débiles y los desarrollos industriales relacionados que serían necesarios para asegurar la viabilidad de una producción a gran escala generalizada.

A continuación se presentan algunas conclusiones importantes del contenido de la introducción de esta tesis.

- Las importantes implicaciones económicas y sanitarias de la aparición de las tecnologías modernas de refrigeración son incuestionablemente beneficionsas, y la importancia de reducir su elevado consumo energético y las implicaciones ecológicas que representan, es un tema de gran relevancia en un mundo con una demanda creciente de refrigeración. Aquí es donde se ha afirmado que el enfriamiento magnético resulta beneficioso y podría ser una alternativa. Sin embargo, estas ya viejas afirmaciones tienen que ser confrontadas con la realidad en un escenario industrial dominado por una tecnología compresión de vapor madura, pero que aún está introduciendo mejoras que hacen cada día más difícil la posibilidad de obtener una tecnología superior. Mientras tanto, el desarrollo de la tecnología de enfriamiento magnético parece estar un poco estancado en los últimos años y la respuesta a la pregunta de si esta tecnología llegará alguna vez al mercado de los electrodomésticos sigue siendo incierta.

- En la sección 1.7 se presentan algunas reflexiones personales y un análisis sobre el punto de operación y condiciones de prueba de un refrigerador magnético en ambientes reales, de acuerdo con especificaciones industriales y prácticas comunes. Estas consideraciones se pueden resumir afirmando que los trabajos de investigación en refrigeración magnética rara vez tienen en cuenta las condiciones de trabajo reales de los refrigeradores comerciales. A menudo se centran en resultados máximos o mínimos, sin tener en cuenta otros problemas industriales importantes como la estabilidad ante perturbaciones y la respuesta correspondiente de los sistemas. Esto lleva a la investigación académica a centrarse en puntos de trabajo de máximo COP sin mayores consideraciones. Desde el punto de vista operacional (y por lo tanto, de los cálculos de la potencia de enfriamiento máxima del dispositivo), puede ser mejor focalizarse en la estabilidad operacional, ya que la operación al COP máximo puede ser inestable, dando lugar a amplias oscilaciones de temperatura. Trabajar al COP máximo con algunos materiales significa un diseño demasiado ajustado a las especificaciones operativas del dispositivo, lo que no deja suficiente energía de reserva para compensar repentinas demandas de energía de enfriamiento que pueden surgir, sacando la máquina del rango de salto térmico positivo. Esto es especialmente importante en el caso de los materiales FOPT y también debe tenerse en cuenta al diseñar el regenerador—materiales y masa—con materiales SOPT. Las gráficas de potencia de enfriamiento frente a span que aparecen con mucha frecuencia en la literatura sobre refrigeración magnética, deben interpretarse desde un punto de vista más funcional.

En la parte I de este trabajo, se ha presentado una descripción del diseño y construcción de un prototipo rotatorio de refrigeración magnética, basado en el uso de un diseño de imán mejorado y un sistema de bombeo continuo provisto de electroválvulas para el control del flujo de fluido. Debido a las dificultades encontradas y los resultados obtenidos, esta parte de la tesis constituye más una guía de construcción que una presentación de los resultados de ensayos con el prototipo. Se presentan los desafíos afrontados, las lecciones aprendidas, las soluciones adoptadas, los resultados obtenidos y las posibles explicaciones de estos resultados. En todo caso, se pueden extraer algunas lecciones relevantes del abrumador trabajo que representa esta parte.

- Se ha diseñado íntegramente un prototipo rotatorio de refrigeración magnética en el ICMA (ahora INMA) (Universidad de Zaragoza - CSIC) y se ha construido en colaboración con la empresa Dynatech Dynamics & Technology, S. L. U., que se encargaba del montaje del imán permanente en una estructura, y de dotarlo de un mecanismo de rotación, bombas de fluidos, electroválvulas de alta velocidad y un autómata programable basado en el control de válvulas. El resto del dispositivo, tubería de fluido, imán, AMR, sistema de adquisición de datos, etc. han sido diseñados e implementados en la Universidad de Zaragoza.

- Se ha logrado una mejora notable de un diseño de imán compacto de dos polos anterior, utilizando un procedimiento original de optimización, que no solo encuentra los valores óptimos para los parámetros de diseño definidos, sino que también proporciona información sobre la sensibilidad a su variación. El imán fue finalmente diseñado y construido, utilizando solo una pequeña cantidad de material magnético duro, con un gran volumen para alojar materiales magnetocalóricos (MMCs). Este diseño optimizado mejora el imán original:

  1. aumenta el campo máximo final medido a 1.50 T, en comparación con el valor de 1.13 T informado por Eriksen et al., [107], (más de un 7% de aumento) con un campo bajo medido de 0.00 T,
  2. reduce los riesgos de desimanación y saturación gracias a la orientación del campo en los sectores magnéticos de cada polo, la correcta selección de los materiales y la eliminación del menisco en la zona de bajo campo de hierro,
  3. tiene un menor coste de fabricación, ya que la eliminación del menisco disminuye los pasos necesarios,
  4. según los valores del funcional F, la mejora global es superior al 8%.

- La distribución del MMC en el anillo regenerador está bien equilibrada, lo que permite una fácil rotación con un par pequeño.

- La distribución de las regiones de campo y las ocho cavidades independientes del anillo regenerador permiten tener una frecuencia térmica global del ciclo de enfriamiento ocho veces superior a la rotación mecánica del imán, actuando simultáneamente en dos canales.

- El bloque regenerador del prototipo tiene un volumen muy grande que puede contener hasta 2.1 kg de gránulos de materiales LaFeMnSi-H o 2.4 kg de Gd y aleaciones GdEr. Tiene una gran versatilidad en el número de materiales graduados que puede contener, que pueden ser tanto de tipo FOPT, como de tipo SOPT.

A continuación se presentan las conclusiones del funcionamiento del prototipo.

- Los resultados preliminares con un bloque AMR de una sección de Gd, mostraron un salto térmico máximo de 2.1 °C sin carga aplicada, a 700 rpm del motor del imán—es decir, ∼0.79 Hz de frecuencia mecánica y ∼6.32 Hz de la frecuencia térmica general del dispositivo—con un volumen empujado del 100% del volumen vacío de AMR y un desfase entre flujo y magnetización de 20°.

- Las pruebas con un bloque AMR de tres secciones relleno con Gd y compuestos de GdEr muestran un salto térmico de 3 °C sin carga aplicada a 50 rpm del motor del imán—es decir, ∼0.04 Hz frecuencia mecánica y ∼0.67 Hz de la frecuencia térmica general del dispositivo— con un volumen empujado del 33% del volumen vacío de AMR y un desfase entre flujo y magnetización de 0°.

- Con el bloque regenerador de una sección, medidas de la evolución de las temperaturas en termopares situados en contacto con el MMC dieron valores compatibles con el efecto de cambio de campo en las esferas Gd. Siguiendo la forma de su curva cíclica, la forma del campo dada por el imán. La oscilación de temperatura sube a 2.2 K, que es un poco más alta que el salto térmico obtenido entre el foco frío y el foco caliente; sin embargo, los regeneradores no pueden crear un gradiente de temperatura a lo largo del MMC.

- Mediciones de relajación de temperatura de puntos internos del regenerador, tuberías y foco frío hacia la temperatura externa que, en el caso de los regeneradores, es la temperatura del imán y, para las tuberías y la fuente de frío, es la temperatura ambiente, indican importantes pérdidas de calor en el sistema.

- Otras posibles explicaciones no excluyentes del bajo rendimiento observado son:

    1. falta de equivalencia de las impulsiones frías y calientes debido a la incertidumbre en los tiempos reales de apertura y cierre de las electroválvulas,
    2. calentamiento producido por las electroválvulas,
    3. baja resolución y precisión de los sistemas de medición y configuración del prototipo, en relación a las necesidades reales,
    4. variabilidad en el compactado del MMC dentro de las secciones del regenerador, lo que puede provocar condiciones de trabajo diferenciales entre los AMR.

- Las electroválvulas son demasiado ruidosas y consumen mucha energía para cualquier uso en electrodomésticos.

En la parte II de esta tesis, se simula un sistema híbrido termoeléctrico-magnetocalórico (TE-MC) muy simple utilizando parámetros de trabajo de céldas Peltier comerciales y las propiedades de un material con una transición de fase magnetoestructural de primer orden, como $La(Fe,Si)_{13}H_{1.65}$. Los resultados se comparan con los correspondientes a un sistema TE puro y uno magnetocalórico puro con diodos térmicos ideales.

Un TE-MC se forma con una placa MMC insertada entre dos celdas termoeléctricas con la idea de combinar las mejores partes de ambas tecnologías—es decir, refrigeración magnética y comportamiento del diodo térmico, con un COP muy alto en condiciones de bombeo de calor muy bajo. Las conclusiones de este estudio se presentan a continuación.

- Se ha introducido una ecuación maestra original que modela la transferencia de calor para los MMC con transición de primer orden. Esta ecuación se ha utilizado con éxito para modelar el sandwich TE-MC-TE.

- El procedimiento analítico presentado demuestra que la inclusión del MMC puede mejorar mucho la eficiencia del TE por sí sólo, únicamente si se realizan los cálculos adecuados para determinar las condiciones de trabajo del sandwichpara un MMC dado.

- Los parámetros del sistema deben elegirse con cuidado, ya que los parámetros del MMC y del TE están correlacionados. Las corrientes están también relacionadas y fijando tres de ellas, se determina la cuarta. Escogiendo bien las cifras, el COP y la potencia frigorífica son mayores para el sistema híbrido. La ausencia de estas consideraciones, junto con el uso de parámetros no correlacionados, parece ser el origen del mal comportamiento observado por de Vries y van der Meer en [22], llevándolos a una conclusión negativa errónea.

- Para corrientes bajas (por ejemplo, 0.1 A) el COP de la celda Peltier considerada aumentó de 24, en el caso termoeléctrico puro, a 31 en el caso del dispositivo híbrido.

- Con la misma potencia de enfriamiento, el sistema híbrido realista tiene mayor eficiencia que el método Peltier puro, y similar al MC puro con diodos ideales.

- Los dispositivos híbridos TE-MC merecen ser estudiados más a fondo.

Appendices

Appendix A

EU 1060/2010

►**B**

COMMISSION DELEGATED REGULATION (EU) No 1060/2010

of 28 September 2010

supplementing Directive 2010/30/EU of the European Parliament and of the Council with regard to energy labelling of household refrigerating appliances

(Text with EEA relevance)

(OJ L 314, 30.11.2010, p. 17)

Amended by:

		Official Journal		
		No	page	date
►**M1**	Commission Delegated Regulation (EU) No 518/2014 of 5 March 2014	L 147	1	17.5.2014
►**M2**	Commission Delegated Regulation (EU) 2017/254 of 30 November 2016	L 38	1	15.2.2017
►**M3**	Commission Delegated Regulation (EU) 2020/1059 of 27 April 2020	L 232	28	20.7.2020

▼B

COMMISSION DELEGATED REGULATION (EU) No 1060/2010

of 28 September 2010

supplementing Directive 2010/30/EU of the European Parliament and of the Council with regard to energy labelling of household refrigerating appliances

(Text with EEA relevance)

Article 1

Subject matter and scope

1. This Regulation establishes requirements for the labelling of and the provision of supplementary product information on electric mains-operated household refrigerating appliances with a storage volume between 10 and 1 500 litres.

2. This Regulation shall apply to electric mains-operated household refrigerating appliances, including those sold for non-household use or for the refrigeration of items other than foodstuffs and including built-in appliances.

It shall also apply to electric mains-operated household refrigerating appliances that can be battery-operated.

3. This Regulation shall not apply to:

(a) refrigerating appliances that are primarily powered by energy sources other than electricity, such as liquefied petroleum gas (LPG), kerosene and bio-diesel fuels;

(b) battery-operated refrigerating appliances that can be connected to the mains through an AC/DC converter, purchased separately;

(c) custom-made refrigerating appliances, made on a one-off basis and not equivalent to other refrigerating appliance models;

(d) refrigerating appliances for tertiary sector application where the removal of refrigerated foodstuffs is electronically sensed and that information can be automatically transmitted through a network connection to a remote control system for accounting;

(e) appliances where the primary function is not the storage of foodstuffs through refrigeration, such as stand-alone ice-makers or chilled drinks dispensers.

Article 2

Definitions

In addition to the definitions laid down in Article 2 of Directive 2010/30/EU, the following definitions shall apply:

(1) ‘foodstuffs’ means food, ingredients, beverages including wine, and other items primarily intended for consumption which require refrigeration at specified temperatures;

▼B

(2) ‘household refrigerating appliance’ means an insulated cabinet, with one or more compartments, intended for refrigerating or freezing foodstuffs, or for the storage of refrigerated or frozen foodstuffs for non-professional purposes, cooled by one or more energy-consuming processes, including appliances sold as building kits to be assembled by the end-user;

(3) ‘built-in appliance’ means a fixed refrigerating appliance intended to be installed in a cabinet, in a prepared recess in a wall or similar location, and requiring furniture finishing;

(4) ‘refrigerator’ means a refrigerating appliance intended for the preservation of foodstuffs with at least one compartment suitable for the storage of fresh food and/or beverages, including wine;

(5) ‘compression-type refrigerating appliance’ means a refrigerating appliance in which refrigeration is effected by means of a motor-driven compressor;

(6) ‘absorption-type refrigerating appliance’ means a refrigerating appliance in which refrigeration is effected by an absorption process using heat as the energy source;

(7) ‘refrigerator-freezer’ means a refrigerating appliance with at least one fresh-food storage compartment and at least one compartment suitable for the freezing of fresh food and the storage of frozen foodstuffs under three-star storage conditions (the food-freezer compartment);

(8) ‘frozen-food storage cabinet’ means a refrigerating appliance with one or more compartments suitable for the storage of frozen foodstuffs;

(9) ‘food freezer’ means a refrigerating appliance with one or more compartments suitable for freezing foodstuffs with temperatures ranging from ambient temperature down to – 18 °C, and which is also suitable for the storage of frozen foodstuffs under three-star storage conditions; a food freezer may also include two-star sections and/or compartments within the compartment or cabinet;

(10) ‘wine storage appliance’ means a refrigerating appliance that has no compartment other than one or more wine storage compartments;

(11) ‘multi-use appliance’ means a refrigerating appliance that has no compartment other than one or more multi-use compartments;

(12) ‘equivalent household refrigerating appliance’ means a household refrigerating appliance model placed on the market with the same gross and storage volumes, same technical, efficiency and performance characteristics, and same compartment types as another household refrigerating appliance model placed on the market under a different commercial code number by the same manufacturer;

(13) ‘end-user’ means a consumer buying or expected to buy a household refrigerating appliance;

▼B

(14) ‘point of sale’ means a location where household refrigerating appliances are displayed or offered for sale, hire or hire-purchase.

The definitions set out in Annex I shall also apply.

Article 3

Responsibilities of suppliers

Suppliers shall ensure that:

(a) each household refrigerating appliance is supplied with a printed label in the format and containing information as set out in Annex II;

(b) a product fiche, as set out in Annex III, is made available;

(c) the technical documentation as set out in Annex IV is made available on request to the authorities of Member States and to the Commission;

(d) any advertisement for a specific model of household refrigerating appliance contains the energy efficiency class, if the advertisement discloses energy-related or price information;

(e) any technical promotional material concerning a specific model of household refrigerating appliance which describes its specific technical parameters includes the energy efficiency class of that model;

▼M1

(f) an electronic label in the format and containing the information set out in Annex II is made available to dealers for each household refrigerating appliance model placed on the market from 1 January 2015 with a new model identifier. It may also be made available to dealers for other household refrigerating appliance models;

(g) an electronic product fiche as set out in Annex III is made available to dealers for each household refrigerating appliance model placed on the market from 1 January 2015 with a new model identifier. It may also be made available to dealers for other household refrigerating appliance models.

▼B

Article 4

Responsibilities of dealers

Dealers shall ensure that:

(a) each household refrigerating appliance at the point of sale bears the label provided by suppliers in accordance with Article 3(a) on the outside of the front or top of the appliance, in such a way as to be clearly visible;

▼M1

(b) household refrigerating appliances offered for sale, hire or hire purchase where the end-user cannot be expected to see the product displayed, are marketed with the information to be provided by the suppliers in accordance with Annex V. Where the offer for is made through the internet and an electronic label and an electronic product fiche have been made available in accordance with Article 3(f) and 3(g) the provisions of Annex X shall apply instead;

▼B

(c) any advertisement for a specific model of household refrigerating appliance contains its energy efficiency class, if the advertisement discloses energy-related or price information;

(d) any technical promotional material concerning a specific model of household refrigerating appliance, which describes its specific technical parameters, includes the energy efficiency class of that model.

Article 5

Measurement methods

The information to be provided pursuant to Article 3 shall be obtained by reliable, accurate and reproducible measurement procedures, which take into account the recognised state-of-the-art measurement methods, as set out in Annex VI.

Article 6

Verification procedure for market surveillance purposes

Member States shall apply the procedure laid down in Annex VII when assessing the conformity of the declared energy efficiency class, the annual energy consumption, the fresh and frozen food volumes, the freezing capacity and the airborne acoustical noise emissions.

Article 7

Revision

The Commission shall review this Regulation in the light of technological progress no later than four years after its entry into force. The review shall in particular assess the verification tolerances set out in Annex VII and the possibilities for removing or reducing the values of the correction factors set out in Annex VIII.

Article 8

Repeal

Directive 94/2/EC is repealed from 30 November 2011.

Article 9

Transitional provisions

1. Articles 3(d), (e), 4(b), (c) and (d) shall not apply to printed advertisement and printed technical promotional material published before 30 March 2012.

▼B

2. Household refrigerating appliances placed on the market before 30 November 2011 shall comply with the provisions set out in Directive 94/2/EC.

3. Household refrigerating appliances which comply with the provisions of this Regulation and which are placed on the market or offered for sale, hire or hire-purchase before 30 November 2011 shall be regarded as complying with the requirements of Directive 94/2/EC.

Article 10

Entry into force and application

1. This Regulation shall enter into force on the 20th day following its publication in the *Official Journal of the European Union*.

2. It shall apply from 30 November 2011. However, Articles 3(d), (e), 4(b), (c) and (d) shall apply from 30 March 2012.

This Regulation shall be binding in its entirety and directly applicable in all Member States.

▼B

ANNEX I

Definitions applicable for the purposes of Annexes II to IX

For the purposes of Annexes II to IX, the following definitions shall apply:

(a) ‘frost-free system’ means a system automatically operated to prevent the permanent formation of frost, where cooling is provided by forced air circulation, the evaporator or evaporators are defrosted by an automatic defrost system, and the water from defrosting is disposed of automatically;

(b) ‘frost-free compartment’ means any compartment defrosted by a frost-free system;

(c) ‘refrigerator-cellar’ means a refrigerating appliance where at least one fresh-food storage compartment and one cellar compartment, but no frozen-food storage, chill or ice-making compartments, are present;

(d) ‘cellar’ means a refrigerating appliance where only one or more cellar compartments are present;

(e) ‘refrigerator-chiller’ means a refrigerating appliance where at least a fresh-food storage compartment and a chill compartment, but no frozen-food storage compartments, are present;

(f) ‘compartments’ means any of the compartments listed in points (g) to (n);

(g) ‘fresh-food storage compartment’ means a compartment designed for the storage of unfrozen foodstuffs, which may itself be divided into sub-compartments;

(h) ‘cellar compartment’ means a compartment intended for the storage of particular foodstuffs or beverages at a temperature warmer than that of a fresh-food storage compartment;

(i) ‘chill compartment’ means a compartment intended specifically for the storage of highly perishable foodstuffs;

(j) ‘ice-making compartment’ means a low-temperature compartment intended specifically for the freezing and storage of ice;

(k) ‘frozen-food storage compartment’ means a low-temperature compartment intended specifically for the storage of frozen foodstuffs and classified according to temperature as follows:

(i) ‘one-star compartment’: a frozen-food storage compartment in which the temperature is not warmer than – 6 °C;

(ii) ‘two-star compartment’: a frozen-food storage compartment in which the temperature is not warmer than – 12 °C;

(iii) ‘three-star compartment’: a frozen-food storage compartment in which the temperature is not warmer than – 18 °C;

▼B

(iv) ‘food freezer compartment’ (or ‘four-star compartment’): a compartment suitable for freezing at least 4,5 kg of foodstuffs per 100 l of storage volume, and in no case less than 2 kg, from ambient temperature down to – 18 °C over a period of 24 hours, which is also suitable for the storage of frozen food under three-star storage conditions, and may include two-star sections within the compartment;

(v) ‘0-star compartment’: a frozen-food storage compartment in which the temperature is < 0 °C and which can also be used for the freezing and storage of ice but is not intended for the storage of highly perishable foodstuffs;

(l) ‘wine storage compartment’ means a compartment exclusively designed either for short-term wine storage to bring wines to the ideal drinking temperature or for long-term wine storage to allow wine to mature, with the following features:

(i) continuous storage temperature, either pre-set or set manually according to the manufacturer’s instructions, in the range from + 5 °C to + 20 °C;

(ii) storage temperature(s) within a variation over time of less than 0,5 K at each declared ambient temperature specified by the climate class for household refrigerating appliances;

(iii) active or passive control of the compartment humidity in the range from 50 % to 80 %;

(iv) constructed to reduce the transmission of vibration to the compartment, whether from the refrigerator compressor or from any external source;

(m) ‘multi-use compartment’ means a compartment intended for use at two or more of the temperatures of the compartment types and capable of being set by the end-user to continuously maintain the operating temperature range applicable to each compartment type according to the manufacturer’s instructions; however, where a feature can shift temperatures in a compartment to a different operating temperature range for a period of limited duration only (such as a fast-freeze facility), the compartment is not a ‘multi-use compartment’ as defined by this Regulation;

(n) ‘other compartment’ means a compartment, other than a wine storage compartment, intended for the storage of particular foodstuffs at a temperature warmer than + 14 °C;

(o) ‘two-star section’ means part of a food-freezer, a food-freezer compartment, a three-star compartment or a three-star frozen-food storage cabinet which does not have its own individual access door or lid and in which the temperature is not warmer than – 12 °C;

(p) ‘chest freezer’, means a food freezer in which the compartment(s) is (are) accessible from the top of the appliance or which has both top-opening type and upright type compartments but where the gross volume of the top-opening type compartment(s) exceeds 75 % of the total gross volume of the appliance;

▼B

(q) ‘top-opening type’ or ‘chest type’ means a refrigerating appliance with its compartment(s) accessible from the top of the appliance;

(r) ‘upright type’ means a refrigerating appliance with its compartment(s) accessible from the front of the appliance;

(s) ‘fast freeze’ means a reversible feature to be activated by the end-user according to the manufacturer’s instructions, which decreases the storage temperature of the freezer or freezer compartment to achieve faster freezing of unfrozen foodstuffs;

(t) ‘model identifier’ means the code, usually alphanumeric, which distinguishes a specific refrigerating appliance model from other models with the same trade mark or supplier’s name.

▼B

ANNEX II

Label

1. LABEL FOR HOUSEHOLD REFRIGERATING APPLIANCES CLASSIFIED IN ENERGY EFFICIENCY CLASSES A+++ TO C

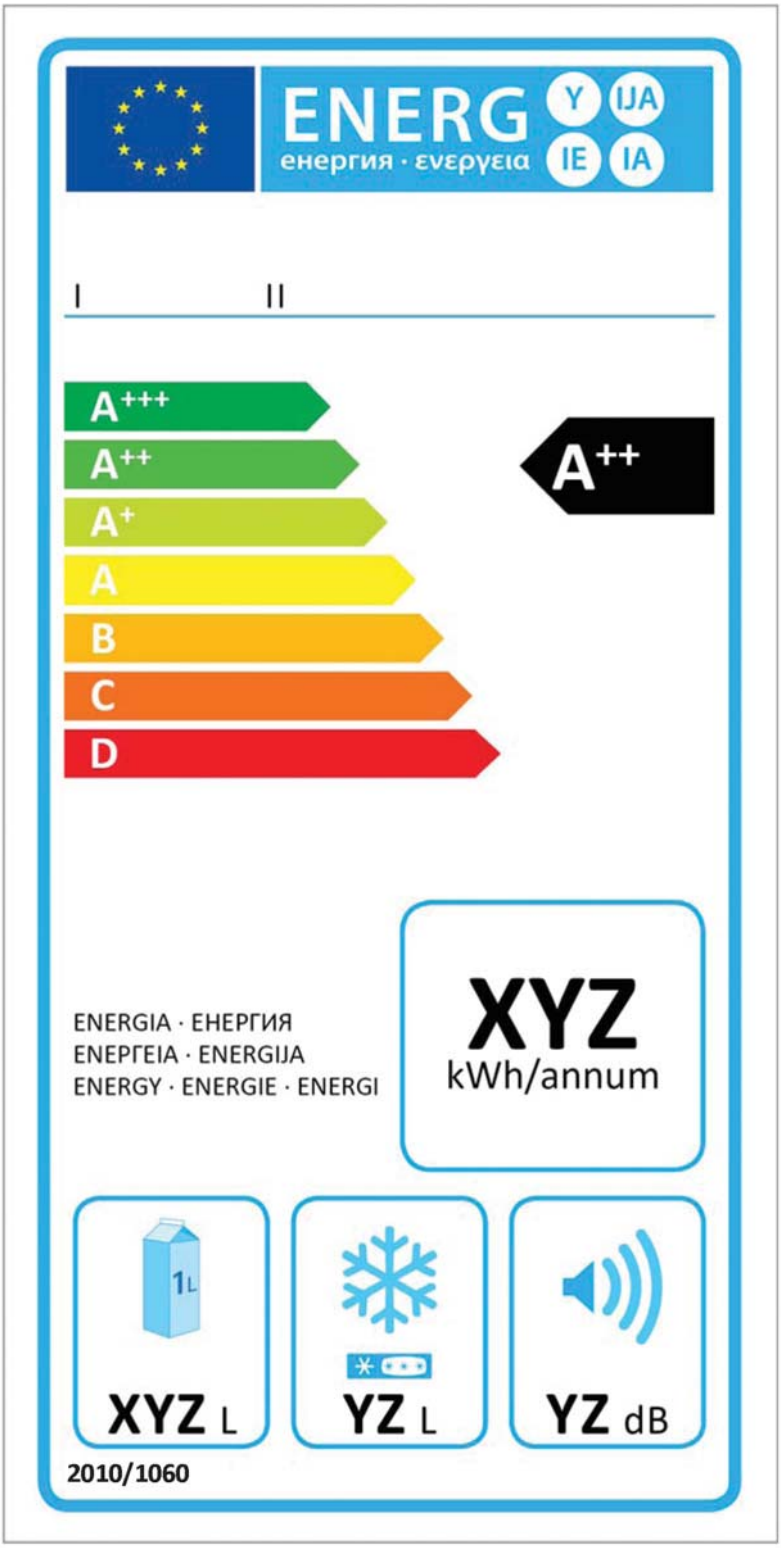

▼B

(1) The following information shall be included in the label:

I. supplier's name or trade mark;

II. supplier's model identifier;

III. the energy efficiency class determined in accordance with Annex IX; the head of the arrow containing the energy efficiency class of the household refrigerating appliance shall be placed at the same height as the head of the arrow of the relevant energy efficiency class;

IV. annual energy consumption (AE_C) in kWh per year, rounded up to the nearest integer and calculated in accordance with point 3(2) of Annex VIII;

V. sum of the storage volumes of all compartments that do not merit a star rating (i.e. operating temperature > – 6 °C), rounded to the nearest integer;

VI. sum of the storage volumes of all frozen-food storage compartments that merit a star rating (i.e. operating temperature ≤ – 6 °C), rounded to the nearest integer and star rating of the compartment with the highest share of that sum; where the household refrigerating appliances has no frozen-food storage compartment(s) the supplier shall declare '- L' instead of a value and leave the position for star rating blank;

VII. airborne acoustical noise emissions expressed in dB(A) re1 pW, rounded to the nearest integer.

However, for wine storage appliances, points V and VI are replaced by the rated capacity in number of standard bottles of 75 centilitres that may be fitted in the appliance in accordance with the manufacturer's instructions.

(2) The design of the label shall be in accordance with point 3(1) of this Annex. By way of derogation, where a model has been awarded an 'EU Ecolabel' under Regulation (EC) No 66/2010 of the European Parliament and of the Council ([1]), a copy of the EU Ecolabel may be added.

([1]) OJ L 27, 30.1.2010, p. 1.

▼B

2. LABEL FOR HOUSEHOLD REFRIGERATING APPLIANCES CLASSIFIED IN ENERGY EFFICIENCY CLASSES D TO G

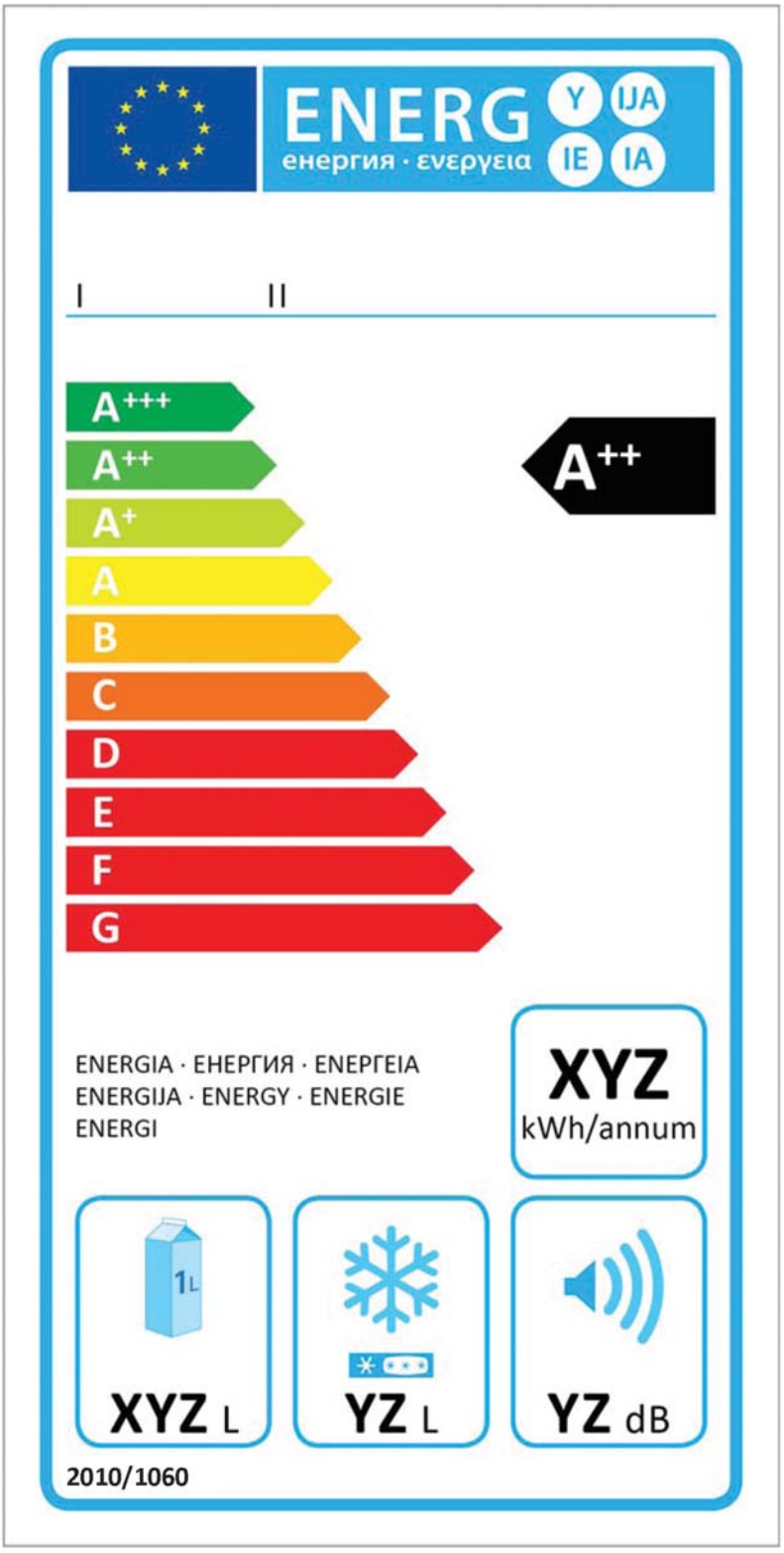

▼B

(1) The information listed in point 1(1) shall be included in this label.

(2) The design of the label shall be in accordance with point 3(2) of this Annex. By way of derogation, where a model has been awarded an 'EU Ecolabel' under Regulation (EC) No 66/2010, a copy of the EU Ecolabel may be added.

3. LABEL DESIGN

(1) For household refrigerating appliances classified in energy efficiency classes A+++ to C, except for wine storage appliances, the design of the label shall be as the following:

▼B

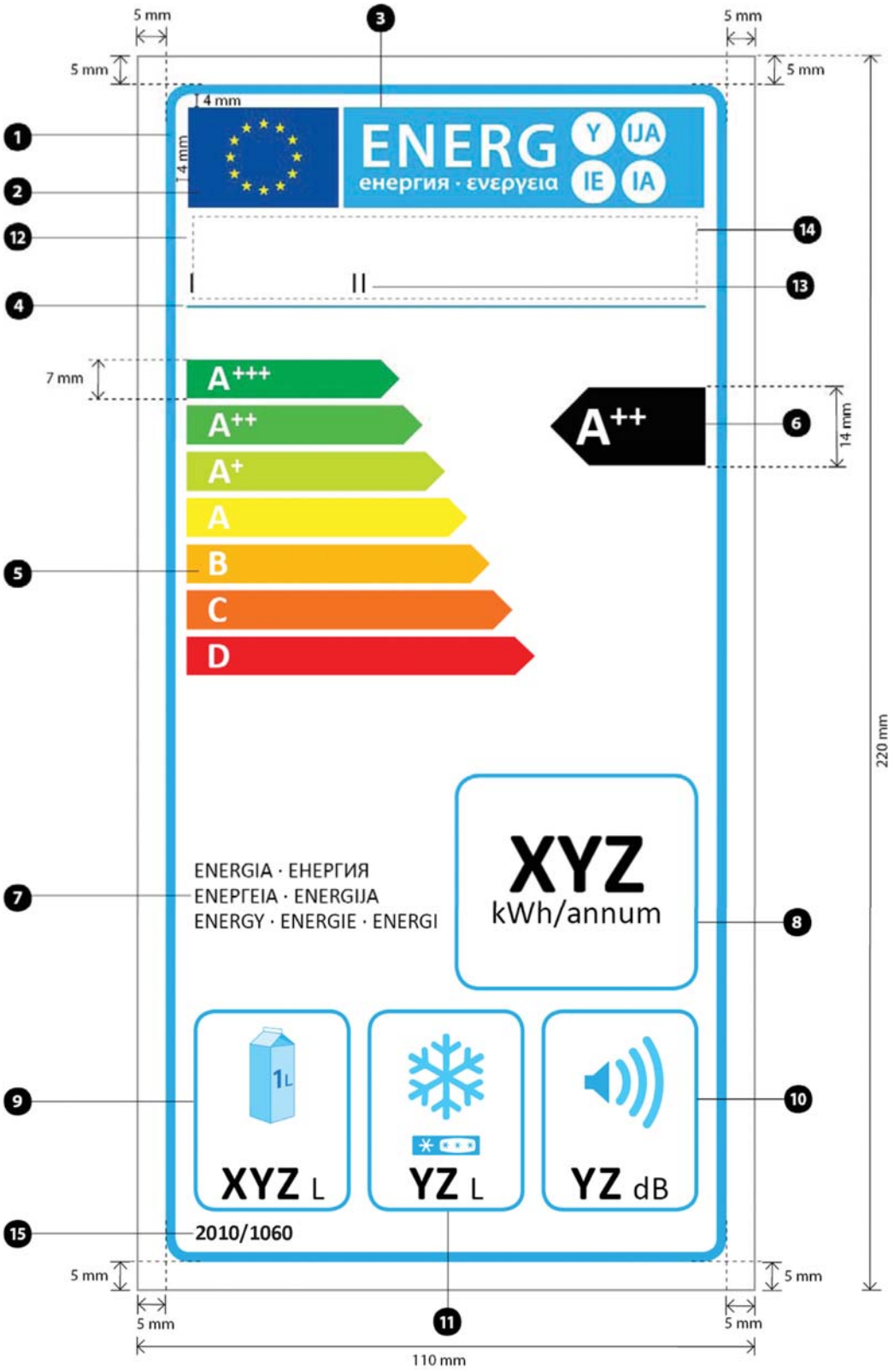
5 mm
5 mm
5 mm
5 mm
3
4 mm
14 mm
ENERG
енергия · ενεργεια
Y
IJA
IE
IA
1
2
12
14
I
II
13
4
7 mm
A+++
A++
A+
A
B
C
D
5
A++
6
14 mm
220 mm
ENERGIA · ЕНЕРГИЯ
ЕНЕРГЕІА · ENERGIJA
ENERGY · ENERGIE · ENERGI
7
XYZ
kWh/annum
8
1L
XYZ L
YZ L
YZ dB
9
10
15
2010/1060
11
5 mm
5 mm
5 mm
5 mm
110 mm

▼B

Whereby:

(a) The label shall be at least 110 mm wide and 220 mm high. Where the label is printed in a larger format, its content shall nevertheless remain proportionate to the specifications above.

(b) The background of the label shall be white.

(c) Colours shall be CMYK — cyan, magenta, yellow and black, following this example: 00-70-X-00: 0 % cyan, 70 % magenta, 100 % yellow, 0 % black.

(d) The label shall fulfil all of the following requirements (numbers refer to the figure above):

❶ **EU label border stroke:** 5 pt — colour: Cyan 100 % – round corners: 3,5 mm.

❷ **EU logo** — colours: X-80-00-00 and 00-00-X-00.

❸ **Energy label**: colour: X-00-00-00.

Pictogram as depicted: EU logo + energy label: width: 92 mm, height: 17 mm.

❹ **Sub-logos border:** 1 pt — colour: Cyan 100 % – length: 92,5 mm.

❺ **A-G scale**

— **Arrow:** height: 7 mm, gap: 0,75 mm — colours:

Highest class: X-00-X-00,

Second class: 70-00-X-00,

Third class: 30-00-X-00,

Fourth class: 00-00-X-00,

Fifth class: 00-30-X-00,

Sixth class: 00-70-X-00,

Last class: 00-X-X-00.

— **Text:** Calibri bold 19 pt, capitals and white; '+' symbols: Calibri bold 13 pt, capitals, white, aligned on a single row.

❻ **Energy efficiency class**

— **Arrow:** width: 26 mm, height: 14 mm, 100 % black;

— **Text:** Calibri bold 29 pt, capitals and white; '+' symbols: Calibri bold 18 pt, capitals, white and aligned on a single row.

❼ **Energy**

— **Text:** Calibri regular 11 pt, capitals, black.

▼B

❽ **Annual energy consumption:**

— **Border:** 3 pt — colour: Cyan 100 % — round corners: 3,5 mm.

— **Value:** Calibri bold 45 pt, 100 % black.

— **Second line:** Calibri regular 17 pt, 100 % black.

❾ **Storage volumes of all compartments that do not merit a star rating:**

— **Border:** 3 pt — colour: Cyan 100 % — round corners: 3,5 mm.

— **Value:** Calibri bold 25 pt, 100 % black. Calibri regular 17 pt, 100 % black.

❿ **Airborne acoustical noise emissions:**

— **Border:** 3 pt — colour: Cyan 100 % — round corners: 3,5 mm.

— **Value:** Calibri bold 25 pt, 100 % black.

Calibri regular 17 pt, 100 % black.

⓫ **Storage volumes of all frozen-food storage compartments that merit a star rating:**

— **Border:** 3 pt — colour: Cyan 100 % — round corners: 3,5 mm.

— **Value:** Calibri bold 25 pt, 100 % black.

Calibri regular 17 pt, 100 % black.

⓬ **Supplier's name or trademark**

⓭ **Supplier's model identifier**

⓮ The supplier's name or trademark and model identifier should fit in a space of 90 x 15 mm.

⓯ **Numbering of the Regulation:**

Text: Calibri bold 11 pt.

(2) For household refrigerating appliances classified in energy efficiency classes D to G, except for wine storage appliances, the design of the label shall be the following:

▼B

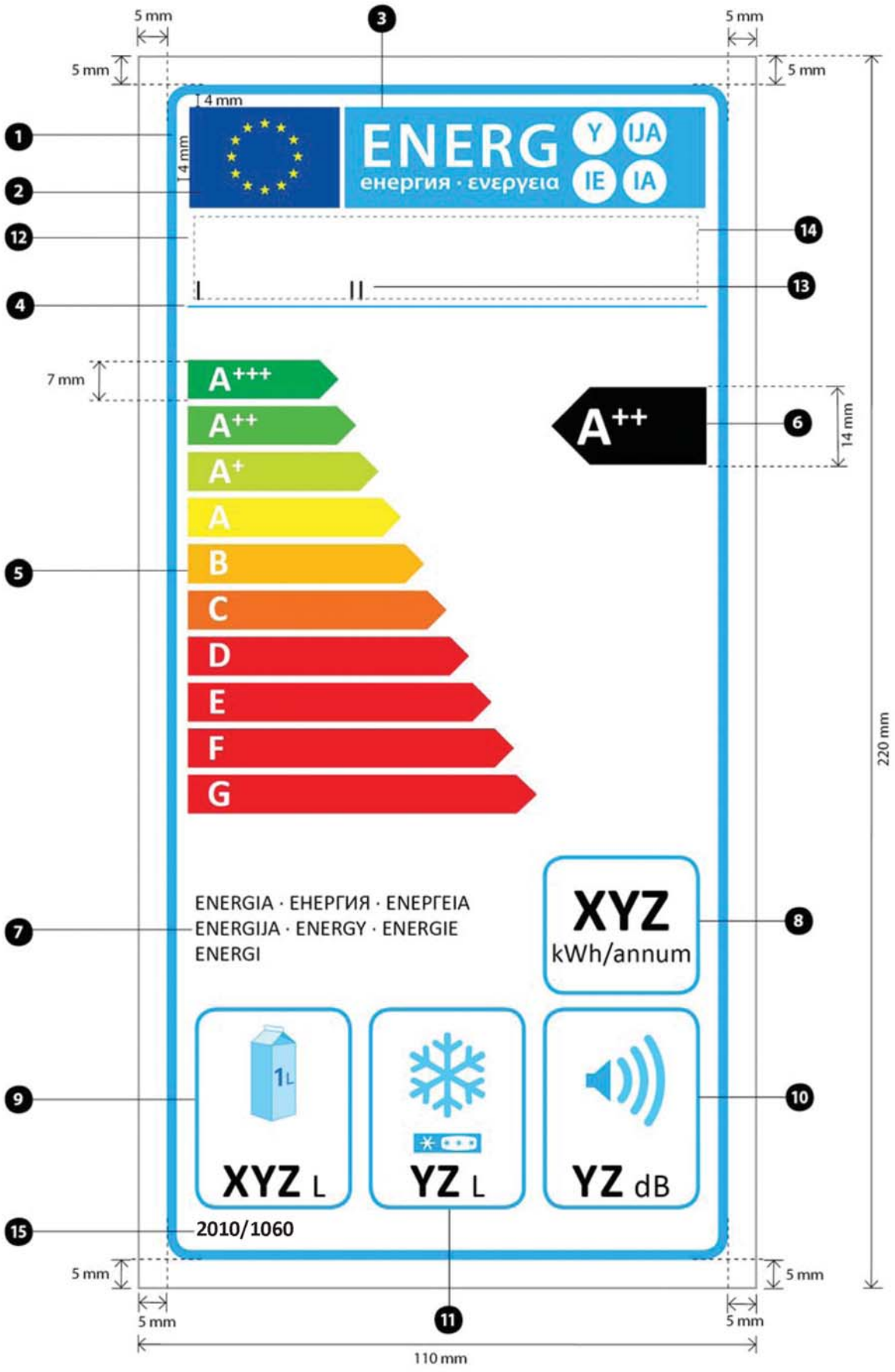
5 mm
5 mm
5 mm
5 mm
4 mm
4 mm
ENERG
енергия · ενεργεια
Y
IJA
IE
IA
1
2
3
4
5
6
7
8
9
10
11
12
13
14
15
7 mm
A+++
A++
A+
A
B
C
D
E
F
G
A++
14 mm
220 mm
ENERGIA · ЕНЕРГИЯ · ΕΝΕΡΓΕΙΑ
ENERGIJA · ENERGY · ENERGIE
ENERGI
XYZ
kWh/annum
1L
XYZ L
YZ L
YZ dB
2010/1060
5 mm
5 mm
5 mm
5 mm
110 mm

▼B

Whereby:

The design of the label shall be in accordance with point 3(1) of this Annex except for Number 8 where the following applies:

❽ **Annual energy consumption:**

— **Border:** 3 pt — colour: Cyan 100 % — round corners: 3,5 mm.

— **Value:** Calibri bold 32 pt, 100 % black.

— **Second line:** Calibri regular 14 pt, 100 % black.

(3) For wine storage appliances, the design of the label shall be the following:

▼B

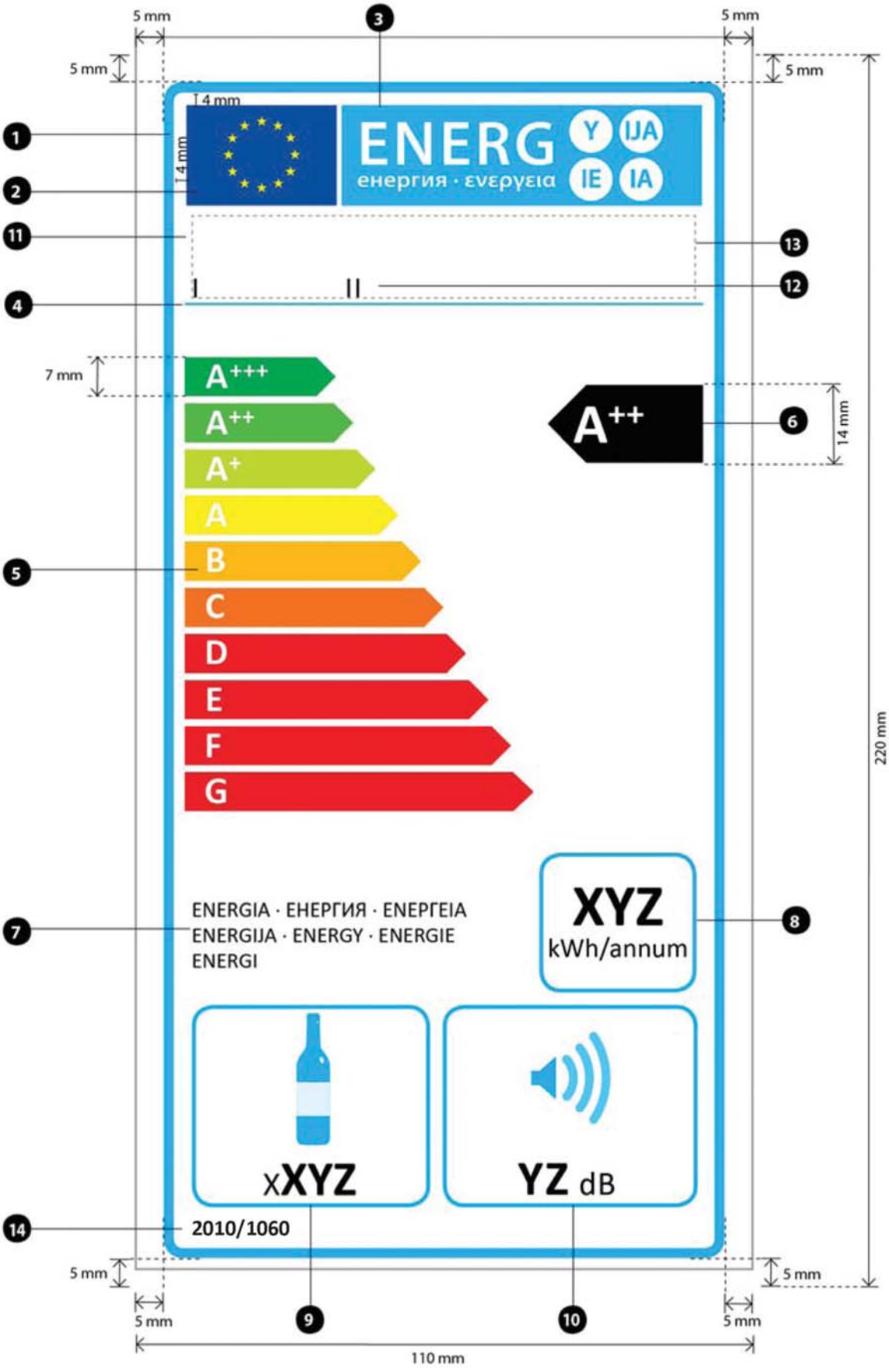
5 mm
5 mm
5 mm
5 mm
14 mm
14 mm
ENERG
енергия · ενεργεια
Y
IJA
IE
IA
I
II
7 mm
A+++
A++
A+
A
B
C
D
E
F
G
A++
14 mm
220 mm
ENERGIA · ЕНЕРГИЯ · ΕΝΕΡΓΕΙΑ
ENERGIJA · ENERGY · ENERGIE
ENERGI
XYZ
kWh/annum
xXYZ
YZ dB
2010/1060
5 mm
5 mm
5 mm
5 mm
110 mm
1
2
3
4
5
6
7
8
9
10
11
12
13
14

▼B

Whereby:

(a) The label shall be at least 110 mm wide and 220 mm high. Where the label is printed in a larger format, its content shall nevertheless remain proportionate to the specifications above.

(b) The background of the label shall be white.

(c) Colours shall be CMYK — cyan, magenta, yellow and black, following this example: 00-70-X-00: 0 % cyan, 70 % magenta, 100 % yellow, 0 % black.

(d) The label shall fulfil all of the following requirements (numbers refer to the figure above):

❶ **EU label border stroke:** 5 pt — colour: Cyan 100 % – round corners: 3,5 mm.

❷ **EU logo** — colours: X-80-00-00 and 00-00-X-00.

❸ **Energy label**: colour: X-00-00-00.

Pictogram as depicted: EU logo + energy label: width: 92 mm, height: 17 mm.

❹ **Sub-logos border:** 1 pt — colour: Cyan 100 % — length: 92,5 mm.

❺ **A-G scale**

— **Arrow:** height: 7 mm, gap: 0,75 mm — colours:

Highest class: X-00-X-00,

Second class: 70-00-X-00,

Third class: 30-00-X-00,

Fourth class: 00-00-X-00,

Fifth class: 00-30-X-00,

Sixth class: 00-70-X-00,

Last class(es): 00-X-X-00.

— **Text:** Calibri bold 19 pt, capitals and white; '+' symbols: Calibri bold 13 pt, capitals, white, aligned on a single row.

❻ **Energy efficiency class**

— **Arrow:** width: 26 mm, height: 14 mm, 100 % black;

— **Text:** Calibri bold 29 pt, capitals, white; '+' symbols: Calibri bold 18 pt, capitals, white, aligned on a single row.

❼ **Energy**

— **Text:** Calibri regular 11 pt, capitals, black.

▼B

❽ **Annual energy consumption:**

— **Border:** 2 pt — colour: Cyan 100 % — round corners: 3,5 mm.

— **Value:** Calibri bold 30 pt, 100 % black.

— **Second line:** Calibri regular 14 pt, 100 % black.

❾ **Rated capacity in number of standard wine bottles:**

— **Border:** 2 pt — colour: Cyan 100 % — round corners: 3,5 mm.

— **Value**: Calibri bold 28 pt, 100 % black.

Calibri regular 15 pt, 100 % black.

❿ **Airborne acoustical noise emissions:**

— **Border:** 2 pt — colour: Cyan 100 % — round corners: 3,5 mm.

— **Value**: Calibri bold 25 pt, 100 % black.

Calibri regular 17 pt, 100 % black.

⓫ **Supplier's name or trademark**

⓬ **Supplier's model identifier**

⓭ The suppliers' name or trade mark and model identifier should fit in a space of 90 × 15 mm

⓮ **Numbering of the Regulation:**

Text: Calibri bold 11 pt.

▼B

ANNEX III

Product Fiche

1. The information in the product fiche shall be provided in the following order and shall be included in the product brochure or other literature provided with the product:

(a) supplier's name or trade mark;

(b) supplier's model identifier as defined in Annex I, point (t);

(c) category of the household refrigerating appliance model in accordance with point 1 of Annex VIII;

(d) energy efficiency class of the model in accordance with Annex IX;

(e) where the model has been awarded an 'EU Ecolabel award' under Regulation (EC) No 66/2010, this information may be included;

(f) annual energy consumption (AE_C) in kWh per year, rounded up to the nearest integer and calculated in accordance with point 3(2) of Annex VIII. It shall be described as: 'Energy consumption "XYZ" kWh per year, based on standard test results for 24 hours. Actual energy consumption will depend on how the appliance is used and where it is located';

(g) storage volume of each compartment and applicable star rating in accordance with point 1(1)VI of Annex II, if any;

(h) the design temperature of 'other compartments' within the meaning of point (n) of Annex I. For wine storage compartments, the coldest storage temperature, either pre-set in the compartment or capable of being set by an end-user and capable of being maintained continuously according to the manufacturer's instructions, shall be given;

(i) the mention 'frost-free' for the relevant compartment(s), as defined in point (b) of Annex I;

(j) 'power cut safe "X" h' defined as 'temperature rise time';

(k) 'freezing capacity' in kg/24 h;

(l) 'climate class' in accordance with point 1, Table 3 of Annex VIII, and expressed as: 'Climate class: W [*climate class*]. This appliance is intended to be used at an ambient temperature between "X" [*lowest temperature*] °C and "X" [*highest temperature*] °C';

(m) airborne acoustical noise emissions expressed in dB(A) re1 pW, rounded to the nearest integer;

▼B

(n) if the model is intended to be a built-in appliance, an indication to this effect;

(o) for wine storage appliances, the following information: ‘This appliance is intended to be used exclusively for the storage of wine’. This point shall not apply to household refrigerating appliances that are not specifically designed for wine storage but may nevertheless be used for this purpose, nor to household refrigerating appliances that have a wine storage compartment combined with any other compartment type.

2. One fiche may cover a number of refrigerating appliances models supplied by the same supplier.

3. The information contained in the fiche may be given in the form of a copy of the label, either in colour or in black and white. Where this is the case, the information listed in point 1 not already displayed on the label shall also be provided.

▼B

ANNEX IV

Technical documentation

1. The technical documentation referred to in Article 3(c) shall include:

   (a) the name and address of the supplier;

   (b) a general description of the refrigerating appliance model, sufficient for it to be unequivocally and easily identified;

   (c) where appropriate, the references of the harmonised standards applied;

   (d) where appropriate, the other technical standards and specifications used;

   (e) identification and signature of the person empowered to bind the supplier;

   (f) technical parameters for measurements, established in accordance with Annex VIII:

      (i) overall dimensions;

      (ii) overall space required in use;

      (iii) total gross volumes(s);

      (iv) storage volume(s) and total storage volume(s);

      (v) star rating(s) of the frozen-food storage compartment(s);

      (vi) defrosting type;

      (vii) storage temperature;

      (viii) energy consumption;

      (ix) temperature rise time;

      (x) freezing capacity;

      (xi) power consumption;

      (xii) wine storage compartment humidity;

      (xiii) airborne acoustical noise emissions;

   (g) the results of calculations performed in accordance with Annex VIII.

2. Where the information included in the technical documentation file for a particular household refrigerating appliance model has been obtained by calculation on the basis of design, or extrapolation from other equivalent refrigerating appliances, or both, the documentation shall include details of such calculations or extrapolations, or both, and of tests undertaken by suppliers to verify the accuracy of the calculations undertaken. The information shall also include a list of all other equivalent household refrigerating appliance models where the information was obtained on the same basis.

▼B

ANNEX V

Information to be provided in the cases where end-users cannot be expected to see the product displayed

1. The information referred to in Article 4(b) shall be provided in the following order:

   (a) the energy efficiency class of the model as defined in Annex IX;

   (b) the annual energy consumption in kWh per year, rounded up to the nearest integer and calculated in accordance with point 3(2) of Annex VIII;

   (c) the storage volume of each compartment and applicable star rating in accordance with point 1(1)VI of Annex II, if any;

   (d) the ‘climate class’ in accordance with point 1, Table 3 of Annex VIII;

   (e) airborne acoustical noise emissions expressed in dB(A) re1 pW, rounded to the nearest integer;

   (f) if the model is intended to be built-in, an indication to this effect;

   (g) for wine storage appliances the following information: ‘This appliance is intended to be used exclusively for the storage of wine’. This point shall not apply to household refrigerating appliances that are not specifically designed for wine storage but may nevertheless be used for this purpose, nor to household refrigerating appliances that have a wine storage compartment combined with any other compartment type.

2. Where other information contained in the product fiche is also provided, it shall be in the form and order specified in Annex III.

3. The size and font in which all the information referred in this Annex is printed or shown shall be legible.

▼B

ANNEX VI

Measurements

1. For the purposes of compliance and verification of compliance with the requirements of this Regulation, measurements shall be made using a reliable, accurate and reproducible measurement procedure that takes into account the generally recognised state-of-the-art measurement methods, including methods set out in documents the reference numbers of which have been published for that purpose in the *Official Journal of the European Union*.

2. GENERAL CONDITIONS FOR TESTING

The following general conditions for testing apply:

(1) if anti-condensation heaters that can be switched on and off by the end-user are provided, they shall be switched on and — if adjustable — set at maximum heating;

(2) if 'through-the-door devices' (such as ice or chilled water/drinks dispensers) which can be switched on and off by the end-user are provided, they shall be switched on during the energy consumption measurement but not operated;

(3) for multi-use appliances and compartments, the storage temperature during the measurement of energy consumption shall be the nominal temperature of the coldest compartment type as claimed for continuous normal use according to the manufacturer's instructions;

(4) the energy consumption of a household refrigerating appliance shall be determined in the coldest configuration, according to the manufacturer's instructions for continuous normal use for any 'other compartment' as defined in Annex VIII, Table 5.

3. TECHNICAL PARAMETERS

The following parameters shall be established:

(a) 'overall dimensions', which are measured to the nearest millimetre;

(b) 'overall space required in use', which is measured to the nearest millimetre;

(c) 'total gross volumes(s)', which is measured to the nearest whole number of cubic decimetres or litres;

(d) 'storage volume(s) and total storage volume(s)', which is measured to the nearest whole number of cubic decimetres or of litres;

(e) 'defrosting type';

(f) 'storage temperature';

(g) 'energy consumption' which is expressed in kilowatt hours per 24 hours (kWh/24h), to three decimal places;

(h) 'temperature rise time';

(i) 'freezing capacity';

(j) 'wine storage compartment humidity', which is expressed as a percentage rounded to the nearest integer; and

(k) 'airborne acoustical noise emissions'.

▼M2

ANNEX VII

Product compliance verification by market surveillance authorities

The verification tolerances set out in this Annex relate only to the verification of the measured parameters by Member State authorities and shall not be used by the supplier as an allowed tolerance to establish the values in the technical documentation. The values and classes on the label or in the product fiche shall not be more favourable for the supplier than the values reported in the technical documentation.

When verifying the compliance of a product model with the requirements laid down in this Delegated Regulation, for the requirements referred to in this Annex, the authorities of the Member States shall apply the following procedure:

(1) The Member State authorities shall verify one single unit of the model.

(2) The model shall be considered to comply with the applicable requirements if:

(a) the values given in the technical documentation pursuant to Article 5(b) of Directive 2010/30/EU (declared values), and, where applicable, the values used to calculate these values, are not more favourable for the supplier than the corresponding values given in the test reports pursuant to point (iii) of the abovementioned Article; and

(b) the values published on the label and in the product fiche are not more favourable for the supplier than the declared values, and the indicated energy efficiency class is not more favourable for the supplier than the class determined by the declared values; and

(c) when the Member State authorities test the unit of the model, the determined values (the values of the relevant parameters as measured in testing and the values calculated from these measurements) comply with the respective verification tolerances as given in Table 1.

(3) If the results referred to in points 2(a) or (b) are not achieved, the model and all models that have been listed as equivalent household refrigerating appliance models in the supplier's technical documentation shall be considered not to comply with this Delegated Regulation.

(4) If the result referred to in point 2(c) is not achieved, the Member State authorities shall select three additional units of the same model for testing. As an alternative, the three additional units selected may be of one or more different models that have been listed as equivalent models in the supplier's technical documentation.

(5) The model shall be considered to comply with the applicable requirements if for these three units, the arithmetical mean of the determined values complies with the respective tolerances given in Table 1.

(6) If the result referred to in point 5 is not achieved, the model and all models that have been listed as equivalent household refrigerating appliance models in the supplier's technical documentation shall be considered not to comply with this Delegated Regulation.

(7) The Member State authorities shall provide all relevant information to the authorities of the other Member States and to the Commission without delay after a decision being taken on the non-compliance of the model according to points 3 and 6.

▼M2

The Member State authorities shall use the measurement and calculation methods set out in Annexes VI and VIII.

The Member State authorities shall only apply the verification tolerances that are set out in Table 1 and shall only use the procedure described in points 1 to 7 for the requirements referred to in this Annex. No other tolerances, such as those set out in harmonised standards or in any other measurement method, shall be applied.

Table 1

Verification tolerances

Parameters	Verification tolerances
Gross volume	The determined value shall not be less than the declared value by more than 3 % or 1 litre, whichever is the greater value.
Storage volume	The determined value shall not be less than the declared value by more than 3 % or 1 litre, whichever is the greater value. Where the volumes of the cellar compartment and the fresh food storage compartment can be adjusted, relative to one another, by the user, the volume shall be tested when the cellar compartment is adjusted to its minimum volume.
Freezing capacity	The determined value shall not be less than the declared value by more than 10 %.
Energy consumption	The determined value shall not exceed the declared value (E_{24h}) by more than 10 %.
Humidity of wine storage appliances	The determined value for the relative humidity observed in testing shall not exceed the declared range by more than 10 % in any direction.
Airborne acoustical noise emissions	The determined value shall meet the declared value.

▼B

ANNEX VIII

Classification of household refrigerating appliances, method for calculating the equivalent volume and the Energy Efficiency Index

1. CLASSIFICATION OF HOUSEHOLD REFRIGERATING APPLIANCES

Household refrigerating appliances are classified into categories as listed in Table 1.

Each category is defined by the specific compartment composition as specified in Table 2 and is independent of the number of doors and/or drawers.

Table 1

Household refrigerating appliances categories

Category	Designation
1	Refrigerator with one or more fresh-food storage compartments
2	Refrigerator-cellar, Cellar and Wine storage appliances
3	Refrigerator-chiller and Refrigerator with a 0-star compartment
4	Refrigerator with a one-star compartment
5	Refrigerator with a two-star compartment
6	Refrigerator with a three-star compartment
7	Refrigerator-freezer
8	Upright freezer
9	Chest freezer
10	Multi-use and other refrigerating appliances

Household refrigerating appliances that cannot be classified in categories 1 to 9 because of compartment temperature are classified in category 10.

▼B

Table 2

Household refrigerating appliance classification and relevant compartment composition

Nominal temperature (for the EEI) (°C)	Design T	+ 12	+ 12	+ 5	0	0	– 6	– 12	– 18	– 18	Category (number)
Compartment types	Other	Wine storage	Cellar	Fresh food storage	Chill	0-star/Ice making	one-star	two-star	three-star	four-star	
Appliance category	Compartments composition										
REFRIGERATOR WITH ONE OR MORE FRESH-FOOD STORAGE COMPARTMENTS	N	N	N	Y	N	N	N	N	N	N	1
REFRIGERATOR-CELLAR, CELLAR and WINE STORAGE APPLIANCE	O	O	O	Y	N	N	N	N	N	N	2
	O	O	Y	N	N	N	N	N	N	N	
	N	Y	N	N	N	N	N	N	N	N	
REFRIGERATOR-CHILLER and REFRIGERATOR WITH A 0-STAR COMPARTMENT	O	O	O	Y	Y	O	N	N	N	N	3
	O	O	O	Y	O	Y	N	N	N	N	
REFRIGERATOR WITH A ONE-STAR COMPARTMENT	O	O	O	Y	O	O	Y	N	N	N	4
REFRIGERATOR WITH A TWO-STAR COMPARTMENT	O	O	O	Y	O	O	O	Y	N	N	5
REFRIGERATOR WITH A THREE-STAR COMPARTMENT	O	O	O	Y	O	O	O	O	Y	N	6
REFRIGERATOR-FREEZER	O	O	O	Y	O	O	O	O	O	Y	7
UPRIGHT FREEZER	N	N	N	N	N	N	N	O	(Y) [a]	Y	8
CHEST FREEZER	N	N	N	N	N	N	N	O	N	Y	9
MULTI-USE AND OTHER APPLIANCES	O	O	O	O	O	O	O	O	O	O	10

Notes:

Y = the compartment is present; N = the compartment is not present; O = the presence of the compartment is optional;
[a] also includes three-star frozen-food cabinets.

▼B

Household refrigerating appliances are classified in one or more climate classes as specified in Table 3.

Table 3

Climate classes

Class	Symbol	Ambient average temperature °C
Extended temperate	SN	+ 10 to + 32
Temperate	N	+ 16 to + 32
Subtropical	ST	+ 16 to + 38
Tropical	T	+ 16 to + 43

The refrigerating appliance shall be capable of maintaining the required storage temperatures in the different compartments simultaneously and within the permitted temperature deviations (during the defrost cycle) as specified in Table 4 for the different types of household refrigerating appliances and for the appropriate climate classes.

Multi-use appliances and compartments shall be capable of maintaining the required storage temperatures of the different compartment types where these temperatures can be set by the end-user according to the manufacturer's instructions.

Table 4

Storage temperatures

Storage temperatures (°C)							
Other compartment	Wine storage compartment	Cellar compartment	Fresh-food storage compartment	Chill compartment	One-star compartment	Two-star compartment/section	Food freezer and three-star compartment/cabinet
t_{om}	t_{wma}	t_{cm}	t_{1m}, t_{2m}, t_{3m}, t_{ma}	t_{cc}	t*	t**	t***
> + 14	+ 5 ≤ tw_{ma} ≤ + 20	+ 8 ≤ t_{cm} ≤ + 14	0 ≤ t_{1m}, t_{2m}, t_{3m} ≤ + 8; t_{ma} ≤ + 4	− 2 ≤ t_{cc} ≤ + 3	≤ − 6	≤ − 12 [a]	≤ − 18 [a]

Notes:

— t_{om}: storage temperature of the other compartment.
— t_{wma}: storage temperature of the wine storage compartment with a variation of 0,5 K.
— t_{cm}: storage temperature of the cellar compartment.
— t_{1m}, t_{2m}, t_{3m}: storage temperatures of the fresh-food compartment.
— t_{ma}: average storage temperature of the fresh-food compartment.
— t_{cc}: instantaneous storage temperature of the chill compartment.
— t*, t**, t***: maximum temperatures of the frozen-food storage compartments.
— storage temperature for the ice-making compartment and for the '0-star' compartment is below 0 °C.
([a]) for frost-free household refrigerating appliances during the defrost cycle, a temperature deviation of no more than 3 K during a period of 4 hours or 20 % of the duration of the operating cycle, whichever is the shorter, is allowed.

2. CALCULATION OF THE EQUIVALENT VOLUME

The equivalent volume of a household refrigerating appliance is the sum of the equivalent volumes of all compartments. It is calculated in litres and rounded to the nearest integer as:

$$V_{eq} = \left[\sum_{c=1}^{c=n} V_c \times \frac{(25 - T_c)}{20} \times FF_c\right] \times CC \times BI$$

▼B

where:

— n is the number of compartments,

— V_c is the storage volume of the compartment(s),

— T_c is the nominal temperature of the compartment(s) as set out in Table 2,

— $\frac{(25-T_c)}{20}$ is the thermodynamic factor as set in Table 5,

— FF_c, CC and BI are volume correction factors as set out in Table 6.

The thermodynamic correction factor $\frac{(25-T_c)}{20}$ is the temperature difference between the nominal temperature of a compartment T_c (defined in Table 2) and the ambient temperature under standard test conditions at + 25 °C, expressed as a ratio of the same difference for a fresh-food compartment at + 5 °C.

The thermodynamic factors for the compartments described in Annex I, points (g) to (n), are set out in Table 5.

Table 5

Thermodynamic factors for refrigerating appliance compartments

Compartment	Nominal temperature	$(25-T_c)/20$
Other compartment	Design temperature	$\frac{(25-T_c)}{20}$
Cellar compartment/Wine storage compartment	+ 12 °C	0,65
Fresh-food storage compartment	+ 5 °C	1,00
Chill compartment	0 °C	1,25
Ice-making compartment and 0-star compartment	0 °C	1,25
One-star compartment	– 6 °C	1,55
Two-star compartment	– 12 °C	1,85
Three-star compartment	– 18 °C	2,15
Food freezer compartment (four-star compartment)	– 18 °C	2,15

Notes:

(i) for multi-use compartments, the thermodynamic factor is determined by the nominal temperature as given in Table 2 of the coldest compartment type capable of being set by the end-user and maintained continuously according to the manufacturer's instructions;

(ii) for any two-star section (within a freezer) the thermodynamic factor is determined at T_c = – 12 °C;

(iii) for other compartments the thermodynamic factor is determined by the coldest design temperature capable of being set by the end-user and maintained continuously according to the manufacturer's instructions.

▼B

Table 6

Value of the correction factors

Correction factor	Value	Conditions
FF (frost-free)	1,2	For frost-free frozen-food storage compartments
	1	Otherwise
CC (climate class)	1,2	For T class (tropical) appliances
	1,1	For ST class (subtropical) appliances
	1	Otherwise
BI (built-in)	1,2	For built-in appliances under 58 cm in width
	1	Otherwise

Notes:

(i) *FF* is the volume correction factor for frost-free compartments;

(ii) *CC* is the volume correction factor for a given climate class. If a refrigerating appliance is classified in more than one climate class, the climate class with the highest correction factor is used for the calculation of the equivalent volume;

(iii) *BI* is the volume correction factor for built-in appliances.

3. CALCULATION OF THE ENERGY EFFICIENCY INDEX

For the calculation of the Energy Efficiency Index (*EEI*) of a household refrigerating appliance model, the annual energy consumption of the household refrigerating appliance is compared to its standard annual energy consumption.

(1) The Energy Efficiency Index (*EEI*) is calculated and rounded to the first decimal place, as:

$$EEI = \frac{AE_c}{SAE_c} \times 100$$

where:

AE_C = annual energy consumption of the household refrigerating appliance

SAE_C = standard annual energy consumption of the household refrigerating appliance.

(2) The annual energy consumption (AE_C) is calculated in kWh/year and rounded to two decimal places, as:

$$AE_C = E_{24h} \times 365$$

where:

E_{24h} is the energy consumption of the household refrigerating appliance in kWh/24h and rounded to three decimal places.

(3) The standard annual energy consumption (SAE_C) is calculated in kWh/year and rounded to two decimal places, as:

$$SAE_C = V_{eq} \times M + N + CH$$

where:

V_{eq} is the equivalent volume of the household refrigerating appliance

CH is equal to 50 kWh/year for household refrigerating appliances with a chill compartment with a storage volume of at least 15 litres

the *M* and *N* values are given in Table 7 for each household refrigerating appliance category.

▼B

Table 7

***M* and *N* values by household refrigerating appliance category**

Category	*M*	*N*
1	0,233	245
2	0,233	245
3	0,233	245
4	0,643	191
5	0,450	245
6	0,777	303
7	0,777	303
8	0,539	315
9	0,472	286
10	(*)	(*)

(*) *Note:* for Category 10 household refrigerating appliances the *M* and *N* values depend on the temperature and star rating of the compartment with the lowest storage temperature capable of being set by the end-user and maintained continuously according to the manufacturer's instructions. When only an ‘other compartment’ as defined in Table 2 and Annex I, point (n), is present, the *M* and *N* values for Category 1 are used. Appliances with three-star compartments or food-freezer compartments are considered to be refrigerator-freezers.

▼B

ANNEX IX

Energy efficiency classes

The energy efficiency class of a household refrigerating appliance shall be determined on the basis of its Energy Efficiency Index (*EEI*) as set out in Table 1 from 20 December 2011 until 30 June 2014 and Table 2 from 1 July 2014.

The Energy Efficiency Index of a household refrigerating appliance shall be determined in accordance with point 3 of Annex VIII.

Table 1

Energy efficiency classes until 30 June 2014

Energy efficiency class	Energy Efficiency Index
A+++ (most efficient)	$EEI < 22$
A++	$22 \leq EEI < 33$
A+	$33 \leq EEI <$ **44**
A	**44** $\leq EEI < 55$
B	$55 \leq EEI < 75$
C	$75 \leq EEI < 95$
D	$95 \leq EEI < 110$
E	$110 \leq EEI < 125$
F	$125 \leq EEI < 150$
G (least efficient)	$EEI \geq 150$

Table 2

Energy efficiency classes from 1 July 2014

Energy efficiency class	Energy Efficiency Index
A+++ (most efficient)	$EEI < 22$
A++	$22 \leq EEI < 33$
A+	$33 \leq EEI <$ **42**
A	**42** $\leq EEI < 55$
B	$55 \leq EEI < 75$
C	$75 \leq EEI < 95$
D	$95 \leq EEI < 110$
E	$110 \leq EEI < 125$
F	$125 \leq EEI < 150$
G (least efficient)	$EEI \geq 150$

▼M1

ANNEX X

Information to be provided in the case of sale, hire or hire-purchase through the internet

(1) For the purpose of points 2 to 5 of this Annex the following definitions shall apply:

(a) ‘display mechanism’ means any screen, including tactile screen, or other visual technology used for displaying internet content to users;

(b) ‘nested display’ means visual interface where an image or data set is accessed by a mouse click, mouse roll-over or tactile screen expansion of another image or data set;

(c) ‘tactile screen’ means a screen responding to touch, such as that of a tablet computer, slate computer or a smartphone;

(d) ‘alternative text’ means text provided as an alternative to a graphic allowing information to be presented in non-graphical form where display devices cannot render the graphic or as an aid to accessibility such as input to voice synthesis applications.

(2) The appropriate label made available by suppliers in accordance with Article 3(f) shall be shown on the display mechanism in proximity to the price of the product. The size shall be such that the label is clearly visible and legible and shall be proportionate to the size specified in point 3 of Annex II. The label may be displayed using a nested display, in which case the image used for accessing the label shall comply with the specifications laid down in point 3 of this Annex. If nested display is applied, the label shall appear on the first mouse click, mouse roll-over or tactile screen expansion on the image.

(3) The image used for accessing the label in the case of nested display shall:

(a) be an arrow in the colour corresponding to the energy efficiency class of the product on the label;

(b) indicate on the arrow the energy efficiency class of the product in white in a font size equivalent to that of the price; and

(c) have one of the following two formats:

(4) In the case of nested display, the sequence of display of the label shall be as follows:

(a) the image referred to in point 3 of this Annex shall be shown on the display mechanism in proximity to the price of the product;

(b) the image shall link to the label;

▼M1

(c) the label shall be displayed after a mouse click, mouse roll-over or tactile screen expansion on the image;

(d) the label shall be displayed by pop up, new tab, new page or inset screen display;

(e) for magnification of the label on tactile screens, the device conventions for tactile magnification shall apply;

(f) the label shall cease to be displayed by means of a close option or other standard closing mechanism;

(g) the alternative text for the graphic, to be displayed on failure to display the label, shall be the energy efficiency class of the product in a font size equivalent to that of the price.

(5) The appropriate product fiche made available by suppliers in accordance with Article 3(g) shall be shown on the display mechanism in proximity to the price of the product. The size shall be such that the product fiche is clearly visible and legible. The product fiche may be displayed using a nested display, in which case the link used for accessing the fiche shall clearly and legibly indicate ‘Product fiche’. If nested display is used, the product fiche shall appear on the first mouse click, mouse roll-over or tactile screen expansion on the link.

Appendix B

EU 2019/2016

COMMISSION DELEGATED REGULATION (EU) 2019/2016

of 11 March 2019

supplementing Regulation (EU) 2017/1369 of the European Parliament and of the Council with regard to energy labelling of refrigerating appliances and repealing Commission Delegated Regulation (EU) No 1060/2010

(Text with EEA relevance)

THE EUROPEAN COMMISSION,

Having regard to the Treaty on the Functioning of the European Union,

Having regard to Regulation (EU) 2017/1369 of the European Parliament and of the Council of 4 July 2017 setting a framework for energy labelling and repealing Directive 2010/30/EU ([1]), and in particular Article 11(5) and Article 16(1) thereof,

Whereas:

(1) Regulation (EU) 2017/1369 empowers the Commission to adopt delegated acts as regards the labelling or re-scaling of the labelling of product groups representing significant potential for energy savings and, where relevant, other resources.

(2) Provisions on the energy labelling of household refrigerating appliances were established by Commission Delegated Regulation (EU) No 1060/2010 ([2]).

(3) The Communication from the Commission COM(2016) 773 ([3]) (ecodesign working plan) established by the Commission in application of Article 16(1) of Directive 2009/125/EC of the European Parliament and of the Council ([4]) sets out the working priorities under the ecodesign and energy labelling framework for the period 2016-2019. The ecodesign working plan identifies the energy-related product groups to be considered as priorities for the undertaking of preparatory studies and eventual adoption of implementing measures, as well as the review of Commission Regulation (EC) No 643/2009 ([5]) and Delegated Regulation (EU) No 1060/2010.

(4) Measures from the ecodesign working plan have an estimated potential to deliver in total in excess of 260 TWh of annual final energy savings in 2030, which is equivalent to reducing greenhouse gas emissions by approximately 100 million tonnes per year in 2030. Refrigerating appliances is one of the product groups listed in the ecodesign working plan, with an estimated 10 TWh of annual final energy savings in 2030.

(5) Household refrigerating appliances are among the product groups mentioned in Article 11(5)(b) of Regulation (EU) 2017/1369 for which the Commission should adopt a delegated act introducing an A to G rescaled label.

(6) Delegated Regulation (EU) No 1060/2010 requires the Commission to review the Regulation on a regular basis in light of technological progress.

(7) The Commission has reviewed Delegated Regulation (EU) No 1060/2010 as required by its Article 7 and analysed the technical, environmental and economic aspects of refrigerating appliances as well as real-life user behaviour. The review was carried out in close cooperation with stakeholders and interested parties from the Union and third countries. The results of the review were made public and presented to the Consultation Forum established by Article 14 of Regulation (EU) 2017/1369.

(8) The review concluded that there was a need to introduce revised energy labelling requirements for refrigerating appliances.

([1]) OJ L 198, 28.7.2017, p. 1.

([2]) Commission Delegated Regulation (EU) No 1060/2010 of 28 September 2010 supplementing Directive 2010/30/EU of the European Parliament and of the Council with regard to energy labelling of household refrigerating appliances (OJ L 314, 30.11.2010, p. 17).

([3]) Communication from the Commission. Ecodesign working plan 2016-2019 COM(2016) 773 final, 30.11.2016.

([4]) Directive 2009/125/EC of the European Parliament and of the Council of 21 October 2009 establishing a framework for the setting of ecodesign requirements for energy-related products (OJ L 285, 31.10.2009, p. 10).

([5]) Commission Regulation (EC) No 643/2009 of 22 July 2009 implementing Directive 2005/32/EC of the European Parliament and of the Council with regard to ecodesign requirements for household refrigerating appliances (OJ L 191, 23.7.2009, p. 53).

(9) The review concluded that the electricity use of products subject to this Regulation can be further significantly reduced by implementing energy label measures focusing on refrigerating appliances.

(10) Refrigerating appliances with a direct sales function should be subject to a separate energy labelling regulation.

(11) Chest freezers, including professional chest freezers, should be in the scope of this Regulation, as they are out of the scope of the Commission Delegated Regulation (EU) 2015/1094 ([6]) and can be used in other environments than professional environments.

(12) Wine storage appliances and low noise refrigerating appliances (such as minibars), including those with transparent doors, do not have a direct sales function. Wine storage appliances are usually either used in household environments or in restaurants, whereas minibars are usually used in hotel rooms. Therefore, wine storage appliances and minibars, including those with transparent doors should be covered by this Regulation.

(13) Refrigerating appliances that are displayed at trade fairs should bear the energy label if the first unit of the model has already been placed on the market or is placed on the market at the trade fair.

(14) The electricity used by household refrigerating appliances accounts for a significant share of total household electricity demand in the Union. In addition to the energy efficiency improvements already achieved, the scope for further reducing the energy consumption of household refrigerating appliances is substantial.

(15) The review has shown that the electricity consumption of products subject to this Regulation can be further reduced significantly by implementing energy label measures focusing on energy efficiency and annual energy consumption. In order for end-users to make an informed decision, information on airborne acoustical noise and the compartment types should also be included.

(16) The relevant product parameters should be measured using reliable, accurate and reproducible methods. Those methods should take into account recognised state-of-the-art measurement methods including, where available, harmonised standards adopted by the European standardisation bodies, as listed in Annex I to Regulation (EU) No 1025/2012 of the European Parliament and of the Council ([7]).

(17) To improve the effectiveness of this Regulation, products that automatically alter their performance in test conditions to improve the declared parameters should be prohibited.

(18) Recognising the growth of sales of energy-related products through internet hosting platforms, rather than directly from suppliers' websites, it should be clarified that internet sales platforms should be responsible for enabling the displaying of the label provided by the supplier in proximity to the price. They should inform the supplier of that obligation, but should not be responsible for the accuracy or content of the label and the product information sheet provided. However, in application of Article 14(1)(b) of Directive 2000/31/EC of the European Parliament and of the Council ([8]) on electronic commerce, such internet hosting platforms should act expeditiously to remove or to disable access to information about the product in question if they are aware of the non-compliance (e.g. missing, incomplete or incorrect label or product information sheet) for example if informed by the market surveillance authority. A supplier selling directly to end-users via its own website is covered by dealers' distance selling obligations referred to in Article 5 of Regulation (EU) 2017/1369.

(19) The measures provided for in this Regulation were discussed by the Consultation Forum and the Member State experts in accordance Article 14 of Regulation (EU) 2017/1369.

(20) Delegated Regulation (EU) No 1060/2010 should therefore be repealed,

([6]) Commission Delegated Regulation (EU) 2015/1094 of 5 May 2015 supplementing Directive 2010/30/EU of the European Parliament and of the Council with regard to energy labelling of professional refrigerated storage cabinets (OJ L 177, 8.7.2015, p. 2).

([7]) Regulation (EU) No 1025/2012 of the European Parliament and of the Council of 25 October 2012 on European standardisation, amending Council Directives 89/686/EEC and 93/15/EEC and Directives 94/9/EC, 94/25/EC, 95/16/EC, 97/23/EC, 98/34/EC, 2004/22/EC, 2007/23/EC, 2009/23/EC and 2009/105/EC of the European Parliament and of the Council and repealing Council Decision 87/95/EEC and Decision No 1673/2006/EC of the European Parliament and of the Council (OJ L 316, 14.11.2012, p. 12).

([8]) Directive 2000/31/EC of the European Parliament and of the Council of 8 June 2000 on certain legal aspects of information society services, in particular electronic commerce, in the Internal Market (Directive on electronic commerce) (OJ L 178, 17.7.2000, p. 1).

HAS ADOPTED THIS REGULATION:

Article 1

Subject matter and scope

1. This Regulation establishes requirements for the labelling of, and the provision of supplementary product information on, electric mains-operated refrigerating appliances with a volume of more than 10 litres and of less than or equal to 1 500 litres.

2. This Regulation does not apply to:

(a) professional refrigerated storage cabinets and blast cabinets, with the exception of professional chest freezers;

(b) refrigerating appliances with a direct sales function;

(c) mobile refrigerating appliances;

(d) appliances where the primary function is not the storage of foodstuffs through refrigeration.

Article 2

Definitions

For the purpose of this Regulation, the following definitions shall apply:

(1) 'mains' or 'electric mains' means the electricity supply from the grid of 230 (± 10 %) volt of alternating current at 50 Hz;

(2) 'refrigerating appliance' means an insulated cabinet with one or more compartments that are controlled at specific temperatures, cooled by natural or forced convection whereby the cooling is obtained by one or more energy consuming means;

(3) 'compartment' means an enclosed space within a refrigerating appliance, separated from other compartment(s) by a partition, container, or similar construction, which is directly accessible through one or more external doors and may itself be divided into sub-compartments. For the purpose of this Regulation, unless specified otherwise, compartment refers to both compartments and sub-compartments;

(4) 'external door' is the part of a cabinet that can be moved or removed to at least allow the load to be moved from the exterior to the interior or from the interior to the exterior of the cabinet;

(5) 'sub-compartment' means an enclosed space in a compartment having a different operating temperature range from the compartment in which it is located;

(6) 'total volume' (V) means the volume of the space within the inside liner of the refrigerating appliance, equal to the sum of the compartment volumes, expressed in dm^3 or litres;

(7) 'compartment volume' (V_c) means the volume of the space within the inside liner of the compartment, expressed in dm^3 or litres;

(8) 'professional refrigerated storage cabinet' means an insulated refrigerating appliance integrating one or more compartments accessible via one or more doors or drawers, capable of continuously maintaining the temperature of foodstuffs within prescribed limits at chilled or frozen operating temperature, using a vapour compression cycle, and used for the storage of foodstuffs in non-household environments but not for the display to or access by customers, as defined in Commission Regulation (EU) 2015/1095 ([9]);

(9) 'blast cabinet' means an insulated refrigerating appliance primarily intended to rapidly cool hot foodstuffs to below 10 °C in the case of chilling and below - 18 °C in the case of freezing, as defined in Regulation (EU) 2015/1095;

([9]) Commission Regulation (EU) 2015/1095 of 5 May 2015 implementing Directive 2009/125/EC of the European Parliament and of the Council with regard to ecodesign requirements for professional refrigerated storage cabinets, blast cabinets, condensing units and process chillers (OJ L 177, 8.7.2015, p. 19).

(10) 'professional chest freezer' means a freezer in which the compartment(s) is accessible from the top of the appliance or which has both top-opening type and upright type compartments but where the gross volume of the top-opening type compartment(s) exceeds 75 % of the total gross volume of the appliance, used for the storage of foodstuffs in non-household environments;

(11) 'freezer' means a refrigerating appliance with only 4-star compartments;

(12) 'freezer compartment' or '4-star compartment' means a frozen compartment with a target temperature and storage conditions of - 18 °C and which fulfils the requirements for the freezing capacity;

(13) 'frozen compartment' means a compartment type with a target temperature equal to or below 0 °C; that is a 0-star, 1-star, 2-star, 3-star or 4-star compartment, as set out in Annex IV, Table 3;

(14) 'compartment type' means the declared compartment type in accordance with the refrigerating performance parameters T_{min}, T_{max}, T_c and others set out in Annex IV, Table 3;

(15) 'target temperature' (T_c) means the reference temperature inside a compartment during testing, as set out in Annex IV, Table 3, and is the temperature for testing energy consumption expressed as the average over time and over a set of sensors;

(16) 'minimum temperature' (T_{min}) means the minimum temperature inside a compartment during storage testing, as set out in Annex IV, Table 3;

(17) 'maximum temperature' (T_{max}) means the maximum temperature inside a compartment during storage testing, as set out in Annex IV, Table 3;

(18) '0-star compartment' and 'ice-making compartment' means a frozen compartment with a target temperature and storage conditions of 0 °C, as set out in Annex IV, Table 3;

(19) '1-star compartment' means a frozen compartment with a target temperature and storage conditions of - 6 °C, as set out in Annex IV, Table 3;

(20) '2-star compartment' means a frozen compartment with a target temperature and storage conditions of - 12 °C, as set out in Annex IV, Table 3;

(21) '3-star compartment' means a frozen compartment with a target temperature and storage conditions of - 18 °C, as set out in Annex IV, Table 3;

(22) 'refrigerating appliance with a direct sales function' means a refrigerating appliance used for the functions of displaying and selling items at specified temperatures below the ambient temperature to customers, accessible directly through open sides or via one or more doors, or drawers, or both, including also cabinets with areas used for storage or assisted serving of items not accessible by the customers and excluding minibars and wine storage appliances, as defined in Commission Regulation (EU) 2019/2024 ([10]);

(23) 'minibar' means a refrigerating appliance with a total volume of maximum 60 litres, which is primary intended for the storage and sales of foodstuffs in hotel rooms and similar premises;

(24) 'wine storage appliance' means a dedicated refrigerating appliance for the storage of wine, with precision temperature control for the storage conditions and target temperature of a wine storage compartment, as defined in Annex IV, Table 3, and equipped with anti-vibration measures;

(25) 'dedicated refrigerating appliance' means a refrigerating appliance with only one type of compartment;

(26) 'wine storage compartment' means an unfrozen compartment with a target temperature of 12 °C, an internal humidity range from 50 % to 80 % and storage conditions ranging from 5 °C to 20 °C, as defined in Annex IV, Table 3;

([10]) Commission Regulation (EU) 2019/2024 of 1 October 2019 laying down ecodesign requirements for refrigerating appliances with a direct sales function pursuant to Directive 2009/125/EC of the European Parliament and of the Council (see page 313 of this Official Journal).

(27) 'unfrozen compartment' means a compartment type with a target temperature equal to or above 4 °C; that is a pantry, wine storage, cellar or fresh food compartment with storage conditions and target temperatures, as set out in Annex IV, Table 3;

(28) 'pantry compartment' means an unfrozen compartment with a target temperature of 17 °C and storage conditions ranging from 14 °C to 20 °C, as set out in Annex IV, Table 3;

(29) 'cellar compartment' means an unfrozen compartment with a target temperature of 12 °C and storage conditions ranging from 2 °C to 14 °C, as set out in Annex IV, Table 3;

(30) 'fresh food compartment' means an unfrozen compartment with a target temperature of 4 °C and storage conditions ranging from 0 °C and 8 °C, as set out in Annex IV, Table 3;

(31) 'mobile refrigerating appliance' means a refrigerating appliance that can be used where there is no access to the mains electricity grid and that uses extra low-voltage electricity (< 120V DC) or fuel or both as the energy source for the refrigeration functionality, including a refrigerating appliance that, in addition to extra low voltage electricity or fuel, or both, can be electric mains operated. An appliance placed on the market with an AC/DC converter is not a mobile refrigerating appliance;

(32) 'foodstuffs' means food, ingredients, beverages, including wine, and other items primarily used for consumption which require refrigeration at specified temperatures;

(33) 'point of sale' means a location where refrigerating appliances are displayed or offered for sale, hire or hire-purchase;

(34) 'built-in appliance' means a refrigerating appliance that is designed, tested and marketed exclusively:

(a) to be installed in cabinetry or encased (top, bottom and sides) by panels;

(b) to be securely fastened to the sides, top or floor of the cabinetry or panels; and

(c) to be equipped with an integral factory-finished face or to be fitted with a custom front panel;

(35) 'energy efficiency index' (EEI) means an index number for the relative energy efficiency of a refrigeration appliance, expressed in percentage, as set out in point 5 of Annex IV.

For the purposes of the Annexes, additional definitions are set out in Annex I.

Article 3

Obligations of suppliers

1. Suppliers shall ensure that:

(a) each refrigerating appliance is supplied with a printed label in the format as set out in Annex III;

(b) the parameters of the product information sheet, set out in Annex V, are entered into the product database;

(c) if specifically requested by the dealer, the product information sheet shall be made available in printed form;

(d) the content of the technical documentation, set out in Annex VI, is entered into the product database;

(e) any visual advertisement for a specific model of refrigerating appliances contains the energy efficiency class and the range of energy efficiency classes available on the label in accordance with Annex VII and Annex VIII;

(f) any technical promotional material concerning a specific model of refrigerating appliances, including technical promotional material on the internet, which describes its specific technical parameters includes the energy efficiency class of that model and the range of energy efficiency classes available on the label, in accordance with Annex VII;

(g) an electronic label in the format and containing the information, as set out in Annex III, is made available to dealers for each refrigerating appliance model;

(h) an electronic product information sheet, as set out in Annex V, is made available to dealers for each refrigerating appliance model.

2. The energy efficiency class shall be based on the energy efficiency index calculated in accordance with Annex II.

Article 4

Obligations of dealers

Dealers shall ensure that:

(a) each refrigerating appliance, at the point of sale, including at trade fairs, bears the label provided by suppliers in accordance with point 1(a) of Article 3, with the label being displayed for built-in appliances in such a way as to be clearly visible, and for all other refrigerating appliances in such a way as to be clearly visible on the outside of the front or top of the refrigerating appliance;

(b) in the event of distance selling, the label and product information sheet are provided in accordance with Annexes VII and VIII;

(c) any visual advertisement for a specific model of refrigerating appliance, including on the internet, contains the energy efficiency class and the range of energy efficiency classes available on the label, in accordance with Annex VII;

(d) any technical promotional material concerning a specific model of refrigerating appliance, including technical promotional material on the internet, which describes its specific technical parameters includes the energy efficiency class of that model and the range of energy efficiency classes available on the label, in accordance with Annex VII.

Article 5

Obligations of internet hosting platforms

Where a hosting service provider as referred to in Article 14 of Directive 2000/31/EC allows the direct selling of refrigerating appliances through its internet site, the service provider shall enable the showing of the electronic label and electronic product information sheet provided by the dealer on the display mechanism in accordance with the provisions of Annex VIII and shall inform the dealer of the obligation to display them.

Article 6

Measurement methods

The information to be provided pursuant to Articles 3 and 4 shall be obtained by reliable, accurate and reproducible measurement and calculation methods, which take into account the recognised state-of-the-art measurement and calculation methods set out in Annex IV.

Article 7

Verification procedure for market surveillance purposes

Member States shall apply the verification procedure laid down in Annex IX when performing the market surveillance checks referred to in paragraph 3 of Article 8 of Regulation (EU) 2017/1369.

Article 8

Review

The Commission shall review this Regulation in the light of technological progress and present the results of this assessment, including, if appropriate, a draft revision proposal, of this review to the Consultation Forum no later than 25 December 2025. This review shall, among other matters, assess the possibility to:

(a) address circular economy aspects;

(b) introduce icons for compartments that may help reduce food waste; and

(c) introduce icons for the annual energy consumption.

Article 9

Repeal

Delegated Regulation (EU) No 1060/2010 is repealed as of 1 March 2021.

Article 10

Transitional measures

As from 25 December 2019 until 28 February 2021, the product fiche required under point 1(b) of Article 3 of Delegated Regulation (EU) No 1060/2010 may be made available through the product database instead of being provided in printed form with the product. In that case the supplier shall ensure that if specifically requested by the dealer, the product fiche shall be made available in printed form.

Article 11

Entry into force and application

This Regulation shall enter into force on the twentieth day following that of its publication in the *Official Journal of the European Union*.

It shall apply from 1 March 2021. However, Article 10 shall apply from 25 December 2019 and point 1(a), (b) and (c) of Article 3 shall apply from 1 November 2020.

This Regulation shall be binding in its entirety and directly applicable in all Member States.

Done at Brussels, 11 March 2019.

For the Commission

The President

Jean-Claude JUNCKER

ANNEX I

Definitions applicable for the Annexes

The following definitions shall apply:

(1) 'quick response (QR) code' means a matrix barcode included on the energy label of a product model that links to that model's information in the public part of the product database;

(2) 'annual energy consumption' (*AE*) means the average daily energy consumption multiplied by 365 (days per year), expressed in kilowatt hour per year (kWh/a), as calculated in accordance with point 3 of Annex IV;

(3) 'daily energy consumption' (E_{daily}) means the electricity used by a refrigerating appliance over 24 hours at reference conditions, expressed in kilowatt hour per 24 hours (kWh/24h), calculated in accordance with point 3 of Annex IV;

(4) 'freezing capacity' means the amount of fresh foodstuffs that can be frozen in a freezer compartment in 24 h; it shall not be lower than 4,5 kg per 24 h per 100 litres of volume of the freezer compartment, with a minimum of 2,0 kg/24h;

(5) 'chill compartment' means a compartment which is able to control its average temperature within a certain range without user-adjustments of its control, with a target temperature equal to 2 °C, and storage conditions ranging from - 3 °C to 3 °C, as set out in Annex IV, Table 3;

(6) 'airborne acoustical noise emission' means the sound power level of a refrigerating appliance, expressed in dB(A) re 1 pW (A-weighted);

(7) 'anti-condensation heater' means a heater which prevents condensation on the refrigeration appliance;

(8) 'ambient controlled anti-condensation heater' means an anti-condensation heater where the heating capacity depends on either the ambient temperature or the ambient humidity or both;

(9) 'auxiliary energy' (E_{aux}) means the energy used by an ambient controlled anti-condensation heater, expressed in kilowatt hour per annum (kWh/a);

(10) 'dispenser' means a device that dispenses chilled or frozen load on demand from a refrigerating appliance, such as ice-cube dispensers or chilled water dispensers;

(11) 'variable temperature compartment' means a compartment intended for use as two (or more) alternative compartment types (for example a compartment that can be either a fresh food compartment or freezer compartment) and which is capable of being set by a user to continuously maintain the operating temperature range applicable for each declared compartment type. A compartment intended for use as a single compartment type that can also meet storage conditions of other compartment types (for example a chill compartment that may also fulfil 0-star requirements) is not a variable temperature compartment;

(12) 'network' means a communication infrastructure with a topology of links, an architecture, including the physical components, organisational principles, communication procedures and formats (protocols);

(13) '2-star section' means part of a 3-star or 4-star compartment which does not have its own individual access door or lid and with target temperature and storage conditions of - 12 °C;

(14) 'climate class' means the range of ambient temperatures, as set out in point 1(j) of Annex IV, in which the refrigerating appliances are intended to be used, and for which the required storage conditions specified in Annex IV, Table 3 are met simultaneously in all compartment(s);

(15) 'defrost and recovery period' means the period from the initiation of a defrost control cycle until stable operating conditions are re-established;

(16) 'auto-defrost' means a feature by which compartments are defrosted without user intervention to initiate the removal of frost accumulation at all temperature-control settings or to restore normal operation, and the disposal of the defrost water is automatic;

(17) 'defrosting type' means the method to remove frost accumulation on the evaporator(s) of a refrigerating appliance; that is auto-defrost or manual defrost;

(18) 'manual defrost' means not having an auto-defrost function;

(19) 'low noise refrigerating appliance' means a refrigerating appliance without vapour compression and with an air-borne acoustical noise emission lower than 27 A-weighted decibel referred to 1 pico watt (dB(A) re 1 pW);

(20) 'steady-state power consumption' (P_{ss}) means the average power consumption in steady-state conditions, expressed in watt (W);

(21) 'incremental defrost and recovery energy consumption' ($\Delta E_{d\text{-}f}$) means the extra average energy consumption for a defrost and recovery operation expressed in watt hour (Wh);

(22) 'defrost interval' ($t_{d\text{-}f}$) means the representative average interval, expressed in hour (h), between one time of activation of the defrost heater and the next in two subsequent defrost and recovery cycle; or if there is no defrost heater one time of deactivation of the compressor and the next in two subsequent defrost and recovery cycles;

(23) 'load factor' (L) means a factor accounting for the extra (beyond what is already anticipated through the higher average ambient temperature for testing) cooling load from introducing warm foodstuffs, with values as set out in point 3(a) of Annex IV;

(24) 'standard annual energy consumption' (SAE) means the reference annual energy consumption of a refrigerating appliance, expressed in kilowatt hour per year (kWh/a), as calculated in accordance with point 4 of Annex IV;

(25) 'combi parameter' (C) means a modelling parameter that takes into account the synergy effect when different compartment types are combined in one appliance, with values as set out in Annex IV, Table 4;

(26) 'door heat loss factor' (D) means a compensation factor for combi appliances according to the number of different temperature compartments or the number of external doors, whichever is lower and as set out in Annex IV, Table 5. For this factor, 'compartment' does not refer to sub-compartment;

(27) 'combi appliance' means a refrigerating appliance that has more than one compartment type of which at least one unfrozen compartment;

(28) 'defrost factor' (A_c) means a compensation factor that takes into account whether the refrigerating appliance has an auto-defrost or a manual defrost, with values as set out in Annex IV, Table 5;

(29) 'built-in factor' (B_c) means a compensation factor that takes into account whether the refrigerating appliance is built-in or freestanding, with values as set out in Annex IV, Table 5;

(30) 'freestanding appliance' means a refrigerating appliance that is not a built-in appliance;

(31) 'M_c' and 'N_c' means modelling parameters that take into account the volume-dependence of the energy use, with values as set out in Annex IV, Table 4;

(32) 'thermodynamic parameter' (r_c) means a modelling parameter which corrects the standard annual energy consumption to an ambient temperature of 24 °C, with values as set out in Annex IV, Table 4;

(33) 'overall dimensions' means the space taken up by the refrigerating appliance (height, width and depth) with doors or lids closed, expressed in millimetres (mm);

(34) 'temperature rise time' means the time taken, after the operation of the refrigerated system has been interrupted, for the temperature in a 3- or 4-star compartment to increase from -18 to - 9 °C expressed in hours (h);

(35) 'winter setting' means a control feature for a combi appliance with one compressor and one thermostat, which according to the supplier's instructions can be used in ambient temperatures below +16 °C, consisting of a switching device or function that guarantees, even if it would not be required for the compartment where the thermostat is located, that the compressor keeps on working to maintain the proper storage temperatures in the other compartments;

(36) 'fast freeze' means a feature that can be activated by the end-user according to the supplier's instructions, which decreases the storage temperature of the freezer compartment(s) to achieve a faster freezing of unfrozen foodstuffs;

(37) 'freezer compartment' or '4-star compartment' means a frozen compartment with a target temperature and storage conditions of - 18 °C and which fulfils the requirements for the freezing capacity;

(38) 'display mechanism' means any screen, including tactile screen, or other visual technology used for displaying internet content to users;

(39) 'tactile screen' means a screen responding to touch, such as that of a tablet computer, slate computer or a smartphone;

(40) 'nested display' means visual interface where an image or data set is accessed by a mouse click, mouse roll-over or tactile screen expansion of another image or data set;

(41) 'alternative text' means text provided as an alternative to a graphic allowing information to be presented in non-graphical form where display devices cannot render the graphic or as an aid to accessibility such as input to voice synthesis applications.

ANNEX II

Energy efficiency classes and airborne acoustical emission classes

The energy efficiency class of refrigerating appliances shall be determined on the basis of the energy efficiency index (EEI) as set out in Table 1.

Table 1

Energy efficiency classes of refrigerating appliances

Energy efficiency class	Energy efficiency index (EEI)
A	EEI ≤ 41
B	42 < EEI ≤ 51
C	51 < EEI ≤ 64
D	64 < EEI ≤ 80
E	80 < EEI ≤ 100
F	100 < EEI ≤ 125
G	EEI > 125

The EEI of a refrigerating appliance shall be determined in accordance with point 5 of Annex IV.

Table 2

Airborne acoustical noise emission classes

Airborne acoustical noise emission	Airborne acoustical noise emission class
< 30 dB(A) re 1 pW	A
≥ 30 dB(A) re 1 pW and < 36 dB(A) re 1 pW	B
≥ 36 dB(A) re 1 pW and < 42 dB(A) re 1 pW	C
≥ 42 dB(A) re 1 pW	D

ANNEX III

Label for refrigerating appliances

1. LABEL FOR REFRIGERATING APPLIANCES, EXCEPT FOR WINE STORAGE APPLIANCES

1.1. Label:

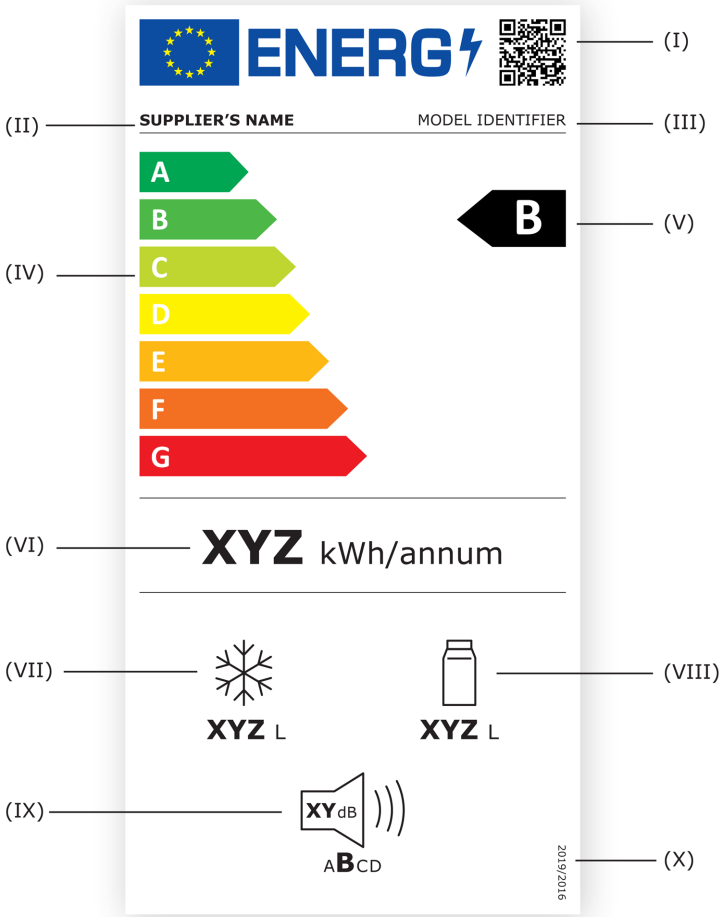

1.2. The following information shall be included in the label:

I. the QR code;

II. supplier's name or trade mark;

III. supplier's model identifier;

IV. scale of energy efficiency classes from A to G;

V. the energy efficiency class determined in accordance with Annex II;

VI. annual energy consumption (*AE*), expressed in kWh per year and rounded to the nearest integer;

VII.

— the sum of the volumes of the frozen compartment(s), expressed in litres and rounded to the nearest integer;

— if the refrigerating appliance does not contain frozen compartment(s) the pictogram and the value in litres in VII shall be omitted;

VIII.

— the sum of the volumes of the chill compartment(s) and the unfrozen compartment(s), expressed in litres and rounded to the nearest integer;

— if the refrigerating appliance does not contain unfrozen compartment(s) and chill compartment(s) the pictogram and the value in litres in VIII shall be omitted;

IX. airborne acoustical noise emissions, expressed in dB(A) re 1 pW and rounded to the nearest integer. The airborne acoustical noise emission class, as set out in Table 2;

X. the number of this Regulation, that is '2019/2016'.

2. LABEL FOR WINE STORAGE APPLIANCES

2.1. Label:

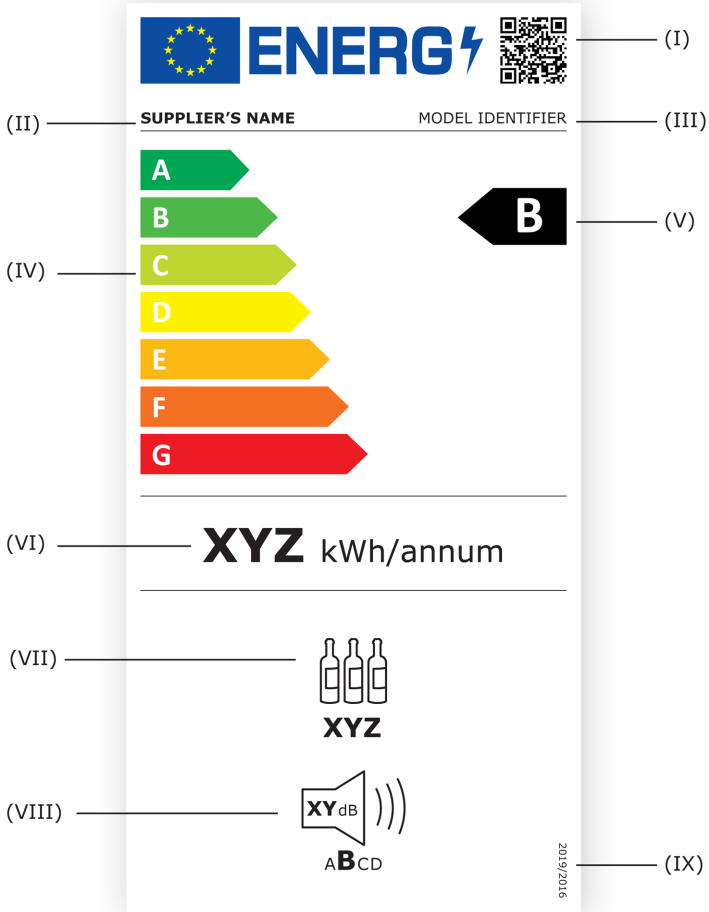

2.2. The following information shall be included in the label:

I. QR code;

II. supplier's name or trade mark;

III. supplier's model identifier;

IV. scale of energy efficiency classes from A to G;

V. the energy efficiency class determined in accordance with Annex II;

VI. *AE*, expressed in kWh per year and rounded to the nearest integer;

VII. the number of standard wine bottles that can be stored in the wine storage appliance;

VIII. airborne acoustical noise emissions, expressed in dB(A) re 1 pW and rounded to the nearest integer. The airborne acoustical noise emission class, as set out in Table 2;

IX. the number of this Regulation that is '2019/2016'.

3. LABEL DESIGNS

3.1. Label design for refrigerating appliances, except for wine storage appliances

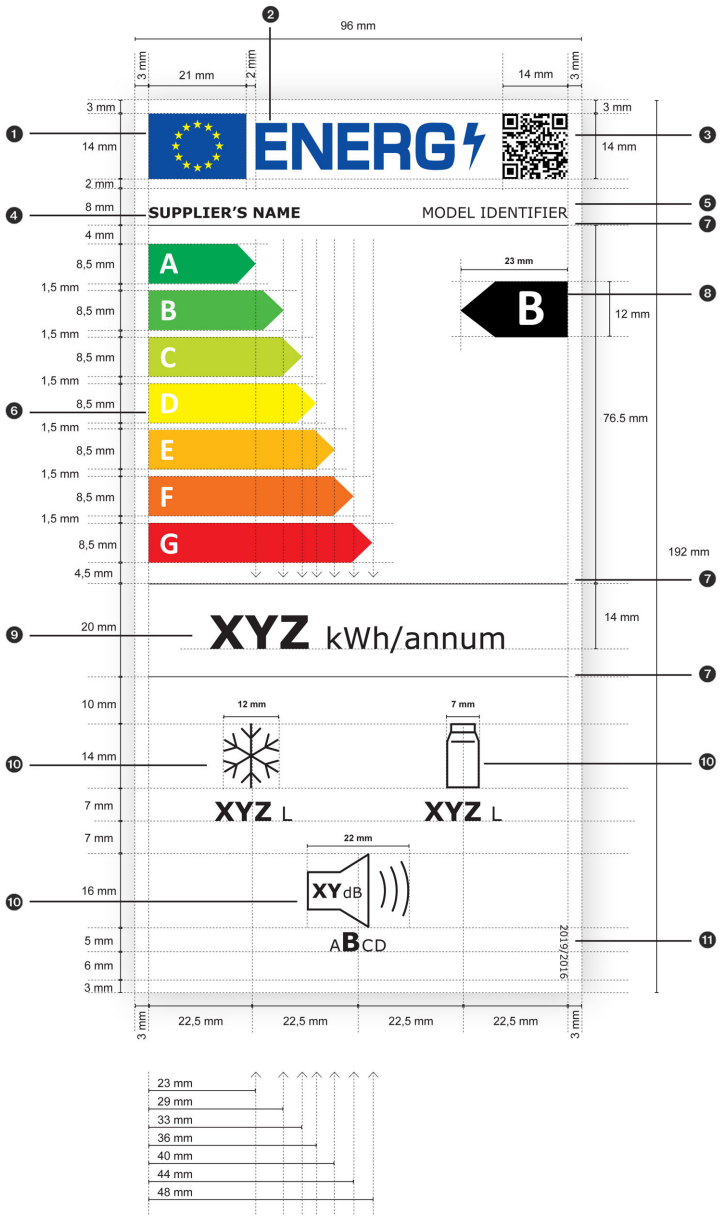

3.2. Label design for wine storage appliances

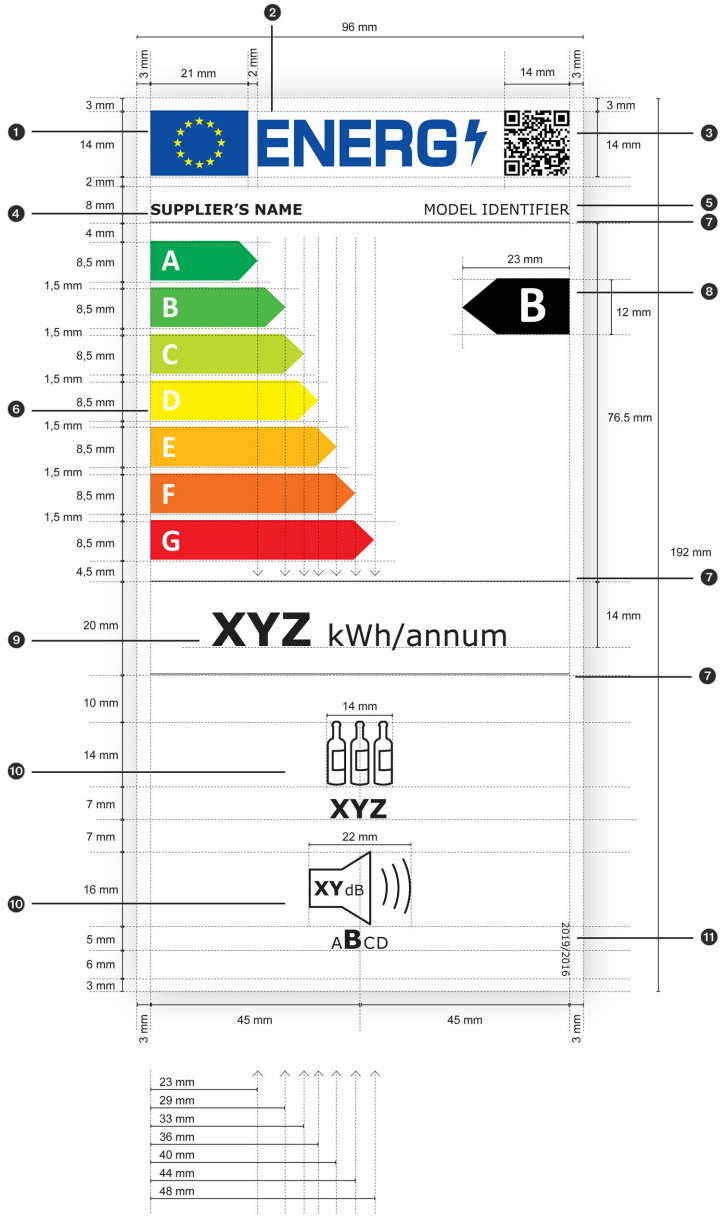

3.3. Whereby:

(a) The labels shall be at least 96 mm wide and 192 mm high. Where the label is printed in a larger format, its content shall nevertheless remain proportionate to the specifications above.

(b) The background of the label shall be 100 % white.

(c) The typefaces shall be Verdana and Calibri.

(d) The dimensions and specifications of the elements constituting the label shall be as indicated in the label designs for refrigerating appliances and for wine storage appliances.

(e) Colours shall be CMYK – cyan, magenta, yellow and black, following this example: 0,70,100,0: 0 % cyan, 70 % magenta, 100 % yellow, 0 % black.

(f) The label shall fulfil all the following requirements (numbers refer to the figures above):

❶ the colours of the EU logo shall be as follows:

— the background: 100,80,0,0;

— the stars: 0,0,100,0;

❷ the colour of the energy logo shall be: 100,80,0,0;

❸ the QR code shall be 100 % black;

❹ the supplier's name shall be 100 % black and in Verdana Bold, 9 pt;

❺ the model identifier shall be 100 % black and in Verdana Regular 9 pt;

❻ the A to G scale shall be as follows:

— the letters of the energy efficiency scale shall be 100 % white and in Calibri Bold 19 pt; the letters shall be centred on an axis at 4,5 mm from the left side of the arrows;

— the colours of the A to G scale arrows shall be as follows:

— A-class: 100,0,100,0;

— B-class: 70,0,100,0;

— C-class: 30,0,100,0;

— D-class: 0,0,100,0;

— E-class: 0,30,100,0;

— F-class: 0,70,100,0;

— G-class: 0,100,100,0;

❼ the internal dividers shall have a weight of 0,5 pt and the colour shall be 100 % black;

❽ the letter of the energy efficiency class shall be 100 % white and in Calibri Bold 33 pt. The energy efficiency class arrow and the corresponding arrow in the A to G scale shall be positioned in such a way that their tips are aligned. The letter in the energy efficiency class arrow shall be positioned in the centre of the rectangular part of the arrow which shall be 100 % black;

❾ the annual energy consumption value shall be in Verdana Bold 28 pt; 'kWh/annum' shall be in Verdana Regular 18 pt. The value and unit shall be centred and 100 % black;

❿ the pictograms shall be as shown as in the label designs and as follows:

— the pictograms' lines shall have a weight of 1,2 pt and they and the texts (numbers and units) shall be 100 % black;

— the text under the pictogram(s) shall be in Verdana Bold 16 pt with the unit in Verdana Regular 12 pt, and it shall be centred under the pictogram;

— for refrigerating appliances, except wine storage appliances: if the appliance contains only frozen compartment(s) or only unfrozen compartment(s), only the relevant pictogram in the top row, as set out in point 1.2 VII and VIII, shall be shown and centred between the two vertical borders of the energy label;

— the airborne acoustical noise emission pictogram: the number of decibels in the loudspeaker shall be in Verdana Bold 12 pt, with the unit 'dB' in Verdana Regular 9 pt; the range of noise classes (A to D) shall be centred under the pictogram, with the letter of the applicable noise class in Verdana Bold 16 pt and the other letters of the noise classes in Verdana Regular 10 pt;

⓫ the number of the regulation shall be 100 % black and in Verdana Regular 6 pt.

ANNEX IV

Measurement methods and calculations

For the purposes of compliance and verification of compliance with the requirements of this Regulation, measurements and calculations shall be made using harmonised standards, or other reliable, accurate and reproducible methods, which takes into account the generally recognised state-of-the-art methods and are in line with the provisions set out below. The reference numbers of these harmonised standards have been published for this purpose in the *Official Journal of the European Union*:

1. General conditions for testing:

(a) for refrigerating appliances with anti-condensation heaters that can be switched on and off by the end-user, the anti-condensation heaters shall be switched on and — if adjustable — set at maximum heating and included in the annual energy consumption (*AE*) as daily energy consumption (E_{daily});

(b) for refrigerating appliances with ambient controlled anti-condensation heaters, the ambient controlled electric anti-condensation heaters shall be switched off or otherwise disabled, where possible, during the measurement of energy consumption;

(c) for refrigerating appliances with dispensers that can be switched on and off by the end-user, the dispensers shall be switched on during the energy consumption test but not operating;

(d) for the measurement of energy consumption, variable temperature compartments shall operate at the lowest temperature that can be set by the end-user to continuously maintain the temperature range, as set out in Table 3, of the compartment type which has the lowest temperature;

(e) for refrigerating appliances that can be connected to a network, the communication module shall be activated but there is no need to have a specific type of communication or data exchange or both during the energy consumption test. During the energy consumption test it has to be ensured that the unit is connected to a network;

(f) for the performance of chill compartments:

(1) for a variable temperature compartment rated as a fresh food and/or chill compartment, the energy efficiency index (EEI) shall be determined for each temperature condition and the highest value shall be applied;

(2) a chill compartment shall be able to control its average temperature within a certain range without user-adjustments of its control, this can be verified during the energy consumption tests at 16 °C and 32 °C ambient temperature;

(g) for adjustable volume compartments, when the volumes of two compartments are adjustable relative to one another by the end-user, the energy consumption and the volume shall be tested when the volume of the compartment with the higher target temperature is adjusted to its minimum volume;

(h) the specific freezing capacity is calculated as 12 times the light load weight, divided by the freezing time to bring the temperature of the light load from +25 to - 18 °C at an ambient temperature of 25 °C expressed in kg/12h and rounded to one decimal place; the light load weight is 3,5 kg per 100 litre of the compartment volume of the frozen compartments, and shall be at least 2,0 kg;

(i) for 4-star compartments, the specific freezing capacity shall be such that the freezing time to bring the temperature of the light load (3,5 kg/100 l) from +25 to - 18 °C at an ambient temperature of 25 °C, is smaller than or equal to 18,5 h;

(j) for the determination of the climate classes, the acronym for the ambient temperature range, that is SN, N, ST or T:

(1) the extended temperate (SN) has a temperature range from 10 °C to 32 °C;

(2) the temperate (N) has a temperature range from 16 °C to 32 °C;

(3) the subtropical (ST) has a temperature range from 16 °C to 38 °C; and

(4) the tropical (T) has a temperature range from 16 °C to 43 °C.

2. Storage conditions and target temperatures per compartment type:

Table 3 sets out the storage conditions and target temperature per compartment type.

3. Determination of the *AE*:

(a) For all refrigerating appliances, except for low noise refrigerating appliances:

The energy consumption shall be determined by testing at an ambient temperature of 16 °C and 32 °C.

To determine the energy consumption, the average air temperatures in each compartment shall be equal to or below the target temperatures specified in Table 3 for each compartment type claimed by the supplier. Values above and below target temperatures may be used to estimate the energy consumption at the target temperature for each relevant compartment by interpolation, as appropriate.

The main components of energy consumption to be determined are:

— a set of steady state power consumption values (P_{ss}) in W and rounded to one decimal place, each at a specific ambient temperature and at a set of compartment temperatures, which are not necessarily the target temperatures;

— the representative incremental defrost and recovery energy consumption ($\Delta E_{d\text{-}f}$), in Wh and rounded to one decimal place, for products with one or more auto-defrost systems (each with its own defrost control cycle) measured at an ambient temperature of 16 °C ($\Delta E_{d\text{-}f16}$) and 32 °C ($\Delta E_{d\text{-}f32}$);

— defrost interval ($t_{d\text{-}f}$), expressed in h and rounded to three decimal places, for products with one or more defrost systems (each with its own defrost control cycle) measured at an ambient temperature of 16 °C ($t_{d\text{-}f16}$) and 32 °C ($t_{d\text{-}f32}$). $t_{d\text{-}f}$ shall be determined for each system under a certain range of conditions;

— for each test performed the P_{ss} and $\Delta E^{d\text{-}f}$ are added together to form a daily energy consumption at a certain ambient temperature $E_T = 0{,}001 \times 24 \times (P_{ss} + \Delta E_{d\text{-}f}/t_{d\text{-}f})$, expressed in kWh/24h, specific to the settings applied;

— E_{aux}, expressed in kWh/a and rounded to three decimal places. E_{aux} is limited to the ambient controlled anti-condensation heater and is determined from the heater's power consumption at a number of ambient temperature and humidity conditions, multiplied with the probability that this ambient temperature and humidity condition occurs and summed; this result is subsequently multiplied with a loss factor to account for heat leakage into the compartment and its subsequent removal by the refrigeration system.

Table 3

Storage conditions and target temperature per compartment type

Group	Compartment type	Note	Storage conditions		T_c
			Tmin	*Tmax*	
Name	*Name*	*no.*	°C	°C	°C
Unfrozen compartments	Pantry	(1)	+14	+20	+17
	Wine storage	(2) (6)	+5	+20	+12
	Cellar	(1)	+2	+14	+12
	Fresh food	(1)	0	+8	+4
Chill compartment	Chill	(3)	-3	+3	+2

Group	Compartment type	Note	Storage conditions		T_c
			Tmin	*Tmax*	
Name	*Name*	*no.*	°C	°C	°C
Frozen compartments	0-star & ice-making	(4)	*n.a.*	0	0
	1-star	(4)	*n.a.*	-6	-6
	2-star	(4) (5)	*n.a.*	-12	-12
	3-star	(4) (5)	*n.a.*	-18	-18
	freezer (4-star)	(4) (5)	*n.a.*	-18	-18

Notes

(1) $\boldsymbol{T_{min}}$ and $\boldsymbol{T_{max}}$ are the average values measured over the test period (average over time and over a set of sensors).
(2) The average temperature variation over the test period for each sensor shall be no more than ± 0,5 kelvin (K). During a defrost and recovery period the average of all sensors is not permitted to rise more than 1,5 K above the average value of the compartment.
(3) $\boldsymbol{T_{min}}$ and $\boldsymbol{T_{max}}$ are instantaneous values during the test period.
(4) $\boldsymbol{T_{max}}$ is the maximum value measured over the test period (maximum over time and over a set of sensors).
(5) If the compartment is of the auto-defrosting type, the temperature (defined as the maximum of all sensors) is not permitted to rise more than 3,0 K during a defrost and recovery period.
(6) $\boldsymbol{T_{min}}$ and $\boldsymbol{T_{max}}$ are the average values measured over the test period (average over time for each sensor) and define the maximum allowed temperature operating range
n.a.=not applicable

Each of these parameters shall be determined through a separate test or set of tests. Measurement data is averaged over a test period which is taken after the appliance has been in operation for a certain time. To improve the efficiency and accuracy of testing, the length of the test period shall not be fixed; it shall be such that the appliance is in steady state condition during this test period. This is validated by examining all data within this test period against a set of stability criteria and whether enough data could be collected in this steady state.

AE, expressed in kWh/a and rounded to two decimal places, shall be calculated as follows:

$$AE = 365 \times E_{daily}/L + E_{aux}$$

with

— the load factor L = 0,9 for refrigerating appliances with only frozen compartments and L = 1,0 for all other appliances; and

— with $E_{daily,}$ expressed in kWh/24h and rounded to three decimal places calculated from E_T at an ambient temperature of 16 °C (E_{16}) and at an ambient temperature of 32 °C (E_{32}) as follows:

$$E_{daily} = 0{,}5 \times (E_{16} + E_{32})$$

where E_{16} and E_{32} are derived by interpolation of the energy test at the target temperatures set out in Table 3.

(b) For low noise refrigerating appliances:

The energy consumption shall be determined as provided for in point 3(a), but at an ambient temperature of 25 °C instead of at 16 °C and 32 °C.

E_{daily}, expressed in kWh/24h and rounded to three decimal places for the calculation of the *AE* is then as follows:

$$E_{daily} = E_{25}$$

where E_{25} is E_T at an ambient temperature of 25 °C and derived by interpolation of the energy tests at the target temperatures listed in Table 3.

4. Determination of the standard annual energy consumption (*SAE*):

(a) For all refrigerating appliances:

SAE, expressed in kWh/a, and rounded to two decimal places, is calculated as follows:

$$SAE = C \times D \times \sum_{c=1}^{n} A_c \times B_c \times [V_c V] \times (N_c + V \times r_c \times M_c)$$

where

— c is the index number for a compartment type ranging from 1 to n, with n the total number of compartment types;

— V_c, expressed in dm^3 or litres and rounded to the first decimal place is the compartment volume;

— V, expressed in dm^3 or litres and rounded to the nearest integer is the volume with $V \leq \sum_{c=1}^{n} V_c$;

— r_c, N_c, M_c and C are modelling parameters specific to each compartment with values as set out in Table 4; and

— A_c, B_c and D are the compensation factors with values as set out in Table 5.

When carrying out the calculations above, for the variable temperature compartments, the compartment type with the lowest target temperature for which it is declared suitable is chosen.

(b) Modelling parameters per compartment type for the calculation of *SAE*:

The modelling parameters are set out in Table 4.

Table 4

The values of the modelling parameters per compartment type

Compartment type	r_c [a]	N_c	M_c	C
Pantry	0,35	75	0,12	between 1,15 and 1,56 for combi appliances with 3-or 4-star compartments [b], 1,15 for other combi appliances, 1,00 for other refrigerating appliances
Wine storage	0,60			
Cellar	0,60			
Fresh food	1,00			
Chill	1,10	138	0,12	
0-star & ice-making	1,20	138	0,15	
1-star	1,50			
2-star	1,80			
3-star	2,10			
Freezer (4-star)	2,10			

[a] $r_c = (T_a - T_c)/20$; with T_a = 24 °C and T_c with values as set out in Table 3.

[b] C for combi appliances with 3-or 4-star compartments is determined as follows:
where *frzf* is the 3- or 4-star compartment volume V_{fr} as a fraction of V with $frzf = V_{fr}/V$:
— if $frzf \leq 0{,}3$ then $C = 1{,}3 + 0{,}87 \times frzf$;
— else if $0{,}3 < frzf < 0{,}7$ then $C = 1{,}87 - 1{,}0275 \times frzf$;
— else $C = 1{,}15$.

(c) Compensation factors per compartment type in the calculation of *SAE:*

The compensation factors are set out in Table 5.

Table 5

The values of the compensation factors per compartment type

<table>
<tr><th rowspan="2">Compartment type</th><th colspan="2">A_c</th><th colspan="2">B_c</th><th colspan="4">D</th></tr>
<tr><th>Manual defrost</th><th>Auto-defrost</th><th>Freestanding appliance</th><th>Built-in appliance</th><th>≤ 2 [a]</th><th>3 [a]</th><th>4 [a]</th><th>> 4 [a]</th></tr>
<tr><td>Pantry</td><td rowspan="5">1,00</td><td rowspan="5"></td><td rowspan="11">1,00</td><td rowspan="4">1,02</td><td rowspan="11">1,00</td><td rowspan="11">1,02</td><td rowspan="11">1,035</td><td rowspan="11">1,05</td></tr>
<tr><td>Wine storage</td></tr>
<tr><td>Cellar</td></tr>
<tr><td>Fresh food</td></tr>
<tr><td>Chill</td><td>1,03</td></tr>
<tr><td>0-star & ice-making</td><td rowspan="6">1,00</td><td rowspan="6">1,10</td><td rowspan="6">1,05</td></tr>
<tr><td>1-star</td></tr>
<tr><td>2-star</td></tr>
<tr><td>3-star</td></tr>
<tr><td>Freezer (4-star)</td></tr>
</table>

[a] number of external doors or compartments, whichever is lowest.

5. Determination of the EEI:

EEI, expressed in % and rounded to the first decimal place, calculated as:

$$EEI = AE/SAE.$$

ANNEX V

Product information sheet

Pursuant to point 1(b) of Article 3, the supplier shall enter into the product database the information as set out in Table 6. If the refrigerating appliance contains multiple compartments of the same type, the lines for these compartments shall be repeated. If a certain compartment type is not present, the compartment parameters and values shall be '-'.

Table 6

Product information sheet

Supplier's name or trade mark:

Supplier's address [b]**:**

Model identifier:

Type of refrigerating appliance:

Low-noise appliance:	[yes/no]	Design type:	[built-in/ freestanding]
Wine storage appliance:	[yes/no]	Other refrigerating appliance:	[yes/no]

General product parameters:

Parameter		Value	Parameter	Value
Overall dimensions (millimetre)	Height	x	Total volume (dm^3 or l)	x
	Width	x		
	Depth	x		
EEI		x	Energy efficiency class	[A/B/C/D/E/F/G] [c]
Airborne acoustical noise emissions (dB(A) re 1 pW)		x	Airborne acoustical noise emission class	[A/B/C/D] [c]
Annual energy consumption (kWh/a)		x,xx	Climate class:	[extended temperate/ temperate/ subtropical/ tropical]
Minimum ambient temperature (°C), for which the refrigerating appliance is suitable		x [c]	Maximum ambient temperature (°C), for which the refrigerating appliance is suitable	x [c]
Winter setting		[yes/no]		

Compartment Parameters:

Compartment type		Compartment parameters and values			
		Compartment Volume (dm³ or l)	Recommended temperature setting for optimised food storage (°C) These settings shall not contradict the storage conditions set out in Annex IV, Table 3	Freezing capacity (kg/24 h)	Defrosting type (auto-defrost = A, manual defrost = M)
Pantry	[yes/no]	x,x	x	—	[A/M]
Wine storage	[yes/no]	x,x	x	—	[A/M]
Cellar	[yes/no]	x,x	x	—	[A/M]
Fresh food	[yes/no]	x,x	x	—	[A/M]
Chill	[yes/no]	x,x	x	—	[A/M]
0-star or ice- making	[yes/no]	x,x	x	—	[A/M]
1-star	[yes/no]	x,x	x	—	[A/M]
2-star	[yes/no]	x,x	x	—	[A/M]
3-star	[yes/no]	x,x	x	—	[A/M]
4-star	[yes/no]	x,x	x	x,xx	[A/M]
2-star section	[yes/no]	x,x	x	—	[A/M]
Variable temperature compartment	compartment types	x,x	x	x,xx (for 4-star compartments) or -	[A/M]

For 4-star compartments

Fast freeze facility	[yes/no]

Light source parameters [a] [b]:	
Type of light source	[type]
Energy efficiency class	[A/B/C/D/E/F/G]

Minimum duration of the guarantee offered by the manufacturer [b]:

Additional information:

Weblink to the manufacturer's website, where the information in point 4(a) Annex of Commission Regulation (EU) 2019/2019 [1] [b] is found:

[a] as determined in accordance with Commission Delegated Regulation (EU) 2019/2015 [2].
[b] changes to these items shall not be considered relevant for the purposes of point 4 of Article 4 of Regulation (EU) 2017/1369.
[c] if the product database automatically generates the definitive content of this cell the supplier shall not enter these data.

[1] Commission Regulation (EU) 2019/2019 of 1 October 2019 laying down ecodesign requirements for refrigerating appliances pursuant to Directive 2009/125/EC of the European Parliament and of the Council and repealing Commission Regulation (EC) No 643/2009 (see page 187 of this Official Journal).

[2] Commission Delegated Regulation (EU) 2019/2015 of 11 March 2019 supplementing Regulation (EU) 2017/1369 of the European Parliament and of the Council with regard to energy labelling of light sources and repealing Commission Delegated Regulation (EU) No 874/2012 (see page 68 of this Official Journal).

ANNEX VI

Technical documentation

1. The technical documentation referred to in point 1(d) of Article 3 shall include the following elements:

   (a) the information as set out in Annex V;

   (b) the information as set out in Table 7. If the refrigerating appliance contains multiple compartments of the same type, the lines for these compartments shall be repeated. If a certain compartment type is not present, the compartment parameters and values shall be '-'. If a parameter is not applicable, the values of that parameter shall be '-'.

Table 7

Additional information to be included in the technical documentation

A general description of the refrigerating model, sufficient for it to be unequivocally and easily identified:

Product specifications:

General product specifications:

Parameter	Value	Parameter	Value
Annual energy consumption (kWh/a)	x	Auxiliary energy (kWh/a)	x
Standard annual energy consumption (kWh/a)	x,xx	EEI (%)	x
Temperature rise time (h)	x,xx	Combi parameter	x,xx
Door heat loss factor	x,xxx	Load factor	x,x
Anti-condensation heater type	[manual on-off/ambient/other/ none]		

Additional product specifications for refrigerating appliances, except for low noise refrigerating appliances:

Parameter	Value	Parameter	Value
Daily energy consumption at 16 °C (kWh/24h)	x,xxx	Daily energy consumption at 32 °C (kWh/24h)	x,xxx
Incremental defrost and recovery energy consumption [a] at 16 °C (Wh)	x,x	incremental defrost and recovery energy consumption [a] at 32 °C (Wh)	x,x
Defrost interval [a] at 16 °C (h)	x,x	Defrost interval [a] at 32 °C (h)	x,x

Additional product specifications for low noise refrigerating appliances:

Parameter	Value	Parameter	Value
Daily energy consumption at 25 °C (kWh/24h)	x,xxx	Defrost interval ([a]) at 25 °C (h)	x,x

Compartment specifications:

Compartment type	Compartment parameters and values					
	Target temperature (°C)	Thermodynamic parameter (r_c)	N_c	M_c	Defrost factor (A_c)	Built-in factor (B_c)
Pantry	x	x,xx	x	x,xx	x,xx	x,xx
Wine storage	x	x,xx	x	x,xx	x,xx	x,xx
Cellar	x	x,xx	x	x,xx	x,xx	x,xx
Fresh food	x	x,xx	x	x,xx	x,xx	x,xx
Chill	x	x,xx	x	x,xx	x,xx	x,xx
0-star or ice making	x	x,xx	x	x,xx	x,xx	x,xx
1-star	x	x,xx	x	x,xx	x,xx	x,xx
2-star	x	x,xx	x	x,xx	x,xx	x,xx
3-star	x	x,xx	x	x,xx	x,xx	x,xx
4-star	x	x,xx	x	x,xx	x,xx	x,xx
2-star section	x	x,xx	x	x,xx	x,xx	x,xx
Variable temperature compartment	x	x,xx	x	x,xx	x,xx	x,xx

Additional information:
The references of the harmonised standards or other reliable accurate and reproducible methods applied:
A list of all equivalent models, including model identifiers:
[a] only for products with one or more auto-defrost systems

2. Where the information included in the technical documentation for a particular model has been obtained:

(a) from a model that has the same technical characteristics relevant for the technical information to be provided but is produced by a different manufacturer; or

(b) by calculation on the basis of design or extrapolation from another model of the same or a different manufacturer; or both.

The technical documentation shall include the details of such calculation, the assessment undertaken by the manufacturer to verify the accuracy of the calculation and, where appropriate, the declaration of identity between the models of different manufacturers.

ANNEX VII

Information to be provided in visual advertisements, in technical promotional material, in distance selling, except distance selling on the internet

1. In visual advertisements, for the purposes of ensuring conformity with the requirements laid down in point 1(e) of Article 3 and point 1(c) of Article 4, the energy efficiency class and the range of energy efficiency classes available on the label shall be shown as set out in point 4 of this Annex.
2. In technical promotional material, for the purposes of ensuring conformity with the requirements laid down in point 1(f) of Article 3 and point 1(d) of Article 4 the energy efficiency class and the range of energy efficiency classes available on the label shall be shown as set out in point 4 of this Annex.
3. Any paper-based distance selling must show the energy efficiency class and the range of energy efficiency classes available on the label as set out in point 4 of this Annex.
4. The energy efficiency class and the range of energy efficiency classes shall be shown, as indicated in Figure 1, with:
   (a) an arrow, containing the letter of the energy efficiency class in 100 % white, Calibri Bold and in a font size at least equivalent to that of the price, when the price is shown;
   (b) the colour of the arrow matching the colour of the energy efficiency class;
   (c) the range of available energy efficiency classes in 100 % black; and,
   (d) the size shall be such that the arrow is clearly visible and legible. The letter in the energy efficiency class arrow shall be positioned in the centre of the rectangular part of the arrow, with a border of 0,5 pt in 100 % black placed around the arrow and the letter of the energy efficiency class.

   By way of derogation, if the visual advertisement, technical promotional material or paper-based distance selling is printed in monochrome, the arrow can be in monochrome in that visual advertisement, technical promotional material or paper-based distance selling.

Figure 1

Coloured/monochrome left/right arrow, with range of energy efficiency classes indicated

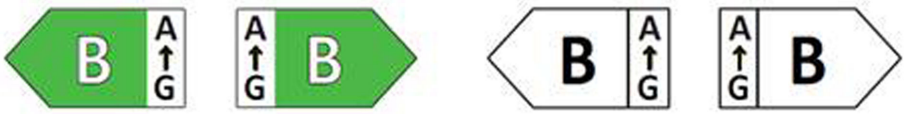

5. Telemarketing-based distance selling must specifically inform the customer of the energy efficiency class of the product and of the range of energy efficiency classes available on the label, and that the customer can access the full label and the product information sheet through a free access website, or by requesting a printed copy.
6. For all the situations mentioned in points 1 to 3 and 5, it must be possible for the customer to obtain, on request, a printed copy of the label and the product information sheet.

ANNEX VIII

Information to be provided in the case of distance selling through the internet

1. The appropriate label made available by suppliers in accordance with point 1(g) of Article 3 shall be shown on the display mechanism in proximity to the price of the product. The size shall be such that the label is clearly visible and legible and shall be proportionate to the size specified in point 3(1) and 3(2) of Annex III for refrigerating appliances. The label may be displayed using a nested display, in which case the image used for accessing the label shall comply with the specifications laid down in point 3 of this Annex. If nested display is applied, the label shall appear on the first mouse click, mouse roll-over or tactile screen expansion on the image.
2. The image used for accessing the label in the case of nested display, as indicated in Figure 2, shall:
   (a) be an arrow in the colour corresponding to the energy efficiency class of the product on the label;
   (b) indicate the energy efficiency class of the product on the arrow in 100 % white, Calibri Bold and in a font size equivalent to that of the price;
   (c) have the range of available energy efficiency classes in 100 % black; and,
   (d) have one of the following two formats, and its size shall be such that the arrow is clearly visible and legible. The letter in the energy efficiency class arrow shall be positioned in the centre of the rectangular part of the arrow, with a visible border in 100 % black placed around the arrow and the letter of the energy efficiency class:

Figure 2

Coloured left/right arrow, with range of energy efficiency classes indicated

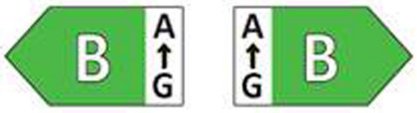

3. In the case of a nested display, the sequence of display of the label shall be as follows:
   (a) the image referred to in point 2 of this Annex shall be shown on the display mechanism in proximity to the price of the product;
   (b) the image shall link to the label set out in Annex III;
   (c) the label shall be displayed after a mouse click, mouse roll-over or tactile screen expansion on the image;
   (d) the label shall be displayed by pop up, new tab, new page or inset screen display;
   (e) for magnification of the label on tactile screens, the device conventions for tactile magnification shall apply;
   (f) the label shall cease to be displayed by means of a close option or other standard closing mechanism;
   (g) the alternative text for the graphic, to be displayed on failure to display the label, shall be the energy efficiency class of the product in a font size equivalent to that of the price.
4. The electronic product information sheet made available by suppliers in accordance with point 1(b) of Article 3 shall be shown on the display mechanism in proximity to the price of the product. The size shall be such that the product information sheet is clearly visible and legible. The product information sheet may be displayed using a nested display or by referring to the product database, in which case the link used for accessing the product information sheet shall clearly and legibly indicate 'Product information sheet'. If a nested display is used, the product information sheet shall appear on the first mouse click, mouse roll-over or tactile screen expansion on the link.

ANNEX IX

Verification procedure for market surveillance purposes

The verification tolerances set out in this Annex relate only to the verification of the declared parameters by Member State authorities and shall not be used by the supplier as an allowed tolerance to establish the values in the technical documentation. The values and classes on the label or in the product information sheet shall not be more favourable for the supplier than the values reported in the technical documentation.

Where a model has been designed to be able to detect it is being tested (e.g. by recognising the test conditions or test cycle), and to react specifically by automatically altering its performance during the test with the objective of reaching a more favourable level for any of the parameters specified in this Regulation or included in the technical documentation or included in any of the documentation provided, the model and all equivalent models shall be considered not compliant.

When verifying the compliance of a product model with the requirements laid down in this Regulation, the authorities of the Member States shall apply the following procedure:

(1) The Member State authorities shall verify one single unit of the model.

(2) The model shall be considered to comply with the applicable requirements if:

(a) the values given in the technical documentation pursuant to Article 3(3) of Regulation (EU) 2017/1369 (declared values), and, where applicable, the values used to calculate these values, are not more favourable for the supplier than the corresponding values given in the test reports; and

(b) the values published on the label and in the product information sheet are not more favourable for the supplier than the declared values, and the indicated energy efficiency class and the airborne acoustical noise emission class are not more favourable for the supplier than the class determined by the declared values; and

(c) when the Member State authorities test the unit of the model, the determined values (that is the values of the relevant parameters as measured in testing and the values calculated from these measurements) comply with the respective verification tolerances as given in Table 8.

(3) If the results referred to in points 2(a) and (b) are not achieved, the model and all equivalent models shall be considered not to comply with this Regulation.

(4) If the result referred to in point 2(c) is not achieved, the Member State authorities shall select three additional units of the same model for testing. As an alternative, the three additional units selected may be of one or more equivalent models.

(5) The model shall be considered to comply with the applicable requirements if for these three units the arithmetic mean of the determined values complies with the respective tolerances given in Table 8.

(6) If the result referred to in point 5 is not achieved, the model and all equivalent models shall be considered not to comply with this Regulation.

(7) The Member State authorities shall provide all relevant information to the authorities of the other Member States and to the Commission without delay once a decision has been taken on the non-compliance of the model according to points 3 and 6.

The Member State authorities shall use the measurement and calculation methods set out in Annex IV.

The Member State authorities shall only apply the verification tolerances set out in Table 8 and shall only use the procedure set out in points 1 to 7 for the requirements referred to in this Annex. For the parameters in Table 8, no other tolerances, such as those set out in harmonised standards or in any other measurement method, shall be applied.

Table 8

Verification tolerances for measured parameters

Parameters	Verification tolerances
Total volume and compartment volume	The determined value [a] shall not be more than 3 % or 1 litre lower — whichever is the greater value — than the declared value.
Freezing capacity	The determined value [a] shall not be more than 10 % lower than the declared value.
$E_{16,}$ E_{32}	The determined value [a] shall not be more than 10 % higher than the declared value.
E_{aux}	The determined value [a] shall not be more than 10 % higher than the declared value.
Annual energy consumption	The determined value [a] shall not be more than 10 % higher than the declared value.
Internal humidity of wine storage appliances (%)	The determined value [a] shall not differ from the declared value by more than 10 %.
Airborne acoustical noise emissions	The determined value [a] shall not be more than 2 dB(A) re 1 pW more than the declared value.
Temperature rise time	The determined value [a] shall not be more than 15 % higher than the declared value.

[a] in the case of three additional units tested as prescribed in point 4, the determined value means the arithmetic mean of the values determined for these three additional units.

Appendix C

Drawings

Note: The scale on the drawings corresponds only to the original paper size and not to this document's size.

Regenerator block

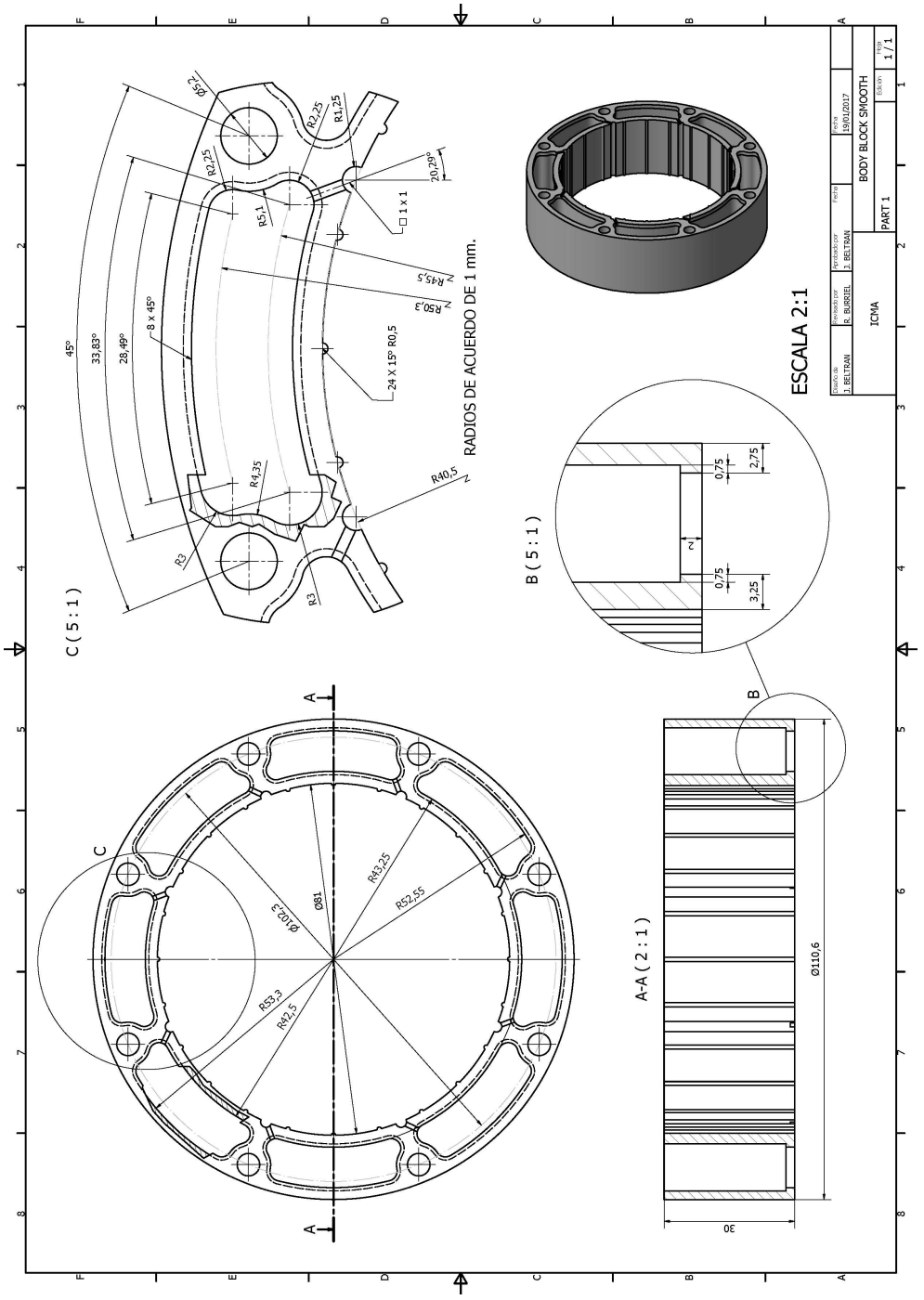

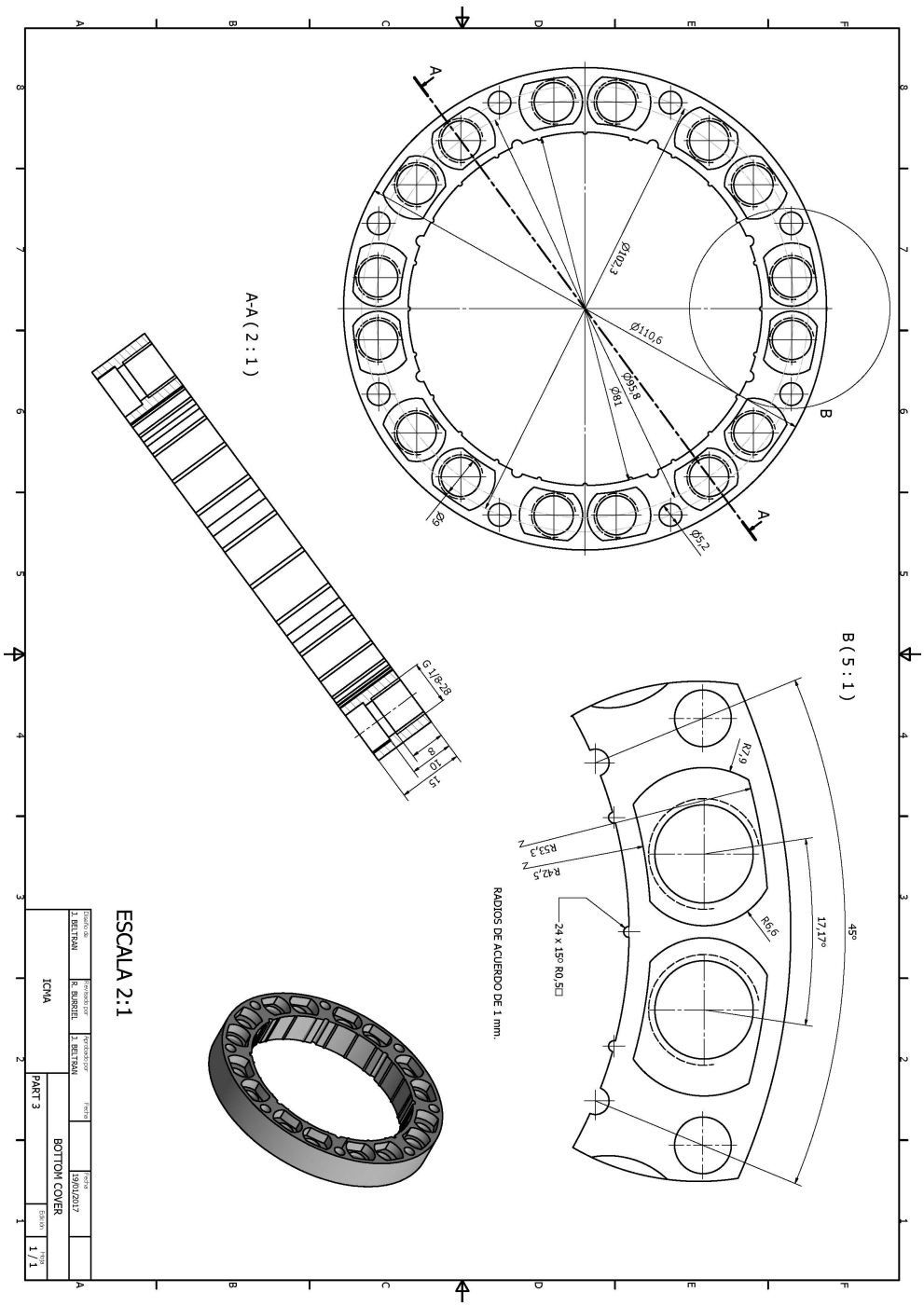
A-A (2 : 1)
B (5 : 1)
Ø102,3
Ø110,6
Ø55,8
Ø81
Ø6
Ø5,2
G 1/8-28
15
12
8
R7,9
R53,3
R42,5
R66
17,17°
45°
24 x 15° R0,5
RADIOS DE ACUERDO DE 1 mm.
ESCALA 2:1
DIBUJADO
J. BELTRAN
COMPROBADO
R. BURGEL
APROBADO
J. BELTRAN
FECHA
19/01/2017
ICMA
PART 3
BOTTOM COVER
ESCALA
1/1
HOJA
1/1

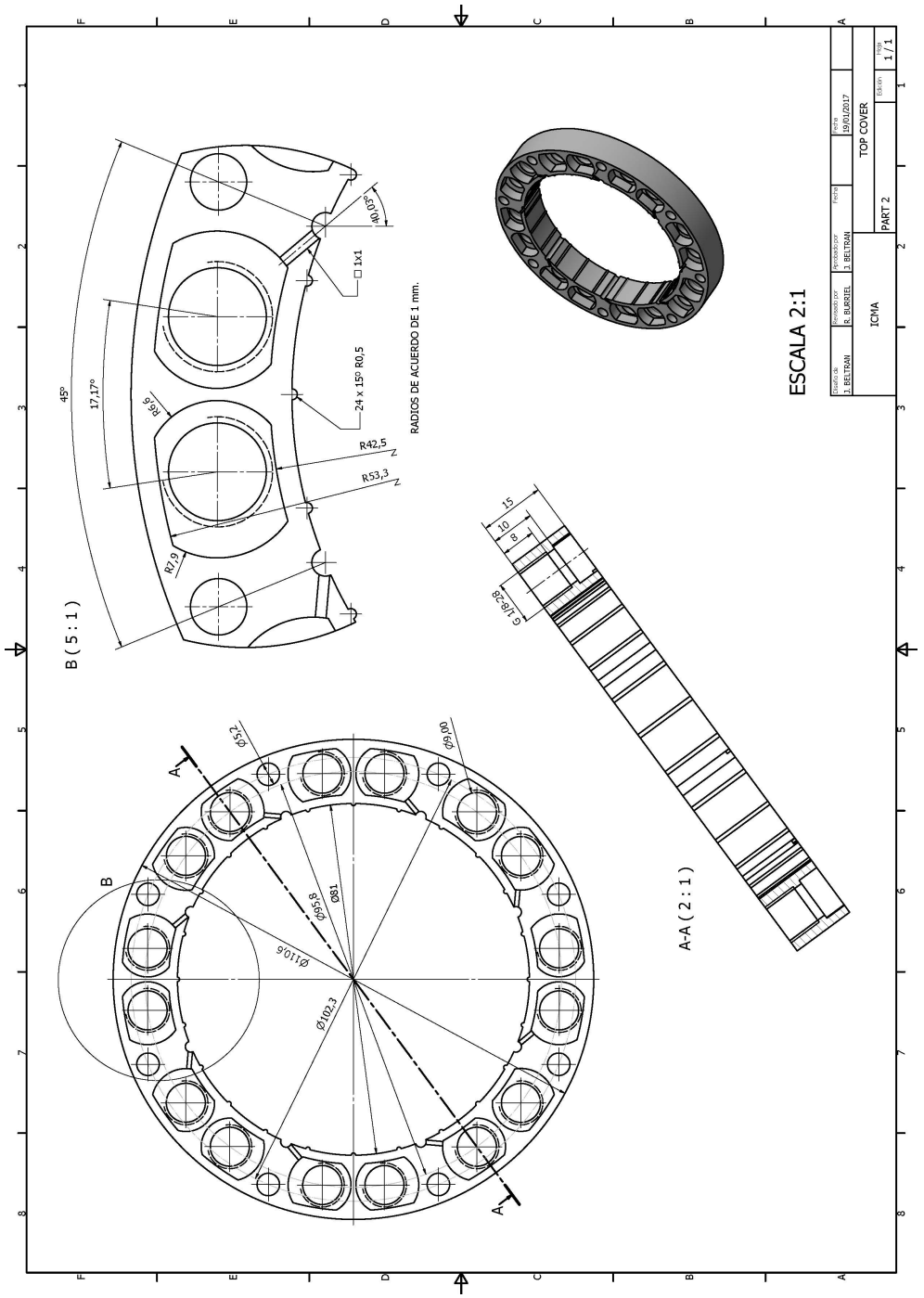
ESCALA 2:1
B (5 : 1)
A-A (2 : 1)
RADIOS DE ACUERDO DE 1 mm.
45°
17,17°
R6,6
R7,9
R42,5
R53,3
24 x 15° R0,5
□ 1x1
10°
15
10
8
6,1/6,28
Ø52
Ø60
Ø95,8
180
Ø110,6
Ø102,3
A
B
ICMA
PART 2
TOP COVER
19/01/2017
1 / 1

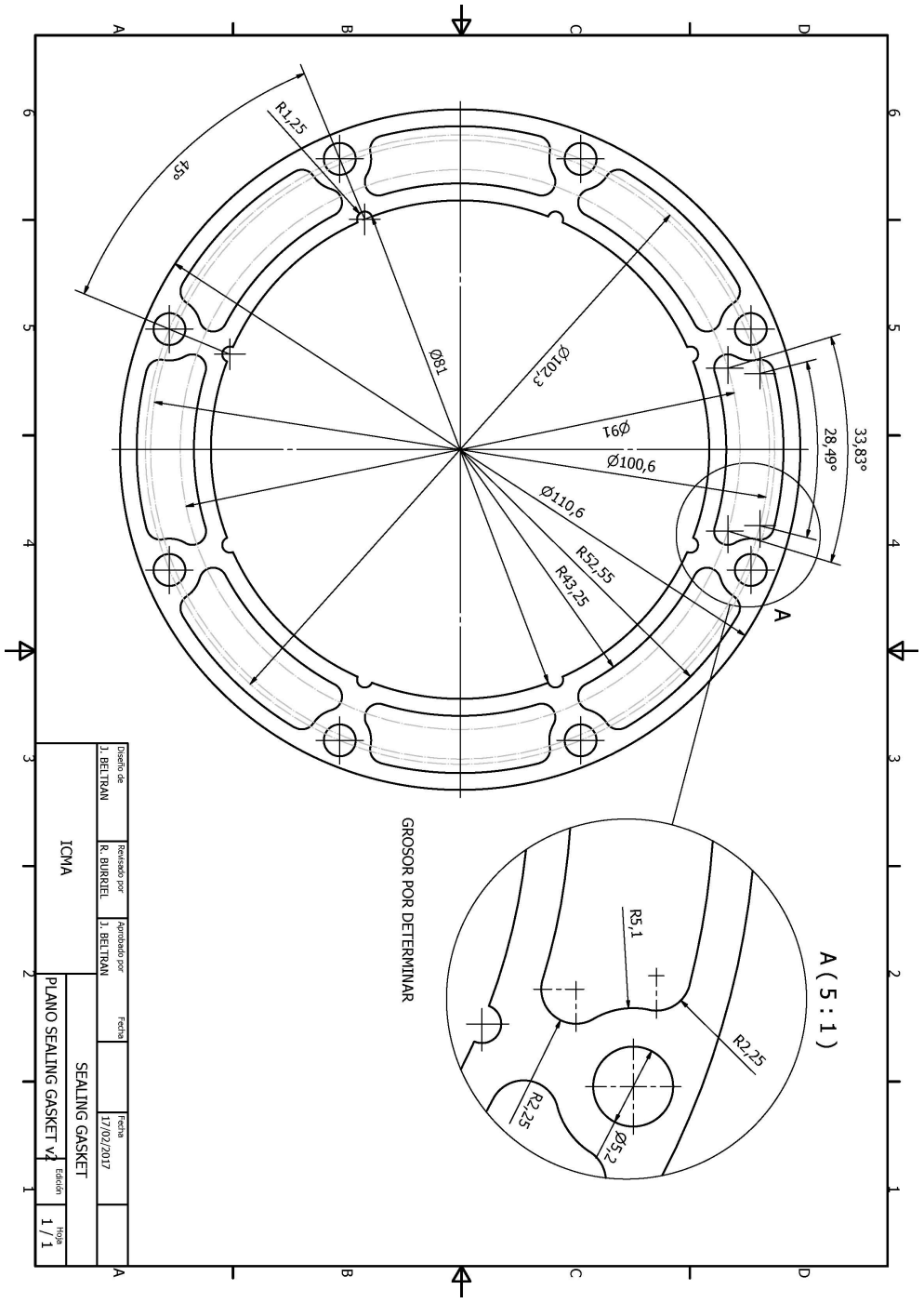
R1,25
45°
Ø81
Ø102,3
Ø91
Ø100,6
Ø110,6
R52,55
R43,25
33,83°
28,49°
A
A (5 : 1)
R5,1
R2,25
R2,25
Ø5,2
GROSOR POR DETERMINAR
Diseño de
J. BELTRAN
Revisado por
R. BURRIEL
Aprobado por
J. BELTRAN
Fecha
17/02/2017
ICMA
SEALING GASKET
PLANO SEALING GASKET v2
Edición
Hoja
1 / 1

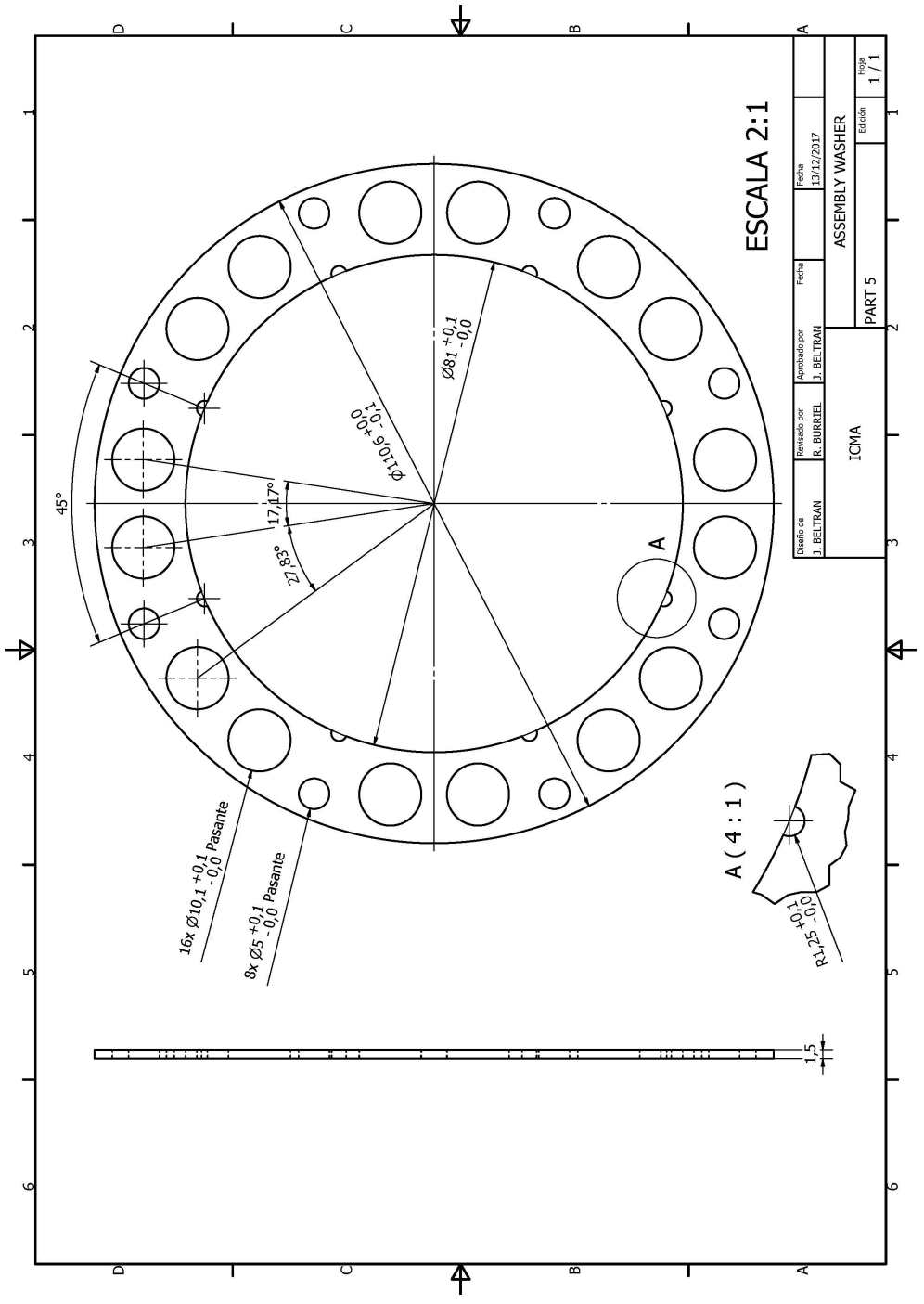
ESCALA 2:1
45°
17,17°
27,83°
Ø110,6 +0,0 -0,1
Ø81 +0,1 -0,0
16x Ø10,1 +0,1 -0,0 Pasante
8x Ø5 +0,1 -0,0 Pasante
A
A (4 : 1)
R1,25 +0,1 -0,0
1,5
Diseño de J. BELTRAN
Revisado por R. BURRIEL
Aprobado por J. BELTRAN
Fecha
Fecha 13/12/2017
ICMA
ASSEMBLY WASHER
PART 5
Edición
Hoja 1 / 1

Cold spot 1

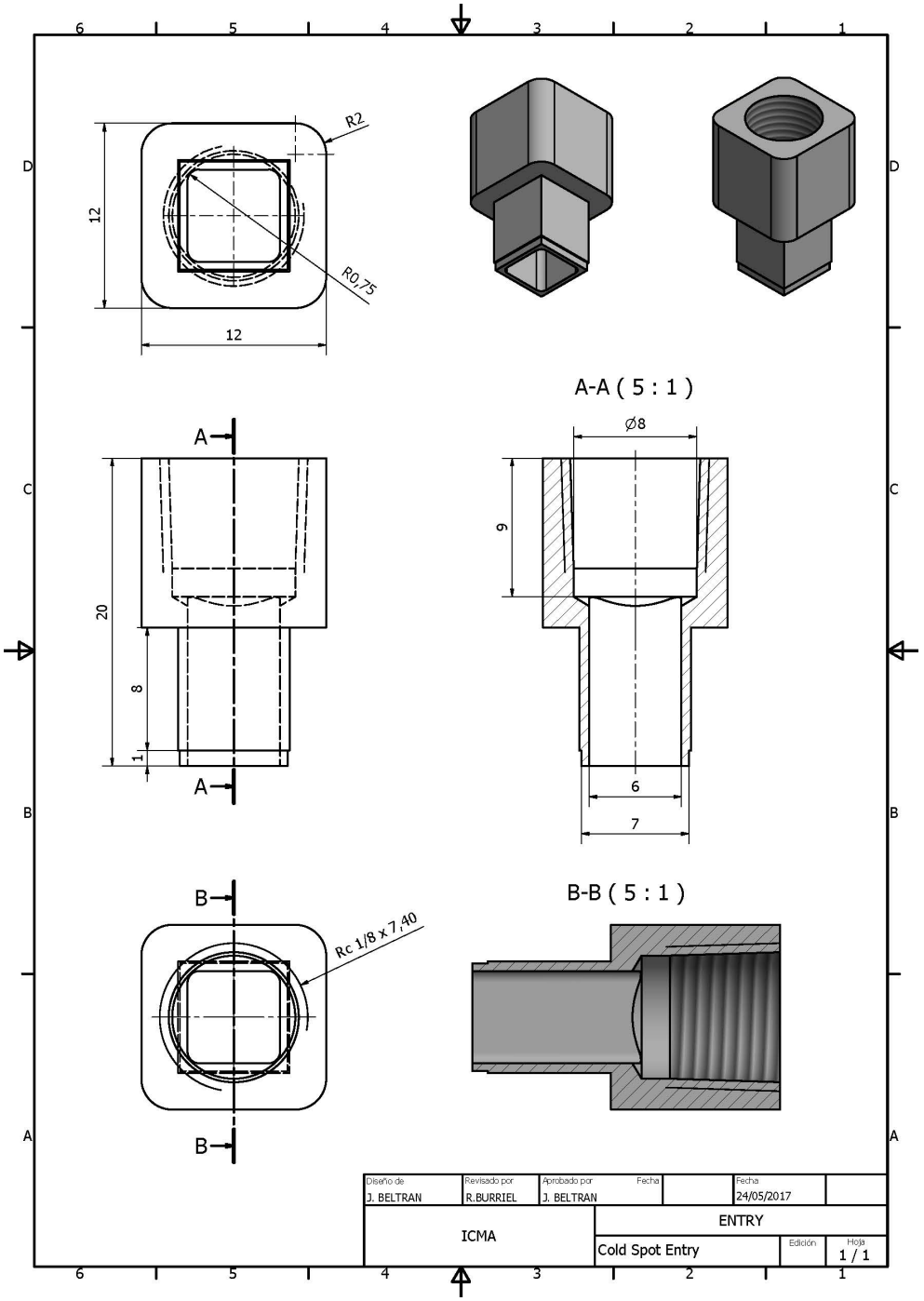
R2
R0,75
12
12
A-A (5 : 1)
A
A
20
8
1
Ø8
9
6
7
B
B
Rc 1/8 x 7,40
B-B (5 : 1)
Diseño de
J. BELTRAN
Revisado por
R.BURRIEL
Aprobado por
J. BELTRAN
Fecha
Fecha
24/05/2017
ICMA
ENTRY
Cold Spot Entry
Edición
Hoja
1 / 1

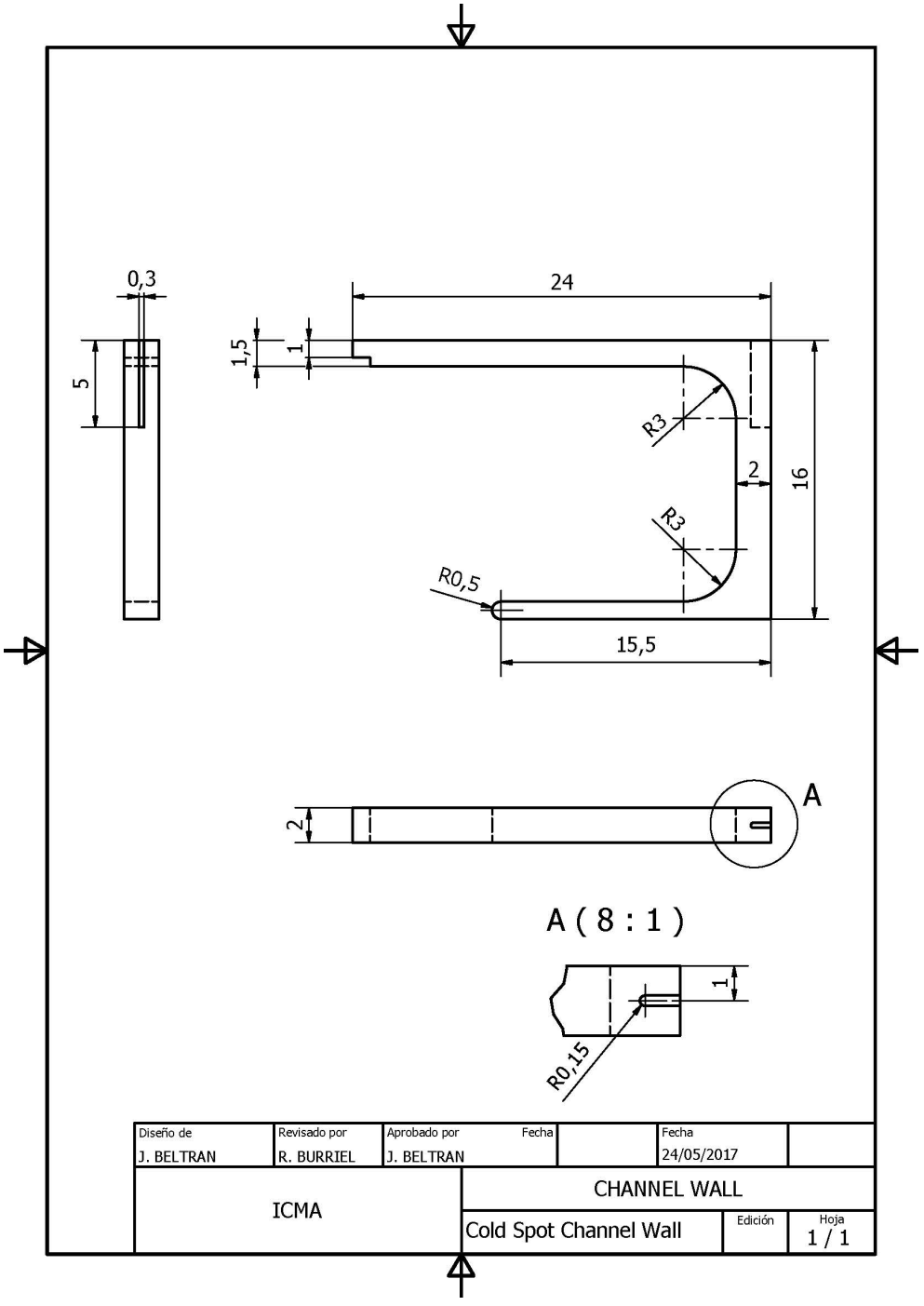
0,3
5
1,5
1
24
R3
2
16
R3
R0,5
15,5
2
A
A (8 : 1)
1
R0,15
Diseño de
J. BELTRAN
Revisado por
R. BURRIEL
Aprobado por
J. BELTRAN
Fecha
Fecha
24/05/2017
ICMA
CHANNEL WALL
Cold Spot Channel Wall
Edición
Hoja
1 / 1

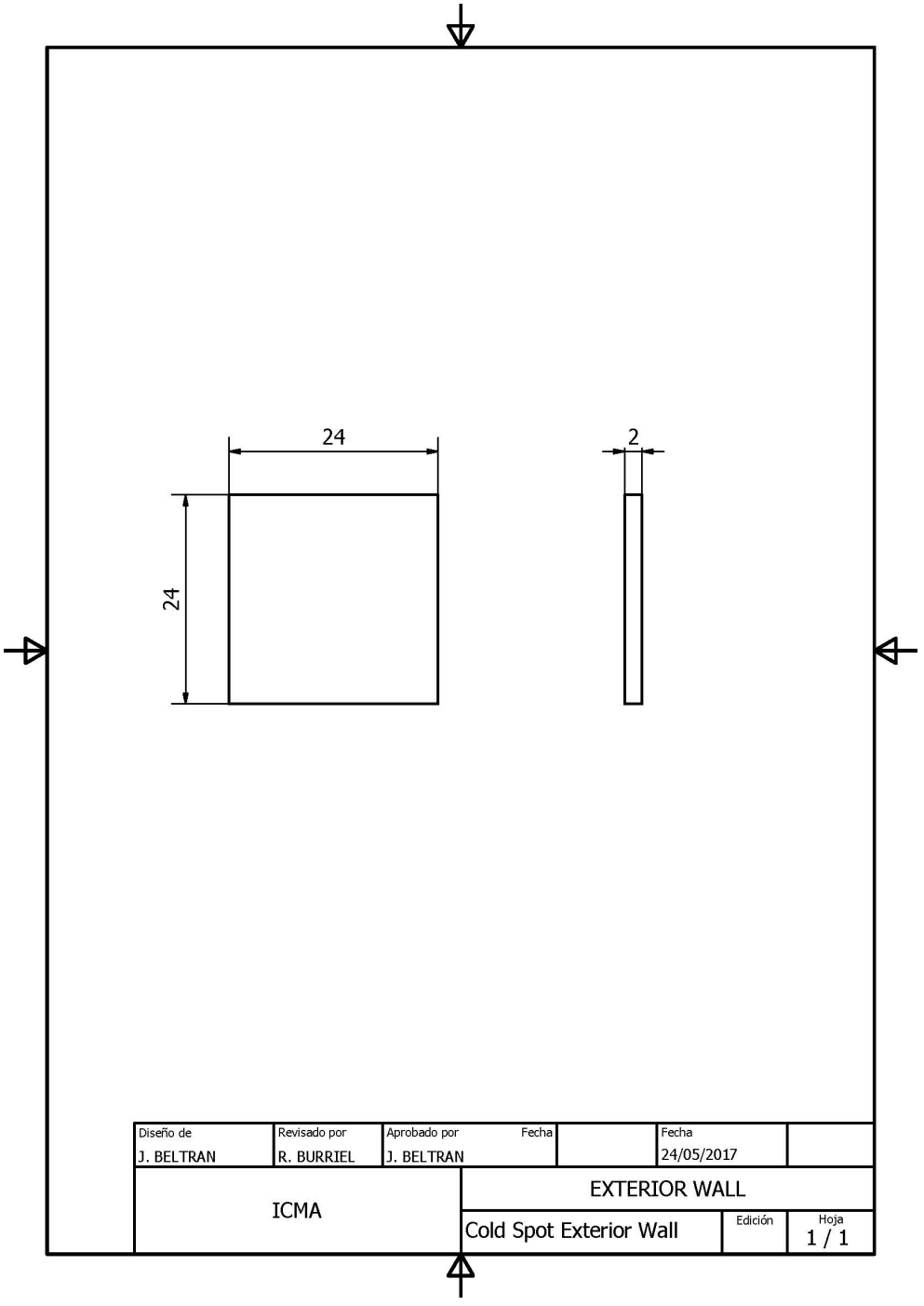
24
2
24
Diseño de
J. BELTRAN
Revisado por
R. BURRIEL
Aprobado por
J. BELTRAN
Fecha
Fecha
24/05/2017
ICMA
EXTERIOR WALL
Cold Spot Exterior Wall
Edición
Hoja
1 / 1

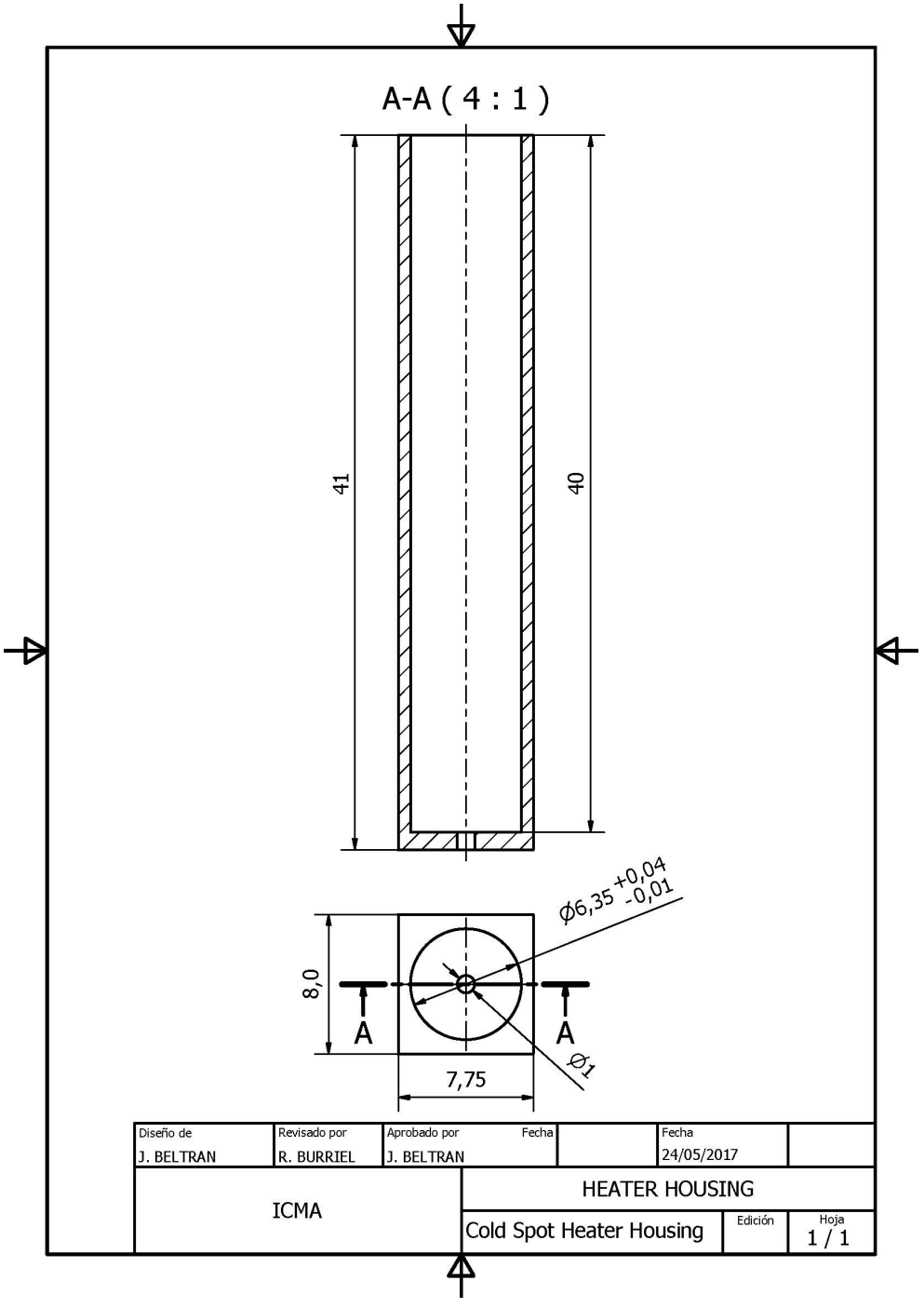
A-A (4 : 1)
41
40
Ø6,35 +0,04 -0,01
8,0
A
A
7,75
Ø1
Diseño de
J. BELTRAN
Revisado por
R. BURRIEL
Aprobado por
J. BELTRAN
Fecha
Fecha
24/05/2017
ICMA
HEATER HOUSING
Cold Spot Heater Housing
Edición
Hoja
1 / 1

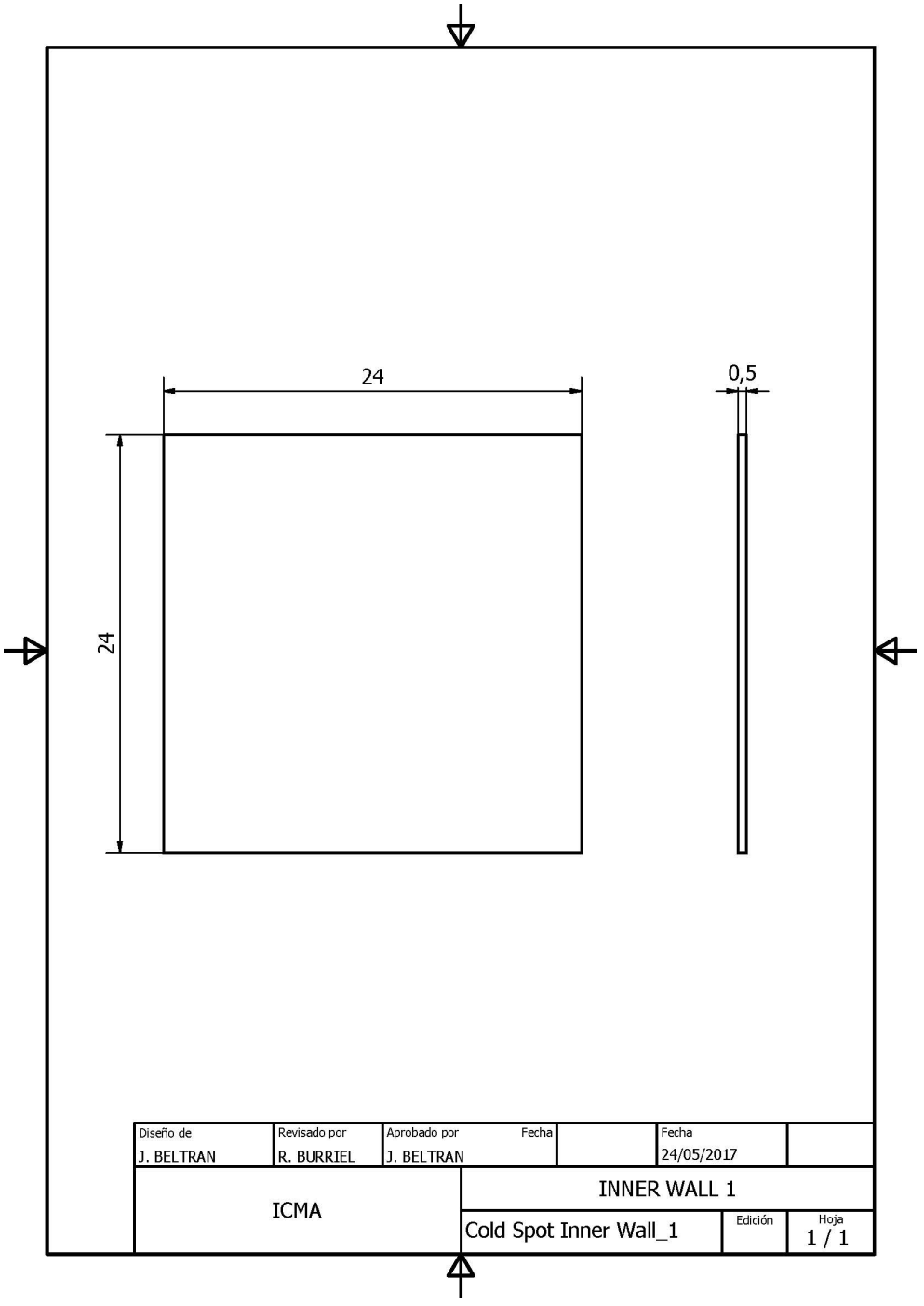
24
0,5
24
Diseño de
J. BELTRAN
Revisado por
R. BURRIEL
Aprobado por
J. BELTRAN
Fecha
Fecha
24/05/2017
ICMA
INNER WALL 1
Cold Spot Inner Wall_1
Edición
Hoja
1 / 1

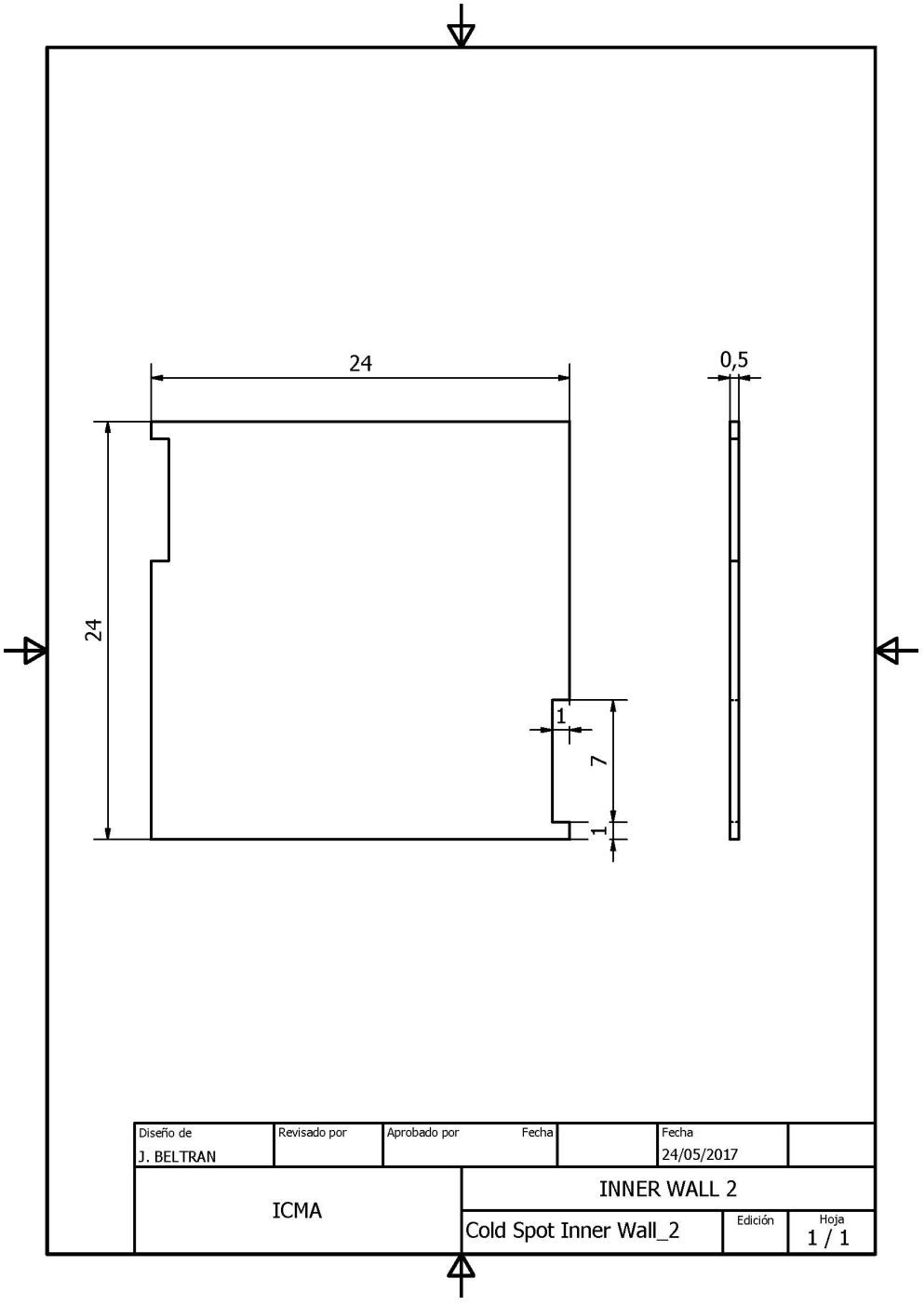
24
0,5
24
1
7
1
Diseño de
J. BELTRAN
Revisado por
Aprobado por
Fecha
Fecha
24/05/2017
ICMA
INNER WALL 2
Cold Spot Inner Wall_2
Edición
Hoja
1 / 1

Cold spot 2

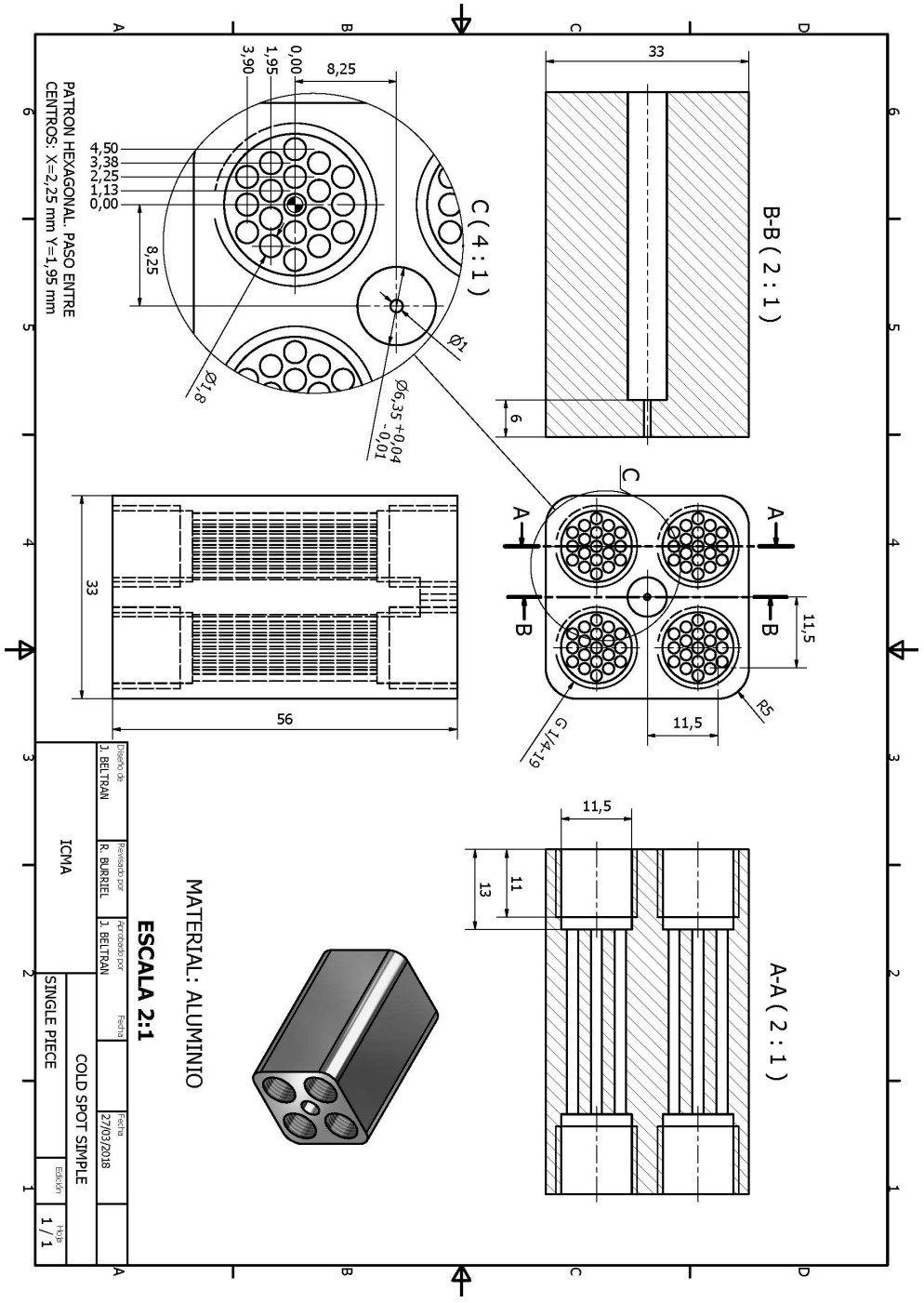
PATRON HEXAGONAL. PASO ENTRE CENTROS: X=2,25 mm Y=1,95 mm
C (4 : 1)
B-B (2 : 1)
A-A (2 : 1)
33
8,25
0,00
1,95
3,90
4,50
3,38
2,25
1,13
0,00
Ø1
Ø1,8
Ø6,35 +0,04 -0,01
6
11,5
R5
G 1/4-19
56
13
11
MATERIAL: ALUMINIO
ESCALA 2:1
ICMA
J. BELTRAN
R. BURRIEL
J. BELTRAN
27/03/2018
COLD SPOT SIMPLE
SINGLE PIECE
1 / 1

Cold spot 3

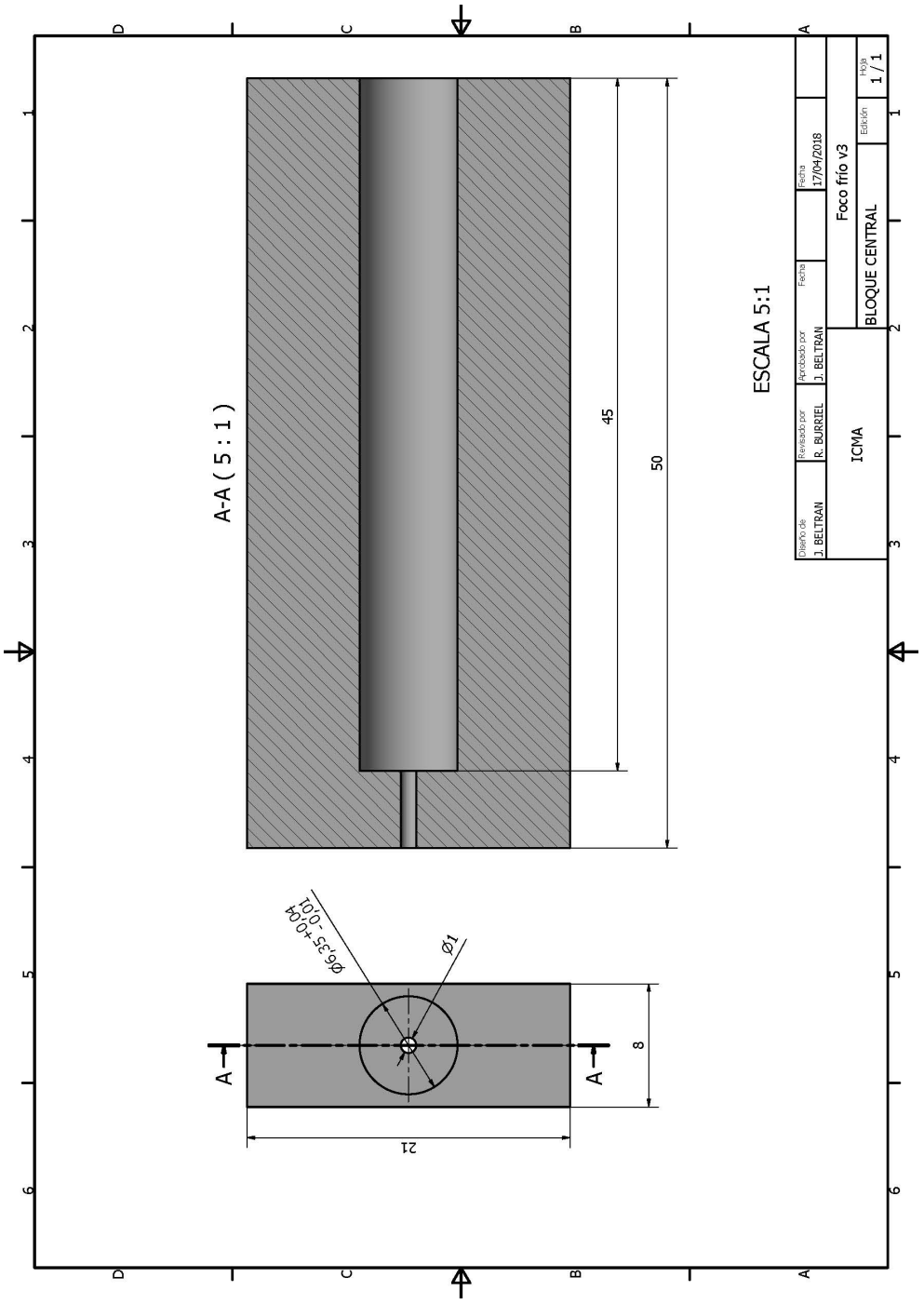
A-A (5 : 1)
45
50
ESCALA 5:1
Ø6,35 +0,04 -0,01
Ø1
A
A
8
21
Diseño de: J. BELTRAN
Revisado por: R. BURRIEL
Aprobado por: J. BELTRAN
Fechas
ICMA
Foco frío v3
BLOQUE CENTRAL
Fecha 17/04/2018
Edición
Hoja 1 / 1

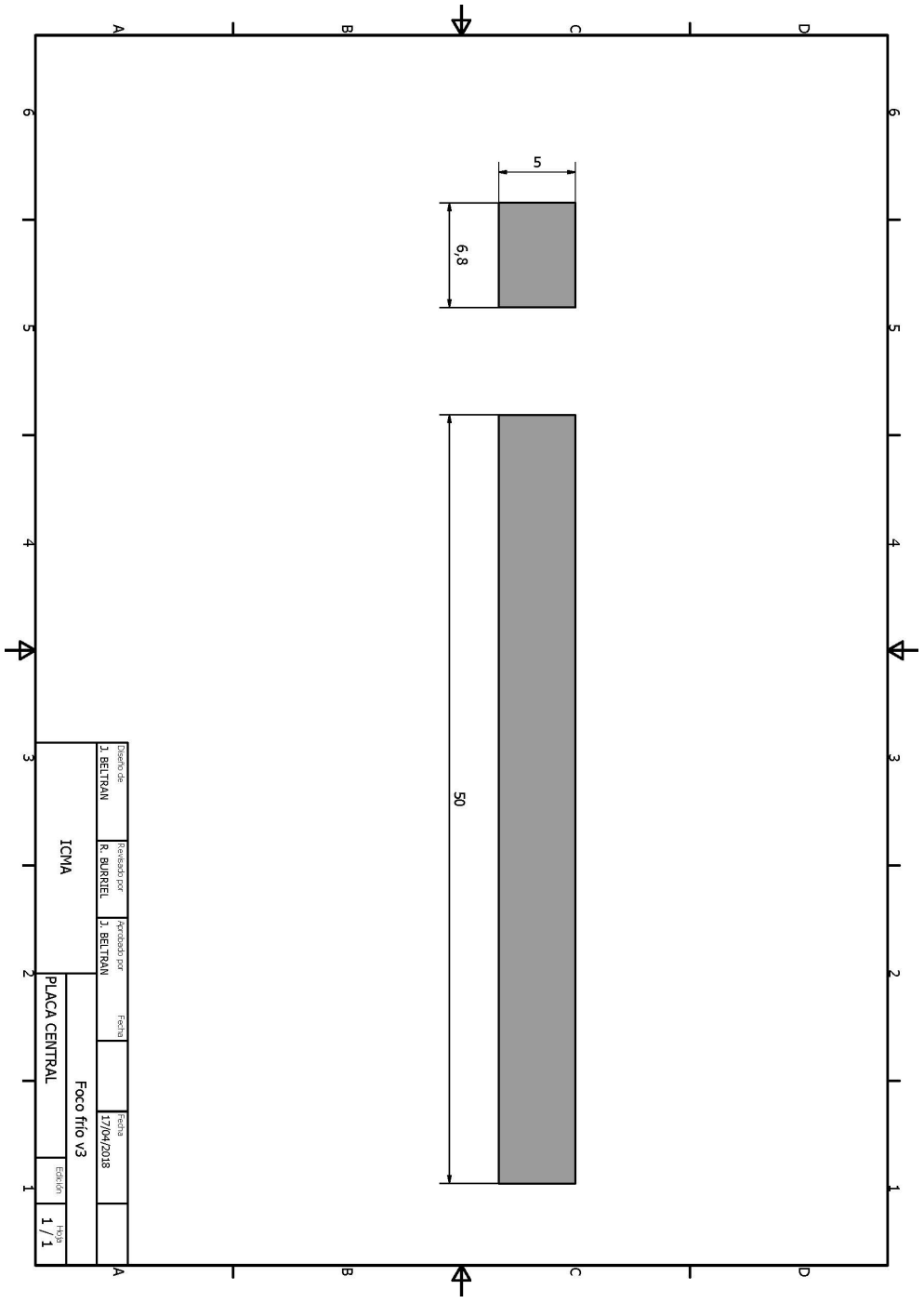
5
6,8
50
Diseño de
J. BELTRAN
Revisado por
R. BURRIEL
Aprobado por
J. BELTRAN
Fecha
Fecha
17/04/2018
ICMA
PLACA CENTRAL
Foco frío v3
Edición
Hoja
1 / 1

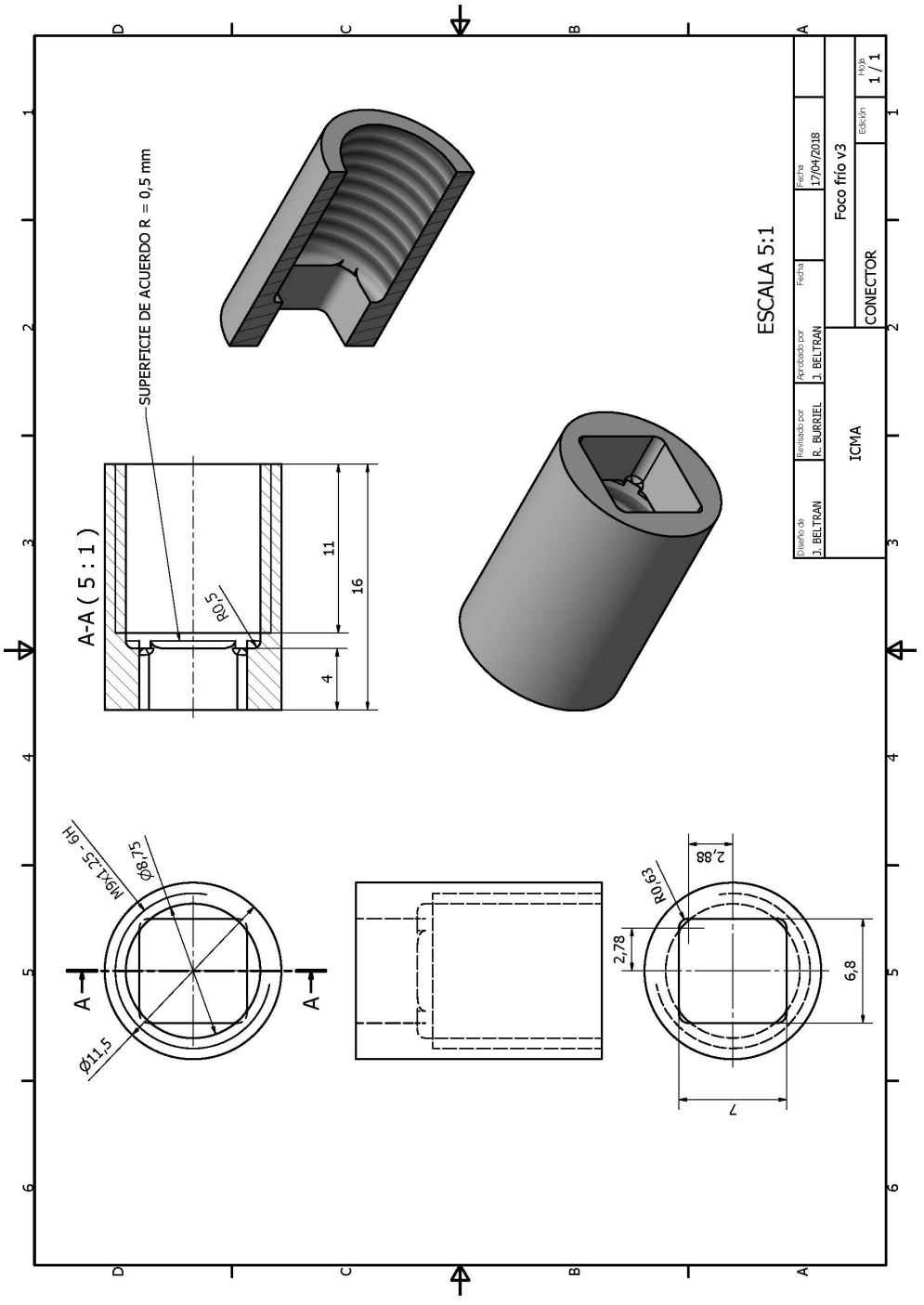
SUPERFICIE DE ACUERDO R = 0,5 mm
A-A (5 : 1)
R0,5
11
16
4
ESCALA 5:1
M9X1,25 - 6H
Ø8,75
Ø11,5
A
A
R0,63
2,88
2,78
6,8
7
Foco frío v3
CONECTOR
ICMA
Diseño de: J. BELTRAN
Revisado por: R. BURRIEL
Aprobado por: J. BELTRAN
Fecha: 17/04/2018
Edición
Hoja 1 / 1

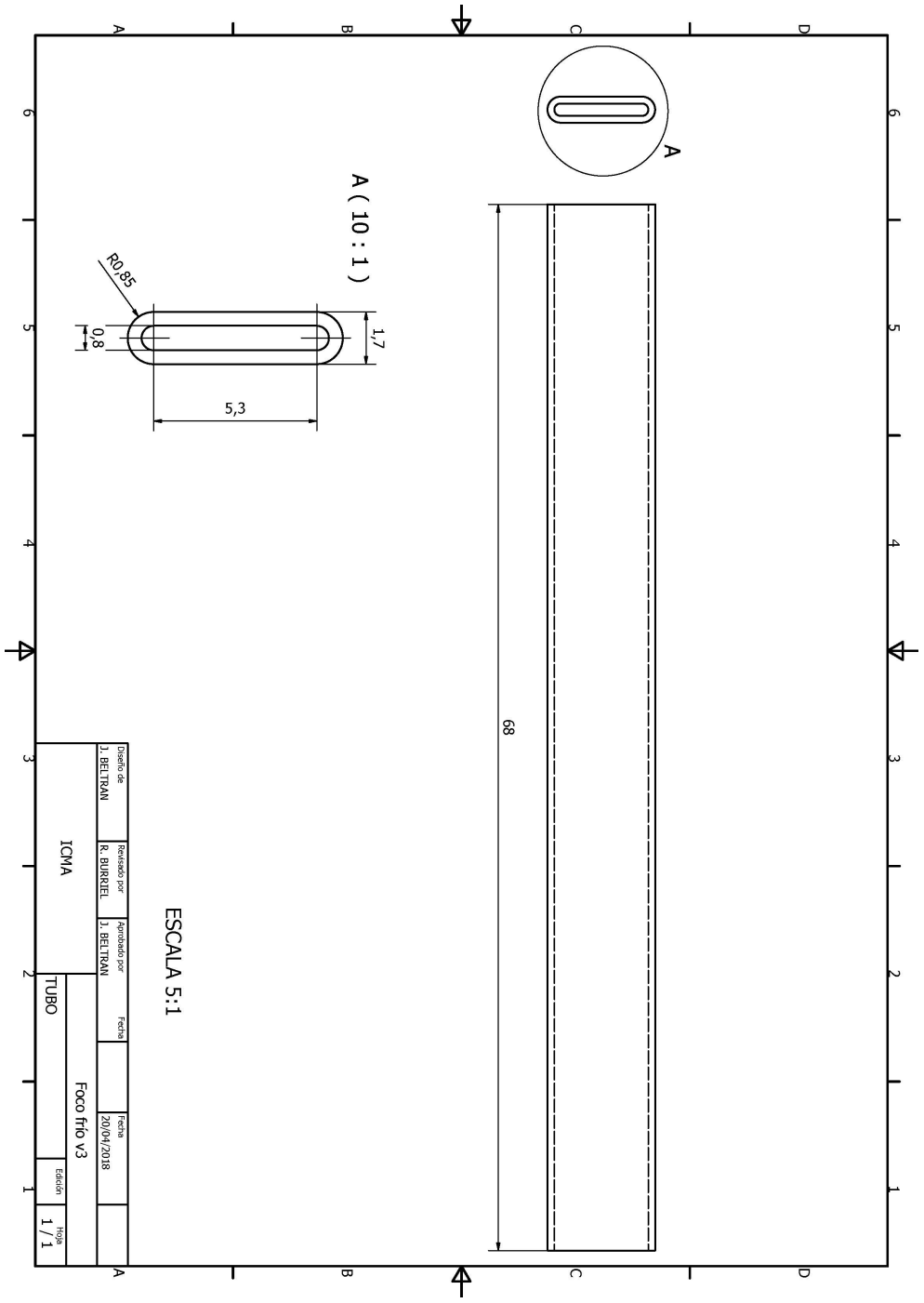
A
A (10 : 1)
R0,85
0,8
1,7
5,3
68
ESCALA 5:1
Diseño de
J. BELTRAN
Revisado por
R. BURRIEL
Aprobado por
J. BELTRAN
Fecha
20/04/2018
ICMA
TUBO
Foco frío v3
Edición
Hoja
1 / 1

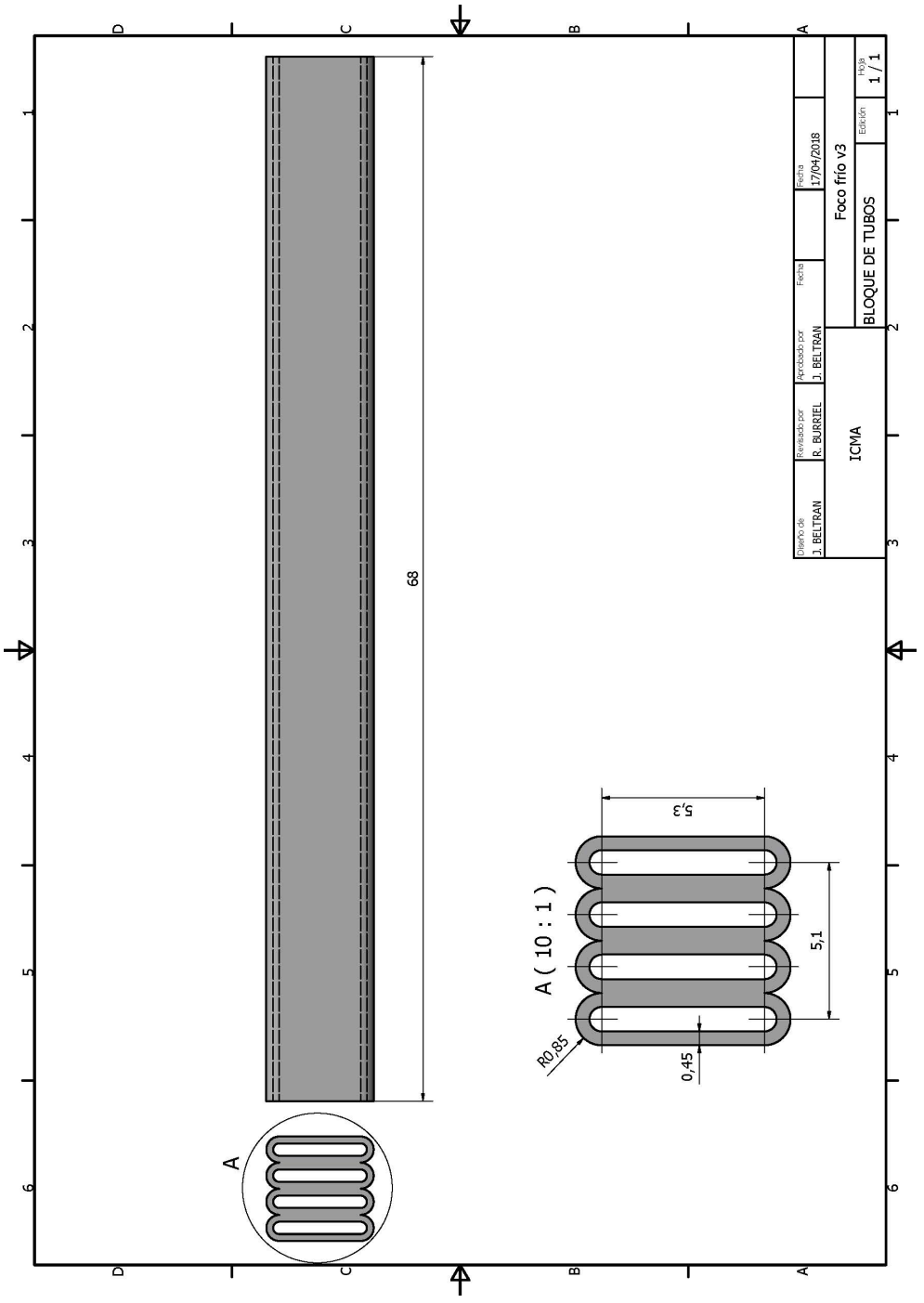
68
A
A (10 : 1)
5,3
5,1
R0,85
0,45
Diseño de: J. BELTRAN
Revisado por: R. BURRIEL
Aprobado por: J. BELTRAN
Fecha
Fecha: 17/04/2018
ICMA
Foco frío v3
BLOQUE DE TUBOS
Edición
Hoja 1 / 1

Magnet

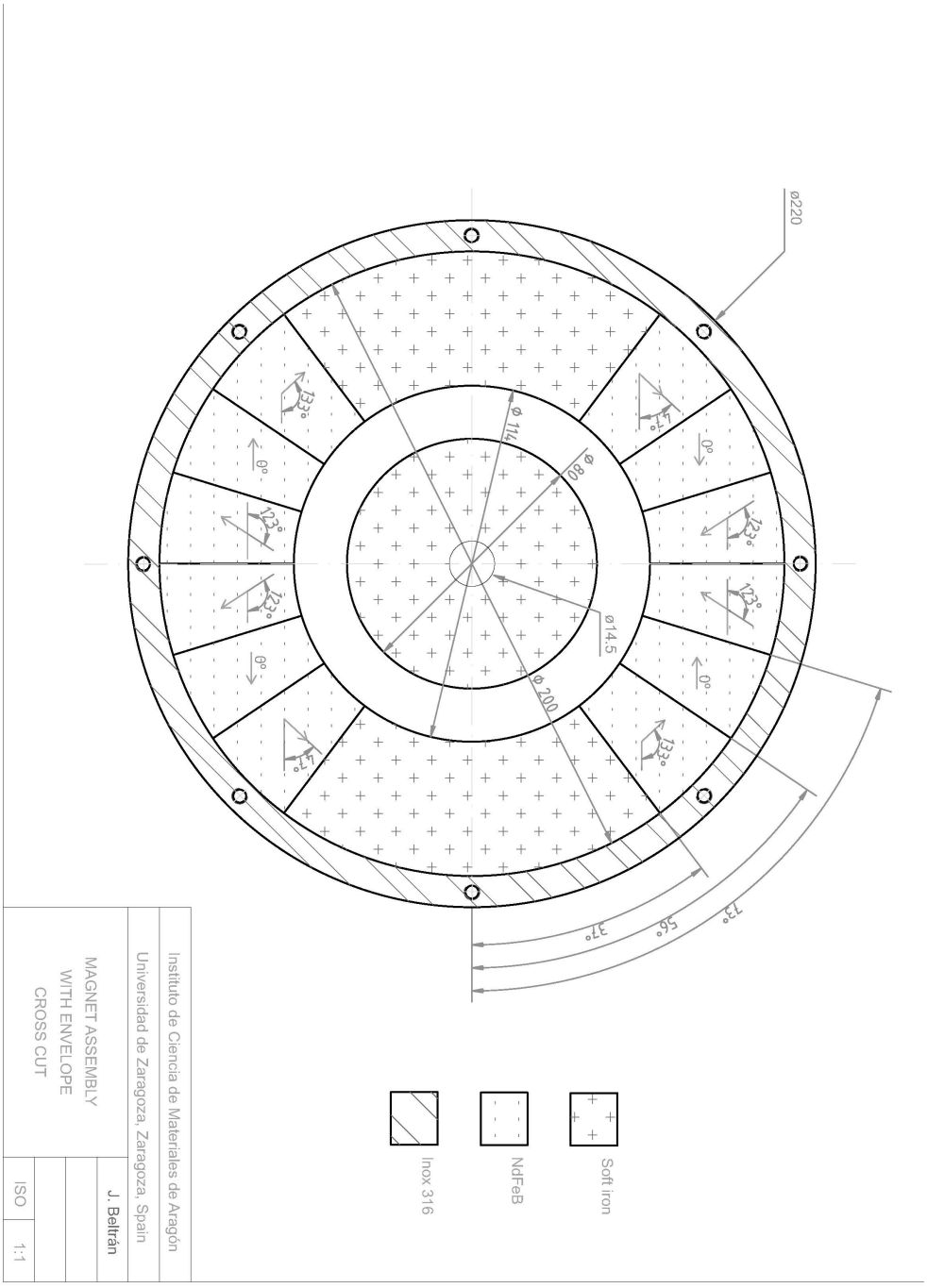
ø220
ø 114
ø 80
ø14.5
ø 200
33°
0°
123°
73°
56°
37°
Inox 316
NdFeB
Soft iron
Instituto de Ciencia de Materiales de Aragón
Universidad de Zaragoza, Zaragoza, Spain
J. Beltrán
MAGNET ASSEMBLY
WITH ENVELOPE
CROSS CUT
ISO
1:1

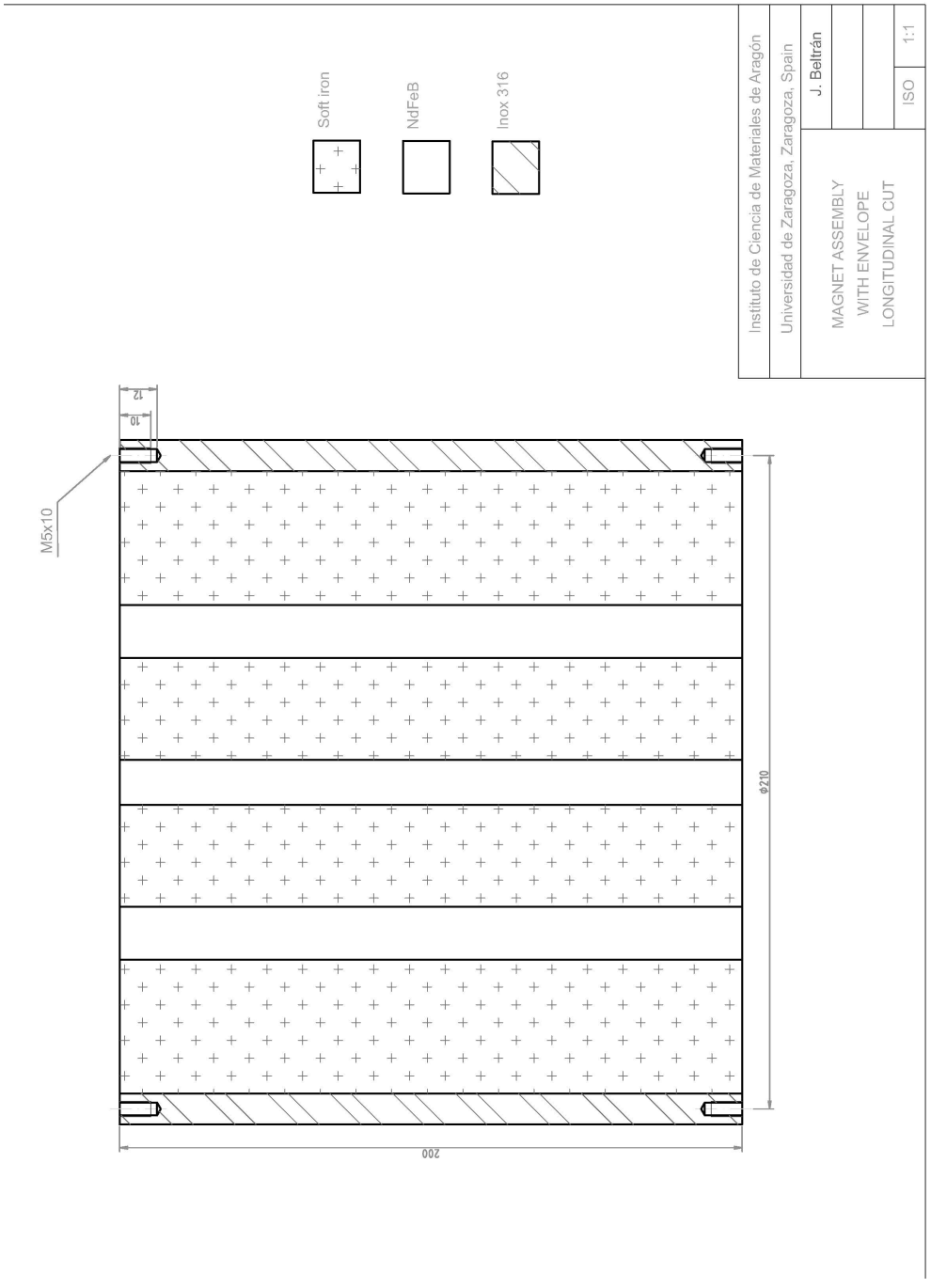
Soft iron
NdFeB
Inox 316
Instituto de Ciencia de Materiales de Aragón
Universidad de Zaragoza, Zaragoza, Spain
J. Beltrán
MAGNET ASSEMBLY
WITH ENVELOPE
LONGITUDINAL CUT
ISO
1:1
M5x10
12
10
ϕ210
200

Stamping tools

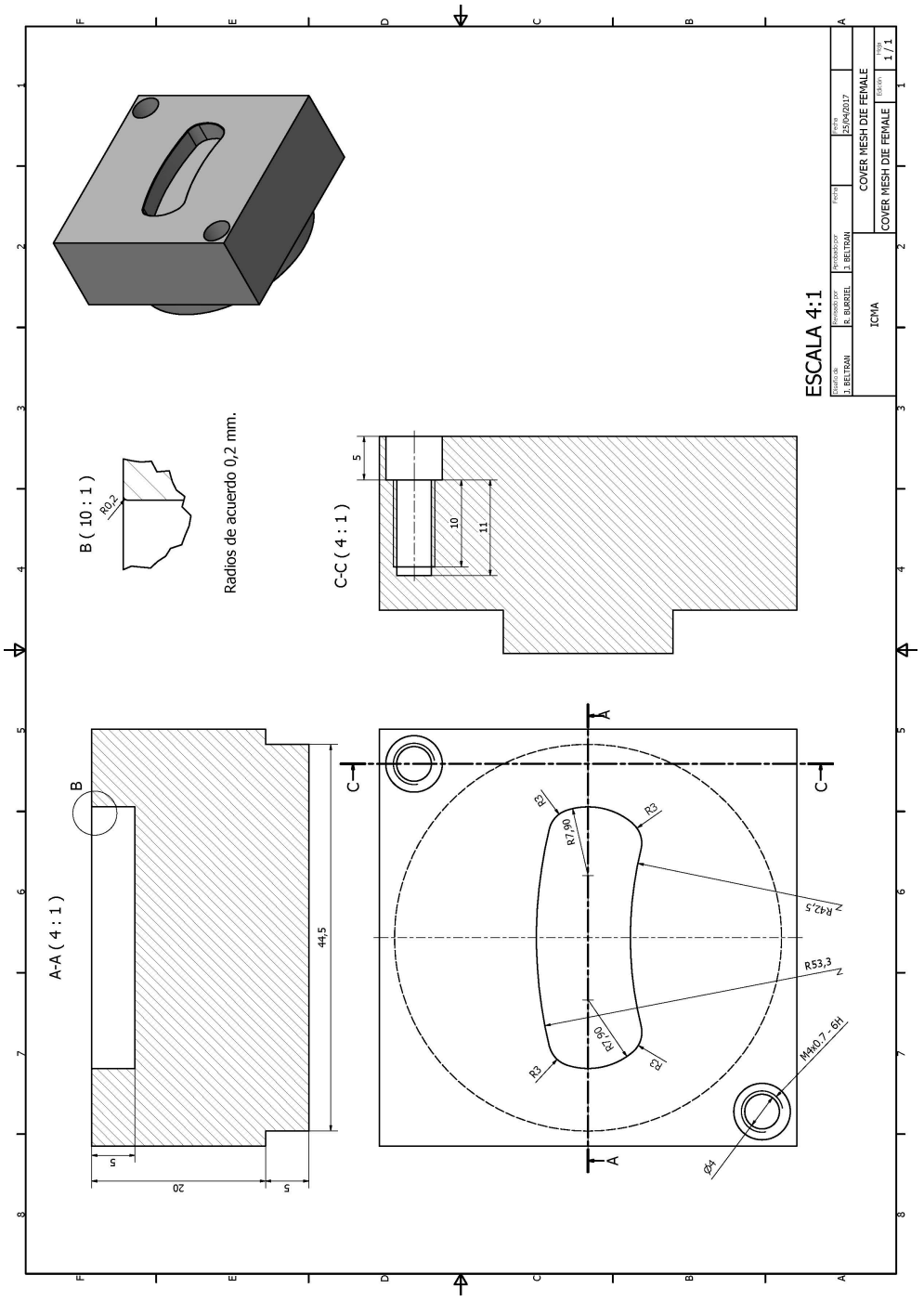

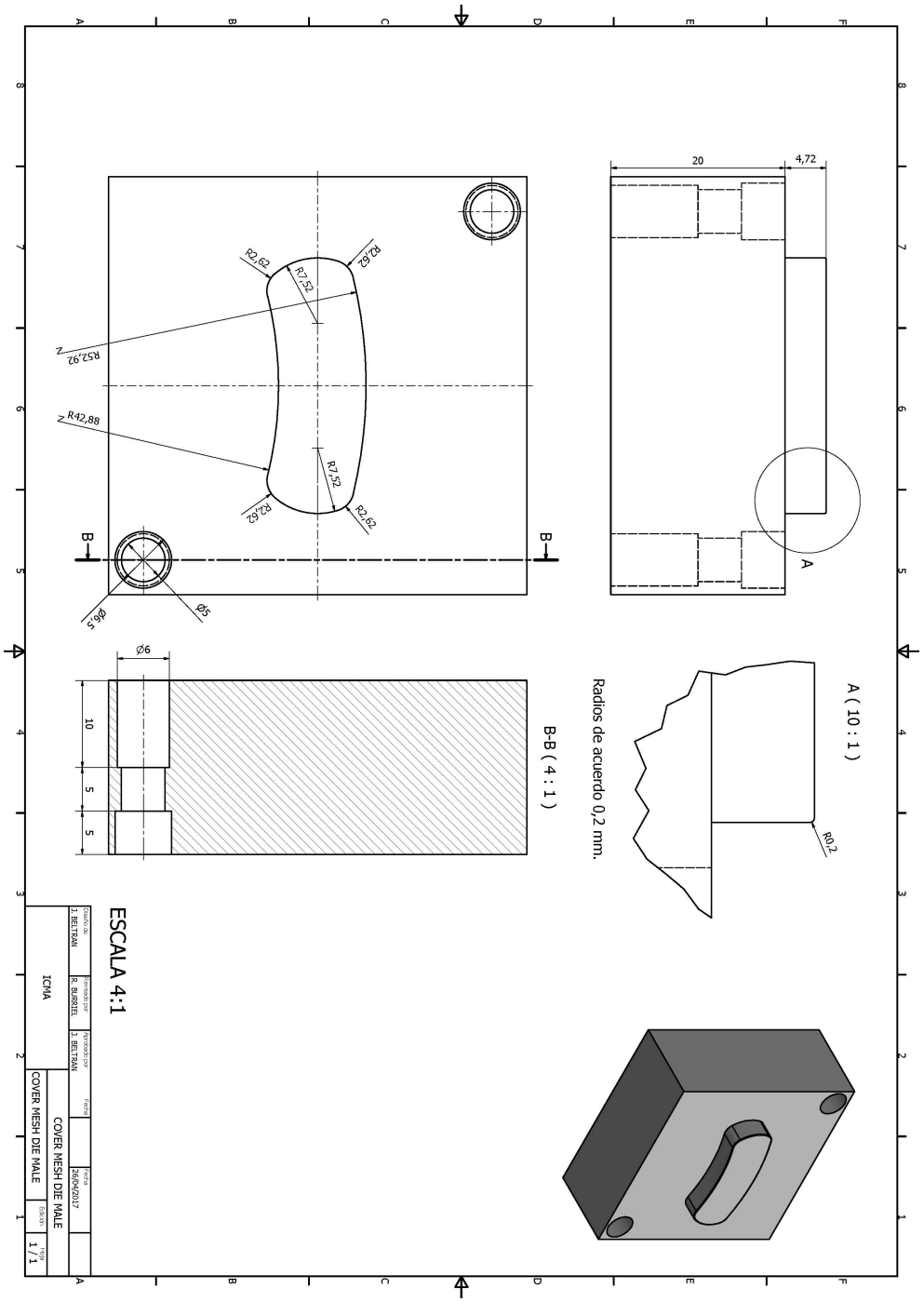
20
4,72
R0,62
R7,52
R2,62
R52,92
R42,88
R7,52
R2,62
R2,62
B
B
Ø8,5
Ø5
A
A (10 : 1)
Radios de acuerdo 0,2 mm.
R0,2
Ø6
10
5
5
B-B (4 : 1)
ESCALA 4:1
ICMA
COVER MESH DIE MALE
1 / 1

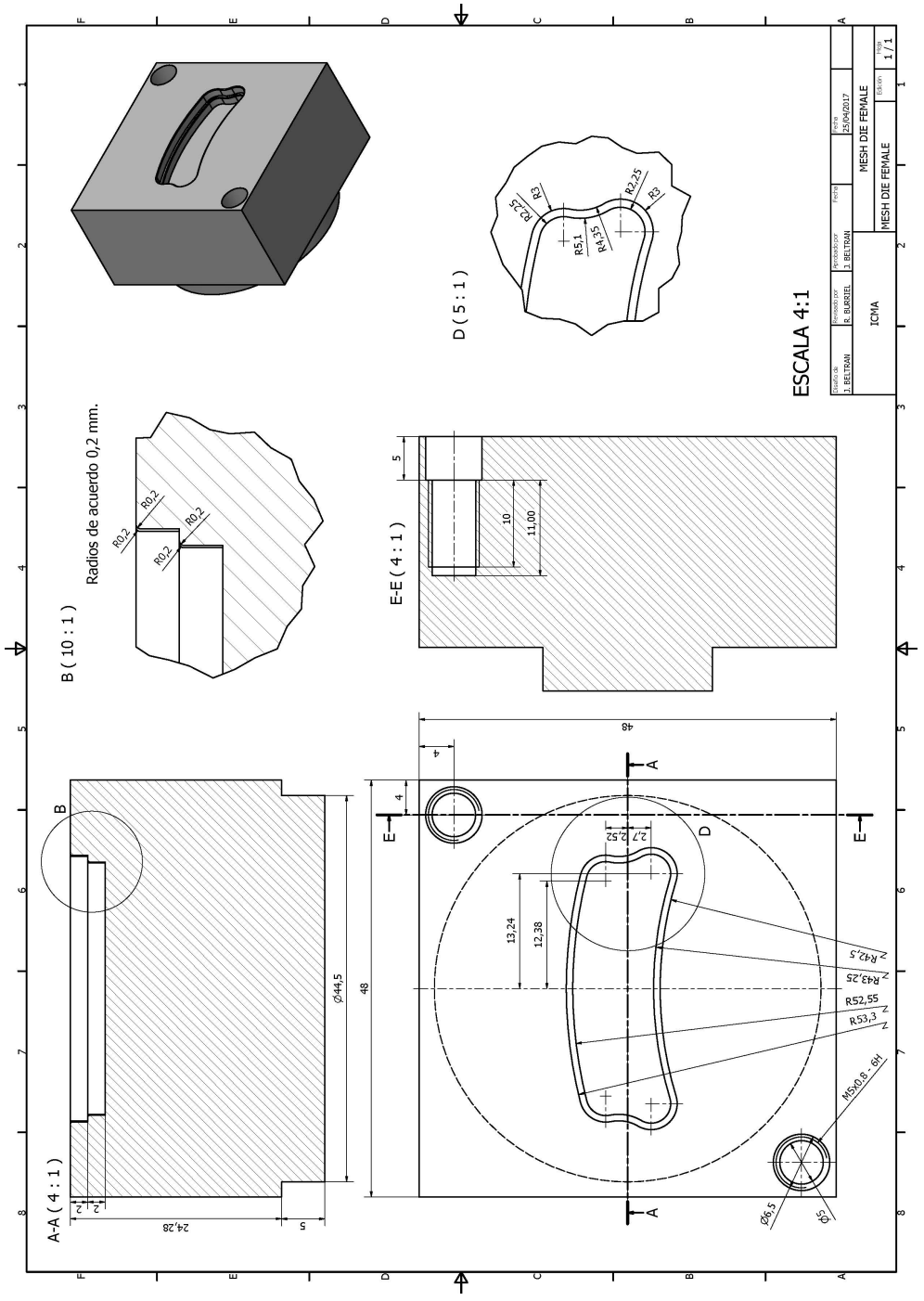
ESCALA 4:1
MESH DIE FEMALE
ICMA
J. BELTRAN
R. BURSTEL
J. BELTRAN
25/04/2017
1 / 1
D (5 : 1)
R2,25
R3
R2,75
R2
R5,1
R4,55
B (10 : 1)
Radios de acuerdo 0,2 mm.
R0,2
E-E (4 : 1)
10
11,00
5
A-A (4 : 1)
B
24,28
2
2
5
Ø44,5
48
4
4
A
A
E
E
D
2,7
2,52
13,24
12,38
R43,25
R43,5
R52,55
R53,3
M5x0,8 - 6H
Ø6,5
Ø3

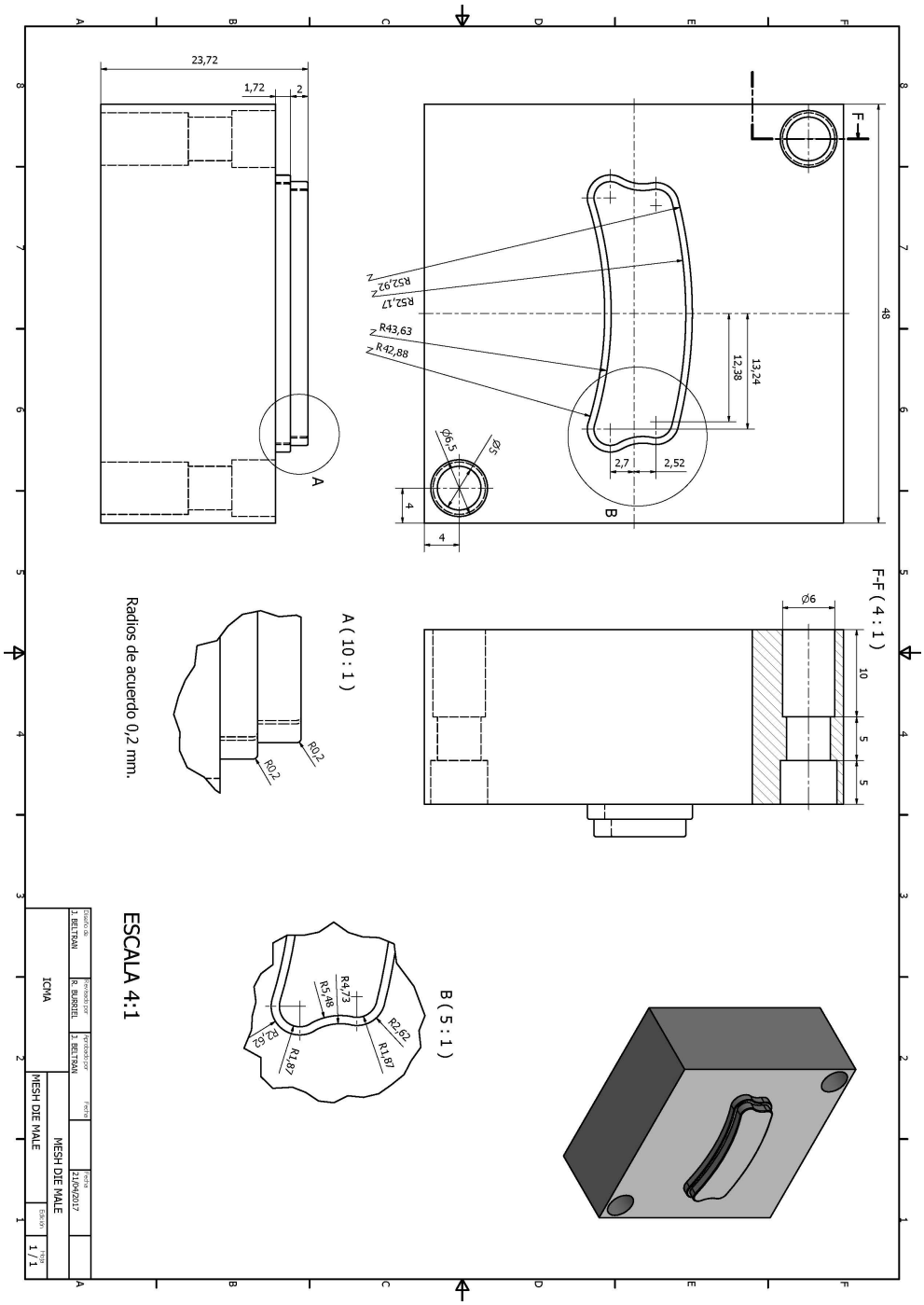
23,72
1,72
2
A
R52,92
R52,17
R43,63
R42,88
13,24
12,38
48
2,7
2,52
4
4
Ø6,5
Ø5
B
F
F-F (4 : 1)
Ø6
10
5
5
A (10 : 1)
R0,2
R0,2
Radios de acuerdo 0,2 mm.
B (5 : 1)
R4,73
R5,48
R2,62
R2,62
R2,62
R1,87
R1,87
ESCALA 4:1
ICMA
MESH DIE MALE
MESH DIE MALE
1 / 1
21/04/2017

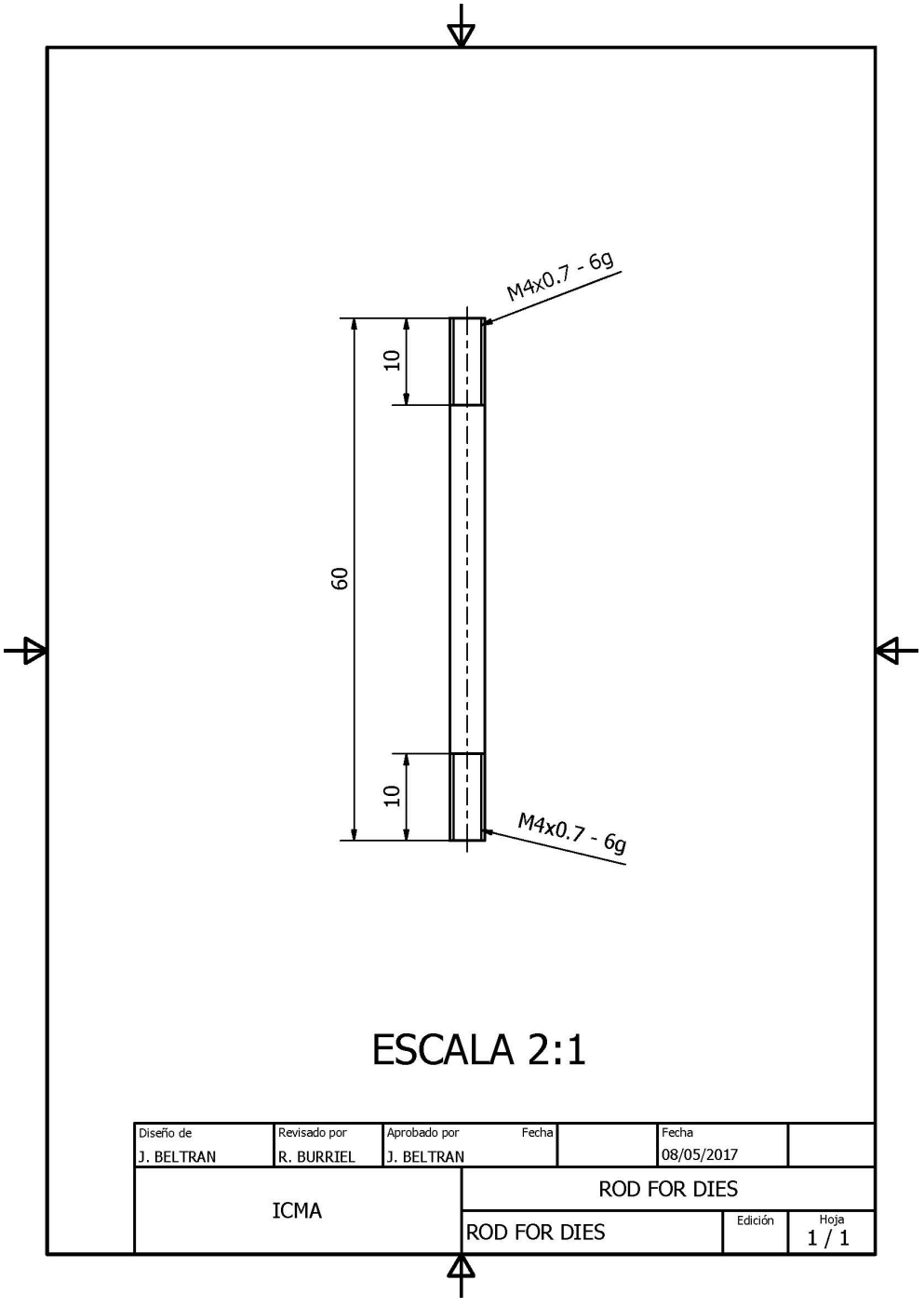
M4x0.7 - 6g
10
60
10
M4x0.7 - 6g
ESCALA 2:1
Diseño de
J. BELTRAN
Revisado por
R. BURRIEL
Aprobado por
J. BELTRAN
Fecha
Fecha
08/05/2017
ICMA
ROD FOR DIES
ROD FOR DIES
Edición
Hoja
1 / 1

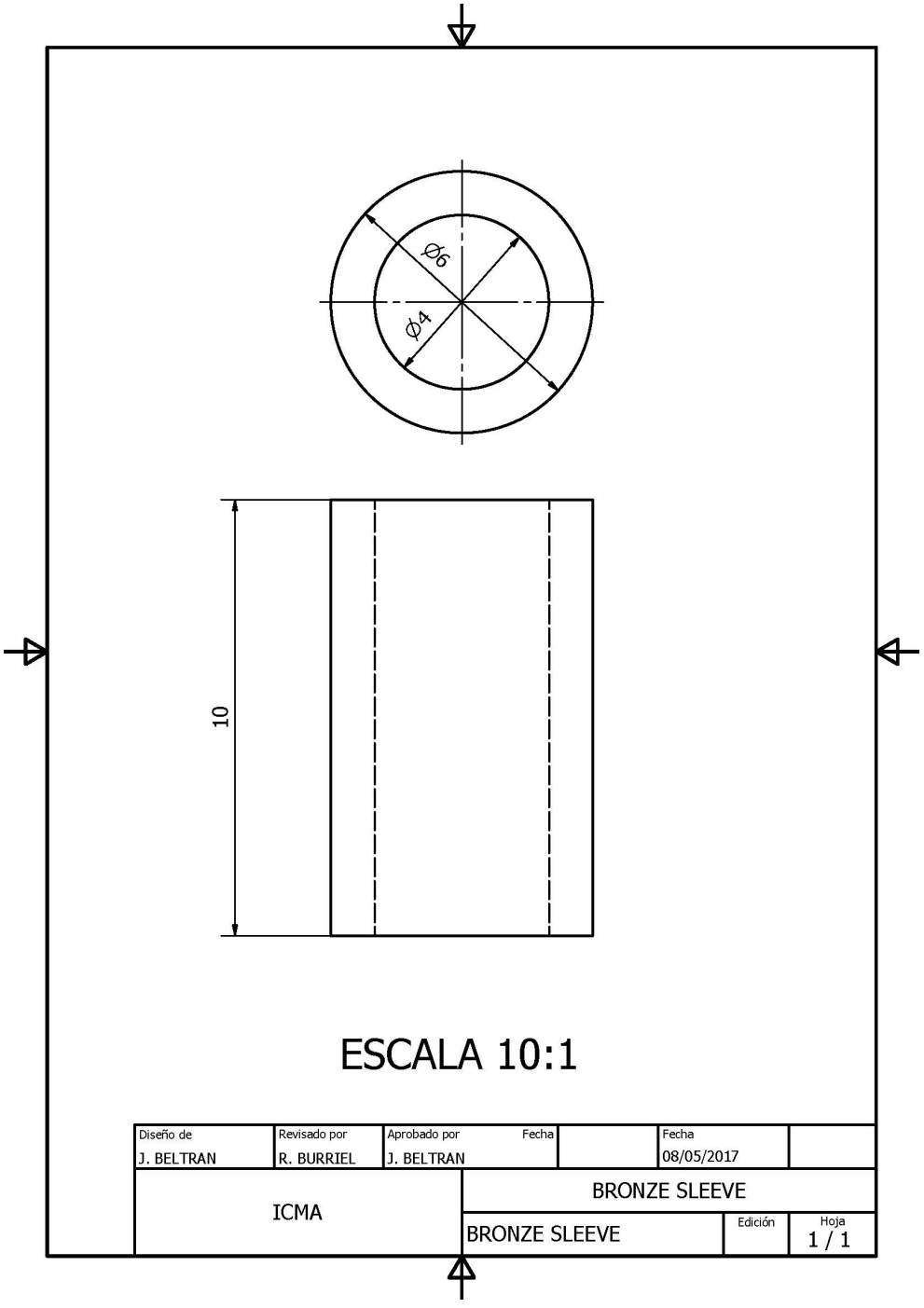
ϕ6
ϕ4
10
ESCALA 10:1
Diseño de
J. BELTRAN
Revisado por
R. BURRIEL
Aprobado por
J. BELTRAN
Fecha
Fecha
08/05/2017
ICMA
BRONZE SLEEVE
BRONZE SLEEVE
Edición
Hoja
1 / 1

General scheme

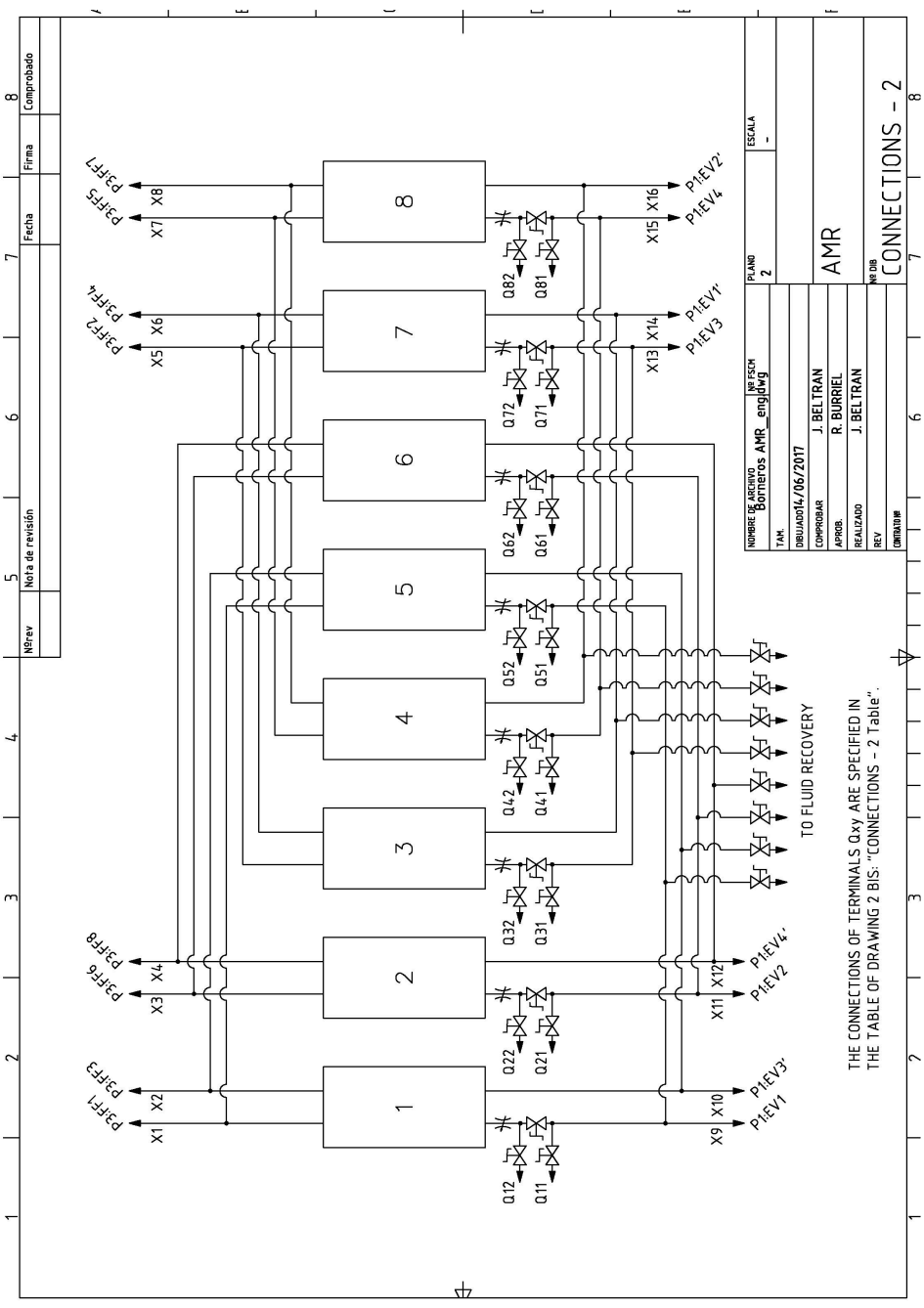

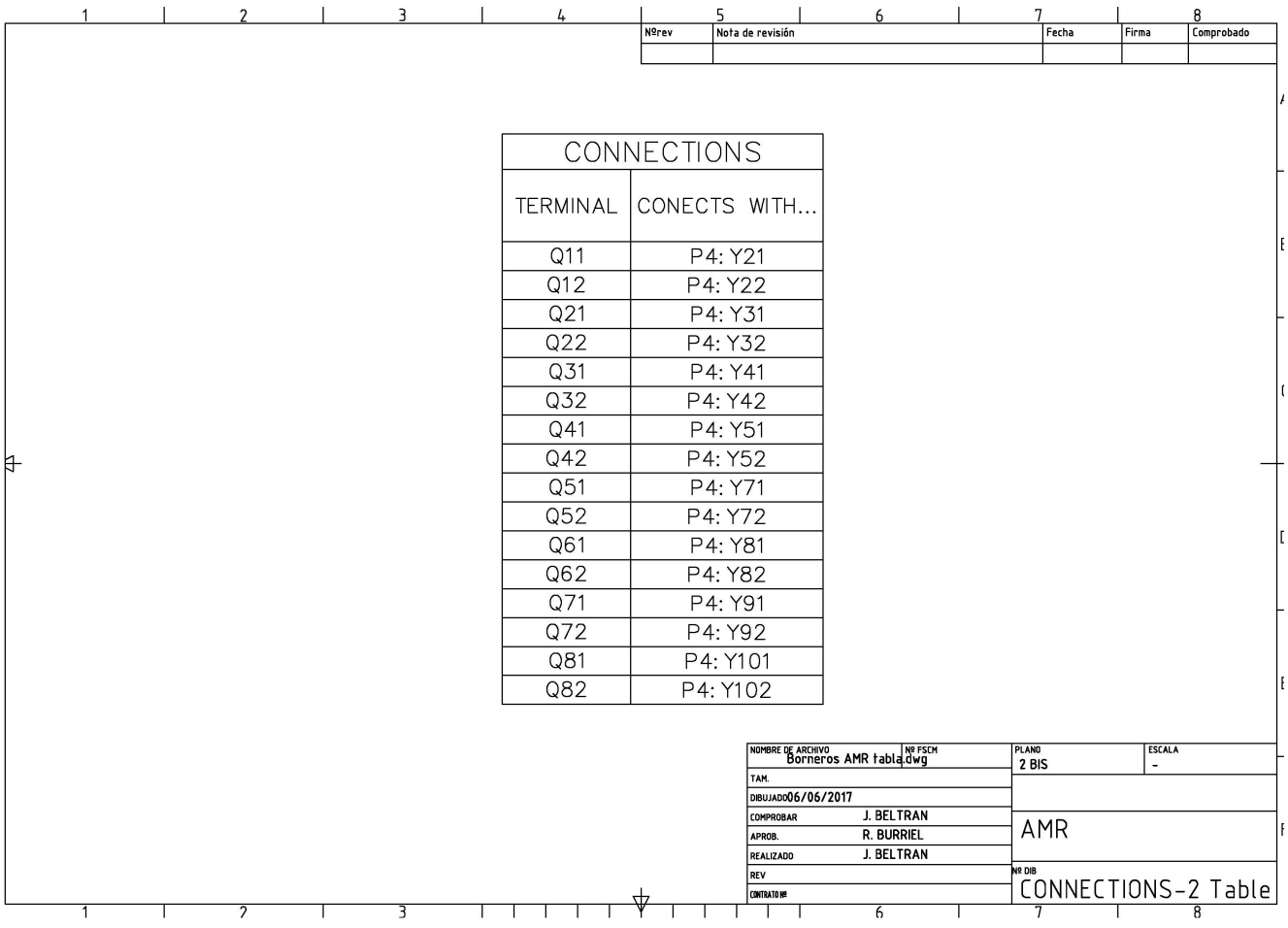

Nºrev	Nota de revisión	Fecha	Firma	Comprobado

CONNECTIONS	
TERMINAL	CONECTS WITH...
Q11	P4: Y21
Q12	P4: Y22
Q21	P4: Y31
Q22	P4: Y32
Q31	P4: Y41
Q32	P4: Y42
Q41	P4: Y51
Q42	P4: Y52
Q51	P4: Y71
Q52	P4: Y72
Q61	P4: Y81
Q62	P4: Y82
Q71	P4: Y91
Q72	P4: Y92
Q81	P4: Y101
Q82	P4: Y102

NOMBRE DE ARCHIVO: Borneros AMR tabla.dwg	Nº FSCM	PLANO: 2 BIS	ESCALA: -
TAM.			
DIBUJADO 06/06/2017			
COMPROBAR	J. BELTRAN	AMR	
APROB.	R. BURRIEL		
REALIZADO	J. BELTRAN	Nº DIB.	
REV		CONNECTIONS-2 Table	
CONTRATO Nº			

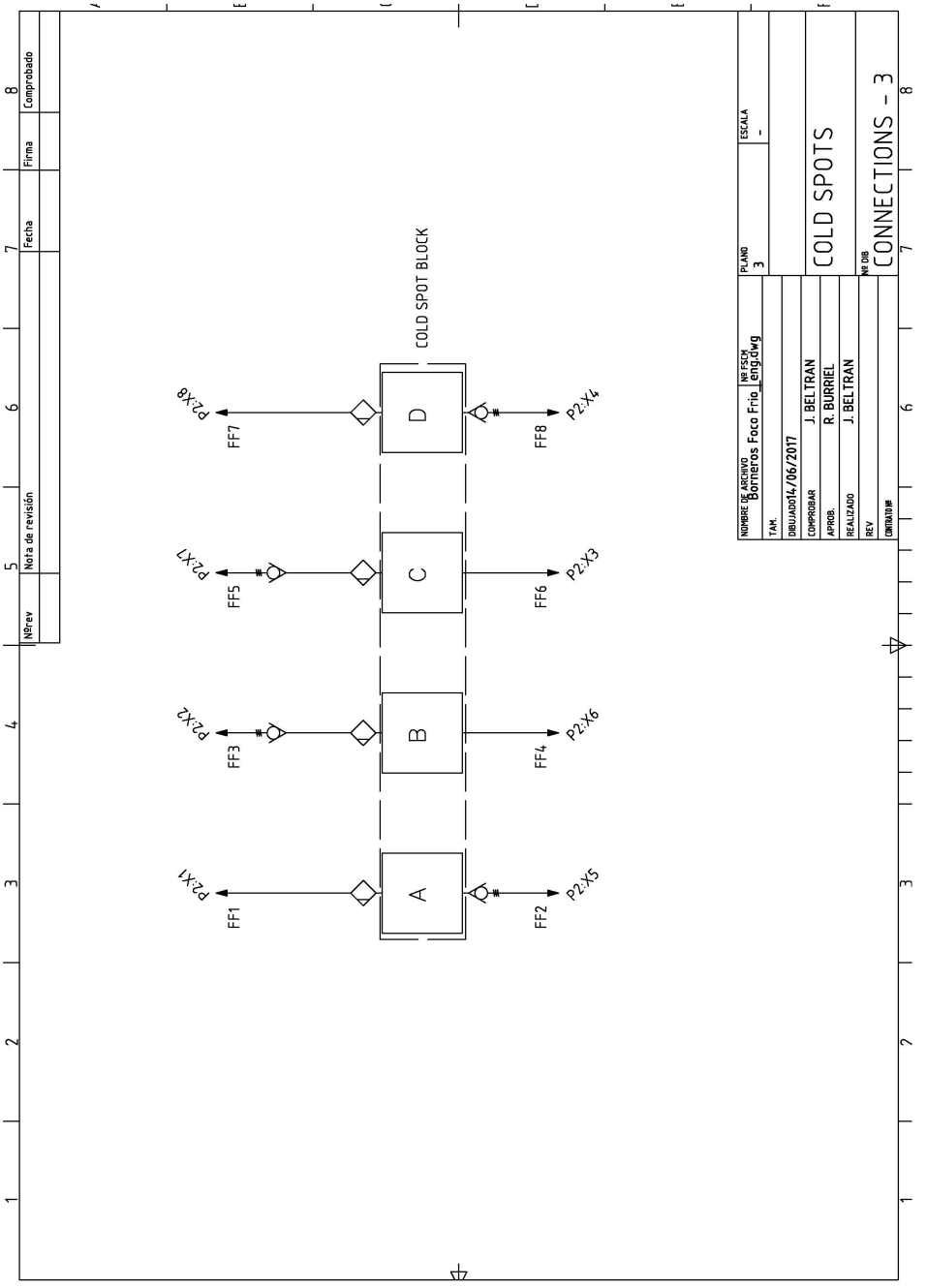
COLD SPOT BLOCK
A
B
C
D
FF1
FF2
FF3
FF4
FF5
FF6
FF7
FF8
P2:X1
P2:X5
P2:X2
P2:X6
P2:X7
P2:X3
P2:X8
P2:X4
CONNECTIONS - 3
COLD SPOTS
J. BELTRAN
R. BURRIEL
J. BELTRAN
14/06/2017
Botticelos Foco Frio_engl.dwg
ESCALA
PLANO
Nota de revisión
Fecha
Firma
Comprobado

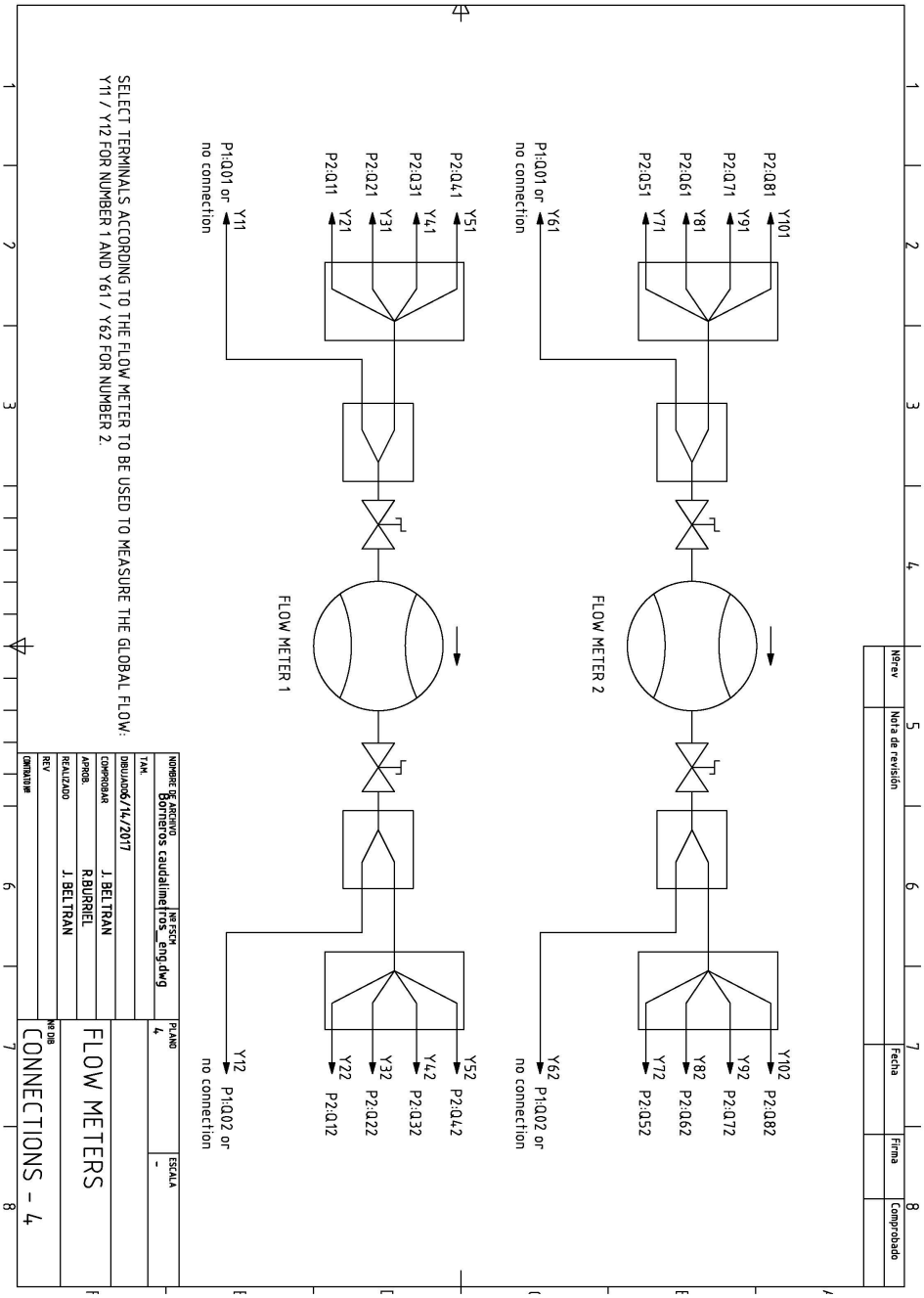
P2:Q81
Y101
P2:Q71
Y91
P2:Q61
Y81
P2:Q51
Y71
P1:Q01 or
no connection
Y61
FLOW METER 2
Y102
P2:Q82
Y92
P2:Q72
Y82
P2:Q62
Y72
P2:Q52
Y62
P1:Q02 or
no connection
P2:Q41
Y51
P2:Q31
Y41
P2:Q21
Y31
P2:Q11
Y21
P1:Q01 or
no connection
Y11
FLOW METER 1
Y52
P2:Q42
Y42
P2:Q32
Y32
P2:Q22
Y22
P2:Q12
Y12
P1:Q02 or
no connection
SELECT TERMINALS ACCORDING TO THE FLOW METER TO BE USED TO MEASURE THE GLOBAL FLOW:
Y11 / Y12 FOR NUMBER 1 AND Y61 / Y62 FOR NUMBER 2.
Nºrev
Nota de revisión
Fecha
Firma
Comprobado
NOMBRE DE ARCHIVO
Borneros caudalimetros_eng.dwg
Nº FSCM
TAM.
DIBUJADO
6/14/2017
J. BELTRAN
COMPROBAR
R.BURRIEL
APROB.
J. BELTRAN
REALIZADO
REV
ORIGINAL
PLANO
4
ESCALA
-
Nº DIB
FLOW METERS
CONNECTIONS - 4

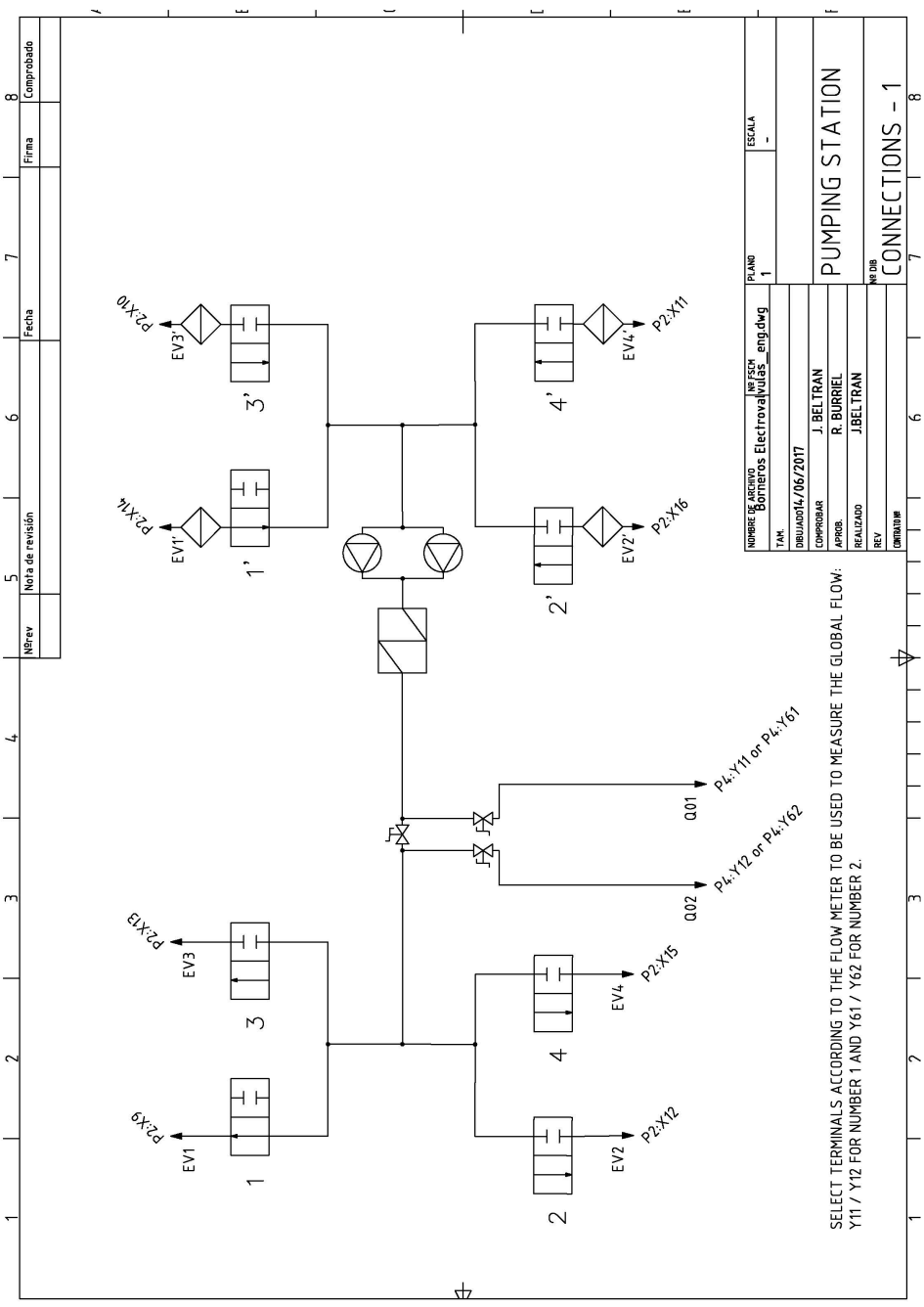
EV1
EV2
EV3
EV4
EV1'
EV2'
EV3'
EV4'
P2:X9
P2:X12
P2:X13
P2:X15
P2:X14
P2:X16
P2:X10
P2:X11
1
2
3
4
1'
2'
3'
4'
Q01
Q02
P4:Y11 or P4:Y61
P4:Y12 or P4:Y62
SELECT TERMINALS ACCORDING TO THE FLOW METER TO BE USED TO MEASURE THE GLOBAL FLOW:
Y11 / Y12 FOR NUMBER 1 AND Y61 / Y62 FOR NUMBER 2.
PUMPING STATION
CONNECTIONS - 1
Botticelos Electroval
J. BELTRAN
R. BURRIEL
J.BELTRAN
14/06/2017

Lifting frame

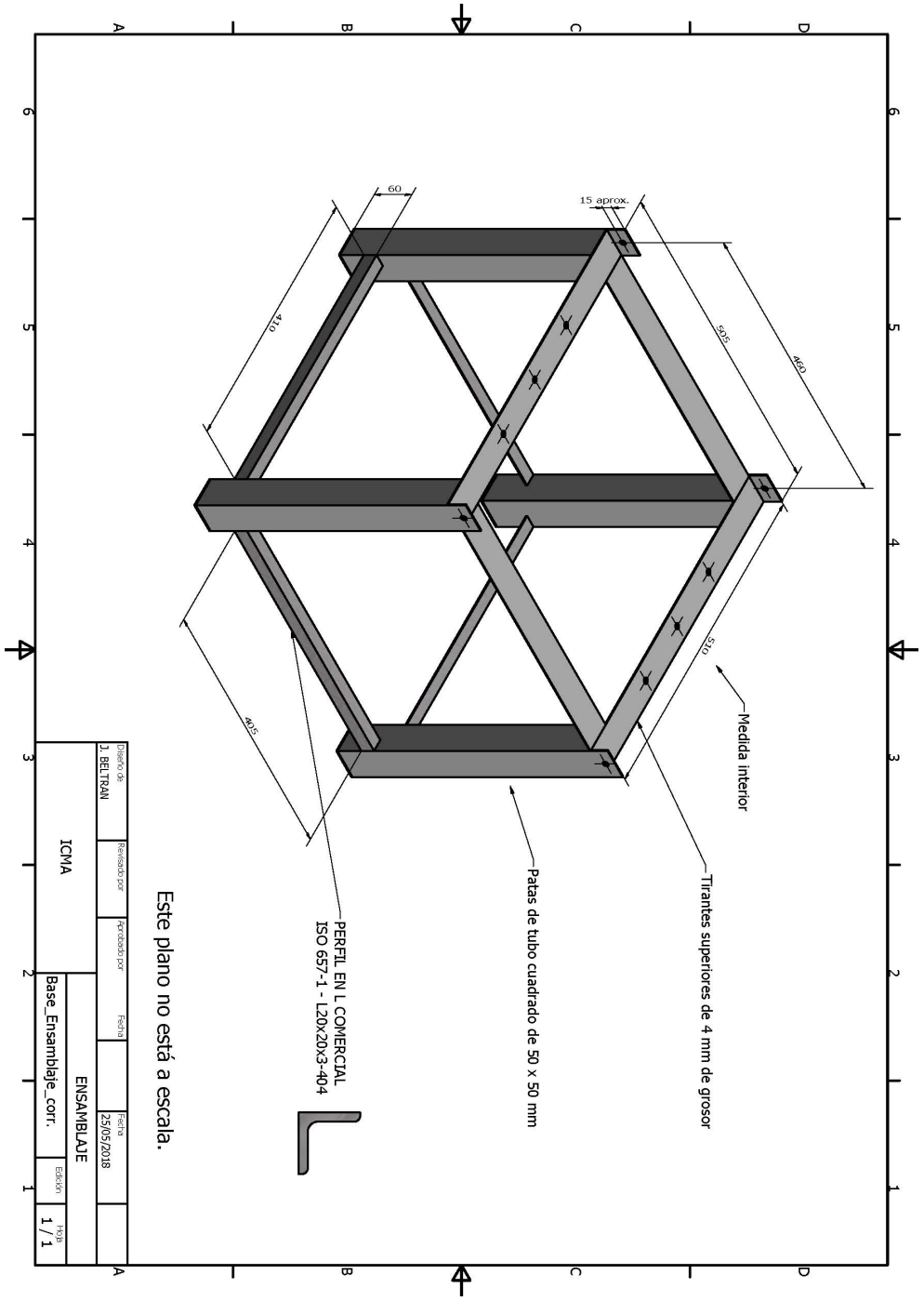

Bibliography

[1] A. Kitanovski, J. Tušek, U. Tomc, U. Plaznik, M. Ožbolt, and A. Poredoš, *Magnetocaloric energy conversion: From theory to applications*, Springer International Publishing (2015).

[2] J. L. Dupont, P. Domanski, P. Lebrun, and F. Ziegler (2019), URL https://iifiir.org/en/documents/39816/download.

[3] H. Ritchie, *Energy production and consumption* (2020), URL https://ourworldindata.org/energy-production-consumption.

[4] J. Henley, The Guardian (2015), ISSN 0261-3077, URL https://www.theguardian.com/environment/2015/oct/26/cold-economy-cop21-global-warming-carbon-emissions.

[5] (2020), URL https://www.iea.org.

[6] (2015), URL https://www.ucsusa.org/resources/what-oil-shale.

[7] (2016), URL https://www.ucsusa.org/resources/what-are-tar-sands.

[8] V. K. Pecharsky and K. A. Gschneidner Jr., J. Magn. Magn. Mater. **200**, 44 (1999).

[9] D. Coulomb, J. L. Dupont, A. Pichard, and IIF-IIR (2015), URL https://iifiir.org/en/documents/37047/download.

[10] D. F. Birol, *The Future of Cooling* (2018), URL https://www.iea.org/reports/the-future-of-cooling.

[11] J. Steven Brown and P. A. Domanski, Applied Thermal Engineering **64**, 252–262 (2014), ISSN 13594311.

[12] A. Kitanovski, U. Plaznik, U. Tomc, and A. Poredoš, Int. J. Refrig. **57**, 288–298 (2015), ISSN 01407007.

[13] S. Qian, D. Nasuta, A. Rhoads, Y. Wang, Y. Geng, Y. Hwang, R. Radermacher, and I. Takeuchi, International Journal of Refrigeration **62**, 177–192 (2016), ISSN 01407007.

[14] N. A. de Oliveira, Journal of Applied Physics **109**, 053515 (2011), ISSN 0021-8979, 1089-7550.

[15] J. A. Shaw, C. B. Churchill, and M. A. Iadicola, Experimental Techniques **32**, 55–62 (2008).

[16] U. Tomc, J. Tušek, A. Kitanovski, and A. Poredoš, Appl. Therm. Eng. **58**, 1 (2013).

[17] A. Kitanovski and P. W. Egolf, International Journal of Refrigeration **33**, 449–464 (2010), ISSN 01407007.

[18] D. J. Silva, B. D. Bordalo, A. M. Pereira, J. Ventura, and J. P. Araújo, Appl. Energy **93**, 570–574 (2012), ISSN 03062619.

[19] D. Silva, J. Ventura, J. Araújo, and A. Pereira, Applied Energy **113**, 1149–1154 (2014), ISSN 03062619.

[20] U. Olsen, C. Bahl, K. Engelbrecht, K. Nielsen, Y. Tasaki, and H. Takahashi, International Journal of Refrigeration **37**, 194–200 (2014), ISSN 01407007.

[21] U. Tomc, J. Tušek, A. Kitanovski, and A. Poredoš, Int. J. Refrigeration **37**, 185 (2014).

[22] W. de Vries and T. H. van der Meer, Applied Thermal Engineering **111**, 377–386 (2017), ISSN 13594311.

[23] A. Tishin and Y. Spichkin, *The magnetocaloric effect and its applications*, Institute of Physics Publishing, Bristol and Philadelphia (2003).

[24] K. Gschneidner Jr. and V. Pecharsky, Int. J. Refrigeration **31**, 945 (2008).

[25] J. F. Papp, E. L. Bray, D. L. Edelstein, M. D. Fenton, D. E. Guberman, J. B. Hedrick, J. D. Jorgenson, P. H. Kuck, K. B. Shedd, and A. C. Tolcin, *Factors that influence the price of Al, Cd, Co, Cu, Fe, Ni, Pb, Rare Earth Elements, and Zn*, no. 1356 in Open-File Report (2008).

[26] G. Pitron, *La guerra de los mentales raros: la cara oculta de la transición energética y digital* (Península, 2019), ISBN 978-84-9942-843-7.

[27] K. Habib, L. Hamelin, and H. Wenzel, Journal of Cleaner Production **133**, 850–858 (2016), ISSN 09596526.

[28] A. L. Gulley, E. A. McCullough, and K. B. Shedd, Resources Policy **62**, 317–323 (2019), ISSN 03014207.

[29] K. Habib, Journal of Cleaner Production **230**, 90–97 (2019), ISSN 09596526.

[30] B. Liu, N. Zhu, Y. Li, P. Wu, Z. Dang, and Y. Ke, Process Safety and Environmental Protection **124**, 317–325 (2019), ISSN 09575820.

[31] F. Liu, A. Porvali, J. Wang, H. Wang, C. Peng, B. P. Wilson, and M. Lundström, Minerals Engineering **145**, 106097 (2020), ISSN 08926875.

[32] K. Gandha, G. Ouyang, S. Gupta, V. Kunc, M. Parans Paranthaman, and I. C. Nlebedim, Waste Management **90**, 94–99 (2019), ISSN 0956053X.

[33] W. Judge and G. Azimi, Hydrometallurgy **196**, 105435 (2020), ISSN 0304386X.

[34] A. Kumari, M. K. Jha, and D. D. Pathak, Journal of Environmental Management **273**, 111063 (2020), ISSN 03014797.

[35] M. Zakotnik and C. Tudor, Waste Management **44**, 48–54 (2015), ISSN 0956053X.

[36] B. Monfared, R. Furberg, and B. Palm, International Journal of Refrigeration **42**, 69–76 (2014), ISSN 01407007.

[37] R. Bjørk, C. Bahl, and K. Nielsen, International Journal of Refrigeration **63**, 48–62 (2016), ISSN 01407007.

[38] D. Beers, M. Benedict, and M. Schroeder, in *Delft Days on Magnetocalorics* (2015), p. 14.

[39] C. Zimm, A. Boeder, B. Mueller, K. Rule, and S. L. Russek, MRS Bulletin **43**, 274–279 (2018), ISSN 0883-7694, 1938-1425.

[40] A. Kitanovski, U. Tomc, and A. Poderos, *Future developments in magnetocaloric refrigeration and heat pumping.* (2016).

[41] *Thermag 2018 - Proceedings.pdf* (International Institute of Refrigeration, 2018), ISBN 978-2-36215-028-9.

[42] K. Klinar, U. Tomc, B. Jelenc, S. Nosan, and A. Kitanovski, Applied Energy **236**, 1062–1077 (2019), ISSN 03062619.

[43] A. Smith, Eur. Phys. J. H **38**, 507 (2013).

[44] B. Yu, M. Liu, P. Egolf, and A. Kitanovski, Int. J. Refrigeration **33**, 1029 (2010).

[45] W. Thomson, *Cyclopedia of the physical sciences*, 2nd edn., J. P. Nichol (ed.). Richard Green and Company, London and Glasgow p. 838 (1860).

[46] P. Weiss and A. Piccard, J. Phys. (Paris) **7**, 103 (1917).

[47] E. Warburg, Ann. Phys. (Leipzig) **249**, 141 (1881).

[48] A. M. Tishin, K. A. Gschneidner Jr., and V. K. Pecharsky, Phys. Rev. B **59**, 503 (1999).

[49] S. C. Collins and F. J. Zimmerman, Phys. Rev. **90**, 991 (1953).

[50] C. V. Heer, C. B. Barnes, and J. G. Daunt, Rev. Sci. Instr. **25**, 1088 (1954).

[51] E. L. Resler and R. E. Rosensweig, AIAA J. **2 (8)**, 1418 (1964).

[52] E. L. Resler and R. E. Rosensweig, J. Eng. Power **89 (3)**, 399 (1967).

[53] G. V. Brown, J. Appl. Phys. **47**, 3673 (1976).

[54] W. A. Steyert, US patent, No. 4107935 (1978).

[55] W. A. Steyert, Journal of Applied Physics **49**, 1216–1226 (1978), ISSN 0021-8979, 1089-7550.

[56] L. D. Kirol, US patent, No. 4727722 (1988).

[57] G. Green, J. Chafe, J. Stevens, and J. Humphrey, Adv. Cryo. Eng. **35**, 1165 (1990).

[58] C. Zimm, A. Jastrab, A. Sternberg, V. Pecharsky, K. A. Gschneidner Jr., M. Osborne, and I. Anderson, Adv. Cryog. Eng. **43**, 1759 (1998).

[59] V. K. Pecharsky and K. A. Gschneidner Jr., Phys. Rev. Lett. **78 (23)**, 4494 (1997).

[60] L. Tocado, E. Palacios, and R. Burriel, J. Appl. Phys. **105**, 093918 (2009).

[61] J. Lyubina, J. Phys. D: Appl. Phys. **50**, 0532002 (2017).

[62] A. Smith, C. R. H. Bahl, R. Bjørk, K. Engelbrecht, K. K. Nielsen, and N. Pryds, Adv. Energy Mater. **2**, 1288 (2012).

[63] K. Engelbrecht and C. R. H. Bahl, Journal of Applied Physics **108**, 123918 (2010), ISSN 0021-8979, 1089-7550.

[64] V. Basso, C. P. Sasso, G. Bertotti, and M. LoBue, Int. J. Refrigeration **29**, 1358 (2006).

[65] K. K. Nielsen and K. Engelbrecht, Journal of Physics D: Applied Physics **45**, 145001 (2012), ISSN 0022-3727, 1361-6463.

[66] V. Franco, J. S. Blázquez, J. J. Ipus, J. Y. Law, L. M. Moreno-Ramírez, and A. Conde, Prog. Mater. Sci. **93**, 112–232 (2018), ISSN 00796425.

[67] J. F. Elliott, S. Legvold, and F. H. Spedding, Physical Review **91**, 28–30 (1953), ISSN 0031-899X.

[68] H. E. Nigh, S. Legvold, and F. H. Spedding, Physical Review **132**, 1092–1097 (1963), ISSN 0031-899X.

[69] C. D. Graham, Journal of Applied Physics **36**, 1135–1136 (1965), ISSN 0021-8979, 1089-7550.

[70] J. W. Cable and E. O. Wollan, Physical Review **165**, 733–734 (1968), ISSN 0031-899X.

[71] S. Y. Dan'kov, A. M. Tishin, V. K. Pecharsky, and K. A. Gschneidner, Physical Review B **57**, 3478–3490 (1998), ISSN 0163-1829, 1095-3795.

[72] J. Lyubina, M. D. Kuz'min, K. Nenkov, O. Gutfleisch, M. Richter, D. L. Schlagel, T. A. Lograsso, and K. A. Gschneidner, Physical Review B **83**, 012403 (2011), ISSN 1098-0121, 1550-235X.

[73] S. V. Taskaev, V. D. Buchelnikov, A. P. Pellenen, M. D. Kuz'min, K. P. Skokov, D. Y. Karpenkov, D. S. Bataev, and O. Gutfleisch, Journal of Applied Physics **113**, 17A933 (2013), ISSN 0021-8979, 1089-7550.

[74] K. A. Gschneidner Jr., V. K. Pecharsky, and A. O. Tsokol, Reports on Progress in Physics **68**, 1479–1539 (2005), ISSN 0034-4885, 1361-6633.

[75] V. Pecharsky and K. A. Gschneidner Jr., Adv. Mater. **13 (9)**, 683 (2001).

[76] E. Palacios, G. F. Wang, R. Burriel, V. Provenzano, and R. D. Shull, J. Phys.: Conf. Ser. **200**, 092011 (2010).

[77] F. Hu, B. Shen, J. Sun, Z. Cheng, G. Rao, and X. Zhang, Appl. Phys. Lett. **78**, 3675 (2001).

[78] A. Fujita, S. Fujieda, Y. Hasegawa, and K. Fukamichi, Phys. Rev. B **67 (10)**, 104416 (2003).

[79] M. Katter, V. Zellmann, G. Reppel, and K. Uestuener, IEEE Transactions on Magnetics **44**, 3044–3047 (2008), ISSN 0018-9464.

[80] B. R. Hansen, M. Katter, L. T. Kuhn, C. R. H. Bahl, A. Smith, and C. E. Ancona-Torres, in *Proceedings of 3rd International Conference of the IIR on Magnetic Refrigeration at Room Temperature - Des Moines, Iowa, United States* (2009), p. 67–73, URL http://www.ucs.iastate.edu/mnet/thermag/home.html.

[81] R. Bjørk, C. R. H. Bahl, and M. Katter, Journal of Magnetism and Magnetic Materials **322**, 3882–3888 (2010), ISSN 03048853, arXiv: 1410.1988.

[82] A. Barcza, M. Katter, V. Zellmann, S. Russek, S. Jacobs, and C. Zimm, IEEE Trans. Magn. **47 (10)**, 3391 (2011).

[83] E. Brück, O. Tegus, D. T. C. Thanh, N. T. Trung, and K. H. J. Buschow, Int. J. Refrigeration **31**, 763 (2008).

[84] N. H. Dung, Z. Q. Ou, L. Caron, L. Zhang, D. T. C. Thanh, G. A. de Wijs, R. A. de Groot, K. H. J. Buschow, and E. Brück, Adv. Energy Mater. **1**, 1215 (2011).

[85] E. Brück, N. T. Trung, Z. Q. Ou, and K. H. J. Buschow, Scr. Mater. **67**, 590 (2012).

[86] F. Guillou, G. Porcari, H. Yibole, N. van Dijk, and E. Brück, Adv. Mater. **26**, 2671 (2014).

[87] M.-H. Phan and S.-C. Yu, Journal of Magnetism and Magnetic Materials **308**, 325–340 (2007).

[88] C. R. H. Bahl, D. Velázquez, K. K. Nielsen, K. Engelbrecht, K. B. Andersen, R. Bulatova, and N. Pryds, Appl. Phys. Lett. **100**, 121905 (2012).

[89] N. A. de Oliveira and P. J. von Ranke, Physical Review B **77**, 214439 (2008), ISSN 1098-0121, 1550-235X.

[90] A. Kitanovski and P. W. Egolf, International Journal of Refrigeration **29**, 3–21 (2006), ISSN 01407007.

[91] M. E. Wood and W. H. Potter, Cryogenics **25 (12)**, 667 (1985).

[92] V. Pecharsky and K. A. Gschneidner Jr., J. Appl. Phys. **90**, 4614 (2001).

[93] K. A. Gschneidner Jr. and V. K. Pecharsky, Annual Review of Materials Science **30**, 387–429 (2000).

[94] T. Lei, K. Engelbrecht, K. K. Nielsen, H. N. Bez, and C. R. H. Bahl, J. Phys. D: Appl. Phys. **49**, 345001 (2016).

[95] C. R. Cross, J. A. Barclay, A. J. DeGregoria, S. R. Jaeger, and J. W. Johnson, Adv. Cryo. Eng. **33**, 767 (1987).

[96] A. Kitanovski, U. Plaznik, J. Tušek, and A. Poredoš, Int. J. Refrigeration **37**, 28 (2014).

[97] F. C. Chen, R. W. Murphy, V. C. Mei, and G. L. Chen, J. Eng. Gas Turbines Power **114**, 715 (1992).

[98] J. A. Barclay, *Wheel-type magnetic refrigerator* (1983), URL https://patents.google.com/patent/US4408463A/en.

[99] J. A. Barclay, *The theory of an active magnetic regenerator*, LA-UR-82-1792 (1983).

[100] J. L. Hall, C. E. Reid, I. G. Spearing, and J. A. Barclay, Adv. Cryog. Eng. **41**, 1653 (1996).

[101] M. Benedict, S. Sherif, D. Beers, and M. Schroeder, Int. J. Refrigeration **70**, 138 (2016).

[102] S. Jacobs, J. Auringer, A. Boeder, J. Chell, L. Komorowski, J. Leonard, S. Russek, and C. Zimm, Int. J. Refrigeration **37**, 84 (2014).

[103] T. Lei, K. K. Nielsen, K. Engelbrecht, C. R. H. Bahl, H. Neves Bez, and C. T. Veje, Journal of Applied Physics **118**, 014903 (2015), ISSN 0021-8979, 1089-7550.

[104] A. Rowe, Int. J. Refrigeration **34**, 168 (2011).

[105] D. Arnold, A. Tura, A. Ruebsaat-Trott, and A. Rowe, Int. J. Refrigeration **37**, 99 (2014).

[106] A. Rowe, in *Proceedings of the Third IIF-IIR Conference on Magnetic Refrigeration at Room Temperature, Des Moines, U.S.A.* (2009), p. 11.

[107] D. Eriksen, K. Engelbrecht, C. R. H. Bahl, R. Bjørk, K. K. Nielsen, A. R. Insinga, and N. Pryds, Int. J. Refrigeration **58**, 14 (2015).

[108] D. Velázquez, *Magnetic Refrigeration at Room Temperature: Design, construction and evaluation of a reciprocating demonstrator and a rotary prototype. Numerical modelling and analysis of an active magnetic regenerator system*, Ph.D. thesis, Prensas Universitarias de Zaragoza (2018).

[109] S. Jacobs, in: Proceedings of the Third IIF-IIR International Conference on Magnetic Refrigeration at Room Temperature, Des Moines, IO, U.S.A. pp. 267–273 (2009).

[110] B. Monfared and B. Palm (International Institute of Refrigeration (IIR), 2016), p. 146–149, dOI: 10.18462/IIR.THERMAG.2016.0142.

[111] T. Lei, K. Navickaitė, K. Engelbrecht, A. Barcza, H. Vieyra, K. K. Nielsen, and C. R. Bahl, Applied Thermal Engineering **128**, 10–19 (2018), ISSN 13594311.

[112] P. Trevizoli, M. Capovilla, G. Peixer, and E. Al. (International Institute of Refrigeration (IIR), 2016), p. 83–86, dOI: 10.18462/IIR.THERMAG.2016.0102.

[113] J. Liu, J. Moore, K. Skokov, M. Krautz, K. Löwe, A. Barcza, M. Katter, and O. Gutfleisch, Scripta Materialia **67**, 584–589 (2012), ISSN 13596462.

[114] W. R. Merida and J. A. Barclay, Advances in Cryogenic Engineering. Advances in Cryogenic Engineering **43**, 1597–1604 (1998), online ISBN: 978-1-4757-9047-4.

[115] T. Wysokinski, X. Xu, and J. Barclay, Cryogenics **42**, 691–696 (2002), ISSN 00112275.

[116] H. Johra, K. Filonenko, P. Heiselberg, C. Veje, T. Lei, S. Dall'Olio, K. Engelbrecht, and C. Bahl, Building Simulation **11**, 753–763 (2018), ISSN 1996-3599, 1996-8744.

[117] B. Huang, J. Lai, D. Zeng, Z. Zheng, B. Harrison, A. Oort, N. van Dijk, and E. Brück, International Journal of Refrigeration **104**, 42–50 (2019), ISSN 01407007.

[118] A. Kitanovski, Advanced Energy Materials **10**, 1903741 (2020), ISSN 1614-6832, 1614-6840.

[119] M. Richard, A. Rowe, and R. Chahine, J. Appl. Phys. **4**, 2146 (2004).

[120] M. Rhodes (John Wiley & Sons, Ltd, Chichester, UK, 2008), chap. 1, p. 450, 2nd ed., ISBN 9780470727102, URL http://doi.wiley.com/10.1002/9780470727102.

[121] I. F. Macdonald, S. El-Sayed, K. Mow, and F. A. L. Dullien, Ind. Eng. Chem. Fundam. **18 (3)**, 199 (1979).

[122] J. F. Beltran-Lopez, M. Sazatornil, E. Palacios, and R. Burriel, Journal of Thermal Analysis and Calorimetry **125**, 579–583 (2016), ISSN 1388-6150, 1588-2926.

[123] J. F. Beltran-Lopez, M. Sazatornil, E. Palacios, and R. Burriel, Journal of Thermal Analysis and Calorimetry **125**, 821–821 (2016), ISSN 1388-6150, 1588-2926.

[124] B. Monfared and B. Palm, Int. J. Refrig. **57**, 103 (2015), ISSN 01407007.

[125] C. Aprea, A. Greco, and A. Maiorino, International Journal of Energy Research **37**, 1475–1487 (2013), ISSN 0363907X.

[126] A. Amiri and K. Vafai, International Journal of Heat and Mass Transfer **41**, 4259–4279 (1998).

[127] C. Zimm, A. Boedera, J. Chella, A. Sternberga, A. Fujita, S. Fujieda, and K. Fukamichic, Int. J. Refrigeration **29**, 1302 (2006).

[128] T. Okamura, K. Yamada, N. Hirano, and S. Nagaya, Int. J. Refrigeration **29**, 1327 (2006).

[129] A. Tura and A. Rowe, in: Proceedings of the Second IIF-IIR International Conference on Magnetic Refrigeration at Room Temperature, Portoroz, Slovenia pp. 363–370 (2007).

[130] D. S. Arnold, A. Tura, and A. Rowe, Int. J. Refrigeration **34**, 178 (2011).

[131] I. Park, Y. Kim, and S. Jeong, Int. J. Refrigeration **36**, 1741 (2013).

[132] D. Eriksen, K. Engelbrecht, C. R. H. Bahl, R. Bjørk, and K. K. Nielsen, Int. J. Refrigeration **103**, 1 (2016).

[133] J. F. Beltrán-López, E. Palacios, D. Velázquez, and R. Burriel, Journal of Applied Physics **126**, 164502 (2019), ISSN 0021-8979, 1089-7550.

[134] R. Bjørk, C. R. H. Bahl, A. Smith, and N. Pryds, Int. J. Refrigeration **33**, 437 (2010).

[135] X. Bohigas, E. Molins, A. Roig, J. Tejada, and X. X. Zhang, IEEE Trans. Magn. **36 (3)**, 538 (2000).

[136] R. Bjørk, C. R. H. Bahl, A. Smith, D. V. Christensen, and N. Pryds, J. Magn. Magn. Mater **322**, 3324 (2010).

[137] W. H. Press, S. A. Teukolsky, W. T. Vetterling, and B. P. Flannery, *Numerical recipes in Fortran 77 and 90* (Cambridge University Press, 1997), 2nd ed., ISBN 0-521-43064-X.

[138] C. Geuzaine and J.-F. Remacle, International Journal for Numerical Methods in Engineering **0**, 1–24 (2009), ISSN 00295981.

[139] P. Dular, C. Geuzaine, A. Genon, and W. Legros, IEEE Transactions on Magnetics **35**, 1682–1685 (1999), ISSN 00189464.

[140] J. E. Dennis and J. J. Moree, SIAM Review **19**, 46–89 (1977).

[141] D. Velázquez, M. Castro, E. Palacios, and R. Burriel, in: Proceedings of the sixth IIF-IIR International Conference on Magnetic Refrigeration at Room Temperature, Victoria, BC, Canada pp. 133–134 (2014).

[142] D. Kraemer, K. McEnaney, Z. Ren, and G. Chen, *Solar Thermoelectric Power Conversion* (Taylor & Francis Group, LLC, 2012), p. 16.

[143] D. Ben-Ayoun and Y. Gelbstein, *Bismuth Telluride Solubility Limit and Dopant Effects on the Electronic Properties of Lead Telluride* (IntechOpen, 2019), ISBN 978-1-78984-528-0.

[144] D. Zhao and G. Tan, Applied Thermal Engineering **66**, 15–24 (2014), ISSN 13594311.

[145] G. Wehmeyer, T. Yabuki, C. Monachon, J. Wu, and C. Dames, Applied Physics Reviews **4**, 041304 (2017), ISSN 1931-9401.

[146] P. Egolf, L. Gravier, T. Francfort, A.-G. Pawlowski, G. Courret, and M. Croci, International Journal of Refrigeration **37**, 176–184 (2014), ISSN 01407007.

[147] J. F. Beltrán-López, E. Palacios, D. Velázquez, and R. Burriel, *Simulation of a hybrid magnetocaloric-thermoelectric refrigerator.* (2018).

[148] B. Monfared, Int. J. Refrig. **74**, 324–332 (2017), ISSN 01407007.

[149] H. B. Callen, *Thermodynamics and an Introduction to Thermostatistics* (John Wiley & Sons Inc., 1985), 2nd ed.

[150] J. Crank and P. Nicolson, Mathematical Proceedings of the Cambridge Philosophical Society **43**, 50–67 (1947), ISSN 0305-0041, 1469-8064.

[151] J. F. Beltran-Lopez, M. Sazatornil, E. Palacios, and R. Burriel, Journal of Thermal Analysis and Calorimetry **125**, 579–583 (2016), ISSN 1388-6150, 1588-2926.

Agradecimientos

Hay mucho por lo que estoy agradecido a muchas personas que durante estos años he tenido la suerte de conocer y tratar. Muchos ni siquiera serán conscientes de ello, pero hay momentos que hasta una simple mirada o el esbozo de una sonrisa en el momento adecuado, suponen mucho. Mi travesía por la Facultad de Ciencias ha sido muy enriquecedora, tanto en lo académico como en lo personal. En mi caso también, bastante duro en lo personal, pero siempre he encontrado apoyos tanto dentro de la institución, como fuera de ella, que me han ayudado a seguir adelante. Con el paso del tiempo, a muchas personas llegas a considerarlas algo más que simples compañeros.

Empezaré por mi director de tesis, Elías Palacios, al que estoy muy agradecido por ayudarme hasta el final, incluso en las situaciones más duras. Ha sido todo un lujo haber podido compartir contigo todo este tiempo, y esos papeles bolígrafo en mano. A una persona con tantos conocimientos no siempre es fácil seguirle el hilo, aunque siempre va quedando algo. Tu sentido crítico nunca deja de asombrarme y te aseguro que de eso, algo se me ha pegado. Gracias por tu paciencia y dedicación contra viento y marea.

No me olvido de Ramón Burriel, que fue codirector de esta tesis hasta su merecida jubilación. Mil gracias por tu ayuda y apoyo en esta singladura. Paciencia y minuciosidad han tenido que ser tus lemas. Gracias por tus sosegadas explicaciones y por ser un revisor tan duro de contentar. Y gracias también por echar una mano cuando ha sido necesario aún después de tu jubilación.

A ambos, Elías y Ramón, les agradezco enormemente haberme dado la posibilidad, primero de trabajar con ellos, y después de hacer esta tesis y por

todo su apoyo tanto en lo laboral, lo académico y, aún más si cabe, en lo personal. Habéis sido un gran complemento el uno del otro y ambos habéis demostrado una gran talla humana. Ha sido todo un privilegio haber podido trabajar con este tándem y formar parte de vuestro grupo del café.

Ha habido otras personas que han hecho más llevadero el viaje. Recuerdo con especial afecto a David Velázquez, que también realizó su tesis con Elías y Ramón. A David le debo mucho por los momentos de terapia café en mano, sentados en cualquier lugar cercano a la puerta de la facultad. Te he echado mucho de menos en esta etapa final. Espero haber sido algo práctico, como me aconsejabas. Gracias por tus aportaciones, consejos y compañerismo. Eres un tío grande, en el sentido más amplio. Gracias también a Miguel Sazatornil, el hombre de los datos, del que recuerdo su amabilidad, sencillez y abstinencia de café. También agradezco a Miguel Castro su colaboración, apoyo y ánimo permanentes.

No me puedo olvidar de otras personas con las que compartí momentos de pausa con café o comida de por medio. Marco Evangelisti y Fernando Luis, ambos miembros del CSIC y grandes personas. Un café sin vosotros no es un café. Gracias por todo vuestro apoyo y ayuda desinteresada. Corrado Tomasi, del que guardo un gran recuerdo de sus estancias. Gracias por todas las charlas de desahogo y por tus visitas cuando pasabas por Zaragoza mientras fue posible. A Alodia Orera, María Ángeles Laguna, Giulia Lorusso, Raquel Alicante, Ana Elisa Berges, Alessandro Fiasconaro y María José Martínez (Pepa), gracias por vuestra grata compañía. Pepa, siempre me acordaré de tus imitaciones con acento argentino. También gracias a Jorge Lobo, por las improvisadas charlas entre pasillos y por su contagioso sentido del humor.

También debo agradecer a la empresa Dynatech, Dynamics & Technology, S. L., y en especial a Ramón del Cacho su gran dedicación al proyecto, en ocasiones más allá del deber. Ramón: tu tenacidad y conocimientos son admirables; ha sido todo un lujo poder trabajar contigo. A Miguel Angel Gil y Tomás Bretón, técnicos de taller, gracias por vuestra disposición y maestría para hacer mis cosas raras. A Ismael Asensio, del Servicio de Mecánica de Precisión, siempre con una sonrisa y buen carácter, aportando ideas útiles. Sin vuestro buen hacer, esto habría sido muchísimo más difícil.

Con todo lo que he pasado estos años de doctorado, esta tesis no habría

llegado a buen fin sin el apoyo de mi esposa, Maricarmen. Gracias por levantarme cada vez que tropezaba, por tu inmenso apoyo moral y por tantas horas que has cedido para que pudiera llevar esto a término. Gracias también a mis hijos, Valero y María, que con tanta comprensión han cedido también buena parte de su merecida atención, y que en tantas ocasiones me han ofrecido su ayuda y me han empujado a seguir adelante. Mil gracias a los tres faroles que alumbran mi camino. Ya es momento de recuperar la atención perdida.

Gracias también a mis hermanos por su paciencia conmigo en los últimos meses... a mis sobrinos, y en especial, a mi sobrino Eduardo, que pasó por este trance hace ya unos años, pero en una edad y condiciones que no tenían nada que ver con mi caso. Aún así, su experiencia compartida siempre ha sido de gran ayuda.

No puedo puedo terminar sin recordar a aquellos que vieron el inicio del camino pero que, lamentablemente, no han podido ver el final de este camino. A mi suegro, Jose Luis, persona sencilla y de gran corazón, que cuidó de sus nietos cuando era necesario mientras pudo. Mis padres, Pedro e Isabel, a quienes debo todo y nunca podré agradecer lo suficiente; y mi tía Carmen, que fue siempre mucho más que una tía. Su apoyo y cariño incondicionales fueron siempre una constante, y piedra angular de lo que soy. Gracias de todo corazón.

Dicen que cuando se cierra una puerta se abre una ventana, y con todo lo que está pasando hoy en día, las ventanas están siempre abiertas. Tan sólo hay que apuntar bien para pasar siempre por el centro del hueco.

Finalmente, como es preceptivo, termino agradeciendo el apoyo económico sufragando tanto los equipos desarrollados, como mi propio salario a:

- BSH Electrodomesticos España S.A., por sufragar el coste material de los equipos desarrollados con esta tesis, y mi salario buena parte del tiempo mediante el proyecto de investigación 2013/0011 (Elementos para un sistema de refrigeración magnética en el rango de temperatura de frigoríficos),
- Ministerio de Ciencia, Innovación y Universidades (MICINN) and FEDER, project code MAT2017-86019-R.